First-Principles Electrochemical Modeling of Hydrogen Evolution Reaction

by

Timothy T. Yang

Bachelor of Science, Physics, University of California, Santa Barbara, 2013

Master of Science, Materials Science and Engineering, University of Pittsburgh, 2017

Submitted to the Graduate Faculty of the

Swanson School of Engineering in partial fulfillment

of the requirement for the degree of

Doctor of Philosophy

University of Pittsburgh

2023

UNIVERSITY OF PITTSBURGH

SWANSON SCHOOL OF ENGINEERING

This dissertation was presented

by

Timothy T. Yang

It was defended on

May 10, 2023

and approved by

Jung-Kun Lee, Ph.D., Mechanical Engineering and Materials Science

Markus Chmielus, Ph.D., Mechanical Engineering and Materials Science

James R. McKone, Ph.D., Chemical and Petroleum Engineering

Dissertation Director: Wissam A. Saidi, Ph.D., Mechanical Engineering and Materials Science

Publications

1. **Timothy T. Yang** & Wissam A. Saidi, Tuning the Hydrogen Evolution Activity of β-Mo_2C Nanoparticles *via* Control of their Growth Conditions, Nanoscale 2017, 9, 3252-3260
2. **Timothy T. Yang**, Teck Leong Tan & Wissam A. Saidi, High Activity toward the Hydrogen Evolution Reaction on the Edges of MoS_2-Supported Platinum Nanoclusters using Cluster Expansion and Electrochemical Modeling, Chem. Mater. 2020, 32, 3, 1315-1321
3. **Timothy T. Yang** & Wissam A. Saidi, Graphene Activation Explains the Enhanced Hydrogen Evolution on Graphene-Coated Molybdenum Carbide Electrocatalysts, J. Phys. Chem. Lett. 2020, 11, 7, 2759-2764
4. Boao Song, Yong Yang, Muztoba Rabbani, **Timothy T. Yang**, Kun He, Xiaobing Hu, Yifei Yuan, Pankaj Ghildiyal, Vinayak P. Dravid, Michael R. Zachariah, Wissam A. Saidi, Yuzi Liu & Reza Shahbazian-Yassar, *In Situ* Oxidation Studies of High-Entropy Alloy Nanoparticles, ACS Nano 2020, 14, 11, 15131-15143
5. Boao Song, **Timothy T. Yang**, Yifei Yuan, Soroosh Sharifi-Asl, Meng Cheng, Wissam A. Saidi, Yuzi Liu & Reza Shahbazian-Yassar, Revealing Sintering Kinetics of MoS_2-Supported Metal Nanocatalysts in Atmospheric Gas Environments *via Operando* Transmission Electron Microscopy, ACS Nano 2020, 14, 4, 4074-4086
6. Boao Song, Yong Yang, **Timothy T. Yang**, Kun He, Xiaobing Hu, Yifei Yuan, Vinayak P. Dravid, Michael R. Zachariah, Wissam A. Saidi, Yuzi Liu & Reza Shahbazian-Yassar, Revealing High-Temperature Reduction Dynamics of High-Entropy Alloy Nanoparticles *via In Situ* Transmission Electron Microscopy, Nano Lett. 2021, 21, 4, 1742-1748

7. **Timothy T. Yang**, Rituja B. Patil, James R. McKone & Wissam A. Saidi, Revisiting Trends in the Exchange Current for Hydrogen Evolution, Catal. Sci. Technol. 2021,11, 6832-6838
8. **Timothy T. Yang** & Wissam A. Saidi, Reconciling the Volcano Trend with the Butler-Volmer Model for the Hydrogen Evolution Reaction, J. Phys. Chem. Lett. 2022, 13, 23, 5310-5315
9. Wissam A. Saidi, Tarak N. Nandi & **Timothy T. Yang**, Designing Multinary Noble Metal-Free Catalyst for Hydrogen Evolution Reaction, Electrochem Sci Adv. 2022, 00, esa12248
10. **Timothy T. Yang**, Anqi Wang, Stephen D. House, Judith Yang, Jung-Kun Lee & Wissam A. Saidi, Computationally Guided Design to Accelerate Discovery of Doped β-Mo_2C Catalysts toward Hydrogen Evolution Reaction, ACS Catal. 2022, 12, 19, 11791-11800
11. **Timothy T. Yang** & Wissam A. Saidi, Simple Approach for Reconciling Cyclic Voltammetry with Hydrogen Adsorption Energy for Hydrogen Evolution Exchange Current, J. Phys. Chem. Lett. 2023, 14, 18, 4164–4171

First-Principles Electrochemical Modeling of Hydrogen Evolution Reaction

Timothy T. Yang, Ph.D.

University of Pittsburgh, 2023

Green hydrogen, a clean and renewable energy carrier, is a sought solution for decarbonization and meeting net-zero greenhouse gas emissions by 2050. The central challenge in producing green hydrogen is to improve electrolysis performance via designing low-cost, high-efficient catalysts for hydrogen evolution reaction (HER) – the cathodic reaction in water splitting.

First-principles simulations provide a simple, yet effective, strategy to screen and identify HER catalysts. For the past two decades, the computational hydrogen adsorption free energy, proposed by Nørskov, has been the norm to gauge the exchange current – the electrochemical current that is generated at zero overpotential and is analogous to the reaction rate. However, this model misses a linkage with the fundamentals of electrochemistry and notably leads to inaccurate predictions of experimental measurements.

My research aims to develop an easy-to-compute model for HER exchange currents building on the Butler-Volmer relation for a one-step, one-charge transfer process. I show that the exchange current is solely a function of the hydrogen adsorption free energy that can be obtained from first-principles methods. Benefiting from an absolute rate constant and the universality of the transfer coefficient, the new model successfully predicts the experimental exchange currents within two-orders of magnitude for various catalysts. This model is further validated by employing a data-driven approach based on experimental cyclic voltammograms – current-potential characteristics obtained from analytical measurements. Beyond Nørskov's approach, the new model, with its rigorous linkage to theoretical electrochemical methods, not only boosts the

prediction accuracy of the exchange current, but also addresses several decades-long controversies in the field.

Using this model in conjunction with first-principles, *ab initio* thermodynamics, and cluster expansion, I determine the catalytic activity towards hydrogen evolution of several low-cost novel catalysts, focusing on molybdenum carbides (Mo_yC). Computational screening shows that doping with titanium or iridium, and the coupling of Mo_yC with graphene increase the HER activity of Mo_yC. These findings are validated experimentally and further confirm the high fidelity of the model. In addition, my overarching theoretical approach for developing the model is transferable to other electrochemical reactions.

Common Abbreviations and Symbols

DFT	density functional theory
NEB	nudged elastic band
OER	oxygen evolution reaction
SHE	standard hydrogen electrode
rds	rate-determining step
CV	cyclic voltammetry
CVs	cyclic voltammograms
BV	Butler-Volmer
VASP	Vienna *Ab Initio* Simulation Package
PBE	Perdew-Burke-Ernzerhof exchange-correlational functional
RPBE	Revised Perdew-Burke-Ernzerhof exchange-correlational functional
vdW	van der Waals
Pt	platinum
Mo_yC	molybdenum carbides
NPs	Nanoparticles
ΔG_{H}	hydrogen adsorption free energy from first-principles
α	transfer coefficient for a one-charge, one-electron transfer process
j_0	exchange current
η	overpotential
k_B	Boltzmann constant
F	Faraday constant
f	reduced Faraday constant
T	temperature
V_{SHE}	potential vs. standard hydrogen electrode
V	volt
eV	electron volt
H^+	proton
H^*	adsorbed hydrogen
H_2	hydrogen gas
e^-	electron
e	electron charge

Table of Contents

List of Tables

List of Figures

Preface

I would like to express my deepest gratitude to all those who have supported me throughout my journey in completing my Ph.D. research and this dissertation. First and foremost, I am immensely grateful to my advisor, Professor Wissam A. Saidi, for his unwavering guidance, invaluable expertise, and continuous encouragement. His dedication to my research, insightful feedback, and commitment to my academic growth have been instrumental in shaping this dissertation and shaping me as a scholar. I am truly fortunate to have had his mentorship.

I extend my sincere appreciation to the members of my dissertation committee, Professors Jung-Kun Lee, Markus Chmielus, and James R. McKone. Their expertise, constructive criticism, and thought-provoking questions have significantly enriched my research. I am grateful for their time, expertise, and valuable suggestions that have contributed to the overall quality of this work. In addition, I express my deepest appreciation to Professor Brian Gleeson, who gave me the opportunity to start my academic journey in the department of the Mechanical Engineering and Materials Science at the University of Pittsburgh

Lastly, my gratitude extends to my family and friends, whose unwavering support, love, and understanding have sustained me throughout this challenging journey. Their belief in my abilities and encouragement during moments of self-doubt have been invaluable. I am forever grateful for their presence in my life.

Thank you all for your unwavering support and encouragement.

Timothy T. Yang

1-0 Introduction

One of the critical challenges in realizing net zero emissions of greenhouse gases by 2050 is to establish hydrogen economy, especially for reducing the cost for green hydrogen production. In this chapter, I will briefly discuss the environmental issues and the current stage of the developments of catalysts for hydrogen evolution reaction. Further, I will touch on the basic concepts of experimental and first-principles studies on catalysts for hydrogen evolution reaction. This chapter underscores the importance of catalyst development for hydrogen evolution reaction as well as providing a basic understanding of my research topics.

1-1 Environmental Issues

The greenhouse effect traps solar radiations inside the Earth's atmosphere providing suitable temperatures for living conditions. However, greenhouse gases, such as carbon dioxide, methane, nitrous oxide and fluorinated gases produced from human activities, trap excess heat in the atmosphere and cause climate change - a long-term shift in weather patterns that may severely impact the lives on Earth. To date, the global averaged surface temperature has risen more than 1℃ since 1970s[13] that resulted in a decrease of artic sea-ice extent from 7 to 5 million square kilometer, as well as a new record high of global sea level (3.6 inch) measured in 2020.[14] While this problem has been noticed as far back as 1896 when Svante Arrhenius published a paper to quantify the impact of carbon dioxide on the atmosphere[15], the global emission of carbon dioxide, which encompasses over 70 weight-percent of the greenhouse gases in each year, has been rising

by about 1% per year since 1960, and nearly 78% greenhouse-gas emissions were contributed by fossil fuels each year from 1970 to 2010.[16-18]

To replace fossil fuels as energy sources, replenished natural sources, such as sun light, wind and water, can generate renewable energies with no greenhouse-gas emissions. One of the most potential solutions is using hydrogen as an energy carrier due to its high gravimetric caloric value of 120 MJ kg^{-1}.[19] Currently, over 90% of hydrogen is produced from fossils through natural gas steam reforming, naphtha/oil reforming, and coal gasification. Only 10% of hydrogen is generated from water electrolysis – a sustainable, renewable, greenhouse gas-free process to produce hydrogen by splitting water molecules into hydrogen and oxygen.[20]

1-2 Water Electrolysis

Hydrogen with a 99.9% purity can be produced through water electrolysis,[21]

$$H_2O_{(liquid)} \rightarrow H_{2(gas)} + \frac{1}{2}O_{2(gas)}$$

An energy input of 237.1 kJ/mol is required to drive the water electrolysis at standard conditions, which is equivalent to 1.23 V.[22,23] A typical water electrolysis proceeds in an electrochemical cell, which is composed of an anode and a cathode immersed in an electrolyte. At the anode, $H_2O_{(liquid)}$ splits into H^+ and $O_{2\,(gas)}$ through oxygen evolution reaction (OER). The electrolyte shuttles H^+ to the cathode to generate $H_{2(gas)}$ through the hydrogen evolution reaction (HER). In an acidic electrolyte, the half-reactions are,

$$H^+ + e^- \rightarrow \frac{1}{2}H_{2(gas)} \qquad \text{(HER)}$$

$$H_2O_{(liquid)} \rightarrow 2H^+ + \frac{1}{2}O_{2(gas)} + 2e^- \quad \text{(OER)}$$

In alkaline electrolyte, the half-reactions are,

$$H_2O_{(liquid)} + e^- \rightarrow \frac{1}{2}H_{2(gas)} + OH^- \quad \text{(HER)}$$

$$2OH^- \rightarrow \frac{1}{2}O_{2(gas)} + H_2O_{(liquid)} + 2e^- \quad \text{(OER)}$$

There are two reaction pathways for HER namely the Volmer-Tafel or the Volmer-Heyrovsky. In acidic media, the elementary steps are

$$H_3O^+ + e^- \leftrightarrow H^* + H_2O \quad \text{(Volmer)}$$

$$H_3O^+ + e^- + H^* \leftrightarrow H_2O + H_2 \quad \text{(Heyrovsky)}$$

$$H^* + H^* \leftrightarrow H_2 \quad \text{(Tafel)}$$

where H^* indicates hydrogen atom in the adsorbed state. In alkaline solution, the elementary steps,

$$H_2O + e^- \leftrightarrow H^* + OH^- \quad \text{(Volmer)}$$

$$H_2O + H^* + e^- \leftrightarrow H_2 + OH^- \quad \text{(Heyrovsky)}$$

$$H^* + H^* \leftrightarrow H_2 \quad \text{(Tafel)}$$

Both of the Volmer and Heyrovsky reactions describe reduction processes of hydrogen atoms resulting in adsorbed hydrogen or hydrogen gas, respectively. The Tafel reaction describes the formation of hydrogen gas from the combination of hydrogen atoms in adsorbed state. The reverse of the HER is called the hydrogen oxidation reaction (HOR), which follows the same elementary steps as listed above except in reverse order. The elementary steps of OER can be found elsewhere (e.g.,[24]) as we are only focusing on HER.

Catalysts play an important role to increase the rate of the reaction. For OER, transition metal oxides are promising catalysts. For example, three-dimensional transition metals hydr(oxy)oxides[25-29] and perovskite materials ABO_3 in alkaline solution. (A: alkali earth or rare

Table 1-1. Recent studies on HER catalysts designed for acidic and basic electrolytes with the reported exchange current densities j_0 (A/cm^2) and the potential to generate the exchange current density of 10 mA/cm^2 (η_{10} in mV).

Catalyst	j_0 (A/cm^2)	η_{10}	Electrolyte	Ref.
Ru-Based Catalysts				
Carbon supported Ru Nanocrystal	1×10^{-3}	n/a	0.5 M KOH	[44]
Ru Nanoclusters Supported on N-Doped Carbon	6×10^{-3}	13	1.0 M KOH	[45]
RuP Clusters Encapsulated in Few Layers of N, P-Doped Carbon	3×10^{-3}	15.6	0.5 M H_2SO_4	[46]
Ru Nanoparticles Attached on MoO_2 Nanoparticles	4×10^{-3}	16	1 M KOH	[47]
Ru Nanoparticles Anchored on Nickle-Metal–Organic Hybrids	3×10^{-3}	22	1 M KOH	[48]
Metal Phosphates				
Nickel Di-Phosphide Composites	*n/a*	134	1 M KOH	[49]
Hierarchical FeNiP/MoOx supported on NiMoO4 Nanorods	3×10^{-3}	20	1 M KOH	[50]
High-entropy Metal Phosphorus Tri-Chalcogenides Nanosheets	9×10^{-4}	65.9	1 M KOH	[51]
Molybdenum Carbides and Sulfides				
MoS_2 (002) and α-MoC (111) In-Plane Heterostructures	n/a	78	0.5 M H_2SO_4	[52]
MoS_2 Monolayer	9×10^{-4}	201	0.5 M H_2SO_4	[53]
Porous Nanostructure β-Mo_2C with a 575 V Lamp Flash	n/a	160	1 M H_2SO_4	[54]
Porous High Surface Area Molybdenum Carbide Aerogel	2×10^{-2}	185	0.5 M H_2SO_4	[55]
MoS_2 Basel Plane with Sodium Dodecyl Sulfate in Electrolyte	n/a	130	0.5 M H_2SO_4	[56]
Single-Atom Platinum				
Single-Atom Pt Immobilized NiO/Ni Heterostructure	21 (A/mg^2 Pt)	26	1 M KOH	[57]
Single-Atom Pt stabilized on Graphene with Chloride Ligands	1×10^{-3}	n/a	0.5 M H_2SO_4	[58]
Others				
Mo1−xNbxSe_2 Nanosheets with Vacancies and Adatom Defects	n/a	140	0.5 M H_2SO_4	[59]
Gold–Rhodium Core–Shell Nanoflowers	n/a	170	1 M KOH	[60]

earth cation; B: 3-d transition metal cation).[30-32] In acidic media, ruthenium and iridium oxides are potential catalysts for OER.[33-37] Since the mid-20th century, platinum has been considered to be the most effective HER catalyst.[38-40] However, platinum is one of the rarest elements with 0.4 μg/kg in earth crust,[41] and thus has a high price that is comparable with gold.[42] In addition, platinum can easily be oxidized in both alkaline and acidic media.[43]

To reduce the use of platinum as HER catalysts, on-going research focuses on several approaches including 1) searching for earth-abundant efficient catalysts such as, molybdenum carbide and molybdenum sulfides, 2) developing low-cost heterostructures as catalysts, 3) refining the morphology of catalysts, and 4) reducing platinum content by stabilizing platinum atoms or platinum nanoclusters on two-dimensional materials including graphene, graphene oxides and carbon matrix.[57,58] Table 1-1 shows some recent studies on HER catalysts in acidic and alkaline media including the two most general experimental descriptors for HER rates: the exchange

current densities and the overpotential at 10 mA/cm^2 (η_{10}). The exchange current density is the current density generated from HER at zero overpotential and η_{10} is the potential required for generating 10 mA/cm^2 current density. The convention of η_{10} is based on designing the solar cell systems with 10% efficiency of solar-to-fuels conversion using 10 mA/cm^2 current density.[61]

1-3 Experimental Study on the Hydrogen Evolution Reaction

In electrochemical analysis, HER activities are measured using a three-electrode system composed of the working, auxiliary and reference electrode. There is a power supply that activates HER between the working electrode and the auxiliary electrode, and the voltage at the working electrode is referenced with respect to the reference electrode. The working electrode is made of the catalyst under investigation, and the auxiliary electrode (counter electrode) is used to regenerate HER redox couples. There are three common reference electrodes: the *normal hydrogen electrode* (NHE)

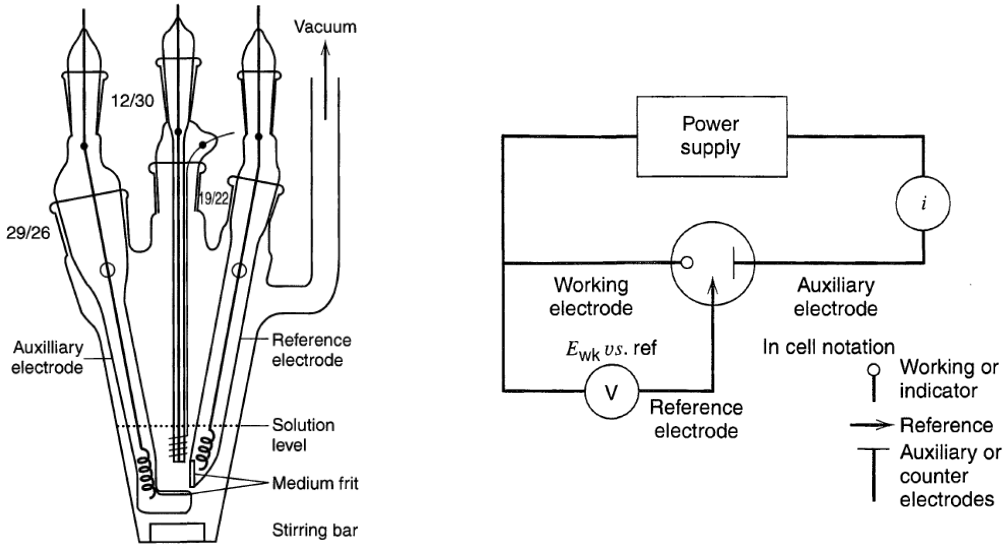

Figure 1-1. Schematic of three-electrode system. The figures are obtained from the chapter 1 in Reference [1].

is a platinum electrode that undergoes the reaction $H^+ \rightarrow H_{2(gas)}$ with H^+ in one normal concentration. If hydrogen gas is bubbling at standard conditions of 25˚C at 1 atm from 1 molarity of proton, the reference electrode is called the *standard hydrogen electrode* (SHE). In more practical situations with varying pH values or proton concentration, the *reversible potential electrode* (RHE) is usually used as a reference electrode, obtained from the NHE as $E_{RHE} = E_{SHE} - 0.059 \times pH$ where $E_{SHE} = 0$ V by definition.[1]

Cyclic voltammetry is a technique to study HER current-voltage characteristics (cyclic voltammogram) by applying a voltage $E(\tau)$ as a function of time τ between the working and auxiliary electrode. Figure 1-2 shows a cyclic voltammogram for HER/HOR on low-index single-crystal platinum surfaces in acid solution at room temperature. The sign conventions for cathodic and anodic currents are negative and positive, respectively. Near 0 V vs. RHE, HER and HOR are reversible; the current densities generated from the two reactions are equal however opposite, thus leading to a zero total current density. At a potential above/below 0 V vs. RHE, an overpotential

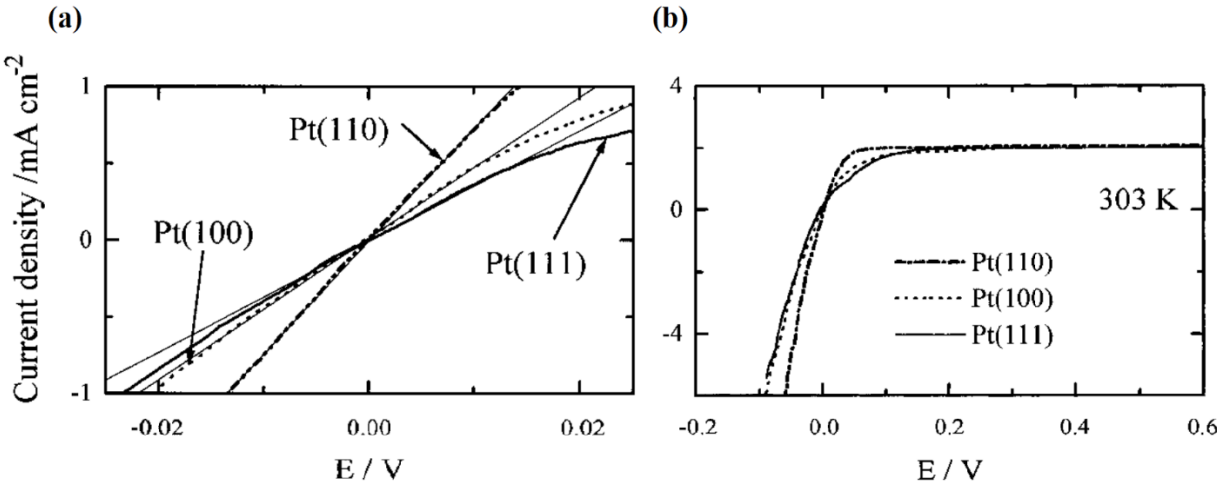

Figure 1-2 (a). The cyclic voltammogram of HER and HOR on platinum electrodes with the exposed (110), (100) and (111) surfaces at 303 K in 0.05 M H_2SO_4. **(b)** The Tafel plot of the HER and HOR of the three surfaces in 0.05 M H_2SO_4 at 274 K. Figures adapted from Ref.[5].

drives the HOR/HER current density linearly with positively/negatively increasing potential. At 0.5 V vs. RHE, HOR current density saturates at a constant value of ~2 mA/cm^2 due to the diffusion limit of H_2.

Tafel analysis provides useful information of HER kinetics. There are two important experimental descriptors that can be obtained from Tafel analysis namely the exchange current density and the Tafel slope. The Tafel slope is defined as the ratio of the logarithm of current density to the overpotential in the linear region near the reversible potential. The value of the Tafel slope is typically used to infer the reaction mechanism: For HER, the values of 120, 40 or 30 mV/dec indicates respectively that the rate-determining step is the Volmer, Heyrovsky or Tafel reaction.[62] Figure 1-3(b) plots the Tafel slope for HER/HOR in alkaline solution, as obtained by taking the logarithm of the current densities from the cyclic voltammogram of Figure 1-3(a). In Figure 1-3(b), the exchange currents can be found by extrapolating the linear regions ($-0.2 <$ V vs. RHE < -0.1) of the HER currents to 0 V vs. RHE. On platinum with (110), (100) and (111) surface terminations, the exchange current density is 7×10^{-4}, 4×10^{-4} and 7×10^{-5} A/cm^2, respectively. The slope of the extrapolated lines is 140 mV/dec indicating that the reaction

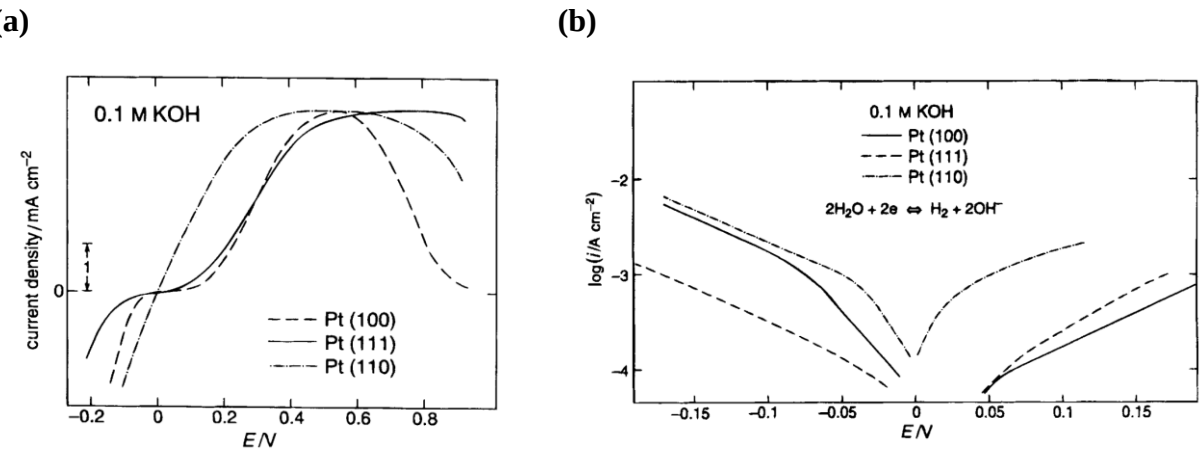

Figure 1-3. (a) The cyclic voltammogram and **(b)** The Tafel plots for the HER and HOR on (100), (111) and (110) platinum surfaces in 0.1 M KOH at 3600 rpm. Figures adapted from Ref. [4].

mechanism is more likely to be the Volmer-Tafel with the Volmer reaction as the rate-determining step. As the analytical current density encompasses all possible reaction pathways, the slope is not equal to the theoretical value of 120 mV/dec.

1-4 First-Principles Investigations of Hydrogen Evolution Reaction

First-principles calculations have been extensively applied for examining the HER kinetics on various systems. Following the Sabatier's principle stipulates that the maximum catalytic rate takes place for moderate interactions between the reactants and catalyst,[63] Nørskov et. al proposed one of the most popular frameworks to predict the HER rate using the hydrogen adsorption free energy ΔG_{H} , typically computed using density functional theory (DFT).[7] ΔG_{H} quantifies the thermodynamic accessibility from hydrogen atoms in proton state to gas state; for $\Delta G_{\mathrm{H}} = 0$, HER has the maximum activity, as with the case of platinum electrodes. When ΔG_{H} is positively or

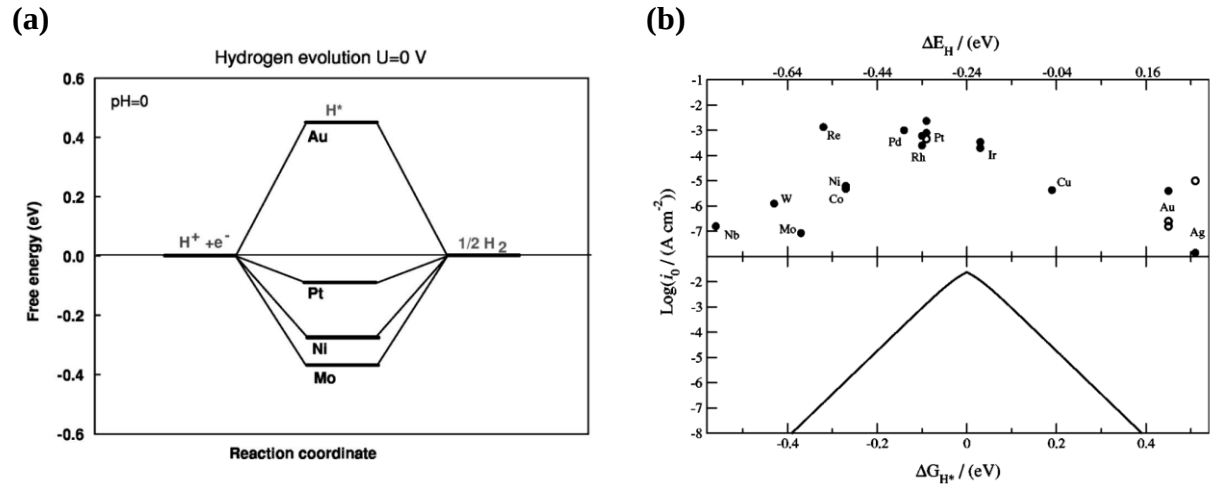

Figure 1-4. (a) Free energy diagram for hydrogen evolution reaction on four transition metals. **(b)** The correlation between the exchange current densities of transition metals and the DFT based hydrogen adsorption free energy ΔG_{H} and hydrogen adsorption energy ΔE_{H}. Figures adapted from Ref. [7].

negatively away from zero, the HER rate decreases because hydrogen atoms prefer to stay respectively in either proton dissolved or gas states. Figure 1-4(a) shows the free energy along the reaction pathways for the selected metals Pt, Au, Ni and Mo. The free energy difference between the two states, $H^+ + e^-$ and H^*, or between H^* and H_2, is the hydrogen adsorption free energy ΔG_H. Figure 1-4(b) shows that the experimentally measured exchange current densities on transition metal surfaces are strongly correlated with the corresponding ΔG_H, as obtained from DFT calculations. The metal surfaces can be grouped into three categories:

1) the precious metals such as Pt, Rh, Pd and Ir that are highly HER active ($\Delta G_H \sim 0$).
2) metals such as Cu, Au and Ag that weakly interact with the reactant H^+ ($\Delta G_H > 0$).
3) metals such as Re, Ni, Co, W, Mo and Nb that strongly interact with H^+.

In addition, ΔG_H is also an indicator of the atomic positions of the HER active sites and adsorption sites. For example, the sites with the lowest ΔG_H are the most probable adsorption sites that will be occupied and the sites with ΔG_H close to zero are the HER active sites.

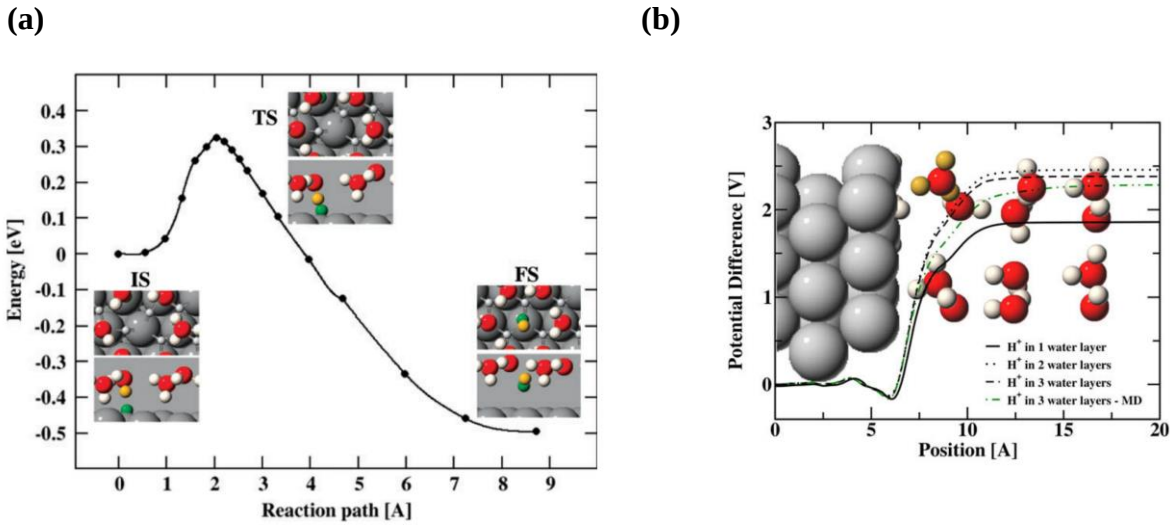

Figure 1-5 (a) The minimum reaction pathway of the Heyrovsky reaction on Pt (111) in acidic media. Figure adapted from Red. [6] **(b)** The DFT calculations on the potential of the Helmholtz layer of Pt (111) surface in acidic solution. Figure adapted from Ref. [11].

HER kinetics can also be investigated using first-principles calculations. Figure 1-5(a) shows the minimum reaction pathway of the Heyrovsky reaction on Pt (111) obtained using the nudged elastic band theory (NEB). The simulation models utilize only one water layer to model bulk water that is shown to be a good approximation. Namely, Nørskov et. al. modeled the solid-liquid interface of an electrochemical system (also known as Helmholtz layer or double layer) with one to three water layers, and showed that the potential of the interface can be well described by one water layer, as shown in Figure 1-5(b).[11] In an actual electrochemical systems, the potential in the Helmholtz double layer remains constant during redox reactions. However, the total charge remains the same in the supercell models employed computationally, which alters the potential in the simulated Helmholtz double layer along the reactions' pathways. To resolve the problem, Nørskov et. al proposed an extrapolation scheme to calculate the activation/reaction energy of redox reactions based on the findings that the free energy stored in the Helmholtz double layer and the potential of the normal hydrogen electrode can be readily obtained from first-principles calculations. Nørskov et. al further proposed a method, utilizing the partial charge transfer effects in the Helmholtz double layer, to mitigate the excessive computational cost incurred with the use of large supercell models.

We have briefly introduced the basics for investigating thermodynamics and kinetics of HER using first-principles calculations and analytical measurements. Although integrated computational and analytical approaches have been to applied to a variety of systems including two-dimensional,[64] coupled[65] and doped surfaces,[66,67] there are still considerable limitations for providing accurate HER mechanisms that may be a bottleneck for developing advanced HER catalysts. These challenges will be discussed in Chapter 2. In Chapter 3, I will focus on discussing computational strategies that are employed to design catalysts.

2-0 Research Motivations and Objectives

Activity, durability, and cost are the major considerations for designing the catalysts for the hydrogen evolution reaction (HER). Table 1-1 shows that the HER performance of the most recently developed HER catalysts still fall behind state-of-the-art platinum electrodes that have optimal exchange currents ~10^{-1} A/cm^2.[68] To reach the optimum HER catalytic activity, several strategies have been applied to study the HER using analytical and first-principles approaches, as reviewed in the previous chapter. In this chapter, I will discuss the limitations of the approaches and introduce general first-principles strategies for HER studies. Further, I will discuss a systematic plan to develop an electrochemical computational model to address and sort out the limitations.

2-1 Limitations on Investigating the HER using Analytical Approach

The cyclic voltammetry (CV) is the most general analytical strategy to directly access and quantify HER activities. However, CV suffers from several shortcomings that impact the understanding of HER at the atomic scale. One of the most obvious shortcomings is that the CV displays the current-potential characteristics from various sources including charge impedance, diffusion and the Faradaic current. While the former two can be much or less corrected, the Faradaic current reflects the overall charge transfer reactions. This hinders identifying the HER active sites, which is essential for optimizing the HER activity via e.g., tailoring synthesis strategies. In addition, many catalysts are prone to oxidization under electrochemical environments, which could lead to

misleading results when measuring the HER currents using CV. Indeed, several transition metals have been detected to be covered with oxide films such as Mo,[69,70], W[71], Nb[72], Ti[73] and Ta[74]. Also, oxide growth on platinum surfaces has been reported in both alkaline and acidic environments.[43]

Mass transfer limitation is also an issue that causes misleading HER rates especially for high HER active catalysts such as Pt, Ir and Pd. Current electrochemical analysis uses a rotating disk electrode that rotates at a fast speed to spin off the hydrogen gas on the electrode surface in order to maximize the diffusion of protons across the stagnant layer to the electrode surface. It has been argued that the exchange current densities on platinum reflect the mass transfer rate and not the true HER rate as the former is the rate-limiting step.[75] Even though ultramicroelectrodes can mitigate the mass transport limitation, only limited catalysts can be made into ultramicroelectrodes depending on particles size and stability due to fabrication difficulties.[76,77]

The HER activity may originate from nanostructure engineering rather than intrinsic properties of the catalyst such as nature of the active sites and hydrogen-catalyst interactions. For example, manipulating exposed facets[78-81] or morphology[82,83] of nanoparticles can lead to enhancements in HER activity. It has also been shown that synergistic effects[84-86,77] between two surfaces and doping mechanisms[87-90] can induce new HER active sites. Although high-resolution electron microscopy is currently the most precise tool that can be used to identify the atomic structure of catalytic surface composition,[91] the chemistry of the surface-atom arrangements can hardly be identified solely using the experimental tool. For example, the atop sites of the basal MoS_2 plane are not HER active while the bridge sites between sulfur atoms at the edge of the plane are HER active.[92,93] Such knowledge on the nature of active sites, which is extracted from first-principled methods, cannot be obtained from analytical electrochemical analysis that only provide the properties of the ensemble of different sites on the electrode.

2-2 Limitations on Investigating the HER based on First Principles

Employing the DFT-based hydrogen adsorption Gibbs free energy ΔG_{H} is one of the most efficient ways to predict the HER activity. For example, the highest HER activity corresponds to a zero value of ΔG_{H} based on the Sabatier's principle. However, it has been recently argued that platinum is not a thermoneutral catalyst with $\Delta \mathrm{G_H}$ that deviates from zero.[94-96] In addition, although a strong correlation between ΔG_{H} and the experimental exchange current densities has been found, $\Delta \mathrm{G_H}$ lacks of accuracy to predict the true experimental values.[7] For example, as shown in Figure 1-4, the errors on the predicted exchange current densities can be up to six orders of magnitude. Although the errors are significant only for the transition metals with large $|\Delta G_{\mathrm{H}}|$ that are less attractive for HER catalysts, the predicted exchange current with $\Delta G_{\mathrm{H}} \sim 0$ can still appreciably deviate from the experimental value. For example, the experimental exchange current of platinum ($\sim 10^{-1}$ A/cm^2)[68] is less than the predicted one ($\sim 10^{-2}$ A/cm^2)[7] by one order magnitude.

Analyzing the hydrogen adsorption Gibbs free energy ΔG_{H} provides a measure of the thermodynamic accessibility to HER activity. However, kinetic details such as the minimum energy pathways and the kinetic barriers cannot be easily obtained from first-principles calculations; NEB calculations suffer from artificial potential changes in the Helmholtz layer due periodic supercell models, and the simulations of electrochemical environments require extensive computational resources. In addition, the current-overpotential relation is important for applications. For example, 10 mA/cm^2 may be achieved by applying a relatively small overpotential for 10% efficient solar-to-fuels conversion in solar cell systems.[61] Although there have been several investigations on the simulations using numerical approaches such as by

Shinagawa[97], Chialvo,[98] Kucernak and Zalitis,[99] none of these previous studies provide an end-to-end approach to compute CV for HER chiefly based on *ab initio* calculations.

2-3 Research Objectives and Hypothesis

The proposal will focus on (1) developing of an easy-to-apply, first-principles electrochemical model for HER and (2) designing novel catalysts for the hydrogen evolution reaction via materials engineering based on first-principles methods.

Development of electrochemical model for HER

The Nørskov's volcano trend has been widely applied to predict HER performance by qualitatively inspecting ΔG_{H}. However, due to its empirical nature, without a clear connection to fundamental electrochemistry, it cannot be applied to quantify the exchange current as well as providing theoretical insights to HER mechanism. My research aims to develop an electrochemical model that can easily and accurately quantify the exchange current, as well as proving atomistic insights to analytical measurements and atomistic HER mechanism. To achieve the goal, I will focus on the following targets:

- Refine the experimental values of the exchange currents that are utilized for developing the Nørskov's volcano trend
- Re-analyze the relation between the reliable experimental exchange currents and the DFT-based on ΔG_{H}
- Deeply understand the theoretical insights obtained from the DFT-based hydrogen adsorption Gibbs free energy ΔG_{H}

- Deeply understand at the atomic level, theoretical insights obtained from the empirical Butler-Volmer models for HER
- Develop a DFT-based model for HER exchange current
- Develop a DFT-based model of cyclic voltammogram for HER

The Nørskov's volcano trend is developed mainly based on analyzing experimental exchange current values. However, the accuracy of these values was questioned due to experimental limitations such as mass transfer and surface oxidation (more discussion about the experimental limitation on analytical measurements are in Chapters 4, 5 and 6). Thus, I plan to first critically examine the experimental values and select the most reliable ones to re-analyze the volcano trend. Based on the Nørskov's volcano trend that shows an increasing difference between the experimental and computational values of the exchange current with large ΔG_{H}, I hypothesize that the reaction rate, that was assumed to have a constant value in the Nørskov's volcano trend, is metal dependent. Further, to explain the empirical relationship, I plan to build a new electrochemical model from a fundamental relation in electrochemistry that describes the current-potential characteristics – the Butler-Volmer equation for a one-charge, one electron transfer process. I hypothesize that the Butler-Volmer equation can be computed using first principles if the free energy of the HER elementary steps can be quantified using ΔG_{H}. The anticipated results of this research thrust are:

- The electrochemical model can quantify the HER exchange current with high fidelity using only the easy-to-compute hydrogen adsorption free energy ΔG_{H} obtained from first-principles calculations.

- The electrochemical model can be utilized to explain the analytical results that have been remaining controversial for decades because of lacking a strong reconciliation with theoretical electrochemistry. For example, there are disputes on determining the reactions' kinetics based on the Tafel analysis due to an unclear connection between theoretical-quantum mechanical concepts and analytical electrochemistry, which is also compounded by limitations from experiment and modeling.
- The electrochemical model can be utilized to predict experimental results from cyclic voltammetry using end-to-end first-principles calculations.
- The theoretical framework of utilizing the Butler-Volmer equation to build the electrochemical model for HER is general for electrochemical reactions. It is anticipated that the framework can be applied to any electrochemical reaction once an easy-to-compute descriptor for the reaction's thermodynamics is defined from first principles.

Design of low-cost materials as high-efficient HER catalysts

In my research, I aim to design low-cost molybdenum carbides for HER via coupling with graphene and doping with metals. I will focus on the following targets:

- Synergistic effects between molybdenum carbides and two-dimensional supports
- Impacts of doping on the HER mechanism of molybdenum carbides
- Strategies to mitigate surface oxidation of molybdenum carbides

I hypothesize that first-principles strategies and my new computational model can be utilized to design HER catalysts via materials engineering. For designing low-cost molybdenum carbides for HER, effective dopants are selected based on the following criteria: (1) having favorable segregation tendencies where they can be stabilized on the surface; (2) introduce new high active

sites and/or improve on the activity of the intrinsic sites; (3) can mitigate negative surface oxidation tendencies. The anticipated results of this research thrust are:

- Coupling molybdenum carbide with graphene activates graphene for HER
- Most of transition metal dopants can be stabilized into the molybdenum carbides and have favorable segregation tendencies to the surface
- Ti and Ir doping enhance intrinsic HER activity of molybdenum carbides
- Water adsorption and dissociation on the pristine molybdenum carbides decrease HER activity because oxygen and hydroxide occupy the HER active sites

Nitrogen dopants onto the substitutional carbon site can prevent formation of strong C-O bonding, and therefore mitigates water adsorption and dissociation that leads to surface oxidation.

3-0 Computational and Theoretical Methods for Investigating Hydrogen Evolution

In this chapter, I will provide a guide to systematically study the hydrogen evolution reaction (HER) using first-principles calculations that will be applied for the proposed research topics. The core of the first-principles calculations is the hydrogen adsorption free energy ΔG_{H} that can be computed using density functional theory (DFT). In conjunction with *ab initio* thermodynamic analysis, ΔG_{H} can be applied to determine hydrogen adsorption sites and HER active sites. It can also be used to study hydrogen adsorption isotherms as well as HER thermodynamic reaction free energy pathways in electrochemical environments. Further, I will introduce an extrapolated scheme in conjunction with NEB that can be employed to study HER kinetics such as the energy barriers along the HER reaction pathways.

3-1 Hydrogen Adsorption Energy

Hydrogen adsorption energy is the energy required to remove hydrogen atoms in the adsorbed state; a positive/negative value indicates that the adsorption process is endothermic/exothermic. Using DFT calculations, the averaged hydrogen adsorption energy at zero temperature limit is defined as

$$\Delta E_{\mathrm{H}^*} = \frac{1}{n}\left(E_{n\mathrm{H}/slab} - E_{slab} - \frac{1}{2}nE_{\mathrm{H}_2}\right) \tag{3-1}$$

where $E_{n\mathrm{H}/slab}$ and E_{slab} are the energies of the slab with n adsorbed hydrogen atoms and of a clean slab model, respectively. E_{H_2} is the energy of a hydrogen gas molecule. To inspect the

hydrogen adsorption with consecutively increasing n, we use the differential hydrogen adsorption energy defined as

$$\Delta E_{\mathrm{H}^*} = E_{(n+1)\mathrm{H}/slab} - E_{n\mathrm{H}/slab} - \frac{1}{2}E_{\mathrm{H}_2} \quad (3\text{-}2)$$

where $E_{(n+1)\mathrm{H}/slab}$ and $E_{n\mathrm{H}/slab}$ are the energies of the slab model with $(n+1)$ and n adsorbed hydrogen atoms, respectively. That is, this is the adsorption energy of the $(n+1)^{\text{th}}$ adsorbed hydrogen atom on a surface with n pre-adsorbed hydrogen atom, which encompasses the interactions between the pure surface and the pre-adsorbed hydrogen atoms.

3-2 Hydrogen Adsorption Gibbs Free Energy

To study hydrogen adsorption beyond zero-temperature limit, we introduce the hydrogen adsorption free energy ΔG_{H} defined as

$$\Delta G_{\mathrm{H}} = \Delta E_{\mathrm{H}^*} + \Delta E_{ZPE} - T\Delta S \quad (3\text{-}3)$$

Here, the adsorption energy can be either the averaged or the differential ΔE_{H^*} defined in Eq. (3-1) or (3-2). The zero-point energy ΔE_{ZPE} is the phonon energy difference $E_{vib} = \frac{1}{2}\sum_i h\nu_i$, where ν_i the frequency of a phonon i, between the hydrogen in adsorbed state and gas state. For hydrogen adsorption on transition metal surfaces, ΔE_{ZPE} ~0.04 eV is a good approximation irrespective of the metal surface.[2] For other systems, ΔE_{ZPE} can be substantially different from that of the transition metals. For example, ΔE_{ZPE} is ~0.2 eV for hydrogen adsorption on MoC supported graphene system.[86] The change of the entropy ΔS between the hydrogen adsorbed state $S_{\mathrm{H}^*} = 0$ and the gas state $S_{\mathrm{H}_2} = 130.68\ \mathrm{J \cdot K^{-1}mol^{-1}}$ at room temperature can be obtained from the NIST-

JANAF thermochemical tables.[100] At $T = 298$ K, we obtain $T\Delta S = T\left(S_{\mathrm{H}^*} - \frac{1}{2}S_{\mathrm{H}_2}\right) = -0.2$ eV. For $\Delta G_{\mathrm{H}} > 0$ and < 0, HER is endothermic and exothermic, respectively. For $\Delta G_{\mathrm{H}} \approx 0$, HER is thermoneutral that results with the maximum activity.

Equation (3-3) can be defined with either the Eq. (3-1) or (3-2). The former is a good approximation for hydrogen adsorption sites with similar hydrogen adsorption strength. On the other hand, the later one is convenient to study the adsorption strength of a hydrogen atom on a surface with pre-adsorbed hydrogen atoms. In the original literature of the introduction to ΔG_{H}, Nørskov used the averaged ΔE_{H^*} for pristine transition metal surfaces where the adsorption sites are identical and the hydrogen-hydrogen interactions are minimal.[2]

3-3 Nørskov's Exchange Currents Model for the Hydrogen Evolution Reaction

Derived from the basic relation that the current is linearly proportional to the concentration of reactants H^+ (H^*) for $\Delta G_{\mathrm{H}} > 0$ ($\Delta G_{\mathrm{H}} < 0$), Nørskov et al. proposed a simple kinetic model for exchange currents as a function of ΔG_{H},[2] namely,

$$j_0 = \begin{cases} ek_{ana} \exp\left(-\dfrac{\Delta G_{\mathrm{H}}}{k_B \mathrm{T}}\right) C_{tot}(1-\theta) & \text{for } \Delta \mathrm{G_H} > 0 \\ ek_{ana} C_{tot}(1-\theta) & \text{for } \Delta \mathrm{G_H} < 0 \end{cases} \quad (3\text{-}4)$$

where $\theta = K/(1+K)$ with $K = \exp(-\Delta \mathrm{G_H}/k_B T)$, and C_{tot} is the areal concentration of active sites. Note that Eq. (3-4) is equivalent to the original form[2] however C_{tot} is written explicitly. Although the model can be simply computed using a single variable $\Delta \mathrm{G_H}$, it has been seldom applied to estimate experimental exchange currents due to its low prediction accuracy of the

exchange current. Instead, most studies still rely on inspecting the value of ΔG_{H} to identify HER active sites on the catalyst.

3-4 *Ab Initio* Study of Hydrogen Adsorption in Electrochemical Environments

The hydrogen adsorption free energy ΔG_{H} can be utilized to study hydrogen adsorption profile on an electrode surface under electrochemical environments. For an electrode surface with n adsorbed hydrogen atoms with an applied potential U, we can define the total adsorption free energy as

$$\Delta G_{tot} = \sum_{n} \Delta G_{\mathrm{H}} - n|e|\eta \tag{3-5}$$

where $\eta = U - U_{SHE}$ is the overpotential, which is defined as the applied potential U with respect to the standard hydrogen potential U_{SHE}. To obtain the hydrogen coverage as a function of applied potential, we inspect the values of ΔG_{tot} with all possible n at each potential U in the potential window of interest. The hydrogen coverage that is stable at a given potential U corresponds to the configuration with the lowest ΔG_{tot} .

We apply Eq. (3-5) to study the hydrogen coverage as a function of U for Pt, Ir, Co and Ag metals as shown as the dashed lines in Figure 5-2. For Pt and Ir with $\Delta G_{\mathrm{H}} \approx 0$, the hydrogen coverage is approximately 0.5 ML at 0.1 V vs. SHE, and rapidly reaches 1 ML at 0 V vs. SHE. This is in line with the experimental cyclic voltammogram[101] showing that hydrogen atoms are adsorbed at positive potentials. For Co with $\Delta G_{\mathrm{H}} < 0$, the surface coverage reaches 1 ML at 0.25 V vs. SHE, indicating that the adsorption process is highly exothermic. On the other hand, for Ag

with $\Delta G_{\mathrm{H}} > 0$, the adsorption is endothermic with the surface reaching 0.1 ML at a very negative potential of −0.7 eV.

Among different adsorption isotherms, hydrogen coverage for the metal surfaces can be well described by the Langmuir and Frumkin isotherms defined as[2,5]

$$\begin{aligned} [\theta/(1-\theta)] &= K\exp(-Uf) && \text{(Langmuir)} \\ [\theta/(1-\theta)]\exp(-g\theta) &= K\exp(-Uf) && \text{(Frumkin)} \end{aligned} \tag{3-6}$$

where $K = \exp(-\Delta G_{\mathrm{H}}/k_B T)$ and $f = F/RT$ with F the Faraday constant. Figure 5-2 compares the Langmuir and Frumkin isotherms with the ab-initio curves. For Pt, Ir, Co and Ag, respectively, the Langmuir model can be well-fitted with the ab-initio curves as inferred from the high r-square values of 0.87, 0.97, 0.98 and 0.98. In the Frumkin isotherm, the interactions between adsorbates are described by constant g i.e., $g > 0$ and $g < 0$ for repulsive and attractive interactions, and $g = 0$ for no interactions.

3-5 *Ab Initio* Thermodynamics of Hydrogen Evolution Reaction

The thermodynamics of the HER can be analyzed from investigating the free energy of the three elementary steps,

$$\Delta g = \begin{cases} G_{\mathrm{H}^*} - (G_{\mathrm{H}^+} - |e|\eta) & \text{(Volmer)} \\ G_{\mathrm{H}_2} - (G_{\mathrm{H}^*} + G_{\mathrm{H}^+} - |e|\eta) & \text{(Heyrovsky)} \\ G_{\mathrm{H}_2} - 2G_{\mathrm{H}^*} & \text{(Tafel)} \end{cases} \tag{3-7}$$

where G_{H^+}, G_{H^*} and G_{H_2} are the free energy of the hydrogen atom at the proton, adsorbed state and gas state, respectively. To compute Δg for the three reactions, we will first build the connection with the hydrogen adsorption free energy ΔG_{H}. From Eq. (3.3), we can recognize that

ΔG_{H} is *the free energy of hydrogen atoms at adsorbed state with respect to hydrogen gas under the standard conditions of 298 K and 1 atm*, which can be expressed as $\Delta G_{\mathrm{H}} = G_{\mathrm{H}^*} - \frac{1}{2} G_{\mathrm{H}_2}$. In addition, we will also utilize the relation that $G_{\mathrm{H}^+} = |e| U_{SHE} + \frac{1}{2} G_{\mathrm{H}_2}$, where $\mathrm{G}_{\mathrm{H}^+}$ is the free energy of proton at the standard conditions. This relationship is justified given that H^+ is in equilibrium with H_2(g) at SHE. Using the above relations, we can rewrite Eq. (3-7) as

$$\Delta g = \begin{cases} \Delta G_{\mathrm{H}} + |e|\eta & \text{(Volmer)} \\ -\Delta G_{\mathrm{H}} + |e|\eta & \text{(Heyrovsky)} \\ -2\Delta G_{\mathrm{H}} & \text{(Tafel)} \end{cases} \quad (3\text{-}8)$$

3-6 Extrapolated Scheme

The minimum reaction pathways can be obtained from first-principles calculations using NEB theory. However, due to the limitation that the total charge in simulation models remains constant, that is, the potential in the simulated Helmholtz double layer changes during the reaction pathways, the energy differences between different states do not represent the true condition that the potential in the Helmholtz double layer remains nearly constant along the reaction pathways. To address such limitation, Nørskov et al. used the capacitance of the Helmholtz double layer to correct the energy differences by the following relation,

$$\begin{cases} E_2(\Phi_1) - E_1(\Phi_1) = E_2(\Phi_2) - E_1(\Phi_1) + (q_2 - q_1)(\Phi_2 - \Phi_1)/\,2 \\ E_2(\Phi_2) - E_1(\Phi_2) = E_2(\Phi_2) - E_1(\Phi_1) - (q_2 - q_1)(\Phi_2 - \Phi_1)/\,2 \end{cases} \quad (3\text{-}9)$$

where $E_1(\Phi_1)$ and $E_2(\Phi_2)$ are the DFT energies with the corresponding work functions of Φ_1 and Φ_2 at state 1 and state 2, respectively. The work function $\Phi = \mathcal{E}_V - \mathcal{E}_F$ can be obtained from calculating the fermi energy $\mathcal{E}_F$ and the vacuum energy $\mathcal{E}_V$ of the slab models. q_1 and q_2 are the

interfacial charge at states 1 and 2, respectively, that can be obtained from calculating the excess charge on the surface, e.g., using Bader charge analysis. To calculate the reaction barriers (reaction energies), states 1 and state 2 in Eq. (3-9) are specified for the initial state and transition (final) state, respectively.

To extrapolate the reaction barriers and the reaction energies to any potential, or work function Φ, we use the relation that $\frac{d\Delta E(\Phi)}{d(\Phi)} = -\Delta q$ where ΔE is $E_2(\Phi) - E_1(\Phi)$ at any Φ and $\Delta q = q_2 - q_1$. The relation is obtained from subtracting the two expressions in Eq. (3-9) and is given a physical interpretation based on the Butler-Volmer relation for a single electron transfer process assuming that the transfer coefficient is $\alpha = -\Delta q$. The standard hydrogen electrode (SHE) is the potential where the kinetic studies are of interest, and can be corelated with the work function of the metal catalyst electrode,

$$U_{\mathrm{SHE}} = \frac{\Phi - \Phi_{\mathrm{SHE}}}{e} \tag{3-10}$$

where Φ_{SHE} is the absolute potential of the standard hydrogen electrode, that is determined to be 4.44 eV experimentally.[102]

4-0 Revisiting Trends in Exchange Current for Hydrogen Evolution Reaction

Note: The chapter is based on the published manuscript *Revisiting trends in the exchange current for hydrogen evolution* (Yang, T. T., Patil, R. B., McKone, J. R. & Saidi, W. A., Catal. Sci. Technol., 2021, 11, 6832). Most of the writings are not rephrased.

Nørskov and collaborators proposed a simple kinetic model to explain the volcano relation for the hydrogen evolution reaction (HER) on transition metal surfaces in such that $j_0 = k_{ana} f(\Delta G_{\mathrm{H}})$ where j_0 is the exchange current density, $f(\Delta G_{\mathrm{H}})$ is a function of the hydrogen adsorption free energy ΔG_{H} as computed from density functional theory (DFT), and k_{ana} is a universal rate constant. From observing noticeable discrepancies between the computed j_0 using the simple kinetic model and experimental j_0 for various transition metals, and these discrepancies increase with ΔG_{H}, I hypothesize that k_{ana} is metal-dependent that can be correlated to ΔG_{H}. Focusing on the HER in acidic medium, I revisit the original experimental data and find that the fidelity of this kinetic model can be significantly improved by invoking metal-dependence on k_{ana} such that the logarithm of k_{ana} linearly depends on the absolute value of ΔG_{H}. I further confirm this relationship using additional experimental data points obtained from a critical review of the available literature. My analyses show that the new model decreases the discrepancy between calculated and experimental exchange current density values by up to four orders of magnitude.

4-1 Introduction

The Sabatier's principal is the herald of the descriptors of chemical reactions for screening the materials for the design of electrocatalysts. It states that that the optimal reaction rate corresponds to a moderate interaction between the reactant and the catalytic surface. That is, the interaction can neither be too strong nor too weak.[63] In the year of 1947, Bockris[103] studied a group of the metals which are less active for HER, and found that the overpotential showed a direct trend with the current density while a reverse trend with the work function. In addition, the trend of the overpotential and the work function was not obvious with the atomic number. between the atomic number. Ten years later, a linear trend between the HER exchange currents and the work functions of two different groups of metals were discovered by Conway and Bockris from studying the correlations between the exchange current, work function, d-band electron orbitals and the heat of hydrogen adsorption.[104] The trend between the exchange current and the work function was extensively studied by Petrenko[105] and Kita[106] in the 1970s. Not long after that, Trasatti proposed a significant work on discussing the correlations between the exchange current, the work function, the metals' zero-point energies and the Pauling electronegativities.[107]

On the other direction, a more correlated descriptor to the Sabatier's principal than the work function and the other material's properties is the hydrogen adsorption strength. In the year of 1958, Parsons proposed the descriptor Δg^0 – the standard free energy change of the reaction $H_2 \rightarrow H^*$ where H_2 and H^* are the hydrogen atoms at the gas and adsorbed phase. Following the Butler-Volmer relation, Parsons developed theoretical models for the HER reaction pathways and show the volcano trend of Δg^0 and exchange currents.[108] At $\Delta g^0 = 0$, the exchange current has the maximum value while the logarithm of exchange currents linearly decreases when Δg^0 positively and negatively deviates from zero. The same concept is independently proposed

Gerischer.[109] Trasatti[107] attempted to measure Δg^0 using the Eley-Stevenson method.[110] However, the experimental results contradicted with the theoretical values that the optimal exchange current did not appear at $\Delta g^0 = 0$.

In the year of 2004, Nørskov and collaborators proposed a computational based hydrogen adsorption free energy ΔG_{H} as a descriptor for HER. From studying a large dataset of experimental exchange current densities for transition metal surfaces, they confirmed the Parsons theoretical volcano trend by showing a zero value ΔG_{H} for the maximum exchange current density on platinum electrode. Further, they build a simple kinetic model for exchange current to explain the volcano trend.[111] We will refer to this model as the Nørskov simple kinetic model hereafter. The easy-to-compute descriptor ΔG_{H} provides a rational approach to catalyst design, which improves on expensive traditional trial-and-error methodologies. The Nørskov simple kinetic model has been widely accepted by the electrochemistry community (e.g., see Refs.[23,112,113]), and evolved as a guiding principle in the design of not only HER catalysts but electrocatalysts in general.[114-118]

Several criticisms on the Nørskov model have been made: In the Nørskov model the theoretical ΔG_{H} is obtained for the most stable pure metallic surface. However, Schmickler et.al argued that several of the metals are oxide-covered such as Ag and Mo, or exhibit amorphous surface structure. It was also discussed that the electrostatic effects on metal-water interfaces and the effects from the adsorption of water and oxygen were not included in the Nørskov model.[119] The d-band characteristics were also needed to put into consideration for the model.[120,121] To simplify all the uncertainties, Nørskov included all these effects into a rate constant, suggesting that it is universal for all metals. Peterson et.at investigated the HER kinetic pathways on Pt (111) and show that the hydrogen atoms with ΔG_{H} positively away from zero are HER active while the ones with ΔG_{H} close to a zero value are less HER active.[94] Different from the HER pathways

studied by Peterson, Nørskov et. al includes the diffusion of hydrogen atoms on Pt (111) surface to show that the hydrogen atoms with ΔG_{H} close to zero are HER active.[6] Several studies proposed HER models based on microkinetic analysis.[99,122] However, these models are generally complex with many parameters that are obtained by some approximation for by fitting to experimental data. *These caveats notwithstanding, the Nørskov model remains a leading framework for the design of HER catalysts and heterogeneous electrocatalysts in general.*[114-118]

4-2 Nørskov's Exchange Current Model

We will revisit the Nørskov's simple kinetic model and show that the calculated exchange current densities deviate from the corresponding experimental values by up to six orders of magnitude.[111] To reduce the discrepancy, we will impose an material-dependent rate constant rather than the universal constant assumed in the Nørskov model[111]. Specifically, the material-dependent rate constant is a function of $\Delta \mathrm{G_H}$. Further, we will validate the findings based on reliable data obtained from a critical review of experimental exchange current densities on transition metal surfaces from the available research literature.

In the Nørskov model, the exchange current density j_0, which describes the magnitude of the forward and reverse reaction rates at equilibrium, is defined as

$$j_0 = \begin{cases} ek_{ana} \exp\left(-\Delta G_{\mathrm{H}}/k_B \mathrm{T}\right) C_{tot}(1-\theta) & \text{for } \Delta G_{\mathrm{H}} > 0 \\ ek_{ana} C_{tot}(1-\theta) & \text{for } \Delta G_{\mathrm{H}} < 0 \end{cases} \quad (4\text{-}1)$$

where e is the charge of an electron and C_{tot} is the areal concentration of adsorption sites. Note that while the Nørskov model was presented in terms of the exchange current (e.g., amps), Eq. (4-

1) is defined in terms of the exchange current density (e.g., amps per square cm), which necessitates the inclusion of an area-normalized C_{tot}. The model is derived from the basic relation that the current is linearly proportional to the concentration of reactants H^+ (H^*) for $\Delta G_H > 0$ ($\Delta G_H < 0$). Further, k_{ana} encompasses several factors such as additional concentration factors due to applied and formal potentials, reaction rates for all elementary steps, and the effects from transfer coefficients in microkinetic models.[62,99,122] Based on *ab initio* thermodynamic analysis,[123] we assume that the hydrogen coverage is at the lowest limit for metal surfaces that repel hydrogen (i.e., with $\Delta G_H > 0$), and attains a full monolayer coverage for surfaces that are attractive to hydrogen (i.e., with $\Delta G_H < 0$). At a given temperature T, the fraction of surface occupied sites by hydrogen follows the Langmuir model such that $\theta = K/(1+K)$ with $K = \exp(-\Delta G_H/k_B T)$. k_{ana} is the rate constant that is assumed to have a universal value for all metals, which is taken as $k_{ana} = 200$ $s^{-1}site^{-1}$ by linearly fitting exchange currents to experimental data.[111] In a previous study we have shown that k_{ana} assumes a different value for β-Mo_2C nanoparticles by fitting to experimental results.[124]

The hydrogen adsorption free energy ΔG_H is obtained from the free energy difference between the hydrogen in gas phase and in adsorbed phase, which can be computed as,

$$\Delta G_H = \Delta E_{H^*} + \Delta E_{ZPE} - T\Delta S \quad (4\text{-}2)$$

where ΔE_{ZPE} is the zero-point energy that is found to be less than 0.05 eV for all metals, consistent with prior results.[111] ΔS is the entropy between the hydrogen adsorbed state and the gas state. It can be approximated as $-\frac{1}{2}S^0_{H_2}$ where $S^0_{H_2} = 1.35\times10^{-3}$ eV/K is the entropy of hydrogen in the gas phase at room temperature, as obtained from experimental measurements.[125] The hydrogen adsorption energy ΔE_{H^*} is defined as,

$$\Delta E_{\mathrm{H}^*} = \frac{1}{n}\left(E_{n\mathrm{H}/slab} - E_{slab} - \frac{1}{2}nE_{\mathrm{H}_2}\right) \tag{4-3}$$

where n is the number of adsorbed hydrogen atoms, $E_{n\mathrm{H}/slab}$ and E_{slab} are the energies of the slab with n adsorbed hydrogen atoms (H^*) and of a clean slab respectively, and E_{H_2} is the energy of H_2 in gas phase. All terms in Eq. (4-3) are directly computed from DFT. The Nørskov model of Eq. (4-1) shows that the maximum catalytic activity is at $\Delta G_{\mathrm{H}} = 0$ and the activity decreases when ΔG_{H} moves away from zero, thus reproducing the volcano relationship for exchange current and adsorption free energy ΔG_{H}.

The data labeled "Nørskov Model / Nørskov Data" in Figure 4-1 shows the experimental exchange current densities j_0 obtained from the original report vs. the computed values based on the Nørskov model. For consistency, we use the same ΔG_{H} values as in the original report to compute j_0 from Eq. (4-1). As seen in Figure 4-1, the Nørskov model qualitatively captures the

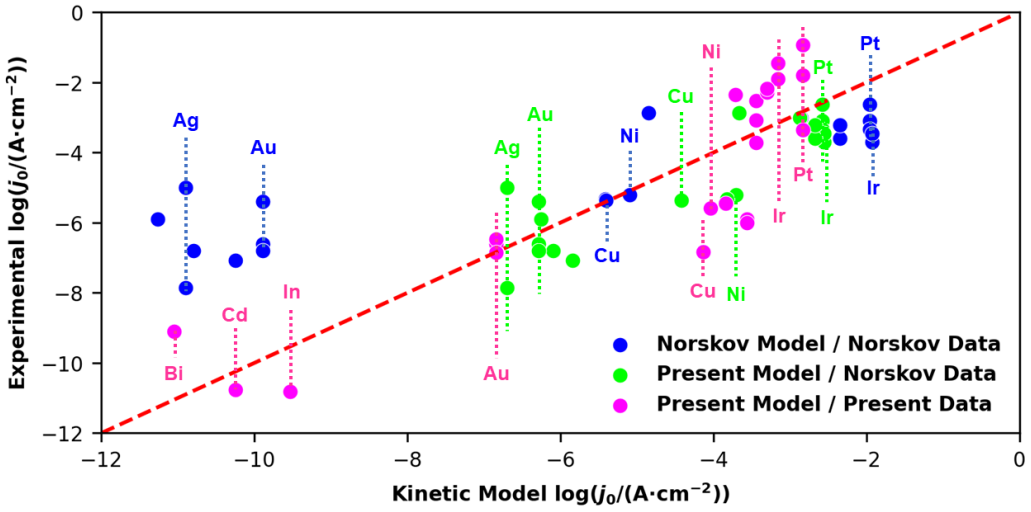

Figure 4-1. Comparison of experimental and calculated exchange current densities. We use the experimental data provided from the original work of Ref. [2](Nørskov Data) and our database (Present Data). The models from the original work (Nørskov Model) and our modified model (Present Model) are used for the calculation of j_0. To avoid clutter, we only labeled few elements belonging to three categories that are excellent (Pt and Ir), moderate (Ni and Cu) and poor (Ag, Au, Bi, In and Cd) HER catalysts. All data are shown in Table 4-3.

experimental trend for the currents among the different metals. However, the model underestimates the experimental exchange currents by 3 ~ 6 orders of magnitude for the metal surfaces with low HER activity such as W, Nb, Au, and Ag, while it is in better agreement (within two orders of magnitude) for the highly catalytic surfaces of Pt, Pd, Ir, and Rh. We further confirm that the underestimation of exchange currents on low activity surfaces is not due to experimental errors. For example, for Bi, In and Cd, the experimental values are ~10^{-10} A/cm^2 that we have carefully examined from available literature (see Table 4-7). In contrast, the corresponding exchange currents obtained from Nørskov model are ~10^{-21}, ~10^{-17} and ~10^{-19} A/cm^2, respectively. The large discrepancy between experimental and theoretical predictions, in addition to the systematic variation in the discrepancy, strongly suggests that the model does not capture one or more relevant physical parameters.

4-3 Metal-Dependent Rate Constant

In the Nørskov model, the rate constant k_{ana} is assumed to be constant for all metals, which was justified considering that k_{ana} includes mainly effects of solvent reorganization during proton transfer to electrode surfaces. However, this approximation is too simplistic given the significant differences in the HER kinetics between highly efficient surfaces such as Pt and Ir, and surfaces with lower HER activity such as W and Ag. For example, a very weak H-binding surface is likely to have a transition state that is similar in nature to a surface-bound hydrogen (the Volmer reaction as the rate-determining step), whereas a strong H-binding surface is likely to have a transition state that resembles H^+ in the electrolyte or a weakly bound H_2 (the Heyrovsky or the Tafel reaction is rate-determining). Thus, outer-sphere effects that can be rationalized as the reorganization of

solvents[126] may be more significant for strong H-binding surfaces than weak H-binding surfaces.[127] Further, other factors contribute to different HER dynamics between metal surfaces, such as the solution pH and the composition and structure of the double layer, particularly for inefficient catalysts that require very large overpotentials (and commensurately large electric fields across the double layer) to drive the HER.[128]

Re-examining the data provided in the original report[111], our analyses clearly show that a universal k_{ana} value is not justified. Figure 4-2 presents implied k_{ana} values obtained from linear regression analysis of Eq. (4-1) using experimental j_0 values and the DFT computed ΔG_{H}. This approach amounts to testing the hypothesis that deviations between the experimental and DFT-predicted j_0 using the Nørskov Model can be attributed to a metal-dependent value of k_{ana}. As seen in the figure, for both low and high coverage limits, k_{ana} varies systematically with ΔG_{H} over several orders of magnitude, where metals that weakly interact with hydrogen have low k_{ana} values and those that strongly interact with hydrogen, either repulsive or attractive, have

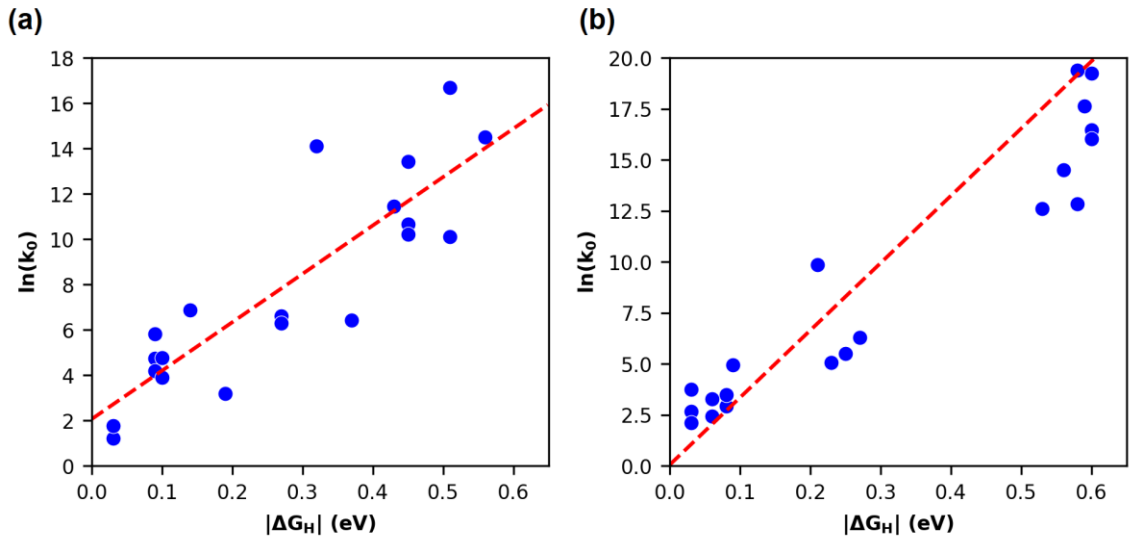

Figure 4-2. The correlation of $\ln(k_{ana})$ vs. absolute value for the hydrogen adsorption free energy $|\Delta G_{\mathrm{H}}|$ calculated from DFT for **(a)** low- and **(b)** high-coverage limits. All data including experimental currents and computed ΔG_{H} are from Ref. [7]

larger k_{ana} values. Further, as shown in Figure 4-2, we find a strong linear correlation between $\ln(k_{ana})$ and $|\Delta G_{\mathrm{H}}|$. Indeed, invoking this linear relationship is found to substantially decrease the inconsistency between the kinetic model and the experimental values, as shown in Figure 4-1 for the data labeled "Present Model / Nørskov Data". We conclude from the analysis based on data in Ref. [111] that k_{ana} is not universal but is material-specific, at least to the extent that efficient versus inefficient metals should exhibit characteristically different k_{ana} values. Notably, when restricted to a model that only incorporates metals with a similar range of H-binding energies, this effect is diminished – hence the fit is relatively good near the peak of the volcano only.

Recently, the Brønsted–Evans–Polanyi (BEP) relation, a linear relation between a reaction's free energy and its activation energy E_{avt}, is confirmed for the HER on pure metal

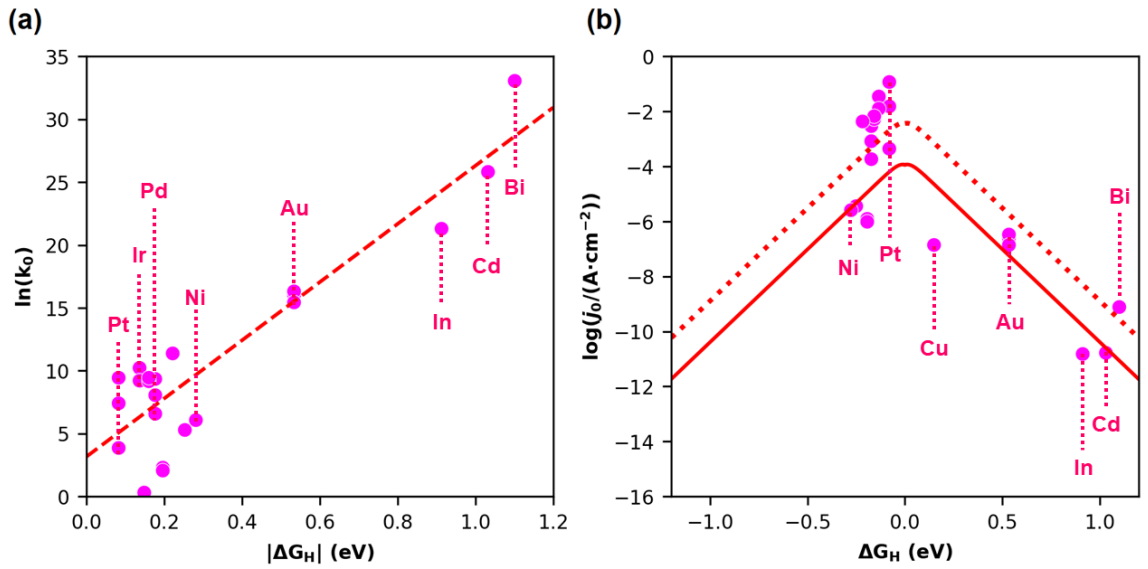

Figure 4-3. (a) Correlation between $\ln(k_{ana})$ and $|\Delta G_{\mathrm{H}}|$ using "Present Data" of Figure 4-1 (see Table 4-3). From the linear fitting, we obtain $\ln(k_{ana}) = 23.16|\Delta G_{\mathrm{H}}| + 3.17$ with a correlation factor of $r^2 = 0.82$. **(b)** The new volcano curve of j_0 based on the Present Model / Present Data. The dotted and solid red lines are obtained using Eq. (4-1) with the maximum and the minimum C_{tot} in our data, respectively.

Table 4-1. The collected exchange current densities from experiments.

Electrode	Reported j_0 (A/cm^2)	Electrolyte	Temperature	Reference
Pt (111)	4.5×10^{-4}			
Pt (100)	6.0×10^{-4}	0.05 M H_2SO_4	303 K	5
Pt (110)	9.8×10^{-4}			
Pt/C	1.6×10^{-2}	0.2 M H_3PO_4	293 K	130
Pt/C	1.2×10^{-1}	0.1 M $HClO_4$	313 K	68
Ir/C	3.6×10^{-2}	0.1 M $HClO_4$	313 K	68
Ir/C	1.28×10^{-2}	0.2 M H_2SO_4	293 K	130
Pd	1.9×10^{-4}	0.5 M H_2SO_4	Not mentioned	131
Pd/C	3.0×10^{-3}	0.1 M $HClO_4$	313 K	68
Pd/C	8.4×10^{-4}	0.1 M $HClO_4$	293 K	130
Rh/C	5.2×10^{-3}	0.1 M $HClO_4$	313 K	68
Rh/C	6.7×10^{-3}	0.1 M $HClO_4$	293 K	130
Ru	4.5×10^{-3}	1M HCl + NaCl	298 K	132
Cu	1.45×10^{-7}	0.1 N HCl	Not mentioned	133
Co	3.6×10^{-6}	1 M H_2SO_4	293 K	134
Ni	2.6×10^{-6}	0.5 M H_2SO_4	295 K	135
Au (111)	2.5×10^{-7}			
Au (100)	0.5×10^{-7}	0.1 M $HClO_4$	Not mentioned	136
Au (110)	0.3×10^{-7}			
Au (111)	3.38×10^{-7}	0.5 M H_2SO_4	Not mentioned	137
Poly Au	1.40×10^{-7}	0.1 M $HClO_4$	Not mentioned	136
Re	1.25×10^{-6}	0.5 M H_2SO_4	298 K	138
Re	1×10^{-6}	0.5 M H_2SO_4	298 K	139
Cd	1.7×10^{-11}	0.5 N H_2SO_4	Not mentioned	140
Bi	8×10^{-10}	4.8 M H_2SO_4	Not mentioned	141
In	1.51×10^{-11}	0.1 M $HClO_4$	303 K	142

surfaces[129] using a computational approach that corrects for finite-size effects in periodic supercell simulations.

For example, for the metals with $\Delta G_{\mathrm{H}} < 0$ ($\Delta G_{\mathrm{H}} > 0$), the activation barrier of the rate-limiting Heyrovsky (Volmer) reaction decreases with increasing (decreasing) ΔG_{H}. The BEP relation on HER is also confirmed experimentally on precious metals of Pt, Ir, Pd and Rh.[143] If we assume that k_{ana} of the Nørskov model is the HER reaction rate constant, it follows from Arrhenius relation that $\ln(k_{ana})$ is linearly proportional to activation energy E_{avt}, and in conjunction with the BEP relationship, we can infer the linear dependence between $\ln(k_{ana})$ and $|\Delta G_{\mathrm{H}}|$ that is obtained using our data-driven approach. Further, the enthalpy-entropy compensation where E_{avt} (or ΔG_{H}) has a linear relationship with entropy[144] suggests that $\ln(k_{ana})$ includes

effects from activation entropy that is metal-dependent[97], which also supports our findings. However, we believe that a careful derivation is needed to formally derive the dependence between k_{ana} and E_{avt}.

To further examine the metal-dependence of k_{ana}, we have compiled an additional set of experimental j_0 values from a thorough literature search (see comments and references in Table 4-7) and re-analyzed ΔG_{H} using different DFT functionals. The comparison between experimental and present model data are shown in Figure 4-1 under "Present Model / Present Data". Figure 4-3(a) shows the correlation between $\ln(k_{ana})$ and $|\Delta G_{\mathrm{H}}|$ and Figure 4-3(b) shows the volcano relationship corresponding to the new data. The DFT calculations are carried out using the Vienna Ab Initio Simulation Package (VASP).[145-147] More details about the DFT computational framework are provided in the Supporting Information. We employ the conventional[148] (PBE) and revised[149] (RPBE) Perdew-Burke-Ernzerhof exchange-correlational functional with and without van der Waals (vdW) corrections[150,151] to assess the variability of the results with the computational framework. The results shown in Figure 4-1 and Figure 4-3 are based on RPBE + vdW; however, the findings are found not to be sensitive to the functional.

The library of experimental exchange current densities[5,68,130-142] labeled as "Present Data" in Figure 4-1 and used in Figure 4-3 was collected from a larger set of prior literature reports, which were then down-selected to only those reports that minimized or otherwise accounted for the impacts of electrolyte/surface contamination, electrode roughness, and mass transfer effects. Table 4-1 summarizes experimental results. A detailed discussion of this down-selection process is included in the Supporting Information. We also chose to exclude metals that are expected to be oxidized under HER conditions in acidic solution, such as Mo, W, and Nb.[152] Finally, we added measurements on Cd, In, and Bi and Ru that were not included in Ref. [111] Figure 4-3 shows that

Table 4-2. Ten best models identified by SISSO. Primary features used are atomic radius (R), atomic number (N), atomic mass (M) period in Periodic Table (P), metal density (ρ), work function (ϕ), electron affinity (E_A), ionization energy (I), Pauling electronegativity (χ), and hydrogen adsorption energy (ΔG_H).

SISSO Model	r2
$((\chi+(\Delta G_H+\chi))+((P\Delta G_H)(\Delta G_H/\chi)))$	0.9795
$(((N\chi)(\chi/M))+((\Delta G_H E_A)(\Delta G_H/\chi)))$	0.9789
$(((PR)(P/M))((PR)(\Delta G_H+\chi)))$	0.9782
$(((M+N)(\chi/M))+((P\Delta G_H)(\Delta G_H/\chi)))$	0.9775
$((\chi(R\chi))+((R\Delta G_H)(\Delta G_H+E_A)))$	0.9768
$(((\Delta G_H+\chi)(\Delta G_H/\chi))((\Delta G_H/\chi)+(\chi/\Delta G_H)))$	0.9766
$((R(\Delta G_H+\chi))+((R\Delta G_H)(\Delta G_H/\chi)))$	0.9762
$(((\Delta G_H+\phi)(\chi/\phi))/((\chi/\phi)+(\phi/\chi)))$	0.9759
$(((R\Delta G_H)(\Delta G_H+E_A))+((R\chi)(\Delta G_H+\chi)))$	0.9753
$((\Delta G_H(\Delta G_H+\chi))((EA/\chi)+(\chi/\Delta G_H)))$	0.9751

considerably more experimental data are available for HER-active metals, which accounts for the greater density of points with small $|\Delta G_H|$. The spread in these data likely reflects uncertainty both in DFT-calculated ΔG_H and experimental j_0.[153] Nonetheless, as shown in Figure 4-3(a), there is a clear linear relationship between $\ln(k_{ana})$ and $|\Delta G_H|$ that can be described as $\ln(k_{ana}) = 23.16|\Delta G_H| + 3.17$. This is specifically evidenced in clustering of three metal groups with characteristically different H binding energies: the precious metals (Pt, Ir, Pd and Rh) near $|\Delta G_H| = 0.1$ eV, the metals near $|\Delta G_H| = 0.5$ eV, and the HER inert metals near $|\Delta G_H| = 1$ eV.

Our results clearly show that ΔG_H more accurately describes j_0 for the HER if we include an additional exponential relationship between $|\Delta G_H|$ on k_{ana} However, it is conceivable that k_{ana} and hence the exchange current density, also depends on other metal properties besides ΔG_H. For instance, previous studies postulated that the HER rate can be modeled by using atomic number, work functions, and Pauling electronegativities as material descriptors.[103-107,154,155] To investigate this, we used a machine learning approach based on SISSO (sure independence screening and sparsifying operator)[156-159] to develop an accurate and physically interpretable model for $\ln(k_{ana})$. We investigated the following primary atomic features in this analysis: empirical radius, mass, number, period in Periodic Table, electron affinity, ionization energy, and Pauling

electronegativity, in addition to the following metal features: density and work function. In the SISSO approach, potential descriptors for $\ln(k_{ana})$ are formed from the primary features with up to ten level interactions of complexity utilizing three mathematical operations (addition, multiplication, and division). The limited size of the experimental dataset (12 metals) precludes a full investigation, and thus, we used a relatively small number of primary features and mathematical operations in the construction of only one-dimensional descriptors. By searching the massive space of potential descriptors, SISSO identified many models for $\ln(k_{ana})$ that capture a large proportion of the variations among different elements. Table 4-2 lists the best ten models with correlation coefficients $r^2 > 0.975$. Notably all these models are found to depend on $|\Delta G_{\mathrm{H}}|$ indicating its prime effect on k_{ana}. However, a larger experimental database is needed to unambiguously validate the findings, and to identify other, if any, important material properties that affect k_{ana}.

In summary, we agree with the original work by Nørskov and collaborators that the trend of j_0 can be explained by a kinetic model that relies on ΔG_{H} as the sole descriptor. However, after carefully analyzing the experimental and computational results, we propose that the same kinetic model better matches with experiments over a wide range of metals by treating the logarithm of the rate constant k_{ana} as a linear function of the absolute value of ΔG_{H}.

4-4 Supporting Information

Computational Details. We use the Vienna Ab Initio Simulation Package (VASP) for the first-principles DFT calculations. We use the Perdew-Burke-Ernzerhof (PBE) exchange-correlational functional and Revised Perdew-Burke-Ernzerhof (RPBE) to solve the Kohn-Sham equations

within periodic boundary conditions, and the PAW pseudopotentials to describe electron-nucleus interactions.[160-163] The dDsC dispersion correction is used for the Van der Waals (vdW) corrections. The electronic self-consistent loops are terminated within energy-change tolerance of 1×10^{-6} eV. The periodic slab models are 3×3 supercells cleaved using the calculated bulk structures in Table 4-1 with a thickness of at least 10 Å. We used 15 Å vacuum perpendicular to the surfaces. The relaxations are done by fixing at least two layers in bulk position and relaxing the top three layers for all surfaces. We use the most stable terminations: for the metals in $Fm\bar{3}m$ and $P6_3/mmc$ phase[164,165], we use (111) and (001), respectively, (111) for Bi and In surfaces[166], and (110) for Mo surface.[167] The calculated free energy ΔG_{H} values in Table 4-4 corresponds to the hydrogen coverages of 1/9 ML or 1 ML for the surfaces with positive or negative ΔG_{H}, respectively. A single water layer is added to test the solvation effects. We find that the effects on adsorption energies are less than 0.05 eV for all the metals therefore not included. Comparing all the ΔG_{H} values for a metal, it is observed that the PBE results are systematically ~0.15 eV less than the results obtained from RPBE for the cases with and without vdW corrections. For each functional, the vdW corrections amounts to less than 0.06 eV. In summary, the trends we show in Figure 4-3 will be similar for the four cases of ΔG_{H} calculations.

Table 4.3. Bulk structures obtained with PBE and RPBE functionals.

	K-points	Phase	PBE	RPBE
Ag	12×12×12	$Fm\bar{3}m$	a=b=c=2.93 α=β=γ=60	a=b=c=2.97 α=β=γ=60
Au	12×12×12	$Fm\bar{3}m$	a=b=c=2.94 α=β=γ=60	a=b=c=2.97 α=β=γ=60
Bi	12×12×12	$R\bar{3}m$	a=b=c=4.83 α=β=γ=56.69	a=b=c=4.99 α=β=γ=54.98
Cd	12×12×12	P63/mmc	a=b=3.05; c=5.59 α=β=90; γ=120	a=b=3.10; c=5.67 α=β=90; γ=120
Co	12×12×12	$Fm\bar{3}m$	a=b=c=2.44 α=β=γ=60	a=b=c=2.46 α=β=γ=60
Co	12×12×12	P63/mmc	a=b=2.45; c=3.95 α=β=90; γ=120	a=b=2.47; c=3.98 α=β=90; γ=120
Cu	12×12×12	$Fm\bar{3}m$	a=b=c=2.57 α=β=γ=60	a=b=c=2.60 α=β=γ=60
In	12×12×12	$R\bar{3}m$	a=b=c=8.49 α=β=γ=23.139	a=b=c=8.61 α=β=γ=23.134
Ir	12×12×12	$Fm\bar{3}m$	a=b=c=2.74 α=β=γ=60	a=b=c=2.75 α=β=γ=60
Mo	8×8×8	$Im\bar{3}m$	a=b=c=2.73 α=β=γ=109.471	a=b=c=2.74 α=β=γ=109.471
Ni	12×12×12	$Fm\bar{3}m$	a=b=c=2.48 α=β=γ=60	a=b=c=2.50 α=β=γ=60
Pd	12×12×12	$Fm\bar{3}m$	a=b=c=2.78 α=β=γ=60	a=b=c=2.81 α=β=γ=60
Pt	12×12×12	$Fm\bar{3}m$	a=b=c=2.81 α=β=γ=60	a=b=c=2.82 α=β=γ=60
Re	12×12×12	P63/mmc	a=b=2.77 c=4.48 α=β=90; γ=120	a=b=2.78; c=4.50 α=β=90; γ=120
Rh	12×12×12	$Fm\bar{3}m$	a=b=c=2.70 α=β=γ=60	a=b=c=2.72 α=β=γ=60
Ru	12×12×12	P63/mmc	a=b=2.72; c=4.28 α=β=90; γ=120	a=b=2.73; c=4.30 α=β=90.000; γ=120
Nb	12×12×12	$Im\bar{3}m$	a=b=c=2.88 α=β=γ=109.471	a=b=c=2.89 α=β=γ=109.471
W	12×12×12	$Im\bar{3}m$	a=b=c=2.75 α=β=γ=109.471	a=b=c=2.76 α=β=γ=109.471

Table 4-4. The calculated ΔG_H from two functionals with and without vdW correction.

	PBE	**RPBE**	**PBE with vdW**	**RPBE with vdW**
Ag	0.416	0.565	0.381	0.527
Au	0.418	0.574	0.388	0.532
Bi	1.040	1.127	1.004	1.099
Cd	1.051	1.038	1.058	1.031
Co ($Fm\bar{3}m$)	-0.355	-0.202	-0.411	-0.252
Co ($P6_3/mmc$)	-0.352	-0.201	-0.407	-0.250
Cu	0.040	0.188	-0.002	0.147
In	0.847	0.948	0.813	0.912
Ir	-0.208	-0.081	-0.273	-0.136
Mo	-0.453	-0.321	3.620	-0.352
Ni	-0.388	-0.231	-0.445	-0.280
Pd	-0.286	-0.123	-0.359	-0.176
Pt	-0.192	-0.038	-0.232	-0.082
Re	-0.293	-0.154	-0.333	-0.195
Rh	-0.270	-0.116	-0.318	-0.159
Ru	-0.330	-0.180	-0.375	-0.220

Table 4-5. The experimental log $(j_0/(A \cdot cm^2))$ from Ref [111] (Nørskov Data) is compared with the calculated log $(j_0/(A \cdot cm^2))$ using Eq. (4-1) with constant $k_{ana} = 200$ s^{-1} (Nørskov Model) and with $k_{ana} = \exp(23.16|\Delta G_H/eV| + 3.17)$ (Present Model).

	Nørskov Data	**Nørskov Model**	**Present Model**
Pt	-3.1	-1.95	-2.58
Pt	-2.63	-1.95	-2.58
Pt	-3.34	-1.95	-2.58
Ir	-3.7	-1.93	-2.55
Ir	-3.46	-1.93	-2.55
Pd	-3	-2.85	-2.87
Pd	-3	-2.85	-2.87
Rh	-3.6	-2.35	-2.67
Rh	-3.22	-2.35	-2.67
Ni	-5.21	-5.09	-3.70
Ni	-5.2	-5.09	-3.70
Co	-5.32	-5.41	-3.82
W	-5.9	-11.26	-6.25
W	-5.9	-11.26	-6.25
Cu	-5.37	-5.41	-4.42
Mo	-7.07	-10.25	-5.84
Re	-2.87	-4.85	-3.66
Nb	-6.8	-10.80	-6.09
Au	-6.6	-9.89	-6.29
Au	-6.8	-9.89	-6.29
Au	-5.4	-9.89	-6.29
Ag	-5	-10.90	-6.69
Ag	-7.85	-10.90	-6.69

Table 4-6. The experimental $\log(j_0/(A \cdot cm^2))$from Table 4-7 (Present Data) is compared with the calculated $\log(j_0/(A \cdot cm^2))$ with $k_{ana} = \exp(23.16|\Delta G_H/\text{eV}| + 3.17)$ (Present Model). The first column label reflects experimental setup. The "Present Model" utilize slabs of well-defined terminations as described before.

	Present Data	**Present Model**
Pt (111)	-3.35	-2.83
Pt/C	-1.80	-2.83
Pt/C	-0.92	-2.83
Ir	-1.44	-3.15
Ir	-1.89	-3.15
Pd	-3.72	-3.44
Pd	-2.52	-3.44
Pd	-3.08	-3.44
Rh/C	-2.28	-3.30
Rh/C	-2.17	-3.30
Ru	-2.35	-3.71
Cu	-6.84	-4.13
Co	-5.44	-3.84
Ni	-5.59	-4.04
Au (111)	-6.60	-6.84
Au (111)	-6.47	-6.84
Poly Au	-6.85	-6.84
Re	-5.90	-3.56
Re	-6.00	-3.56
Bi	-9.10	-11.05
Cd	-10.77	-10.24
In	-10.82	-9.54

Table 4-7. The data used in Figure 4-3 in the main paper. The experimental j_0s are collected from reliable literatures listed in Table 4-6. The calculated $\ln(k_{ana})$ and ΔG_{H} are obtained using Eq. (4-1) and Eq. (4-2), respectively, in the main document. The area is determined from the structures obtained using RPBE functional listed in Table 4-3.

	ΔG_{H}	Exp. j_0	log j_0	$\ln(k_{ana})$	Area (cm^2)	# Sites	Ref.
Pt (111)	-0.082	4.50 × 10-4	-3.35	3.87	6.20×10^{-15}	9	5
Pt/C	-0.082	1.60 × 10-2	-1.80	7.43	6.20×10^{-15}	9	130
Pt/C	-0.082	1.20 × 10-1	-0.92	9.46	6.20×10^{-15}	9	68
Ir	-0.136	3.60 × 10-2	-1.44	10.27	5.89×10^{-15}	9	68
Ir	-0.136	1.28 × 10-2	-1.89	9.23	5.89×10^{-15}	9	130
Pd	-0.176	1.90 × 10-4	-3.72	6.60	6.16×10^{-15}	9	131
Pd	-0.176	3.00 × 10-3	-2.52	9.37	6.16×10^{-15}	9	168
Pd	-0.176	8.4 × 10-4	-3.08	8.08	6.16×10^{-15}	9	130
Rh/C	-0.159	5.20 × 10-3	-2.28	9.20	5.77×10^{-15}	9	68
Rh/C	-0.159	6.70 × 10-3	-2.17	9.45	5.77×10^{-15}	9	130
Ru	-0.220	4.50 × 10-3	-2.35	11.40	5.81×10^{-15}	9	132
Cu	0.147	1.45 × 10-7	-6.84	0.34	5.25×10^{-15}	1	133
Co	-0.252	3.60 × 10-6	-5.44	5.31	4.70×10^{-15}	9	169
Ni	-0.280	2.60 × 10-6	-5.59	6.09	4.89×10^{-15}	9	135
Au (111)	0.532	2.50 × 10-7	-6.60	16.05	6.86×10^{-15}	1	136
Au (111)	0.532	3.38 × 10-7	-6.47	16.35	6.86×10^{-15}	1	137
Poly Au	0.532	1.40 × 10-7	-6.85	15.47	6.86×10^{-15}	1	136
Re	-0.195	1.25 × 10-6	-5.90	2.30	6.04×10^{-15}	9	138
Re	-0.195	1.00 × 10-6	-6.00	2.07	6.04×10^{-15}	9	139
Bi	1.099	8.00 × 10-10	-9.10	33.10	1.65×10^{-14}	1	141
Cd	1.031	1.7 × 10-11	-10.77	25.83	7.49×10^{-15}	1	140
In	0.912	1.5 × 10-11	-10.82	21.33	9.30×10^{-15}	1	142

***Selection of HER Exchange Current Densities from the Research Literature*.** Experimental exchange current densities (Table 4-1) were collected from prior literature reports that showed evidence for a high level of analytical rigor. Each of the following were treated as exclusion criteria by incrementally decreasing a "rigor score" for the associated report:

- Electrolytes were not pre-purified or noted to be of highest available commercial purity
- Counter electrodes comprised materials with higher HER activity than the working electrode; these can dissolve and re-deposit on the working electrode and significantly modify its catalytic activity
- Electrode cleaning protocols (if used) involved exclusions to potentials outside the stability limits for the noted pure metal in strong acid conditions

- Evidence that the working electrode was not completely flat (e.g., roughness factor ≥ 2) and the surface roughness was not taken into consideration in the reported exchange current
- Tafel plots used for kinetic analysis did not give rise to clearly linear behavior over at least 1 order of magnitude in current density
- Mass transfer limitations convoluted kinetic analysis; note this is especially important for high-performing catalysts like Pt, whose HER activity is so high that conventional hydrodynamic methods like RDE cannot achieve a pure kinetic limit
- Control measurements using comparatively well understood HER catalysts (usually Pt) exhibited excessively low or inconsistent catalytic activity

HER measurements exhibiting one of the deficiencies listed above very often suffered from several, which resulted in a subset of measurements with high rigor and another subset with relatively low rigor. Reports with high rigor are shown in the table, and these were used for the regression analyses in the main text. Notes have also been included in Table 4-1 summarizing the associated experimental protocols, where the bold text notes relatively minor experimental concerns or incomplete information. Mo and W entries are included in Table 4-1, but these metals were not included in our analysis because neither is thermodynamically stable as a zerovalent metal under HER conditions in acid; accordingly, DFT-calculated H-binding energies are not directly comparable to experimental results, which most likely involve HER on partially oxidized Mo and W sites. Several other metals (e.g., Ni and Co) are also only stable in an oxidized form at applied potentials near 0 V vs RHE in strong acid solution, but the oxidation products are soluble (and therefore do not irreversibly modify the electrode surface) and rigorous measurements can be executed over sufficiently negative applied potentials to maintain a metallic composition.

The collected exchange current densities from experiments with comments

Electrode	Reported j_0 (A/cm^2)	Electrolyte	Temperature	Reference
Pt (111) Pt (100) Pt (110)	4.5×10^{-4} 6.0×10^{-4} 9.8×10^{-4}	0.05 M H_2SO_4	303 K	[5]
• Studied different crystal facets of Pt at different temperatures • Single crystal electrodes tested, RDE measurement • Low electrolyte concentration chosen to be able to clearly distinguish hydrogen activity • Electrode surface protected by a drop of water, luggin capillary for reference electrode to avoid Cl^- contamination • HUPD characterization correlated to the theoretical charge to determine adsorption layers • Tafel plots determined from the kinetically limited region • Exchange current densities obtained from micropolarization region • **j_0 might still contain contribution from diffusion**				
Pt/C	1.6×10^{-2}	0.2 M H_3PO_4	293 K	[130]
• Studied precious metal catalysts at different pHs • Commercial powders tested, RDE measurement • Luggin capillary, Pt counter • **Performed CVs in 0.1 M KOH prior to testing at different electrolytes (contamination risk)** • ECSA determined from HUPD peaks in 0.1 M KOH • **ECSA obtained from HUPD is 1.6 times lower than that obtained by CO-stripping** • Exchange current densities obtained from Butler-Volmer, are consistent with the measurements from H_2-pump; **may still be transport limited**				
Pt/C	1.2×10^{-1}	0.1 M $HClO_4$	313 K	[68]
• Studied precious metal catalysts at different temperatures • Commercial powders were tested in H_2 pump configuration (speeds up mass transfer) • Pt/C counter/reference electrode, scrupulous cell cleaning • ECSA calculated by CO-stripping at 293 K are consistent with TEM analysis • j_0 values were calculated by Butler Volmer and micro-polarization region, and was within 10 % error				
Ir/C	3.6×10^{-2}	0.1 M $HClO_4$	313 K	[68]
• Studied precious metal catalysts at different temperatures • Commercial powders were tested in H_2 pump configuration • **Pt/C counter/reference electrode**, rigorous cell cleaning • ECSA calculated by CO-stripping at 293 K are consistent with TEM analysis • j_0 values were calculated by Butler Volmer and the micro-polarization region and were nearly same. Oxide covering did not have a huge influence				
Ir/C	1.28×10^{-2}	0.2 M H_2SO_4	293 K	[130]
• Commercial powders tested, RDE measurement • Luggin capillary, **Pt counter** • **Performed CVs in 0.1 M KOH prior to testing at different electrolytes** • ECSA determined from HUPD peaks in 0.1 M KOH • ECSA obtained from HUPD is almost same as that obtained by CO-stripping • Exchange current density values obtained from Butler Volmer, are consistent with the measurements from H_2-pump; **may still be transport limited**				
Pd	1.9×10^{-4}	0.5 M H_2SO_4	Not mentioned	[131]
• Studied nanoporous Pd (powder) • Carbon counter, nitrogen purge, RDE measurement • **Current normalization not mentioned**, appears to be from electrode area • ECSA calculated from C_{dl} • Linear Tafel fitting				
Pd/C	3.0×10^{-3}	0.1 M $HClO_4$	313 K	[68]

- Commercial powders were tested in H_2 pump configuration
- **Pt/C counter/reference electrode**, rigorous cell cleaning
- ECSA calculated by CO-stripping at 293 K are consistent with TEM analysis
- j_0 values were calculated by Butler Volmer and the micropolarization region and were nearly same. Hydride covering did not have a significant influence

Pd/C	8.4×10^{-4}	0.1 M $HClO_4$	293 K	[130]

- Commercial powders tested, RDE measurement
- Luggin capillary, **Pt counter**
- **Performed CVs in 0.1 M KOH prior to testing at different electrolytes**
- ECSA determined from PdO peaks in 0.1 M KOH
- **ECSA obtained from HUPD is slightly lower (by 1.2 times) than that obtained by CO-stripping**
- j_0 values obtained from Butler-Volmer, consistent with the measurements from H_2-pump

Rh/C	5.2×10^{-3}	0.1 M $HClO_4$	313 K	[68]

- Commercial powders were tested in H_2 pump configuration
- **Pt/C counter/reference electrode**, rigorous cell cleaning
- ECSA calculated by CO-stripping at 293 K are consistent with TEM analysis
- j_0 values were calculated by Butler Volmer and the micropolarization region and were nearly same. Oxide covering did not have a significant influence

Rh/C	6.7×10^{-3}	0.1 M $HClO_4$	293 K	[130]

- Commercial powder tested, RDE measurement
- Luggin capillary, **Pt counter**
- **Performed CVs in 0.1 M KOH prior to testing at different electrolytes**
- Currents normalized by ECSA measured in 0.1 M KOH
- **ECSA obtained from HUPD is 1.8 times lower than that obtained by CO-stripping**
- Exchange current density values obtained from Butler Volmer, are consistent with the measurements from H_2-pump

Ru	4.5×10^{-3}	1M HCl + NaCl	298 K	[132]

- Studied Ru cylinder, mounted on ptfe cup
- **Pt counter**, separated from working electrode using frit
- Pre-electrolysis performed but **conditions are unclear** (pre-electrolysis implies rigorous purification)
- After pre-electrolysis potential sequence of +1 V vs RHE for 10 s followed by -1 V for 10 mins was repeated 6 times with final cathodic pulse for 10 minutes. **Rest potential was observed to be -1 V vs RHE**

Cu	1.45×10^{-7}	0.1 N HCl	Not mentioned	[133]

- Wire working electrode
- Graphite counter
- Pre-electrolysis was performed for several hours; **HCl electrolyte may allow for some Cu dissolution**
- Statistical analysis included

Co	3.6×10^{-6}	1 M H_2SO_4	293 K	[134]

- Studied rod electrode, electrolytically polished in H_3PO_4
- Detailed cleaning procedure followed
- Cathodically pre-polarized starting from low current density
- Overpotential increased by applying cathodic current or with several hours of electrolyte contact
- Calculated Tafel slope for the dissolution process, consistent with prior literature

Ni	2.6×10^{-6}	0.5 M H_2SO_4	295 K	[135]

- Studied electrodeposited Ni as control, **Ni could be coated with Ni^{2+} compounds**
- **Pt counter** separated from main cell using glass frit, argon purge
- Electrode was polarized at HER potentials to remove surface oxides
- Tafel plot measured in kinetically controlled regime
- **Tafel slope is higher than theoretical value; attributed to Ni oxidation**
- j_0 obtained from tafel plot

Au (111) Au (100)	2.5×10^{-7} 0.5×10^{-7}	0.1 M $HClO_4$	Not mentioned	[136]

Au (110)	0.3×10^{-7}			

- Studied single crystals with different crystal facets
- Hanging meniscus rotating disc technique, nitrogen purge, Au counter electrode
- Surface of electrode protected with electrolyte drop
- HER activity was independent of the potential history (scanning even to oxidation potentials), contrary to literature, owing to cleaner surfaces and solutions
- **Did not document detailed cell cleaning protocols**
- **Tafel slope in the low potential region is reported (< 150 mV)**

Au (111)	3.38×10^{-7}	0.5 M H_2SO_4	Not mentioned	[137]

- Studied single crystal as control
- **Pt counter**, nitrogen purge, hanging meniscus
- **Current normalized to geometric area; no ECSA**

Poly Au	1.40×10^{-7}	0.1 M $HClO_4$	Not mentioned	[136]

- Hanging meniscus rotating disc technique, nitrogen purge, Au counter electrode
- Surface of electrode protected with electrolyte drop
- HER activity was independent of the potential history (scanning even to oxidation potentials) owing to cleaner surfaces and solutions
- **Did not document detailed cell cleaning protocols**
- **Tafel slope in the low potential region is reported (< 150 mV)**

Re	1.25×10^{-6}	0.5 M H_2SO_4	298 K	[138]

- Polished wire working electrode
- **Pt counter**, hydrogen purge
- Native surface oxide formation was minimized by polarizing at -0.4 V vs NHE
- **Tafel fit included narrow range at low overpotential (-0.11 to -0.2 V vs NHE)**

Re	1×10^{-6}	0.5 M H_2SO_4	298 K	[139]

- Polished wire working electrode
- **Pt counter**, hydrogen purge
- Polarized at -0.1 V vs RHE, claim to have metallic Re
- **Current normalized to geometric area; no ECSA**

Cd	1.7×10^{-11}	0.5 N H_2SO_4	Not mentioned	[140]

- Metal wire working electrode
- Heated electrode in hydrogen
- Detailed cleaning procedure followed
- Electrolyte was purged with pre-purified nitrogen to remove excess oxygen and then purged with hydrogen
- Electrolyte was further purified by pre-electrolysis at 1 mA/cm^2 for 15 – 20 hours

Bi	8×10^{-10}	4.8 M H_2SO_4	Not mentioned	[141]

- Polished metal wire working electrode
- **Pt counter electrode**
- Held the potential at HER potential for 10 mins prior to analysis
- Tafel plot measured in kinetically controlled regime

In	1.51×10^{-11}	0.1 M $HClO_4$	303 K	[142]

- Cylindrical working electrode
- Electropolished at negative potential to remove oxide layer before analysis
- **Pt counter and reference electrode**, Luggin capillary used
- Varied electrode treatment conditions and electrolyte concentration

5-0 Reconciling Volcano Trend with the Butler-Volmer Model for Hydrogen Evolution

Note: The chapter is based on the published manuscript *Reconciling the Volcano Trend with the Butler–Volmer Model for the Hydrogen Evolution Reaction* (Timothy T. Yang and Wissam A. Saidi, J. Phys. Chem. Lett. 2022, 13, 23, 5310–5315). Most of the writings are not rephrased.

The Nørskov's volcano trend has been widely utilized to forecast new optimum catalysts in computational chemistry while the Butler–Volmer (BV) relationship is the norm to explain current–potential characteristics from cyclic voltammetry in analytical chemistry. In Chapter 4, I show that the accuracy of predicting experimental exchange currents using the Nørskov's volcano trend can be significantly enhanced when applying a metal-dependent k_{ana}. However, the empirical relation of k_{ana} as a function of ΔG_{H} has not been explained by the theoretical electrochemistry. I posit that such empirical relation can be linked with electrochemical principles based on the BV equation. Herein, I develop an electrochemical model for the hydrogen evolution reaction exchange currents that reconciles the device-level analytical chemistry, atomic-level volcano trend, and the BV relation. I show that the model is a function of the easy-to-compute hydrogen adsorption energy computed from first principles. Further, the model reproduces with high fidelity the experimental exchange currents for elemental metal catalysts over 15 orders of magnitude, and is consistent with the recently proposed analytical model based on a data-driven approach. The findings based on fundamental electrochemistry principles are general, and can be applied to other reactions including CO_2 reduction, metal oxidation, and lithium (de)intercalation reactions.

5-1 Introduction

Hydrogen evolution reaction (HER) is a critical reaction for hydrogen production using renewable water-splitting methods. Currently, the grand HER challenge is in finding low-cost and high-efficient catalysts to replace or reduce the use of precious platinum, the most efficient HER catalyst. Computational screening using first-principles quantum-mechanical approaches has been instrumental not only for identifying the HER mechanism[56,86,170-173] at the atomic scale but also in material's catalytic efficiency.[124,174-179] Central to the computational design approach, is having a predictive, accurate, and easy-to-compute model to quantify the electrochemical catalytic efficiency of new candidate materials.

Following the Sabatier's principle that the maximum reaction rate corresponds to the optimum reaction activity, Nørskov et al. proposed a computational model based on hydrogen adsorption free energy ΔG_{H} to determine HER exchange currents.[7] The Nørskov model explained the volcano trend - the optimum catalyst has a moderate adsorption strength indicated by $\Delta G_{\mathrm{H}} = 0$ while the exchange currents decrease linearly with increasing or decreasing ΔG_{H}. Such trend is obtained from a simple kinetic model assuming that ΔG_{H} is the only descriptor for exchange currents with other effects universal for all metals. The computational framework based on ΔG_{H} has been widely employed for HER catalysts design owing to the easy-to-compute descriptor, which can be obtained from first-principles quantum mechanical methods.[86,172,180-188]

Despite the success of Nørskov's volcano trend, it has been the center of several debates. For instance, whether catalysts that bind hydrogen thermoneutrally are optimum catalysts for HER was challenged. By investigating the HER kinetic pathways on Pt (111), Peterson et al. argued that the sites that bind hydrogen atoms with $\Delta G_{\mathrm{H}} > 0$ are HER active while the $\Delta G_{\mathrm{H}} \cong 0$ sites are

not.[94] Investigating the same Pt (111) surface, Nørskov et al. showed that hydrogen atoms with $\Delta G_{\mathrm{H}} \cong 0$ are HER active[6] through hopping to the sites identified by Peterson[94] with a negligible diffusion barrier. Schmickler et al. re-examined the Nørskov's volcano trend and showed that the calculated and experimental exchange current densities are off by two orders of magnitude for several metal surfaces.[119] This discrepancy is attributed to the growth of native oxide layers that cover the metal surfaces in an electrochemical environment, which are not accounted for in modeling.[119] In addition, this study argued that Nørskov's kinetic model is too simplistic and does not fully account for the electronic properties of the catalyst. In a recent study, we revisited Nørskov's model and showed that imposing a metal-dependent rate constant decreases the deviations from experimental results by up to four orders of magnitude.[189] Central to this finding was establishing a large reliable experimental data base that was employed within a statistical approach to infer the dependence. Although the revised Nørskov model significantly improves the estimation on exchange currents, it is based on a data-driven approach that lacks a theoretical background. Furthermore, one of the concerns about the original or the revised Nørskov model is that it is not reconcilable with the electrochemical modeling employed experimentally.

In analytical chemistry, HER has been widely evaluated using cyclic voltammetry that provides current-potential ($i - V$) characteristics (cyclic voltammogram) as an output of electrochemical behaviors. The norm to explain the cyclic voltammogram is the empirical Butler-Volmer (BV) relation $i \propto i_0 \exp[(\alpha_a F\eta/RT) - (\alpha_c F\eta/RT)]$ where $\alpha_{a/c}$ are the transfer coefficients for the anode/cathode reaction, F is the Faraday constant, T is the temperature, and η is the overpotential.[190,191] The exchange current i_0 is the most significant descriptor of HER rate, and $\alpha_{a/c}$ is the key indicator of HER kinetics.[62] The BV relation is not only limited to

HER[68,75,130,192-194] but is widely applied for many electrochemical reactions such as electron transfer reactions in modern lithium ion batteries[195-199] and fuel cells[200-202].

Herein, we discuss theoretical insights based on the empirical volcano trend and propose an electrochemical model for the HER exchange-currents. First, we study the dependence of ΔG_{H} on the thermodynamics of the HER pathways and show that the rate-determining step (rds) can be determined solely based on the value of ΔG_{H}. Such dependency allows us to construct an electrochemical model for exchange currents based on the BV relation for a one step, one electron transfer process. We show that the model is solely a function of ΔG_{H} and the transfer coefficient of the rds. Further, we show that the model is equivalent to the revised Nørskov model for proton adsorption process that includes the material-dependent rate constant that was proposed in a previous study based on statistical approach of experimental data[189].

5-2 Derivation of the Gibbs Free Energy for the Hydrogen Evolution Reaction

The overall hydrogen evolution reaction $\mathrm{H^+ + e^- \rightarrow \frac{1}{2} H_2}$ proceeds with the Volmer-Heyrovsky or Volmer-Tafel pathways with,

$$\mathrm{H^+ + e^- \leftrightarrow H^*} \qquad \text{(Volmer)}$$

$$\mathrm{H^* + e^- + H^+ \leftrightarrow H_2} \qquad \text{(Heyrovsky)}$$

$$\mathrm{2H^* \leftrightarrow H_2} \qquad \text{(Tafel)}$$

where $\mathrm{H^+}$, $\mathrm{H^*}$ and $\mathrm{H_2}$ are the hydrogen atoms in liquid, adsorbed and gas state, respectively. The Gibbs free energy of the three elementary reactions are,

$$\Delta g = \begin{cases} G_{\mathrm{H}^*} - (G_{\mathrm{H}^+} - |e|U) = \Delta G_{\mathrm{H}} + |e|\eta & \text{(Volmer)} \\ G_{\mathrm{H}_2} - (G_{\mathrm{H}^*} + G_{\mathrm{H}^+} - |e|U) = -\Delta G_{\mathrm{H}} + |e|\eta & \text{(Heyrovsky)} \\ G_{\mathrm{H}_2} - 2G_{\mathrm{H}^*} = -2\Delta G_{\mathrm{H}} & \text{(Tafel)} \end{cases} \quad (5\text{-}1)$$

where $\eta = U - U_{SHE}$ is the applied potential U in reference to the standard hydrogen electrode (SHE) U_{SHE}. To derive the final form in Eq. (5-1), we define $G_{\mathrm{H}^+} = |e|U_{SHE} + \frac{1}{2}G_{\mathrm{H}_2}$ as H^+ is in equilibrium with H_2(g) at SHE, and use $\Delta G_{\mathrm{H}} = G_{\mathrm{H}^*} - \frac{1}{2}G_{\mathrm{H}_2}$ as proposed by Nørskov.[7]

In the original literature, ΔG_{H} is defined as the free energy of the adsorbed state with respect to hydrogen gas under the standard conditions of 298 K and 1 atm, which is the free energy of the process $\frac{1}{2}\mathrm{H}_2 \rightarrow \mathrm{H}^*$.[7] However, this definition does not link the hydrogen adsorption from gas phase H_2 and from H^+ in acidic solution as stipulated for the overall HER. We posit that such connection can be recovered from Eq. (5-1). For the Volmer reaction, at the equilibrium potential $E = 0$ where the exchange current density is defined, $\Delta g = \Delta G_{\mathrm{H}}$ implies that the free energy change from either the gas phase or the proton phase H^+ are identical. Additionally, for $E = 0$, the opposite signs of ΔG_{H} for the Volmer and the Heyrovsky (or Tafel) suggest that the two elementary steps in a reaction pathway cannot be both endothermic or exothermic at the same time. Therefore, based solely on thermodynamics, we can posit that the Volmer reaction is the rds when $\Delta G_{\mathrm{H}} > 0$ while the Heyrovsky is the rds for $\Delta G_{\mathrm{H}} < 0$. The Tafel reaction can only be the rds at $\Delta G_{\mathrm{H}} = 0$ with additional kinetical conditions where the barrier of the Tafel reaction is the lowest among the three elementary steps. These inferences are indeed justified by the HER kinetics determined from first-principles calculations.[129] Further, the thermodynamic analysis implies that the maximum thermodynamic accessibility for any reaction pathways is at $\Delta G_{\mathrm{H}} = 0$, which agrees with Nørskov's volcano trend.[7]

5-3 Derivation of the Exchange Current Model

In general, the electrochemical current $j = e\left[C_f r_f - C_b r_b\right]$ is contributed by the forward and backward processes of a reaction, where e is the electron charge, and $r_{f/b}$ and $C_{f/b}$ are the rate constant and the reactant concentration for the forward/backward reaction, respectively. $r_{f/b}$ can be expressed with the BV equation for a *one-step, one-electron process* as,[1]

$$\begin{cases} r_f = k_0 \exp[-\alpha f\left(E - E^{0'}\right)] \\ r_b = k_0 \exp\left[(1-\alpha) f\left(E - E^{0'}\right)\right] \end{cases} \tag{5-2}$$

Here, α is the transfer coefficient, E and $E^{0'}$ are the applied and the formal potentials associated with the rds. The standard rate constant k_0 is defined when the forward r_f and backward r_b rates are the same at $E^{0'}$. Using Eq. (5-2), the total electrochemical current can be expressed as,

$$j = ek_0\left\{C_f \exp[-\alpha f\left(E - E^{0'}\right)] - C_b \exp[(1-\alpha) f\left(E - E^{0'}\right)]\right\} \tag{5-3}$$

Under the equilibrium condition $E = E_{eq}$ where E_{eq} is the equilibrium potential, j_f and j_b have equal magnitudes that lead to a zero-total current. This equality defines the exchange current density,

$$j_0 = ek_0 C_f \exp[-\alpha f\left(E_{eq} - E^{0'}\right)] = ek_0 C_b \exp[(1-\alpha) f\left(E_{eq} - E^{0'}\right)] \tag{5-4}$$

Employing the Nernst relation, $\exp[f\left(E_{eq} - E_i^{0'}\right)] = C_f / C_b$, we express the exchange current density of Eq. (5-4) as,

$$j_0 = ek_0 {C_f}^{1-\alpha} {C_b}^{\alpha} \tag{5-5}$$

which is general for any *single step, single electron transfer process*,[1] and thus can be readily applied to the Volmer and Heyrovsky reactions. In addition, from the previous thermodynamic analysis of Eq. (5-1), we show that *the total reaction rate depends on the rds* for all cases except

for the surface with $\Delta G_{\mathrm{H}} = 0$. Based on these conditions, we will utilize Eq. (5-5) for HER in an acidic environment hereafter.

For a water-solid interface that is free from the diffusion limit of H^+ and H_2, only the proton concentration $C_{\mathrm{H^+}}$ near the adsorption sites and the concentration of adsorbed hydrogen atoms $C_{\mathrm{H^*}}$ control the HER process. Therefore, we can approximate the areal concentration of the total adsorption sites as $C_{tot} = C_{\mathrm{H^+}} + C_{\mathrm{H^*}}$.[1] For the Volmer reaction, $C_f = C_{\mathrm{H^+}} = C_{tot}(1-\theta)$ and $C_b = C_{\mathrm{H^*}} = C_{tot}\theta$ where θ is the fraction of occupied sites. For the Heyrovsky reaction, $C_f = C_{\mathrm{H^*}} = C_{tot}\theta$ and $C_b = C_{tot}(1-\theta)$ as the forward reaction is controlled by the concentration of the adsorbed hydrogen atoms for proton reduction process and the backward reaction is controlled by the concentration of hydrogen gas near the empty adsorption sites. In summary, we cast the HER electrochemical exchange current model as,

$$j_0 = \begin{cases} ek_0 C_{tot}(1-\theta)^{(1-\alpha)}\theta^{\alpha} & \text{(Volmer)} \\ ek_0 C_{tot}\theta^{(1-\alpha)}(1-\theta)^{\alpha} & \text{(Heyrovsky)} \end{cases} \quad (5\text{-}6)$$

We note that the Tafel reaction is not a charge-transfer reaction hence cannot be described by the BV relation. The electrochemical model of Eq. (5-6) is general for HER with a distinct rds in acidic environment. Further, Eq. (5-6) is the central equation in our study that follows from fundamental electrochemistry principles in addition to the BV relation for a *one-step, one-electron process*. Considering that a *proton reduction process* begins with the Volmer reaction, this suggests re-writing Eq. (5-6) with H^+ concentration $C_{tot}(1-\theta)$ shown explicitly as,

$$j_0 = \begin{cases} ek_0 C_{tot}(1-\theta)(1-\theta)^{-\alpha}\theta^{\alpha} & \text{(Volmer)} \\ ek_0 C_{tot}(1-\theta)\theta^{(1-\alpha)}(1-\theta)^{(\alpha-1)} & \text{(Heyrovsky)} \end{cases} \quad (5\text{-}7)$$

To validate the new model of Eq. (5-7) and cast into a computationally tractable model, we apply the model to eight transition metal surfaces. First, we obtained the hydrogen adsorption isotherms from ab-initio thermodynamics (See Supporting Information), and compared to three isotherm

models, the Langmuir,[203-205] Frumkin[205,206] and Temkin[203,207].[208] Our analyses show that the Langmuir and Frumkin models agree well with the DFT results with a fitting confidence r^2 values over 0.87 and 0.94, respectively. In the rest of the study, we apply Eq. (5-7) based on the Langmuir model for simplicity as this form is amenable to an analytical solution. In addition, as we will show below, the Langmuir model allows us to gain more insight of the new electrochemical model and to compare with previous models.

Using the Langmuir model $\theta = K/(1+K)$ as well as defining the equilibrium constant as $K = \exp(-\Delta G_{\mathrm{H}}/k_B T)$, we write $(1-\theta)^{-\alpha}\theta^{\alpha}$ and $\theta^{(1-\alpha)}(1-\theta)^{(\alpha-1)}$ in Eq. (5-7) as,

$$j_0 = \begin{cases} ek_0 C_{tot}(1-\theta)\exp(-\alpha\Delta G_{\mathrm{H}}/k_B T) & \text{(Volmer)} \\ ek_0 C_{tot}(1-\theta)\exp(-(1-\alpha)\Delta G_{\mathrm{H}}/k_B T) & \text{(Heyrovsky)} \end{cases} \quad (5\text{-}8)$$

We note that $C_{tot}(1-\theta)$ can also be expressed as a function of ΔG_{H} using the Langmuir model. However, we explicitly include it here to show that the revised Nørskov model with metal-dependent rate constant[189], follows naturally from the new model.

To fully define the new electrochemical model of Eq. (5-8), the rate constant k_0 must be determined. We hypothesize that k_0 is metal independent based on its original definition in Eq. (5-2). To obtain the universal k_0 value, we fit the theoretical model to experimental data. Specifically, we utilize j_0 and α from an experimental data base that we previously compiled, which includes reports that minimized or otherwise accounted for the impacts of electrolyte/surface contamination, electrode roughness, and mass transfer effects[189] (also included in the Supporting Information). Further, we use first-principles methods to compute the adsorption energy ΔG_{H}. Figure 5-1(a) shows the strong linear correlation between the experimental and computed j_0 currents as demonstrated with a r^2 value of 0.89. As seen from the figure, differences between the experimental and calculated j_0 for the 12 metals are within two orders of magnitude, as indicated by the dashed

lines. These results, and particularly the significant correlations between computed and experimental j_0, lend strong credibility to the new model and the universality of k_0. Also, from the fit, we obtain k_0 =126 s^{-1} that can be expressed as $k_0 = \frac{k_B T}{h} exp\left(-\frac{0.65}{k_B T}\right)$, as will be reasoned and justified later.

Figure 5-1(b) shows the computed exchange current densities using Eq. (5-8) with the fitted value of k_0. The blue and the red curves are computed using C_{tot} for Au (or Re) and Pt, respectively, and are in agreement with their experimental values, as shown in green dots.[68,130,136-139] Here we used Pt as a reference given it is the most efficient single metal HER catalyst, and chose Au and Re because these two metals have similar C_{tot} except that Re has $\Delta G_{\mathrm{H}} > 0$ and Au has $\Delta G_{\mathrm{H}} < 0$. As seen from the figure, j_0 for high catalytic metals ($\Delta G_{\mathrm{H}} \cong 0$) is less sensitive to α than j_0 for inert surfaces ($|\Delta G_{\mathrm{H}}| > 0$). For example, for Pt with $\Delta G_{\mathrm{H}} = -0.09$ eV, the calculated j_0 changes by less than half order of magnitude between $\alpha = 0.5$ and 0.8. In contrast, for Au with $\Delta G_{\mathrm{H}} = -0.50$ eV the calculated j_0 differs by more than one order magnitude when α is off by 0.1. The sensitivity of the results to the combination between α and ΔG_{H} is justified given that the current depends exponentially on these terms, as seen in Eq. (5-8).

Having fully defined and established the new electrochemical model based on first-principles methods and experimental results, we show next that this model is in agreement with the revised Nørskov model that accounts for the metal-dependent rate constant[189]. To show this clearly, it is convenient to introduce a new rate constant k_{ana},

$$\ln(k_{ana}) = \begin{cases} (1-\alpha)\dfrac{\Delta G_{\mathrm{H}}}{k_B T} + \ln(k_0) & \text{(Volmer)} \\ -(1-\alpha)\dfrac{\Delta G_{\mathrm{H}}}{k_B T} + \ln(k_0) & \text{(Heyrovsky)} \end{cases} \tag{5-9}$$

This new expression is the summation of the barrier of the backward reaction $(1-\alpha)\frac{\Delta G_{\mathrm{H}}}{k_B T}$ and the metal-independent barrier $\ln(k_0)$. The introduction of k_{ana} is motivated given that Nørskov's model accounts only for the forward proton reduction process where adsorption rate is explicitly shown as $\exp(-\Delta G_{\mathrm{H}}/k_B T)$.[7] Thus, $\ln(k_{ana})$ encompasses all effects except for the forward adsorption rate. Substituting k_0 in Eq. (5-8) with the relations of Eq. (5-9), we obtain,

$$j_0 = \begin{cases} ek_{ana}C_{tot}(1-\theta)\exp(-\Delta G_{\mathrm{H}}/k_B T) & \text{(Volmer)} \\ ek_{ana}C_{\mathrm{tot}}(1-\theta) & \text{(Heyrovsky)} \end{cases} \quad (5\text{-}10)$$

Equation (5-10) is similar to Nørskov's model with two important differences. First, in the original Nørskov's model, j_0 is driven by the proton adsorption through either an endothermic ($\Delta G_{\mathrm{H}} > 0$) or exothermic ($\Delta G_{\mathrm{H}} < 0$) process. Equation (5-10), on the other hand, correlates the two conditions to the Volmer and Heyrovsky reactions as the rds, respectively. This distinction between the two pathways is consistent with the thermodynamic analysis discussion of Eq. (5-1), and with the computed kinetic barriers on metal surfaces[26].

Second, different from the Nørskov's assumption that stipulates the universality of k_{ana} for all metal surfaces, we previously uncovered its material dependence based on a data-driven statistical approach of experimental measurements[189]. Namely, we find that k_{ana} has the empirical form,[189]

$$\ln(k_{ana}) = 23.16|\Delta G_{\mathrm{H}}| + 3.17 \tag{5-11}$$

and is in indeed consistent with the definition of Eq. (5-9). Equating Eqs. (5-9) and (5-11), we find that $(1-\alpha)\frac{\Delta G_{\mathrm{H}}}{k_B T} = 23.16\,\Delta G_{\mathrm{H}}$ implies $\alpha = 0.4$, and $\ln(k_0) = 3.17$ The value obtained for $\alpha = 0.4$ is close to 0.5 that is recommended experimentally.[1,68,130] On the other hand, expressing k_0 in terms of the transition state theory $k_0 = \frac{k_B T}{h}\exp\left(-\frac{\Delta G_0^+}{k_B T}\right)$, we obtain an activation energy $\Delta G_0^+ =$ 0.7 eV that is close to the Tafel activation energy 0.8 eV on twelve pure metal surfaces[6,129].

In summary, this Letter reconciles the volcano trend and the BV empirical relationship. The first is widely employed in computational modeling to design new catalysts based on the easy-

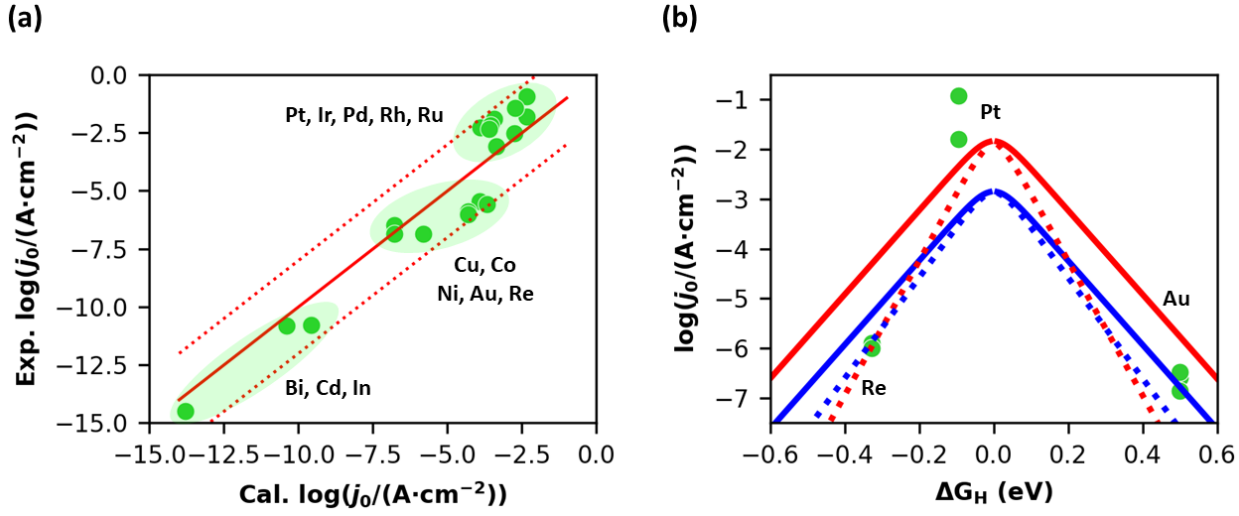

Figure 5-1. (a) Compassion between experimental and calculated j_0 of metal surfaces. The j_0 values are provided in the Supporting Information. **(b)** The computed volcano curves via Eq. (5-8). The red and blue lines are specified with C_{tot} for Pt and Au (or Re). The red (blue) solid and dashed lines are computed with $\alpha = 0.5$ (0.5) and 0.8 (0.6), respectively. The filled green circles show experimental values of Re, Pt, and Au.

to-compute descriptor while the second is the norm in analytical chemistry to interpret cyclic voltammograms. In addition, we derive a new electrochemical model based on the BV relation of a one-step, one-electron transfer process in conjunction with ΔG_{H}, which is easy to compute as it depends only on ΔG_{H} and the transfer coefficient of the rate-determining step. We validate the model by comparing to a large set of experimental-database for metal surfaces that have been verified before. Finally, we show that the model agrees with the Nørskov model after accounting for metals-dependence in the rate constant, which has been uncovered recently based on a data-driven approach.

The framework of constructing the new electrochemical model is not only limited to HER but is general for other electrochemical reactions that follow the BV relation such as CO_2 reduction,[209] metal oxidation[210] and lithium (de)intercalation reactions[209,211]. This is also justified because the Langmuir,[203-205] Frumkin[205,206] and Temkin[203,207] models can be generally applied to adsorption isotherms. Thus, through a systematic study of the empirical relation between the computational adsorption free energy and the experimental exchange currents, a general value of α and k_0 can be found for a reaction with similar electrochemical conditions.

5-4 Supporting Information

Computational Details. The first-principles DFT theory calculations are performed using the Vienna Ab Initio Simulation Package (VASP). The Kohn-Sham equations within periodic boundary conditions are resolved using the Revised Perdew-Burke-Ernzerhof (RPBE) with the PAW pseudopotentials for electron-nucleus interactions.[160-163] The dDsC dispersion correction is used for the van der Waals (vdW) corrections. The energy-change tolerance of electronic self-

consistent loops are within 1×10^{-6} eV. The periodic slab models, with the thickness of at least 10 Å, are cleaved from the 3×3 supercells of well-optimized bulk structures. In addition, 15 Å vacuum is applied perpendicular to the surfaces. For all surfaces, the bottom half of the layers are fixed in bulk position while the other layers are relaxed in the optimization process. The most stable terminations are (111) and (001) for the metals in $Fm\bar{3}m$ and P63/mmc, respectively. phase[164,165]. In addition, we use the termination of (111) and (110) for Bi and In, respectively.[166,167] For DFT calculations, the hydrogen adsorption free energy is defined as

$$\Delta G_{\mathrm{H}} = \Delta E_{\mathrm{H}^*} + \Delta E_{ZPE} + \Delta E_{\mathrm{H_2O}} - T\Delta S + \Delta E_{\mathrm{H_2O}}$$

with

$$\Delta E_{\mathrm{H}^*} = \frac{1}{n}(E_{n\mathrm{H}/slab} - E_{slab} - \frac{1}{2}nE_{\mathrm{H_2}})$$

where $E_{n\mathrm{H}/slab}$ and E_{slab} are the total energies of the surface with n and zero adsorbed hydrogen atoms, respectively. The energy of H_2 molecule $E_{\mathrm{H_2}}$ is obtained using the model of 15 Å vacuum. We use the coverage of 1/9 for all the metal surfaces. We have confirmed that ΔG_{H} values are converged with decreasing and increasing coverage for the surfaces with $\Delta G_{\mathrm{H}} > 0$ and $\Delta G_{\mathrm{H}} < 0$, respectively. The hydrogen adsorption sites, which are the most stable sites with the lowest ΔE_{H^*}, which are the atop sites for Ir and FCC hollow sites for all the other metal surfaces.[123] The change of zero-point energy ΔE_{ZPE} between the hydrogen in adsorbed state to gas state is ~0.04 eV,[2] and the entropic contribution $T\Delta S$ is -0.2 eV at 298 K.[100] The solvation energy $\Delta E_{\mathrm{H_2O}}$ is found to be less than ±0.1 eV for all surfaces calculated by adding a single water layer with an H_3O^+ close to an adsorbed hydrogen in supercell models.

Table 5-1. The trends of hydrogen coverage determined by the ab initio thermodynamic analysis (red lines) are fitted by the Langmuir isotherm (magenta lines) and the Frumkin isotherm (blue lines).

Metal	Langmuir	Frumkin
Pt	0.87	0.94 (g = -3)
Ir	0.97	0.96 (g = -1)
Cu	0.96	0.98 (g = 1)
Au	0.91	0.98 (g = 4)
Ag	0.98	0.98 ($g = \pm$ 1)
Ni	0.97	0.98 (g = -1)
Co	0.98	0.99 (g =-1)
Mo	0.95	0.96 (g =-1)

In the manuscript, we show that the electrochemical model for exchange current of Eq. (5-7) can be written into an exact form when assuming that θ follows the Langmuir isotherm on transition metal surfaces that $\theta = K/(1+K)$. To validate the assumption, we perform an *ab initio* thermodynamic analysis on the hydrogen coverage on transition metal surfaces by calculating the total Gibbs free energy of a system defined as

$$\Delta G_{tot} = \sum_{n} \Delta G_{\mathrm{H}} - n|e|\eta$$

where $\eta = E - U_{SHE}$ is the applied potential U with reference to the normal hydrogen electrode U_{SHE}. ΔG_{H} is the hydrogen adsorption free energy as defined in the main text. n is the number of electrons adsorbed on a surface. At each potential E, we calculate ΔG_{tot} for all possible n values. At a given E, the most probable hydrogen coverage has the lowest ΔG_{tot}. In Figure 5-2, we show the coverage friction θ vs applied potential in dashed red lines. Here, θ is the n that corresponds to the lowest ΔG_{tot} over the maximum number of adsorption sites.

Table 5-2. The detailed values of the computed j_0 and the experimental j_0 in Figure 5-1(a). We provide the calculated ΔG_{H} and the experimental α used in computing j_0.

	ΔG_{H}	Calculated $\log(j_0)$	Experimental $\log(j_0)$	Experimental α	Ref.
Pt/C	-0.09	-2.35	-1.80	0.5	[130]
Pt/C	-0.09	-2.35	-0.92	0.5	[68]
Ir	-0.14	-2.72	-1.44	0.5	[68]
Ir	-0.14	-3.44	-1.89	0.8	[130]
Pd	-0.18	-2.75	-2.52	0.4	[168]
Pd	-0.18	-3.35	-3.08	0.6	[130]
Rh/C	-0.20	-3.89	-2.28	0.7	[68]
Rh/C	-0.20	-3.55	-2.17	0.6	[130]
Ru	-0.25	-3.59	-2.35	0.5	[132]
Cu	0.25	-5.81	-6.84	0.8	[133]
Co	-0.37	-3.91	-5.44	0.4	[169]
Ni	-0.33	-3.68	-5.59	0.4	[135]
Au (111)	0.50	-6.78	-6.60	0.5	[136]
Au (111)	0.50	-6.78	-6.47	0.5	[137]
Poly Au	0.50	-6.78	-6.85	0.5	[136]
Re	-0.33	-4.30	-5.90	0.9	[138]
Re	-0.33	-4.30	-6.00	0.9	[139]
Bi	1.07	-13.80	-14.50	0.6	[141]
Cd	1.03	-9.56	-10.77	0.4	[140]
In	0.91	-10.39	-10.82	0.5	[142]

The Adsorption Isotherms. The Langmuir and Frumkin isotherms describe the pattern that the hydrogen coverage converges to a constant at low and high coverage, and are defined as[2,5]

$$[\theta/(1-\theta)] = K\exp(-Ef) \quad \text{(Langmuir)}$$

$$[\theta/(1-\theta)]\exp(-g\theta) = K\exp(-Ef) \quad \text{(Frumkin)}$$

where $K = \exp(-\Delta G_{\mathrm{H}}/k_B T)$ and $f = F/RT$ where F is the Faraday constant. In Table 5-1, we show the r-square values for fitting the Langmuir and Frumkin isotherms on the hydrogen coverage determined by the ab initio thermodynamics calculations. For the Frumkin isotherm, we show the g values for the best fit. In Figure 5-2 for Pt (111), we show that the Temkin isotherm well describes the region in between $\theta = 0$ and 1. However, it does not capture the full range of the potential.

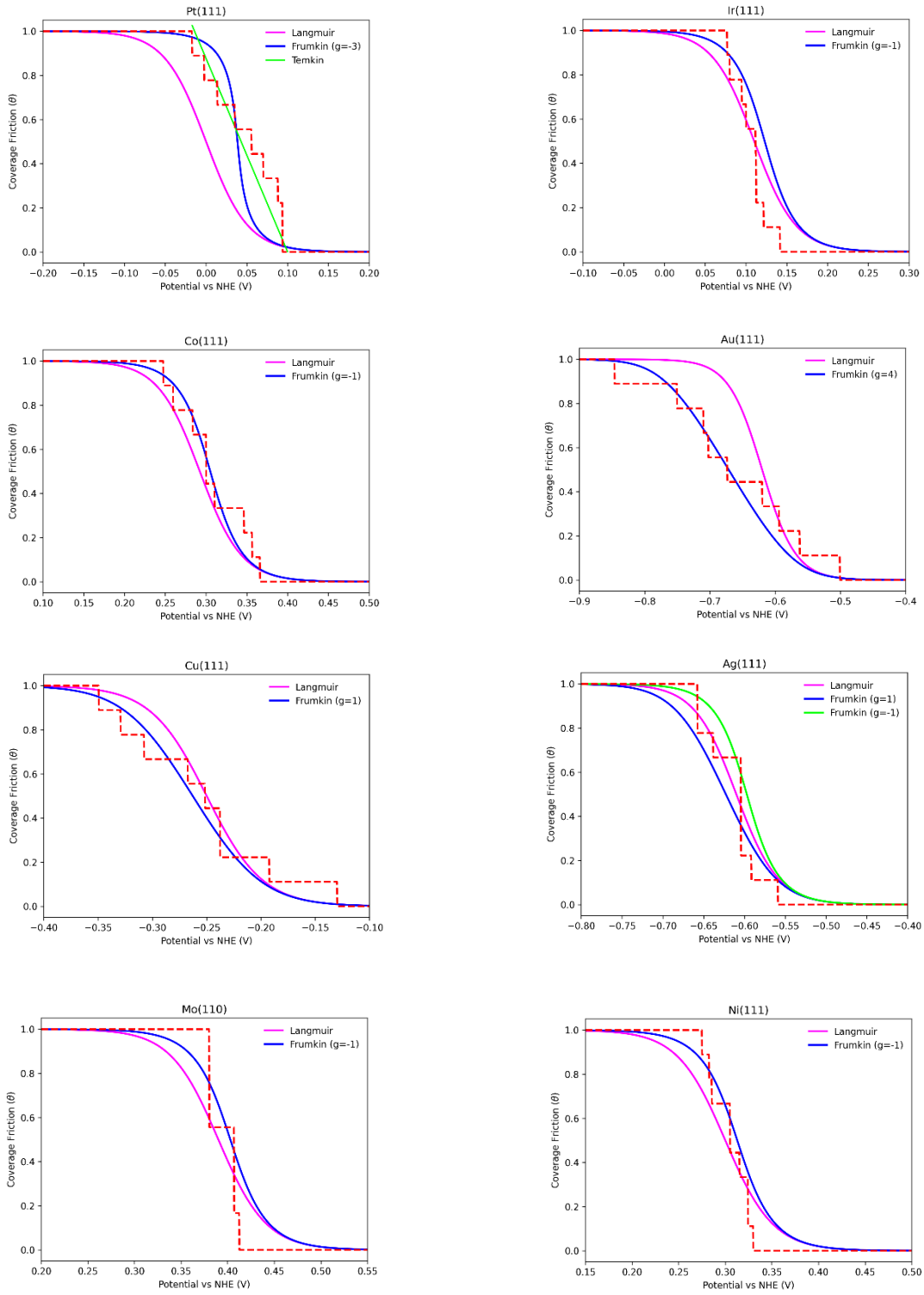

Figure 5-2. The adsorption isotherms on metal surfaces. The red dashed red lines are computed using *ab initio* thermodynamic calculations, the magenta and the blue lines are the fitted lines with the red dashed lines using the Langmuir and Frumkin isotherm models, respectively.

6-0 Cyclic Voltammetry Model for Hydrogen Evolution Exchange Current

Note: The chapter is created from the published manuscript *Simple Approach for Reconciling Cyclic Voltammetry with Hydrogen Adsorption Energy for Hydrogen Evolution Exchange Current* (Timothy T. Yang and Wissam A. Saidi, J. Phys. Chem. Lett. 2023, 14, 18, 4164–4171). Most of the writings are not rephrased.

Chapter 5 explains the empirical relation of k_{ana} using the Butler-Volmer relation and propose an electrochemical model for the exchange current of hydrogen evolution reaction. This model is only a function of ΔG_{H} attributed to the finding of an absolute rate constant and the universal transfer coefficient. Although my electrochemical model is built under the potential-independent limit, I hypothesize that the model can also be applied, or with a small variation on the electrochemical parameters, under the potential-dependent limit. Cyclic voltammetry is a standard technique to analyze current-potential characteristics of the hydrogen evolution reaction. Herein, I develop a computational quantum-scaled cyclic voltammetry model for the hydrogen evolution reaction building on the Butler-Volmer relation for a *one-step, one-charge* transfer process. Owing to a *universal* and *absolute* rate constant verified by fitting to experimental cyclic voltammograms of elemental metals, I show that the model quantifies the exchange current – the main analytical descriptor for the activity of the hydrogen evolution reaction – solely using the hydrogen adsorption free energy obtained from the density functional theory calculations. Furthermore, the model resolves controversies over analytical studies for the hydrogen evolution reaction kinetics.

6-1 Introduction

Green hydrogen is a clean and sustainable energy carrier, which can replace traditional fossil fuels that aggravate the greenhouse effect. Accordingly, it is critical to identify effective routes for green hydrogen production via optimizing electrochemical catalysts for hydrogen evolution reaction (HER) – the cathodic reaction in electrolysis.[86,212-219] Cyclic voltammetry (CV) is a standard technique to obtain current-potential characteristics of electrochemical reactions, which have been routinely analyzed using the Butler-Volmer (BV) relation to infer reaction mechanisms.[68,75,193] However, due to the empirical nature of the BV relation and the lack of justification of the CV at the atomic level, there are invariably controversies on the interpretations of the HER mechanisms deduced from these analytical measurement.[190] In addition, experimental limitations can significantly impact the analysis of the Faradaic currents that further hamper CV measurements. For instance, Gasteiger's group showed that up to a hundred-fold of HER activity on platinum electrode is hindered by slow mass-transport of protons.[68,192,193] Also, Bard et al. showed that the native metal oxide, that grows on electrode surfaces under electrochemical conditions, appreciably affects the CV measurements for the surface of interest due to additional charge-transfer reactions.[220,221]

Several microkinetic analyses have been proposed to interpret the cyclic voltammograms (CVs).[62,98,99,222,223] For modeling HER, Chialvo and collaborators developed a numerical model for HER current in the steady state limit under zero-scan rates;[98] Kucernak and Zalitis constructed general HER microkinetic models to rationalize experimental CVs using kinetic parameters of the elementary steps under different electrochemical conditions by accounting for the spectrum of hydrogen adsorption isotherms.[99] Shinagawa and collaborators derived theoretical microkinetic models to interpret the Tafel slope dependence on hydrogen coverage and HER kinetics.[62]

Generally, while the microkinetic models elucidate, to various degrees of success, experimental CVs at the atomic scale, these are not easily constructed from first-principles. This complexity significantly impacts the development and screening of cost-effective and efficient HER catalysts. The exchange current density j_0 is the main descriptor for electrochemical reaction rate that can be obtained from CV with Tafel analysis. To computationally screen for j_0, Nørskov proposed the density-functional theory (DFT) based hydrogen adsorption free energy ΔG_{H} as an important and sole descriptor in acidic environment – the j_0 decreases with increasing $|\Delta G_{\mathrm{H}}|$, and the maximum j_0 corresponds to zero ΔG_{H}.[7] Although the Nørskov's exchange current model well-establishes the volcano trend qualitatively, it lacked quantitative agreement with experiments. Specifically, the model can only accurately predict j_0 for precious metal electrodes that interact thermoneutrally with hydrogen, but significantly fails to match experimental results by several orders of magnitude for metal electrodes that interact weakly or strongly with hydrogen.[189] Importantly, from a fundamental, and even a practical perspective to analytical chemistry, the Nørskov's exchange current model lacks a connection with the BV relation – a fundamental relation that describes the current-potential characteristics for electrochemical reactions. In our previous work, we employed a data-driven approach to show that the accuracy of the Nørskov's exchange current model can be significantly improved using a material-dependent constant that is linearly correlated with ΔG_{H}.[189] Further, in a follow-up study, we derived a computational model for j_0 from the BV relation for a *one-step, one-electron* transfer process employing ΔG_{H} as the main descriptor.[224] This model, referred to as Yang-Saidi hereafter, accurately computes j_0 solely using the easy-to-compute ΔG_{H} for metals with a wide variation of j_0 up to fifteen orders of magnitude. Importantly, the Yang-Saidi model reconciles the missing link between the Nørskov's exchange current model and the empirical BV relation. Notwithstanding, both the Nørskov and the Yang-Saidi models for j_0 are

limited at the equilibrium potential and cannot be applied at a finite potential to model experimental CVs.

Herein, we develop a CV model for computing exchange currents building on the BV relation for a *one-step, one-charge* transfer process. The computational CV model is confirmed by high-quality fittings to the experimental CVs of twelve transition metal electrodes using the charge transfer coefficient of the rate-determining step (rds), potential-independent activation free energy, and the DFT based hydrogen adsorption free energy ΔG_{H}. Importantly, we find that the experimental exchange currents can be reproduced from the computational CV model solely using ΔG_{H}; thus, reconfirming the Yang-Saidi model for exchange currents and solidifying our finding of an *universal* and *absolute* reaction rate constant for HER.[189,224] The success and high-fidelity of the computational CV model for HER exchange current is attributed to identifying a non-changing reaction mechanism, and hence rds, in the experimentally-relevant potential window for the Faradaic HER currents.

6-2 Theory of the Computational Model for Cyclic Voltammograms

The hydrogen evolution reaction proceeds with the Volmer-Heyrovsky or Volmer-Tafel pathway with the elementary steps,

$$\mathrm{H^+ + e^- \rightarrow H^*} \qquad \text{(Volmer)}$$

$$\mathrm{H^* + e^- + H^+ \rightarrow H_2} \qquad \text{(Heyrovsky)}$$

$$\mathrm{2H^* \rightarrow H_2}\ , \qquad \text{(Tafel)}$$

where $\mathrm{H^+}$, $\mathrm{H^*}$ and $\mathrm{H_2}$ are hydrogen ion, adsorbed hydrogen atom and hydrogen gas, respectively. The overall electrochemical current density is the sum of the forward and backward currents,

$$j = j_f + j_b = e\left[C_f r_f - C_b r_b\right] \tag{6-1}$$

where e is the elementary charge, $r_{f/b}$ and $C_{f/b}$ are the rate constant and the concentration of the reactant for the forward/backward reaction, respectively. Assuming that *the total reaction rate merely depends on the rds*, we can apply the BV equation for a *one-step, one-electron transfer process* to Eq. (6-1) by writing the total reaction rate,[224,225]

$$\begin{cases} r_f = k_f \exp[-\alpha f(E - E^{0'})] \\ r_b = k_b \exp[(1-\alpha) f\left(E - E^{0'}\right)] \end{cases} \tag{6-2}$$

Here, $f = F/RT$, F is the Faraday's constant, R is the gas constant, T is the temperature and E is the applied potential. The transfer coefficient α and the formal potential $E^{0'}$ are specified for the rds. For the purpose of distinguishing from the charge transfer-dependent part of the total reaction rate, i.e., $\exp[-\alpha f(E - E^{0'})]$ or $\exp[(1-\alpha) f\left(E - E^{0'}\right)]$, we introduce the charge transfer-independent rate constants $k_{f/b}$ defined as,

$$\begin{cases} k_f = (k_B T/h) exp(-\Delta G_f^+ / k_B T) \\ k_b = (k_B T/h) exp(-\Delta G_b^+ / k_B T) \end{cases} \tag{6-3}$$

where ΔG_f^+ and ΔG_b^+ are the potential-independent activation energy for the forward and backward reactions, respectively. We note that the Tafel reaction cannot be described by Eq. (6-2) as it is not a charge transfer reaction. Combining Eqs. (6-1) and (6-2), we obtain,

$$j = eC_f\, k_f \exp[-\alpha f\left(E - E^{0'}\right)] - eC_b\, k_b \exp[(1-\alpha) f\left(E - E^{0'}\right)] \tag{6-4}$$

To make Eq. 6-4 amenable to first-principles calculations, we express $C_f = C_{tot}(1-\theta)$, $C_b = C_{tot}\theta$ and $E^{0'} = -\Delta G_{\mathrm{H}}/|e|$ for the Volmer reaction, and $C_f = C_{\mathrm{tot}}\theta$, $C_b = C_{tot}(1-\theta)$ and $E^{0'} = \Delta G_{\mathrm{H}}/|e|$ for the Heyrovsky reaction. See Supporting Information for detailed derivations. Here, C_{tot} is the areal concentration of HER active sites and ΔG_{H} is the DFT based hydrogen adsorption free energy defined in Eq. (3-1) and (3-3). The hydrogen adsorption fraction can be

written in the Langmuir form $\theta = K/(1+K)$ with the equilibrium constant $K = \exp(-\Delta G_{\mathrm{H}}/k_B T)$.[7,189,224] We show in the SI that the Langmuir isotherm successfully describes, with a coefficient of determination $r^2 \sim 0.9$, hydrogen adsorption on metal surfaces. It is in agreement with the results obtained from *ab initio* thermodynamics.

Assuming that the rds dominates the total HER activity with constant values of k_f and k_b throughout the HER potential window, we can apply the constraints that are defined at the equilibrium, that is $k_0 = k_f = k_b$ or $\Delta G_0^+ = \Delta G_f^+ = \Delta G_b^+$. Here, *the standard rate constant* k_0 is *defined when the forward and backward rates are the same at the equilibrium*,[225] and ΔG_0^+ is the forward/backward activation energy at the equilibrium. Further, we assume that the rds is the same throughout the HER potential window, which justifies having a non-changing value α along the reaction pathway. This is justified by our *ab initio* thermodynamics calculations (see Ref. [172] for detailed explanation) showing that the hydrogen adsorption sites are non-changing for all metal surfaces, as the intermediates that interact with different adsorption sites undergo different charge-transfer mechanisms. We note that the proposed computational CV model, which is fully defined in Eqs. (6-2), (6-3) and (6-4), requires the values of ΔG_{H}, ΔG_0^+ and α for computing j. We will show next that the computational CV model is only a function of ΔG_{H} for HER exchange current by confirming that ΔG_0^+ and α are universal for all metal electrodes through fitting to experimental CVs.

6-3 Validation of the Computational Model

To validate and establish the computational CV model of Eq. (6-4), we fit the experimental CVs based on the rds that is inferred by examining ΔG_{H}; the Volmer/Heyrovsky reaction is the rds when

ΔG_{H} is positive/negative, as confirmed theoretically and computationally.[129,224] The experimental CVs of the mono-metallic systems were shortlisted from a larger set of prior literature reports.[5,68,130-142,169] Namely, the selected experiments are based on the criteria that limits or otherwise account for electrolyte/surface contamination, electrode roughness, surface corrosion, mass transfer effects and charge impedance.[189] Especially, for platinum group metal electrodes with the highest activities, the HER currents can be entirely limited by mass diffusion in traditional rotating disk electrode (RDE) measurments.[68,193] To avoid this limitation, we use the experimental CVs from the study of Gasteiger *et al.* that mitigated the mass diffusion limitation using a proton exchange membrane fuel cell setup with a H_2 pump approach.[68] In addition, unlike RDE, this approach can measure the effective surface area with an accuracy higher than 1 mA/cm^2, which is needed to distinguish between the HER activities of the precious metals.[226-229]

For the selected experimental CVs, we carefully inspect the potential region where mass-transport could limit the currents to be non-Faradaic particularly at elevated applied potential. In addition, we ensure that the catalysts do not experience a change in reaction pathways in the HER potential window, which violates the assumption of a non-changing α in Eq. (6-4). Based on this analysis, we concluded that of all investigated metals, Pt, Ir and Re cannot be described with high fidelity using Eq. (6-4) without confining to the potential regions that are free of mass-transfer limitation. Previous studies have shown that the experimental currents for Pt and Ir follow the BV behavior only in the low-overpotential region above -0.05 V vs. SHE (V_{SHE}) as the currents are mass-transfer limited at higher low-overpotential region.[68,230,231] This agrees with our findings where the model of Eq. (6-4) is found to well-describe the experimental CVs in the low-overpotential region -0.05 to 0 V_{SHE} while the experimental currents are lower than the computed currents below -0.05 V_{SHE} (see Supporting Information). For Re, such mass-transfer limited

current are observed below -0.35 V_{SHE} where the noise from the formation of H_2 bubbles are reported in experiment, which alters the determination of the HER current[232] (see Figure 6-5). We note that for Pt and Ir, both the forward and backward charge transfer processes, as described in Eq. (6-4), significantly contributes to the total net current near the equilibrium potential; thus, their CVs exhibit linear dependency between j and V_{SHE}, as shown in Figure 6-1(a) and 6-2(a). This is different from the other metals with $E^{0'}$ values that are away from zero, resulting a negligible backward charge transfer process.

Figures 6-1 and 6-2 show that the computational CV model of Eq. (6-4) fits the experimental CVs with high fidelity, as reflected from the high value of the coefficient of determination, $r^2 > 0.990$. The quality of the fits is determined by whether the model can successfully describe the experimental CVs using the DFT computed ΔG_H, in addition to two

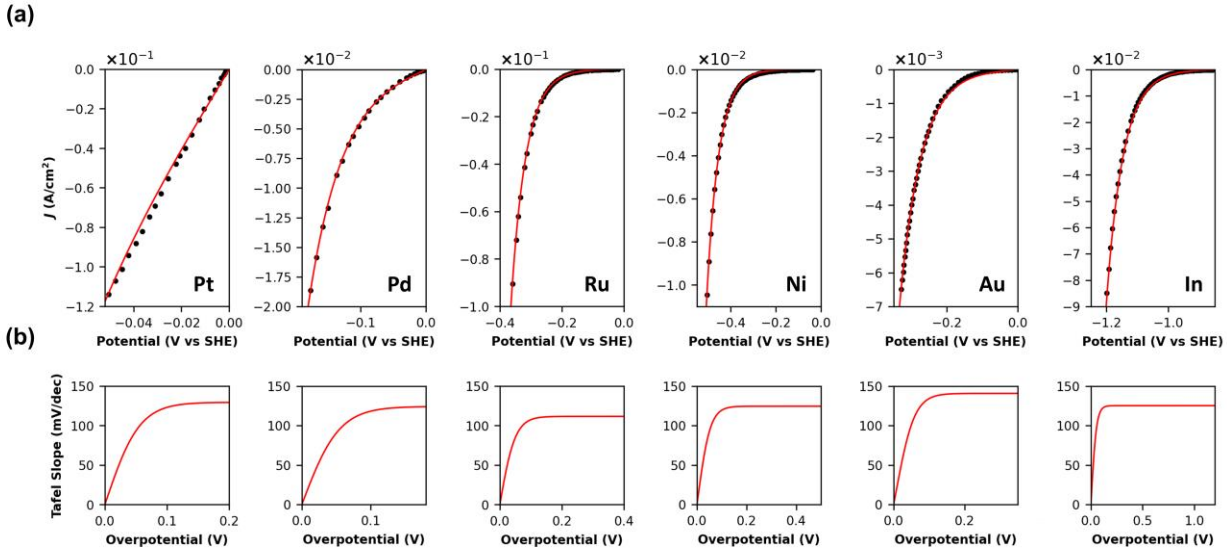

Figure 6-1. (a) The cyclic voltammograms as a function of potential (V vs. SHE) and **(b)** the Tafel slopes as a function of overpotential (V) for six pure-metal electrodes (see also Supporting Information for additional six electrodes). The experimental cyclic voltammograms (black dots) are reproduced from the references listed in Table 6-1 and are fitted with the computational CV model of Eq. (6-4) shown in red line. The Tafel slopes are obtained from the computational CV model of Eq. (6-4).

fitting values ΔG_0^+ and α. Table 1 lists the fitting parameters as well as the experimentally measured Tafel slopes and the numerically computed Tafel slopes from the computational CV model. As seen from the table, the values of α, 0.52 ± 0.15, fall within a narrow range compared to the theoretical range $0 < \alpha < 1$. In addition, the activation energy for the charge transfer-independent rate $\Delta G_0^+ = 0.69 \pm 0.10$ eV is nearly a constant for all metals electrodes despite the wide spectrum of HER activities $-0.92 < \log(j_0/(A \cdot cm^2)) < -12.28$ reported experimentally. For the twelve metal electrodes, the medium (averaged) values $\Delta G_0^+ = 0.69$ eV (0.68 eV) and $\alpha = 0.52$ (0.51) are consistent with the Yang-Saidi model for the exchange current density,[189,224]

$$j_0 = \begin{cases} ek_0 C_{tot}(1-\theta)^{(1-\alpha)}(\theta)^{\alpha} & \text{(Volmer)} \\ ek_0 C_{tot}(\theta)^{(1-\alpha)}(1-\theta)^{\alpha} & \text{(Heyrovsky)} \end{cases} \quad (6\text{-}5)$$

where $\alpha = 0.5$ and $k_0 = (k_B T/h)\exp(-\Delta G_0^+/k_B T)$ with $\Delta G_0^+ = 0.7$ eV is *the absolute form of the standard rate constant*. Note that the Yang-Saidi model of Eq. (6-5) is obtained from Eq. (6-4) following the detailed derivation in our previous works (see Ref. 23 and 24).

Based on the classic BV theory,[233] the physical interpretation of $\alpha = 0.5$ is that the "shape" of the activation barrier of the one-step, one-electron process, i.e., Eq. (6-4) is symmetrical. $\alpha = 0.5$ can be also justified from Marcus theory,[234,235] which stipulates that no work is required to establish the charge transfer reaction at the electrochemical condition where the forward and the backward currents of the charge transfer process have the same behavior with the external potential, i.e., $j_f = -j_b$ at a negative or positive $|E|$ for the forward and the backward reactions, respectively. ΔG_0^+ can be interpreted as the potential independent part of the total activation barrier for HER. Thus, for the most HER active surfaces where the adsorption (Volmer) and desorption (Heyrovsky) can be established without applying an external potential, i.e. $E^{0'} \sim 0$, the overall HER current is determined by the value of ΔG_0^+. We acknowledge that a deeper connection with a theoretical

explanation is still missing for ΔG_0^+. However, the values $\Delta G_0^+ = 0.7$ eV obtained from fitting is consistent with several studies. Using DFT calculations, Sku´lason et al. and Tang et al., showed that the activation barrier for HER to be 0.6 eV with the Heyrovsky reaction as the rds on Pt (111).[6,129] Also, based on solvated jellium method and Marcus theory,[234,235] Peterson et al.,[94] computed the activation barrier 0.77 eV at the thermoneutral condition for the Heyrovsky reaction (rds) on Pt (111).

It can be posited that there are several uncertainties that hinder determining whether ΔG_0^+ and α are truly universal in nature. For example, we use the most stable termination for the calculation of ΔG_{H} although other terminations of the electrodes could contribute to the exchange current. Also, while the experimental currents are assumed to be solely from the rds, there are additional charge transfer reactions originated from H_2O adsorption that are not easily distinguished from the total current.[220,221,236] Nonetheless, we will show next that the

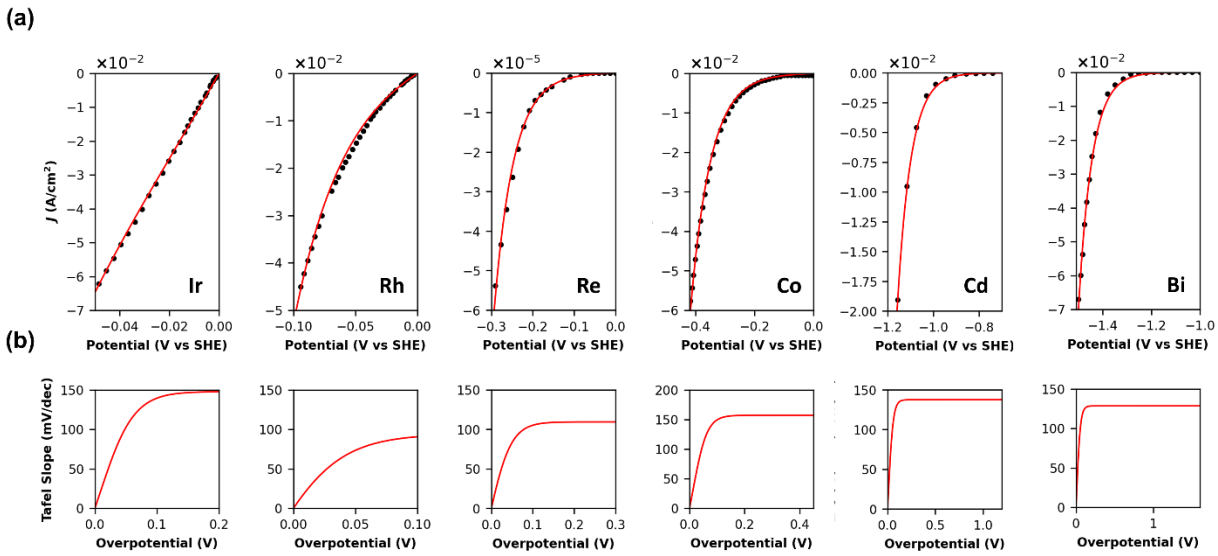

Figure 6-2. (a) The cyclic voltammograms as a function of potential (V vs. SHE) and **(b)** the Tafel slopes as a function of overpotential (V) for six pure-metal electrodes (see also SI for additional six electrodes). The experimental cyclic voltammograms (black dots) are reproduced from the references listed in Table 1 and are fitted with the computational CV model of Eq. (6-4) shown in red line. The Tafel slopes are obtained from the computational CV model of Eq. (6-4).

computational CV model is insensitive to small variations in ΔG_0^+ and α when reproducing the experimental exchange currents.

In Figure 6-3, we report the exchange current densities j_0 obtained from the Yang-Saidi model of Eq. (6-5) with the universal values of $\alpha = 0.5$ and $\Delta G_0^+ = 0.7$ eV. For comparison, we also show j_0 based on the computational CV model of Eq. (6-4) using the fitting values of α and ΔG_0^+, see Table 1. In these calculations, we utilized ΔG_{H} from DFT calculations and the temperatures specified in experiments, as listed in Table 6-1. As seen from the figure, the two sets of j_0 are in agreement despite the wide variations of the metal electrodes reflected with a ΔG_{H} varying from -0.1 eV to 1.1 eV, which corresponds to nearly fourteen-orders of magnitude variations in exchange currents. It should be expected that the experimental j_0 values are in line with the computed ones using the fitting parameters, as Eq. (6-4) or (6-5) show high fitting fidelity with experimental CVs. However, small discrepancies in experimental j_0 values are due to the Tafel analysis when selecting the overpotential region where $\log(j)$ is linearly extrapolated to 0 V_{SHE}. For example, from the experimental CVs of Au (111),[136] we measure j_0 to be 9.7×10^{-6} A/cm^2 at the potential region from -0.1 to -0.2 V_{SHE} overpotential. This value is higher than the reported value of 2.5×10^{-7} A/cm^2 measured below -0.1 V_{SHE}.[136]

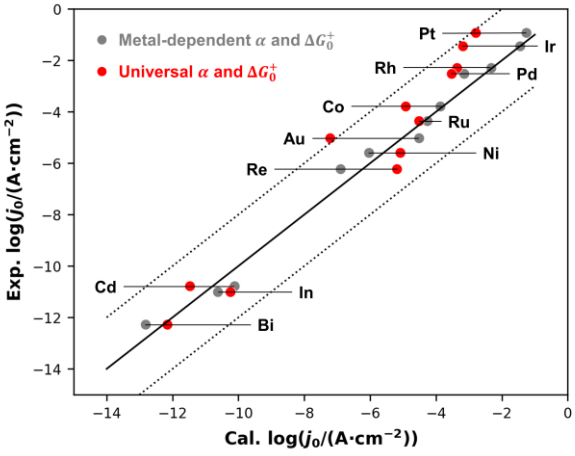

Figure 6-3. Comparison of the computed and the experimental j_0. The computed j_0 values are obtained using the Yang-Saidi model with the universal constants $\alpha = 0.5$ and $\Delta G_0^+ = 0.7$ eV (red scatters), and with the fitted α and ΔG_0^+ in Table 1 (gray scatters). The horizontal lines indicate the experimental j_0 values of the corresponding metal electrodes, and are reported from the references listed in Table 1. The solid line indicates parity and the dashed lines indicate the boundary within two orders of magnitude difference. All the values are listed in Table 6-2 and 6-3.

Our model shows that Pt (111) is the most HER active among the metal surfaces via quantifying the j_0 with $\Delta G_{\mathrm{H}} \sim 0$ eV. However, we note that there is a debate in the community on whether the maximum HER activity corresponds to thermoneutral ΔG_{H}. Peterson et al. showed that hydrogen atoms at atop sites (with $\Delta G_{\mathrm{H}} > 0$ eV) are more active for HER compared to those at the hollow sites (with $\Delta G_{\mathrm{H}} \sim 0$ eV).[94] On the other hand, Tang et al.[129] and Skúlason et al.[6] argued that the Heyrovsky reaction is the rds for H_2 formation, which is associated with the on-top hydrogen atoms that diffuse from the hollow sites (with $\Delta G_{\mathrm{H}} \sim 0$ eV) with a negligible barrier. The findings of Tang and Skúlason based on first-principles are consistent with experimental results showing the hydrogen coverage does not exceed 1 monolayer (ML) [237,238]; i.e., atop sites are very unlikely to be occupied below 1 ML. From our DFT calculations, we find that the hollow sites are the most probable (stable) adsorption sites with $\Delta G_{\mathrm{H}} \sim 0$ eV below 1 ML, and the atop sites are only occupied above 1 ML with $\Delta G_{\mathrm{H}} \sim 0.5$ eV through the Volmer reaction. Therefore, we posit that the atop hydrogen atoms with $\Delta G_{\mathrm{H}} > 0$ are the intermediate states, which are HER "activated" from the thermoneutral hydrogen atoms at the hollow sites with $\Delta G_{\mathrm{H}} \sim 0$.

Herein, not only we show that α and ΔG_0^+ are universal at the equilibrium limit, we have confirmed again in the HER potential window, that such universality is critical for the Yang-Saidi model to be solely a function of the easy-to-compute ΔG_{H}. Although the model using the fitted α and ΔG_0^+, that are materials dependent, has higher accuracy (within one order of magnitude with experimental j_0) for computing j_0 than using the universal ones (within two orders of magnitude with experimental j_0), the universality gives a great advantage to quantify j_0 with a sufficient accuracy without fitting to experimental cyclic voltammograms.

We next assess the accuracy of the CV model to predict the Tafel slope, $b = d\eta/d\log(j)$. In analytical studies, the Tafel slope is routinely employed to uncover the HER reaction pathways

based on the empirical BV relation $j \propto e^{-\alpha_c f \eta}$, where α_c is the empirical cathodic transfer coefficient and η is the overpotential. Note that α_c is distinguished from α in Eq. (6-2) as the former describes the total current while the latter describes the current limited from either the Volmer or the Heyrovsky reaction. It is commonly argued that the rds is determined based on the empirical Tafel slope $b = 2.303RT/F\alpha_c$ where the values 120, 40 and 30 mV/dec correspond to the Volmer, Heyrovsky and the Tafel reactions as the rds, respectively.[239-245] However, these standard values are based on the assumption that $\alpha_c = 0.5$. In addition, there has not been a consensus in the community on determining the rds purely based on these standard values. Shinagawa et. al. utilized microkinetic analysis to argue that the Tafel slope for the Heyrovsky reaction can be either 120 or 40 mV/dec for high or low hydrogen concentrations.[62] Zheng *et al.* argued that the HER activity on high active catalysts are limited by mass-transport yielding a 30 mV/dec Tafel slope, which nevertheless does not indicate that the Tafel reaction as the rds.[246]

To resolve these controversies, we employ the computational CV model to compute the Tafel slope as a function of overpotential $\eta = E - E^{0'}$. Figure 6-1(b) shows that the computed Tafel slope increases with η and converges to a constant value. If the Volmer or the Heyrovsky reaction is the rds, the converged value is $b = 2.303RT/F\alpha$, which can be derived from Eq. (6-4) by neglecting the second term. This approximation is justified given that the current of the rds is polarized away from the equilibrium potential i.e., $E - E^{0'} > 0$ V. This form of the Tafel slope agrees with what was proposed before by Shinagawa *et al.*[62] Further, our results shows that the Tafel slope can be 120 mV/dec for the Heyrovsky reaction at $\theta \approx 1$ with $\alpha \approx 0.5$, in agreement with the arguments of Shinagawa et al.[62]

As seen in the table, all the experimentally measured Tafel slopes are in agreement with our computed values except for Re, Au and Bi. We will elaborate below that the discrepancy

Table 6-1. The values of the parameters for generating the cyclic voltammogram of Figure 6-1(a) using Eq. (6-4). The values of α and ΔG_f^+ are obtained from fitting to the experimental cyclic voltammograms in the references listed below. T is set at 298 K unless reported otherwise in the experimental studies. The experimental Tafel slope (Exp. b) is reported from the references and the calculated Tafel slope (Cal. b) is obtained from the computational CVs.

	Pt	**Ir**	**Pd**	**Rh**	**Re**	**Ru**	**Co**	**Ni**	**Au**	**In**	**Cd**	**Bi**
ΔG_H	-0.08	-0.14	-0.18	-0.16	-0.33	-0.22	-0.25	-0.28	0.53	0.91	1.03	1.07
ΔG_0^+	0.61	0.60	0.68	0.61	0.79	0.68	0.67	0.76	0.58	0.74	0.69	0.78
α	0.48	0.42	0.50	0.66	0.55	0.53	0.37	0.47	0.42	0.48	0.43	0.46
T	313	313	313	313	303	298	293	295	298	303	298	298
Exp. b	124	124	127	95	65	117	163	119	125	120	135	100
Cal. b	129	148	124	91	109	112	157	125	141	125	138	129
Ref.	68	68	68	68	232	132	169	135	136	142	140	141

originates from the selection of the potential region for measuring the Tafel slope. In analytical Tafel analysis, the experimental Tafel slopes are determined in the linear region near the equilibrium potential. Figure 6-1(b) confirms that the linear region is at ~0.1 V overpotential for all metals where the computed Tafel slopes converge to a constant value. For Re, the experimental value of 65 mV/dec is different from the calculated one of 92 mV/dec. This is because our value is obtained from modeling the CVs in the potential region (-0.11 to -0.15 V_{SHE}) while the experimental value is obtained from averaging over a wide potential region (-0.11 to -0.69 V_{SHE})[138] where the HER experiences a change of reaction pathway, as argued before. For Au, there are two reported values 60 and 120 mV/dec at low and high overpotentials, respectively.[62] This can be readily explained by our computed values in Figure 6-1(b) where the Tafel slope increases from 0 to 60 mV/dec for 0 to 0.25 V_{SHE}, and converges to 120 mV/dec above 1 V_{SHE}. For Bi, our converged Tafel slope value is 129 mV/dec determined above 0.3 V overpotential, which is higher than the reported value of 100 mV/dec obtained from the linear fitting in the reported overpotential region of 1.1 to 1.5 overpotential (with respect to 0 V_{SHE}).[141] This can be readily explained from the trend observed in Figure 6-4 – the experimental Tafel slope decreases with decreasing overpotential.

In summary, we propose a computational cyclic voltammetry (CV) model for the exchange current of hydrogen evolution reaction building on the BV relation for a *one-step, one-electron* transfer process. Solely based on the easy-to-compute descriptor ΔG_{H}, the computational CV model reproduces experimental exchange currents for a wide variety of pure metal electrodes with high fidelity. The key success of the computational CV model is attributed to the *universal* and *absolute* reaction rate constant that is confirmed by the fitted values of $\alpha = 0.52 \pm 0.15$ and $\Delta G_0^+ = 0.69 \pm 0.10$ eV from scrutinizing the experimentally relevant potential window for the Faradaic HER currents with a non-changing reaction mechanism. The findings reconfirm the Yang-Saidi model for the exchange current that was derived under equilibrium conditions where HER currents are potential-independent.[189,224] Further, from the computational CV model, we show that the calculated Tafel slopes are comparable with the experimental reported values. Importantly, these results, based on the atomistic view, resolves controversies on the studies of HER mechanism based on empirical Tafel analysis. Our findings are crucial to understand the empirical cyclic voltammetry in views of theoretical electrochemistry, which provides a framework to compute the cyclic voltammetry solely using end-to-end *ab initio* calculations for electrochemical reaction rate.

6-4 Supporting Information

Computational Details. The first-principles DFT calculations are performed using the Vienna Ab Initio Simulation Package (VASP). The Revised Perdew-Burke-Ernzerhof (RPBE) is employed to solve the Kohn-Sham equations within periodic boundary conditions, and the PAW pseudopotentials are utilized to describe electron-nucleus interactions.[160-163] In addition, the Van

der Waals (vdW) corrections are described by the dDsC dispersion correction.[247,248] For all systems, the convergence is determined when the energy-change of the electronic self-consistent loops is within the tolerance of 1×10^{-6} eV. The periodic supercell models are cleaved from the optimized bulk structures. To mitigate the fictitious interactions between periodic images, we use 3×3 supercells that have slabs with 5-layer thickness and 15 Å vacuums perpendicular to the surfaces; the bottom two layers are fixed at bulk position while relaxing the top 3 layers. All the supercell models are as described before except that the Bi surface model has 8 layers with the bottom half layers fixed at bulk position. All metal electrodes are represented by their most stable terminations: for metals in $Fm\bar{3}m$ and $P6_3/mmc$ phase[164,165], we use (111) and (001), respectively. For Bi and In in $R\bar{3}m$, we use (111) termination.[166] For $\Delta G_H > 0$ ($\Delta G_H < 0$), the hydrogen coverage is 1/9 ML (1 ML). The approximation is based on the *ab initio* thermodynamic analysis[123] that has been shown valid for experimental exchange currents.[189,224] We also study the solvation energy ΔE_{H_2O} by adding a single water layer in hexagonal structure with 1/6 ratio for H_3O/H_2O. We find that ΔE_{H_2O} is less than 0.1 for all metal surfaces.

Table 6-2. Variables that are employed to compute the exchange current in Figure 6-2. For computations, we use the bulk structures from our previous work in Ref [224].

	Temperature (K)	**Surface Area (cm^2)**	**ΔG_H (eV)**	**ΔG_0^+ (eV)**	**α**	**# Sites per surface area**
Pt	313	6.20×10^{-15}	-0.082	0.608	0.48	9
Ir	313	5.89×10^{-15}	-0.136	0.605	0.42	9
Rh	313	5.77×10^{-15}	-0.159	0.612	0.66	9
Pd	313	6.16×10^{-15}	-0.176	0.678	0.50	9
Re	303	6.04×10^{-15}	-0.327	0.787	0.55	9
Ru	298	5.81×10^{-15}	-0.220	0.679	0.53	9
Co	293	4.70×10^{-15}	-0.252	0.671	0.37	9
Ni	295	4.89×10^{-15}	-0.280	0.764	0.47	9
Au	298	6.86×10^{-15}	0.532	0.583	0.42	9
Bi	298	1.65×10^{-14}	1.071	0.782	0.46	9
Cd	298	7.49×10^{-15}	1.031	0.692	0.43	9
In	303	9.30×10^{-15}	0.912	0.742	0.48	9

Table 6-3. (a) The experimental $\log(j_0)$ values. **(b)** The computed $\log(j_0)$ using the Yang-Saidi model with $\alpha = 0.5$ and $\Delta G_0^+ = 0.7$ eV and **(c)** the computed $\log(j_0)$ values using the fitted α and ΔG_0^+ reported in Table 1. The unit of j_0 is A/cm^2. The experimental $\log(j_0)$ values are taken directly from the references provided in Table 1. For the references that do not report the values, we measure the values from the reported cyclic voltammogram using Tafel slope analysis; for Co, Au and Bi, $\log(j_0)$ is linearly extrapolated to 0 V vs SHE at the potential window of 0.2 to 0.4 V vs SHE, 0.1 to 0.2 V vs SHE and -1.3 to -1.6 V vs SHE, respectively.

	(a)	**(b)**	**(c)**
Pt	-0.921	-2.792	-1.263
Ir	-1.444	-3.187	-1.453
Rh	-2.284	-3.362	-2.328
Pd	-2.523	-3.526	-3.151
Re	-6.228	-5.192	-6.903
Ru	-4.347	-4.511	-4.268
Co	-3.783	-4.928	-3.873
Ni	-5.585	-5.088	-6.042
Au	-5.013	-7.221	-4.523
Bi	-12.276	-12.162	-12.824
Cd	-10.770	-11.479	-10.123
In	-11.000	-10.244	-10.632

Derivation of the Formal Potential $E^{0'}$. At the reversible HER potential $E = 0$ V vs. SHE, we can apply the Nernst relation to obtain the formal potentials of the rate-determining step,

$$E = 0 = E^{0'} + \frac{RT}{F}\ln\left(\frac{C_f}{C_b}\right)$$

Here, we utilize the total adsorption sites $C_{tot} = C_f + C_b$ by assuming that all the adsorption sites are in contact with either the reactants or products of the rate-determining step near solid-liquid interface. Specifically, each site is in contact with either hydrogen ion H^+, adsorbed hydrogen atom H^* or hydrogen gas molecule H_2. For the Volmer reaction, the concentration of the reactants, i.e., the concentration of proton, $C_f = C_{tot}(1-\theta)$ is the concentration of unoccupied sites, and the concentration of products, i.e., the concentration of adsorbed hydrogen atom, $C_b = C_{tot}\theta$ is the concentration of occupied site. Here, θ is the fraction of adsorption sites. For the Heyrovsky reaction, the reactants are the pairs of adsorbed hydrogen atoms and protons. Therefore, the concentration of the pairs is equal to the concentration of adsorbed hydrogen atoms that $C_f = C_{tot}\theta$, and write $C_b = C_{tot}(1-\theta)$ for the concentration of H_2 formed near the sites that are

previously occupied by the adsorbed hydrogen atoms. With the approximations of C_f and C_b, we can further write Eq. (A-1) as,

$$E^{0'} = \begin{cases} -\frac{RT}{F}\ln\left(\frac{C_{tot}(1-\theta)}{C_{tot}\theta}\right) & \text{(Volmer)} \\ -\frac{RT}{F}\ln\left(\frac{C_{tot}\theta}{C_{tot}(1-\theta)}\right) & \text{(Heyrovsky)} \end{cases}$$

Writing θ with the Langmuir form that $\theta = K/[1+K]$ where $K = \exp(-\Delta G_{\mathrm{H}}/k_B T)$ is the equilibrium constant, we can obtain that

$$E^{0'} = \begin{cases} -\frac{RT}{F}\ln\left(\frac{\frac{1}{1+K}}{\frac{K}{1+K}}\right) = -\frac{\Delta G_{\mathrm{H}}}{|e|} & \text{(Volmer)} \\ -\frac{RT}{F}\ln\left(\frac{\frac{K}{1+K}}{\frac{1}{1+K}}\right) = \frac{\Delta G_{\mathrm{H}}}{|e|} & \text{(Heyrovsky)} \end{cases}$$

Exchange Current and the Tafel slope for Bi. For the purpose to measure the exchange current and resolve the contraversy on the values of the Tafel slope b reported experimetnally and calculated using the computational CV model, we regenerated the experimetal Tafel plot from reference [141], as shown in Figure 6-4. Among the total reported overpotential region 0 to 1.60 V, we focus on analyzing the Tafel slope in the region that displays the most linear behavior, 1.3 to

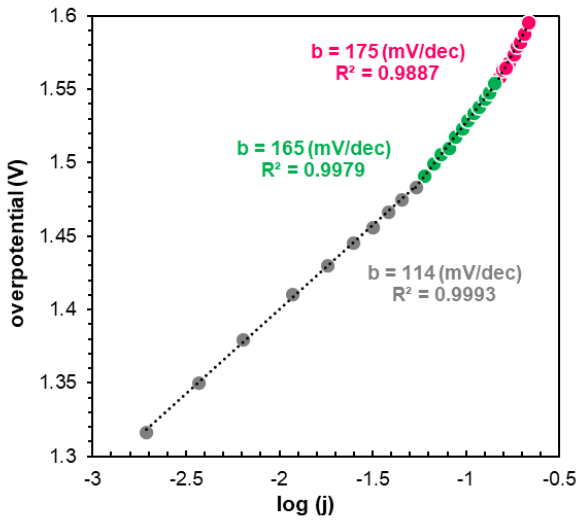

Figure 6-4. The Tafel Plot of Bi electrode. The experimental values are reproduced from reference shown as dots. For the low, medium, high overpotential regions, shown in gray, green, and magenta, respectively, the Tafel slopes are obtained from linear fitting.

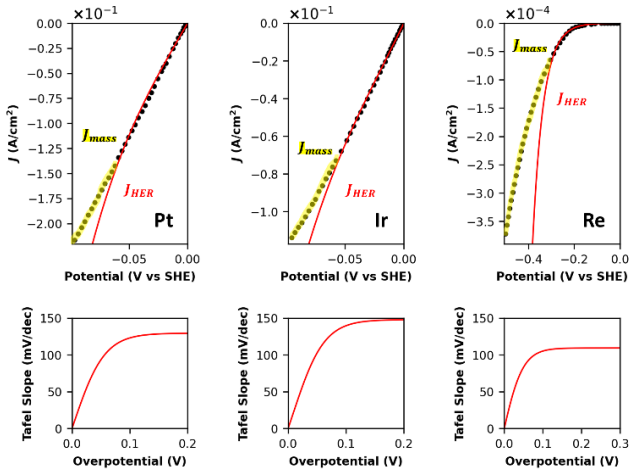

Figure 6-5. Cyclic voltammograms (CVs) of the precious metals. At the elevated potential regions where the experimental cyclic voltammograms (black dots) are heighted, the currents are limited by mass-transfer J_{mass}. Here, J_{mass} are smaller than the currents from HER J_{HER}, which are computational CV model of Eq. (6-4) in the main document. The experimental CVs are reported from the references listed in Table 6-3.

1.60 V. This agrees with our computed Tafel plot in 6-2 that the Tafel slope starts to converge 1.2 V overpotential. The linear fitting is performed in the three overpotential regions; 1.32 to 1.48 V, 1.48 V to 1.55 V and 1.56 V to 1.60 V. The corresponding Tafel slopes calculated from the three regions are 114, 165 and 175 mV/dec, respectively. The trend - the Tafel slope decreases with decreasing overpotential - explains that the experimentally reported Tafel slope of 100 mV/dec obtained from the linear fitting in the reported overpotential region of 1.1 to 1.5 overpotential (with respect to 0 V_{SHE}) is lower than the calculated Tafel slope of 134 mV/dec. We note that the experimental j_0 of Bi is not reported in the original literature. Therefore, we calculate the experimental j_0 by performing the Tafel analysis in the region -1.32 to -1.60 V of the experimental Tafel plot, shown in Figure 6-4, and obtain $\log(j_0)$ of 12.28. We find that the experimental Tafel slope shows a minimal change from -1.30 to -1.60 V. Therefore, performing the linear fitting at a lower potential region, -1.32 to -1.48 V leads to a lower value of $\log(j_0)$ of 14.5 as we showed before[224]. However, this variation of the experimental Tafel slopes measured at different potential region does not affect our results of the Yang-Saidi model as well as our computational CV model.

7-0 Enhanced the Hydrogen Evolution on Graphene-Coated Molybdenum Carbide

Note: The chapter is created from the published manuscript *Graphene Activation Explains the Enhanced Hydrogen Evolution on Graphene-Coated Molybdenum Carbide Electrocatalysts* (Timothy T. Yang and Wissam A. Saidi, *J. Phys. Chem. Lett.* 2020, 11, 7, 2759–2764). Most of the writings are not rephrased.

Graphene has shown high catalytic activities towards the hydrogen evolution reaction when coupled with Molybdenum carbides (Mo_yC). Because graphene is inert to the hydrogen evolution reaction due to the weak interaction with hydrogen, I posit that the enhanced activity originates from modulating the electronic properties of the graphene via coupling with Mo_yC. Herein, I use density functional theory (DFT) calculations in conjunction with *ab initio* thermodynamics and electrochemical modeling on γ-MoC supported graphene to determine the origin of the enhanced HER activities. In addition to previous claims that graphene's main role is to prevent agglomeration of Mo_yC nanoparticles, I show that the interplay between γ-MoC coupling and graphene defect chemistry activates graphene for HER. For all γ-MoC supported graphene systems, the HER mechanism follows Volmer-Heyrovsky pathway with the Heyrovsky reaction as the rate-determining step. To simulate the electrochemical linear sweep voltammetry at the device level, I develop a computational current model purely from the thermodynamic and kinetics descriptors obtained using DFT. This model shows that γ-MoC supported graphene with divacancies is optimum for HER with an exchange current density ~1×10^{-4} A/cm^2 and Tafel slope ~50 mV/dec^{-1}, which is in good agreement with experimental results.

7-1 Introduction

Water electrolysis is a promising approach for hydrogen production with no greenhouse gas emissions as long as renewable energy resources are used to drive water splitting. For this case, hydrogen is generated at the cathode site through hydrogen evolution reaction (HER). Despite the promise of molecular hydrogen for electrochemical energy storage and conversion, the high-cost of the optimum catalyst, platinum, has been the bottleneck of wide-scale deployment for electrochemical hydrogen production.[172,249] Molybdenum carbide (Mo_yC) is an attractive catalyst for HER due to its low cost and high stability.[250,251] Recent studies have demonstrated a good HER catalytic activity of Mo_yC in various structures including nanowires[252], microspheres[253], hierarchically porous architecture[254] or nano-octahedrons[255]. It is generally believed that Mo_2C phases such as β-Mo_2C exhibit excellent HER electrochemical catalytic behaviors[252,256] as their Mo-C mixed bands across the Fermi level provide a platinum-like metallic *d*-band structure.[257,258] On the other hand, MoC phases in hcp, fcc or WC structure (γ-MoC) are less favored for catalytic activities owing to their covalent or mixed ionic–covalent characters.[3,257]

Several studies have shown that the catalytic activities of Mo_yC nanoparticles can be further enhanced by coupling to carbon-based materials.[259-265] To date, the main role of graphene in Mo_yC/graphene heterostructures is not clear. Since graphene is extremely inert to HER,[266] it is generally believed that graphene hinders the aggregation of Mo_yC nanoparticles, therefore maximizing the number of active sites.[253,255,262,264,267] However, previous studies showed that HER activities can also be induced at the interface of heterostructures[268-270] such as nitrogen-doped graphene/g-C_3N_4[271] and graphene/MoS_2.[266,272] This raises the question whether the coupling of graphene to Mo_yC functionalizes graphene towards HER. Moreover, if this is the case, then a

fundamental understanding on the coupling behavior at the nanoscale can provide an opportunity to further enhance the HER activity.

7-2 Adsorption Sites on Supported Graphene

The Zur and McGill scheme[273] is applied to build a supercell model for the heterostructure employing a small lattice misfit between γ-MoC Mo-terminated (001) and graphene. γ-MoC (001) termination is chosen as this is a stable termination with low surface energy[251,257,274]. The optimum interface structure was determined from the minimum of the potential energy surface constructed by shifting graphene with respect to the Mo- or C-terminated MoC and relaxing all atomic coordinates. Using this approach, we find that the Mo-terminated MoC interface to be the most stable with Mo sitting atop C sites of graphene. Using the same interface model, in addition to pristine graphene (MoC-G), we have investigated graphene with Stone-Wales (MoC-SW), monovacancy (MoC-MV) and divacancy (MoC-DV) defects. We find that graphene and γ-MoC form a stable interface. The adhesion energies are relatively large and varies between -1.73 and -2.82 J/m^2 for graphene with or without defects (see Supporting Information). We note that these defects can be controlled by chemical treatments and irradiation techniques.[275]

To study hydrogen adsorption on the surfaces, we use a single hydrogen atom to probe all possible adsorption sites to obtain the differential hydrogen adsorption energy,

$$\Delta E_{\mathrm{H}^*} = E_{(n+1)\mathrm{H}/slab} - E_{n\mathrm{H}/slab} - \frac{1}{2}E_{\mathrm{H}_2} \tag{7-1}$$

where $E_{(n+1)\mathrm{H}/slab}$ and $E_{n\mathrm{H}/slab}$ are the total energies of the system with $n+1$ and n adsorbed hydrogen, and E_{H_2} is the energy of H_2 molecule. Figure 7-1 shows ΔE_{H^*} on all the possible

adsorption sites schematically. On MoC-G, H* is located only on atop C sites whereas hollow and bridge sites are unlikely to be occupied. For MoC-MV and MoC-DV, the most stable sites ($\Delta E_{H^*} = -0.3$ and -0.7 eV) correspond to carbon atoms with dangling bonds. Also, on MoC-SW, a strong adsorption site ($\Delta E_{H^*} = -0.3$ eV) appears at the apex of a pentagon carbon ring. In addition to the direct interaction of H* with C, the Mo d-band orbitals of subsurface Mo layers also affect hydrogen bonding. For example, on MoC-G, the ΔE_{H^*} of H* at the atop sites of C which is supported on top of subsurface Mo is about 1 eV weaker than the C which is at Mo bridge sites. Overall, the filling sequence of these sites follows the adsorption strength: sites having strong interaction with H* are occupied first. This is similar to β-Mo_2C surface as we have verified before.[276] Further, the induced-curvature of graphene due to its interaction with MoC causes sp^2-sp^3 hybridization also affects hydrogen adsorption strength,[277-279] which causes small variations of ΔE_{H^*} on some symmetric sites especially for MoC-DV.

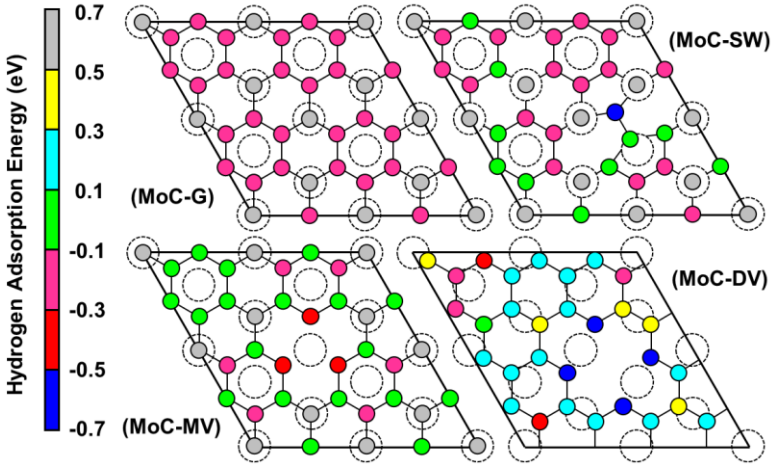

Figure 7-1. The hydrogen adsorption energies ΔE_{H^*} of the HER activation sites on γ-MoC supported graphene with graphene defects. The adsorption sites are located on atop sites of the carbon atoms of surface graphene. These surface carbon atoms are color coded to represent the hydrogen adsorption energy. The supporting sub-layer Mo atoms of γ-MoC are shown as dashed circles.

We compute the hydrogen adsorption free energy ΔG_{H} (obtained from ΔE_{H^*} after adding phonon contributions, see Supporting Information) to study HER thermodynamically. For $\Delta G_{\mathrm{H}} > 0$, HER is endothermic while it is an exothermic process for $\Delta G_{\mathrm{H}} < 0$. The optimum HER activity corresponds to $\Delta G_{\mathrm{H}} \cong 0$, i.e., smallest free energy is needed for hydrogen to switch from gas state to adsorbed state or *vice versa*.[111] Figure 7-2(a) shows ΔG_{H} for different hydrogen coverage C_{H} (defined as number of H^* per surface area). While ΔG_{H} increases monotonically with C_{H} for MoC-G and MoC-SW due to repulsive $\mathrm{H}-\mathrm{H}$ interactions, ΔG_{H} oscillates at low C_{H} for MoC-MV and MoC-DV due to mesomeric effect and compensation of dangling bonds. The mesomeric effect is caused by hydrogen adsorption that breaks graphene π bonds and delocalizes the electrons of H^* at neighboring sites (ortho or para sites). These sites then become favored sites for subsequent hydrogen adsorption.[280]

To determine the hydrogen coverage under different electrochemical environments, we compute the total hydrogen adsorption free energy ΔG_{tot} with considerations of pH and external

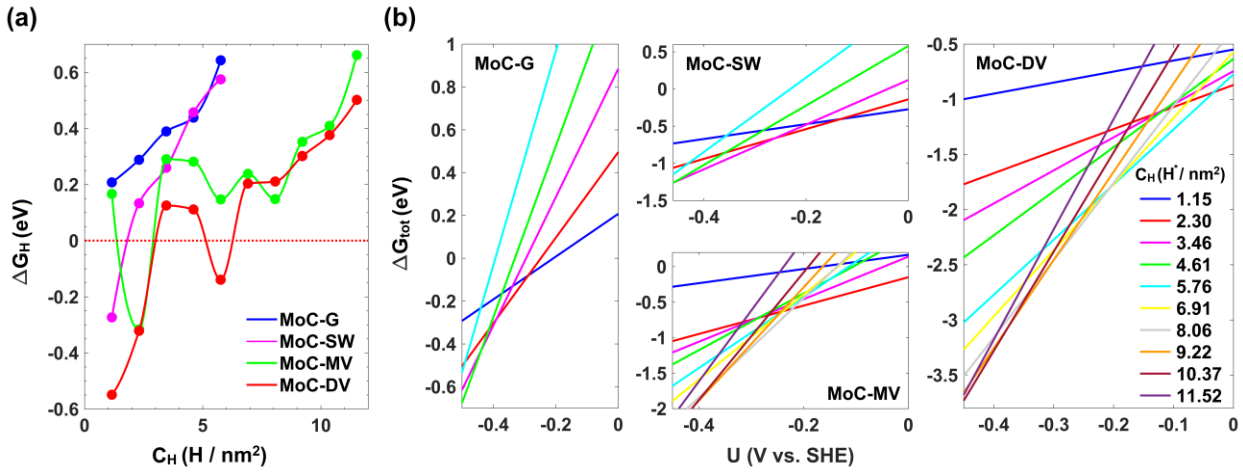

Figure 7-2. (a) Hydrogen adsorption free energy ΔG_{H} as a function of hydrogen coverage C_{H}. The red-dashed line indicates $\Delta G_{\mathrm{H}} = 0$ for the optimum HER rate. **(b)** Total hydrogen adsorption free energy ΔG_{tot} as a function of external potential U at different hydrogen coverages C_{H}. See Figure 6-5 for 3D representations of the adsorption configurations near 0 vs SHE. For Figures 6-2(a) and 6-2(b), we only show the values at the hydrogen coverages that are relevant to the HER potential window from 0 to -0.5V vs. SHE.

potential U (see Supporting Information).[281] Figure 7-2(b) shows ΔG_{tot} of the four coupled systems; the most favored C_{H} has the lowest ΔG_{tot}, and the corresponding ΔG_{H} for different C_{H} is shown in Figure 7-2(a). On MoC-G, H^* interacts weakly with the surface ($\Delta G_{\mathrm{H}} = 0.21$ eV) at $C_{\mathrm{H}} = 1.15$ $\mathrm{H}^*/\mathrm{nm}^2$ from 0 to -0.3 V. In contrast, hydrogen adsorption is stronger on MoC-SW and MoC-MV at 1.15 $\mathrm{H}^*/\mathrm{nm}^2$ ($\Delta G_{\mathrm{H}} = -0.27$ eV) and 2.30 $\mathrm{H}^*/\mathrm{nm}^2$ ($\Delta G_{\mathrm{H}} = -0.32$ eV) below -0.1 V, respectively. Surprisingly, MoC-DV is predicted to have a strong HER activity ($\Delta G_{\mathrm{H}} = -0.14$ eV) at 5.76 $\mathrm{H}^*/\mathrm{nm}^2$ with only a small overpotential -0.05 V. This will be also validated by examining the exchange current density as will be discussed later.

7-3 Mechanism of the Hydrogen Evolution Reaction on Supported Graphene

The overall HER reaction $\mathrm{H}^+ + e^- \rightarrow \frac{1}{2}\mathrm{H}_2$ takes place *via* two possible pathways namely the Volmer-Heyrovsky or the Volmer-Tafel. In an acidic solution, the three elementary steps can be written as,

$$\mathrm{H_3O^+} + e^- \leftrightarrow \mathrm{H^*} + \mathrm{H_2O}; \qquad \text{(Volmer)}$$

$$\mathrm{H_3O^+} + e^- + \mathrm{H^*} \leftrightarrow \mathrm{H_2O} + \mathrm{H_2} \qquad \text{(Heyrovsky)}$$

$$\mathrm{H^*} + \mathrm{H^*} \leftrightarrow \mathrm{H_2}. \qquad \text{(Tafel)}$$

The Volmer reaction refers to hydrogen deposition from liquid water to surface. To form H_2 gas, H^* can either react with H^+ in solution through the Heyrovsky reaction or with another H^* on surface through the Tafel reaction. Figure 7-3 shows that the Volmer-Heyrovsky pathway is preferred for all structures with an activation barrier E_{avt} less than 0.3 eV for the Volmer reaction and 0.9 eV for the Heyrovsky reaction. Thus, the Heyrovsky reaction is the rate-determining step

(rds). In contrast, the Volmer-Tafel pathway is hindered by the large activation barriers ($E_{\mathrm{avt}} >$ 2.4 eV) of the Tafel reaction. For comparison, we also show the corresponding activation barriers on Pt (111) where both of the Volmer-Heyrovsky and the Volmer-Tafel pathways are accessible with E_{avt} than ~0.5 eV.[282] We also use an extrapolation scheme[283,284] to eliminate finite-size effect for reaction energy and activation energy but our conclusions did not change that the Volmer-Heyrovsky is the favorable route with the Heyrovsky reaction as the rds for all systems (see Supporting Information for calculation details and Table 7-2 for the corrected E_{avt}).

7-4 Electrochemical Current Modeling

The overall HER with the Heyrovsky reaction as the rds can be described from the current-potential[285]

$$j = nFk_{ana}C_{tot}\theta \exp(-\alpha f\eta) \tag{7-2}$$

where $f = F/RT$ with F the Faraday constant, R the gas constant and the temperature T is chosen to be at room temperature 298 K. n is the total electron involved per active site, k_{ana} is the rate constant. C_{tot} is the concentration of reactants near the electrode i.e., H^*, which is rationalized as the number of active sites per surface area. The transfer coefficient α is defined as the fraction of the activation barrier induced by η.[225,286] For each γ-MoC supported graphene system, we compute α by evaluating the change of excess charge between transition and initial states using Bader analysis, as suggested by Chan et al.[283] We note that the strategy only gives a rough estimate of α while is waited to be confirmed. See Supporting Information and Table 7-2. We find that $\alpha = 0.1$ ~ 0.35. $\alpha < 0.5$ indicates that the transition state of a reaction is final-state-like rather than initial-

state-like.[225] Thus, for the coupled systems, the transition states are final-state-like as can be also verified from examining the C − H bond length shown in Figure 7-3.

Near the electrode surface, the fraction of hydrogen atoms that are involved in HER can be written as

$$\theta = \begin{cases} \dfrac{1}{K\exp(\eta f)+1} & \text{for } \Delta G_{\mathrm{H}} < 0 \\ \dfrac{K}{\exp(\eta f)+\mathrm{K}} & \text{for } \Delta G_{\mathrm{H}} > 0 \end{cases} \tag{7-3}$$

where $K = \exp(-\Delta G_{\mathrm{H}}/k_B T)$ with the averaged ΔG_{H} among all adsorption sites corresponding to the hydrogen coverage near zero overpotential (see detailed discussion for ΔG_{H} and the derivation of θ in Supporting Information).[111] For $\eta = 0$, θ is of the form of a Langmuir model that has been applied widely to study HER on various catalytists.[111,123,285] θ rapidly increases with η attaining 1 when η is negatively away from 0. Thus, expectantly more hydrogen atoms are involved in HER at negative potentials that can be understood from the enhanced stabilization of H^+ on electrode surface with negative potential. This behavior of θ is also consistent with the trend of increasing C_{H} with negative potential from the *ab initio* thermodynamics results in Figure 7-2(b). Furthermore,

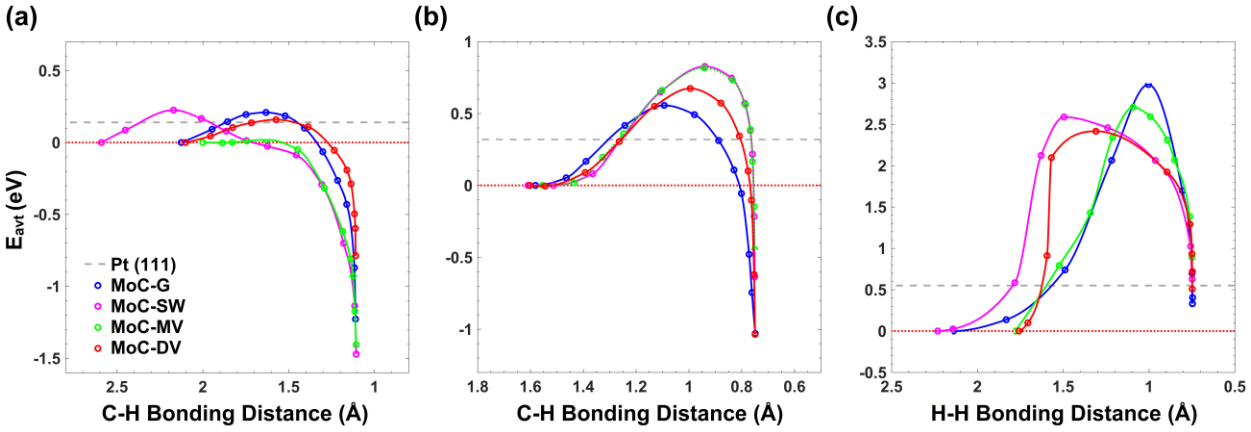

Figure 7-3. Minimum-energy pathways for the **(a)** Volmer, **(b)** Heyrovsky and **(c)** Tafel reactions. The reaction pathway is gauged using the bonding distance between C and H in (a) and (b), or the distance between two hydrogen atoms that are involved in the formation of H_2 in (c). The hydrogen coverage for each reaction is selected at $\eta = -0.05$ V, as shown in Figure 6-2(b). The dots indicate the images employed in the NEB simulations.

H^+ that comes to the surface at higher C_H is more likely to from H_2 as can be seen from Figure 7-2(a) that ΔG_H increases with increasing C_H. Note that ΔG_H is an intrinsic property that is independent to η as defined in the supporting information.

The rate constant k_{ana} ~ 200 site^{-1}s^{-1} is universal for ideal HER catalysts.[111] To validate that this value of k_{ana} is also applicable on the Mo_yC supported graphene systems, we fit Eq. (7-2) to various experimental currents on similar systems (see Supporting Information). We find excellent fits with k_{ana} from 162 to 383 site^{-1}s^{-1}. The obtained range for k_{ana} is consistent with the previous estimate ~200 site^{-1}s^{-1} on transition metals and β-Mo_2C surfaces.[111,276] In addition, the curvature of the experimental currents corresponds to $\alpha = 0.3 \sim 0.4$, which is in good agreement with our computed values from DFT $\alpha = 0.1 \sim 0.35$ for the different γ-MoC supported graphene systems.

Figure 7-4(a) depicts the HER polarization curves from Eqs. (7-2) and (7-3). For comparison, we also reproduce the curves of isolated pure graphene, γ-MoC bulk, and 20 wt% Pt on carbon black (Pt-C) obtained from experiments.[12,251,262] We show clearly that the coupling of γ-MoC and graphene enhances the HER activity, which are sluggish on graphene or γ-MoC bulk in their isolated form. Further, the presence of graphene defect chemistry modulates the HER activities of the coupled systems: MoC-SW shows a similar HER activity with MoC-G while as MoC-MV and MoC-DV displays enhanced activities. Using Eq. (7-2) and (7-3), we calculate the exchange current densities j_0 at zero external potential and are reported in the SI. The MoC-DV has the highest j_0 of ~1×10^{-4} A/cm^2 that is comparable to the optimum HER catalysts.[111]

To further compare with experimental studies, we measure the Tafel slopes $d\eta/d\log(j)$ that is often used to determine the HER mechanism. Figure 7-4(b) shows the Tafel slopes as obtained numerically from the currents in Figure 7-4(a) or in a closed form $-2.303RT/F(1+\alpha)$

that can be derived from Eqs. (7-2) and (7-3). As seen from the figure, the Tafel slope ranges 45 ~ 53 mV/dec^{-1} for the γ-MoC supported graphene systems suggesting that the Heyrovsky is the rds.[240] This corroborates the NEB calculations. It should be noted that even though there is debate in the literature on whether the Tafel slope can be evaluated using $d\eta/d\log(j) = -2.303RT/F(1+\alpha)$,[287] such an expression follows from the exchange current model of Eq. (7-2) that is a very good fit to experimental results as discussed before.

Experimentally, enhanced HER activities have been reported on several graphene-coated Mo_yC catalysts with nitrogen or phosphorous doped graphene, or reduced graphene oxide.[262,288-290] Our study shows that the optimization of these catalysts requires a fine tuning between Mo_yC supports and graphene bonding chemistry. Such interplay between both effects ultimately would stabilize hydrogen on graphene that is otherwise inert. The underpinning of this stabilization is due to charge transfer effect. Extra electrons (holes) on graphene will occupy graphene's anti-bonding π* (bonding π) bands, which weakens graphene π bonding and increases hydrogen stabilization as less energy is required to break the graphene π bonds.[290,291] While Mo_yC in previous experiments

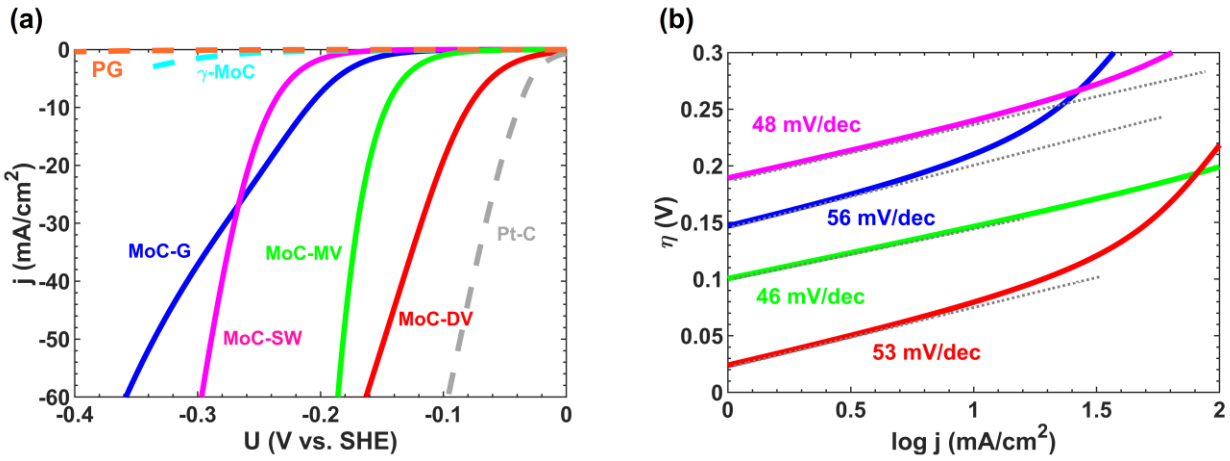

Figure 7-4 (a). The polarization curves for γ-MoC supported graphene systems. For comparison, we show experimental Pt-C from Ref. [3], as well as computed currents for isolated γ-MoC from Ref. [9] and pure graphene (PG) from Ref. [12]. The computed curves are obtained using Eqs. (7-2) and (7-3) with k_{ana} = 200 site^{-1}s^{-1}. **(b)** The Tafel slopes of the corresponding γ-MoC supported graphene systems in (a).

belonged to different phases such as Mo_2C (JCPDS 15-0457[262], 65-8766[289] and 01-079-0744[292]) and MoC (PDF 65-3558)[288], and graphene is modified in different ways, there are two main factors that makes our findings general. First, charge donation from Mo_yC to graphene is expected to be from Mo irrespective of Mo_yC phase, as carbon terminated surfaces are not favorable with graphene. Second, the doping nature of graphene can be characterized by charge buildup or depletion irrespective of the defect chemistry, which directly impacts the bonding of the hydrogen adsorbates.[293,294] These factors explain why our results on γ-MoC supported graphene are similar to experimental results on graphene-coated Mo_yC catalysts[260,288,289] in terms of displaying similar HER exchange rates 1×10^{-4} A/cm^2 and in having the Volmer-Heyrovsky as preferred HER mechanism with the Heyrovsky reaction as rds.

Using first principles calculations, we have investigated the HER on γ-phase MoC supported graphene with graphene defects including Stone-Wales, mono-vacancies and divacancies. We show that the reaction processes take place *via* the fast-rate Volmer reaction followed by the Heyrovsky reaction as the rate-limiting step, while the Tafel reaction experiences high activation barrier over 2 eV. We have used a computational approach to obtain electrochemical linear sweep voltammetry and to quantify the overall HER rate using kinetic and thermodynamic variables obtained from first-principles calculations. We show that the supported γ-phase MoC and divacancy defects play a role to modulate the hydrogen adsorption events resulting in an exchange current density of 1×10^{-4} A/cm^2. This study provides atomistic insights on general graphene coated Mo_yC electrocatalysts.

7-5 Supporting Information

Computational Details. We use the Vienna Ab Initio Simulation Package (VASP) for the first-principles DFT calculations. We use the Perdew-Burke-Ernzerhof (PBE) exchange-correlational functional to solve the Kohn-Sham equations within periodic boundary conditions, and the PAW pseudopotentials to describe electron-nucleus interactions.[160-163] We include Tkatchenko and Scheffler van der Waals corrections for all calculations[150]. The electronic self-consistent loops are terminated within energy-change tolerance of 1×10^{-6} eV. The climbing NEB method is applied for finding minimum energy pathways with the tolerance of 0.05 eV/Å.[295]

To model the HER mechanisms in acidic solution, we use a standard setup for solid-liquid interface by employing a single water monolayer located at ~3 Å above surface to replicate bulk water.[11] In the water monolayer, each H_3O^+ is bonded with three H_2O in Eigen structure.[296] Starting from an ice-like configuration, similar to what was done for Pt (111) with proton

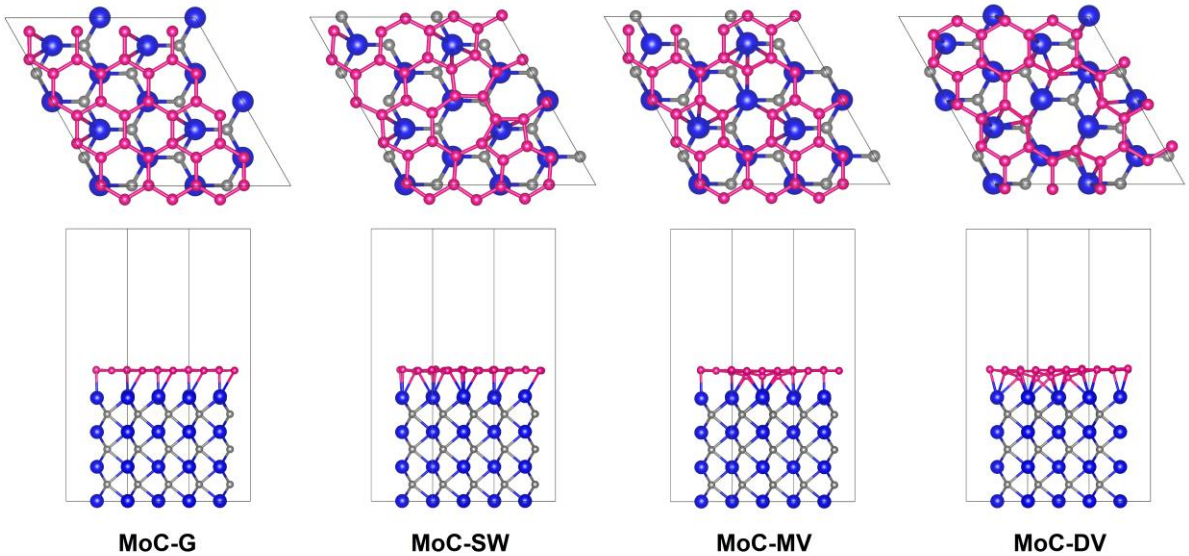

Figure 7-5. The structure of γ-MoC supported graphene systems (top and side views). The carbon atoms of graphene (γ-MoC) are in magenta (gray), and the Mo atoms of γ-MoC are in blue.

concentration of 1/8,[297] we find that the H_2O molecules can be in three different configurations such that their H atoms point toward (H-down) or away (H-up) from the surface, or their molecular planes are in parallel to the surface (H-flat). The most stable water layer corresponds to half of the H_2O molecules in H-down and the other half in H-flat configuration, and a less stable water layer is also found by turning 1/4 H_2O from H-down to H-up configuration. We verified that the different water configurations have a small effect of less than 0.1 eV on the activation barriers of the HER elementary steps.

In DFT calculations, the relaxed γ -phase MoC in $P\bar{6}m2$ hexagonal structure (WC-type) has the lattice parameters of $a = b =$ 2.89 Å and $c =$ 2.81 Å , in agreement with experiments.[298,299] The γ-MoC (001) surface is chosen to couple with graphene as it has been verified to be a stable termination with low surface energy that is exposed on γ-MoC nanoparticles[251,257,274]. The periodic heterostructure slab models are constructed using 4×4 single graphene supported by $2\sqrt{3} \times 2\sqrt{3}$ MoC-(001). The γ-MoC supported graphene is constructed using Zur and McGill scheme whereby the interface translational symmetry is compatible with the symmetry on both sides of the interface.[273] The interface separation between the γ-MoC Mo-terminated (001) and graphene is 2.2 Å. The models are composed of 5-8 atomic layers with a 14 Å vacuum to minimize the interactions between images in non-periodic direction. We fixed bottom 2 ~ 4 layers at bulk positions, and allowed all the other coordinates to relax with a tolerance of 1×10^{-6} eV. We use $2 \times 2 \times 1$ Monkhorst-Pack k-point to sample the Brillion zone and planewave cutoff of 400 eV. For the supported graphene with defects, we have verified that there is no surface reconstruction by doubling the surface supercell.

To quantify the structure stability of γ-MoC (001) Mo-terminated supported graphene, we compute the adhesion energy defined as

$$E_{adh} = \frac{E_{\gamma-\mathrm{MoC}\,/graphene} - E_{\gamma-\mathrm{MoC}} - E_{graphene}}{A}$$

where $E_{\gamma-\mathrm{MoC}\,/graphene}$, $E_{\gamma-\mathrm{MoC}}$ and $E_{graphene}$ are the DFT energies of the γ-MoC (001) Mo-terminated supported graphene system, γ-MoC (001) Mo-terminated surface and unsupported graphene, respectively, and A is the contacting surface area between the two isolated interfaces. The adhesion energy of MoC/graphene systems are summarized in Table 7-1.

Table 7-1. The adhesion energies E_{adh} of γ-MoC (001) Mo-terminated systems. We also show the vertical distance between graphene and γ-MoC (001) in addition to graphene rumpling.

Systems	E_{adh} (J/m^2)	Vertical Distance (Å)	Graphene Rumpling (Å)
MoC-G	-1.73	2.12	0.54
MoC-SW	-1.93	2.12	0.39
MoC-MV	-2.78	2.18	0.05
MoC-DV	-2.82	2.18	0.09

Table 7-1 shows that the adhesion energy of the γ-MoC Mo-terminated (001) supported graphene is -1.73 J/m^2 that is about five times larger than that of SiO_2/graphene[300] (-0.35 J/m^2) interface. Graphene defects are found to enhance the interface stability especially for the case of divacancy defects resulting in the adhesion energy of -2.82 J/m^2. On the other hand, γ-MoC C-terminated

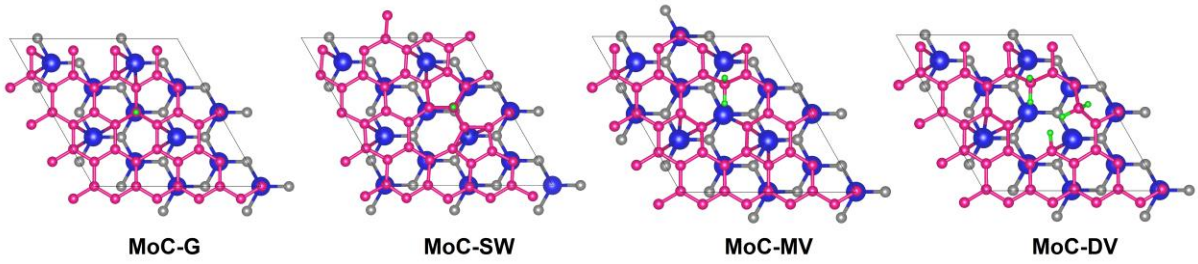

Figure 7-6. The hydrogen adsorption configurations near the HER reversible potential for the four γ-MoC supported graphene systems. The carbon atoms of graphene (γ-MoC) are in magenta (gray), and the Mo atoms of γ-MoC are in blue. The hydrogen atoms are in green. For the MoC-G, MoC-SW, MoC-MV and MoC-DV, the hydrogen coverages are 1/32 ML, 1/32 ML, 2/31 ML and 5/30 ML, respectively (monolayer, H* per surface carbon atoms). These hydrogen coverages are presented by the lowest line near the potential of 0 vs. SHE in Figure 7-2(b).

Table 7-2. ΔE and E_{avt} (in eV) for the three HER elementary steps at U_{SHE} obtained from the model with water layer in H-up and H-down configuration. We list the symmetry factor β of the Volmer and Heyrovsky reaction. Note that $\beta = 0$ for the Tafel reaction as there is no charge transfer between the water layer and the surface.

H-up	**Volmer**			**Heyrovsky**			**Tafel**		
	$\boldsymbol{\Delta E}$	$\boldsymbol{E_{avt}}$	$\boldsymbol{\beta}$	$\boldsymbol{\Delta E}$	$\boldsymbol{E_{avt}}$	$\boldsymbol{\beta}$	$\boldsymbol{\Delta E}$	$\boldsymbol{E_{avt}}$	$\boldsymbol{\beta}$
MoC-G	0.46	0.40	0.07	0.60	0.85	0.12	0.33	2.98	0
MoC-SW	0.30	0.27	0.04	0.82	1.32	0.19	0.63	2.58	0
MoC-MV	0.30	0.30	0.07	0.96	1.62	0.29	0.89	2.70	0
MoC-DV	0.66	0.50	0.10	0.33	1.29	0.28	0.51	2.42	0
H-down	**Volmer**			**Heyrovsky**			**Tafel**		
	$\boldsymbol{\Delta E}$	$\boldsymbol{E_{avt}}$	$\boldsymbol{\beta}$	$\boldsymbol{\Delta E}$	$\boldsymbol{E_{avt}}$	$\boldsymbol{\beta}$	$\boldsymbol{\Delta E}$	$\boldsymbol{E_{avt}}$	$\boldsymbol{\beta}$
MoC-G	0.04	0.46	0.14	0.28	0.94	0.20	0.33	2.98	0
MoC-SW	0.43	0.23	0.00	1.24	1.45	0.27	0.63	2.58	0
MoC-MV	0.61	0.16	0.10	1.06	1.58	0.32	0.89	2.70	0
MoC-DV	0.45	0.45	0.13	0.29	0.69	0.30	0.51	2.42	0

(001) supported graphene are less stable with the adhesion energy of -0.90 J/m^2, and exhibits poor HER activity as an isolated graphene.[266]

Hydrogen adsorption and free energies are determined using Eq. (3-3) with $\Delta E_{\mathrm{ZPE}} = 0.18$ eV which is the averaged value obtained from MoC-G and MoC-DV at low coverages. This is obtained by relaxing graphene and the supporting Mo layer. Comparing to metal surfaces ($\Delta E_{\mathrm{ZPE}} \cong 0.04$ eV), this high value is attributed to the high C-H bond stretching mode.[256] The entropy difference $T\Delta S$ between the adsorbed and gas phase H_2(g) at standard conditions is -0.20 eV as obtained experimentally.[100] The total hydrogen adsorption free energy is defined as,

$$\Delta G_{tot} = \sum_1^n \Delta G_{\mathrm{H}} + n|e|U - k_B T \ln[\mathrm{H}^+] + \Delta E_{\mathrm{water}}$$

Here, the adsorbate-water interactions $\Delta E_{\mathrm{water}}$ is verified to be smaller than $\pm$ 0.1 eV, and hence will be ignored. Also, in acidic environment, $-k_B T \ln[\mathrm{H}^+]$ is negligibly small.

Application of Thermodynamic Exchange Current Model. Using the definition of reversible hydrogen electrode, $G_{\mathrm{H}^+} = |e|U_{\mathrm{SHE}} + \frac{1}{2}G_{\mathrm{H}_2}$, we can write the standard free energy of the Volmer reaction, $2\mathrm{H}^+(aq) + 2e^- \rightarrow \mathrm{H}^+(aq) + e^- + \mathrm{H}^*$, as

$$\Delta G^0 = (G_{\mathrm{H}^*} - |e|U + G_{\mathrm{H}^+}) - (2G_{\mathrm{H}^+} - 2|e|U) = G_{\mathrm{H}^*} + |e|(U - U_{\mathrm{SHE}}) - \frac{1}{2}G_{\mathrm{H}_2}$$

Using the definition of hydrogen adsorption free energy as defined in the main text, $\Delta G_{\mathrm{H}} = G_{\mathrm{H}^*} - \frac{1}{2}G_{\mathrm{H}_2}$, we can get

$$\Delta G^0 = \Delta G_{\mathrm{H}} + |e|\eta$$

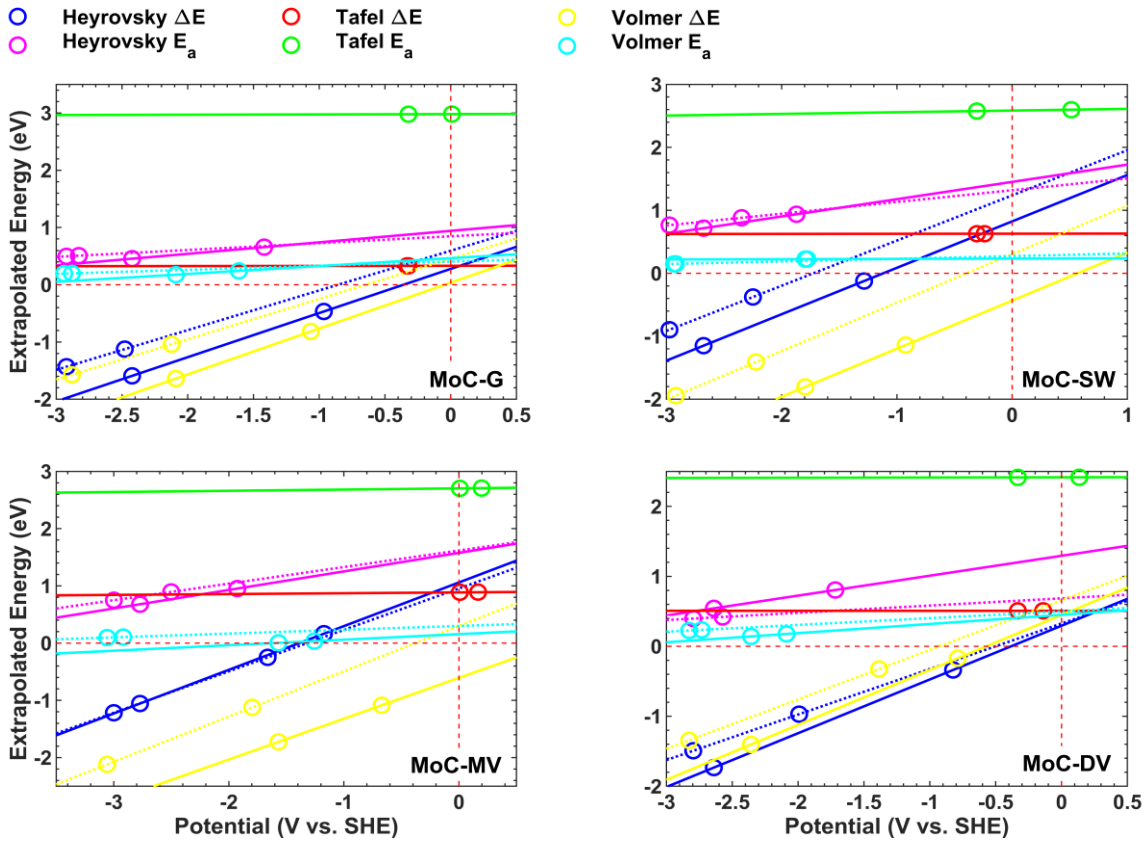

Figure 7-7. The extrapolation scheme of the γ-MoC supported graphene systems. The circles represent the total energies of the initial and final states for ΔE and of the initial and transition states for E_{avt}. The results obtained using the H-up and H-down water layer models are represented by the dashed and the solid lines, respectively.

where $\eta = U - U_{\mathrm{SHE}}$. At equilibrium, $\eta = 0$, the total free energy is zero that $0 = \Delta G_{\mathrm{H}} + k_B T \ln(K)$, which leads to $K_V = \exp\left(-\frac{\Delta G_{\mathrm{H}}}{k_B T}\right)$. The forward and the backward rate of the Volmer reaction are

$$r = \begin{cases} k_V^0 (1-\theta) \exp(-\alpha f \eta) & \text{(forward)} \\ k_{-V}^0 \theta \exp[(1-\alpha) f \eta] & \text{(backward)} \end{cases}$$

At equilibrium, the forward and the backward rates are equal, we can write that $\frac{k_V^0 (1-\theta) \exp(-\alpha f \eta)}{k_{-V}^0 \theta \exp[(1-\alpha) f \eta]} = 1$ or $\theta = \frac{K}{\exp(\eta f)+K}$ where $K_V = \frac{k_V^0}{k_{-V}^0}$ for $\Delta G_{\mathrm{H}} > 0$. If we define that $K = \frac{k_{-V}^0}{k_V^0}$ for $\Delta G_{\mathrm{H}} < 0$, we get the other expression that $\theta = \frac{1}{K_V \exp(\eta f)+1}$. This expression of θ is also obtained by Shinagawa et. al using a theoretical approach.[285] It follows a Langmuir isotherm which is conditioned to three requirements: 1) there is only a monolayer of adsorption sites, 2) the $\mathrm{H}^* - \mathrm{H}^*$ interactions are minimal compare to surface$-\mathrm{H}^*$ interactions, 3) the adsorption sites are identical, and 4) each adsorption site cannot be occupied by more than one H^*. Nørskov et. al. applied such expression of $\theta(\eta = 0)$ to study the thermodynamic exchange currents (defined at zero overpotential) on metal surfaces[111]. These metal surfaces satisfy the requirements: the adsorption sites on metal surfaces are identical with a nearly constant ΔG_{H} below and at $\theta = 1$, which shows negligible $\mathrm{H}^* - \mathrm{H}^*$ interactions. However, the ΔG_{H} sharply increases above $\theta = 1$, which indicates that all the adsorption sites are fully occupied.[123]

We claim that this θ model can also be applied on γ-MoC supported graphene systems. For MoC-G and MoC-SW, we find that a constant $\Delta G_{\mathrm{H}} = 0.2$ eV or -0.2 eV under 1/32 ML (monolayer, H^* per surface carbon atoms), respectively, and ΔG_{H} sharply increases above 1/32 ML. For MoC-MV and MoC-DV, ΔG_{H} wiggles with hydrogen coverage, as can be seen in Figure 7-2(a). However, if we remove the strong adsorption sites, i.e., where the last H^* occupied at 2/31

ML for MoC-MV, or 1/30, 2/30 ML and 5/30 ML for MoC-DV, we can see the same trend (constant ΔG_{H} vs hydrogen coverage) as discussed. We can ignore these stronger adsorption sites because H^{*} adsorbed at these coverages are less likely to be involved in HER than the other sites. Therefore, to compute the exchange current using the thermodynamic exchange current model, we use the averaged ΔG_{H} at the region where ΔG_{H} is nearly constant with increasing hydrogen coverage: 1/32 ML for MoC-G and MoC-SW, and (1, 3, 4, 5, 6, 7)/31 ML and (3, 4, 5, 6, 7)/30 ML, for MoC-MV and MoC-DV, respectively. Eq. (7-2) in the main text, $j = nFk_{ana}C_{tot}\theta \exp(-\alpha f\eta)$, can be written in the Butler-Volmer form as $j = j_0 \exp(-\alpha f\eta)$, where j_0 is a constant called exchange current density. At $\eta = 0$ where j_0 is defined, we can use the averaged ΔG_{H} to compute j_0. The results are shown in Table 7-3.

Table 7-3. The averaged ΔG_{H} used for the exchange current model and the computed j_0.

Systems	**ΔG_{H} (eV)**	**j_0 (A/cm^2)**
MoC-G	0.21	-1.14×10^{-6}
MoC-SW	-0.27	-8.92×10^{-8}
MoC-MV	0.21	-5.78×10^{-6}
MoC-DV	0.10	-3.34×10^{-4}

The value of k_{ana} for the γ-MoC supported graphene systems is determined by fitting the experimental values with the current model of Eq. (7-2) and (7-3) on graphene coated $\mathrm{Mo_yC}$ systems in experiments.[262,288,289] All the experimental currents are perfectly fitted with the model using α in the range of 0.3 and 0.4. Note here that the overall curvature of the experimental currents is controlled by α and is independent to k_{ana}. We show the data in Table 7-4 below. All the currents are fitted with r^2 = 0.99. To derive the Tafel Slope, we employ Eq. (7-2) and Eq. (7-3),

$$j = \begin{cases} nFk_{ana}C_{tot}\dfrac{1}{K\exp(\eta f)+1}\exp(-\alpha f\eta) & \text{for } \Delta G_{\mathrm{H}} < 0 \\ nFk_{ana}C_{tot}\dfrac{K}{\exp(\eta f)+K}\exp(-\alpha f\eta) & \text{for } \Delta G_{\mathrm{H}} > 0 \end{cases}$$

Near the zero overpotential; $K\exp(\eta f) \gg 1$ for $\Delta G_{\mathrm{H}} < 0$ and $\exp(\eta f) \gg K$ for $\Delta G_{\mathrm{H}} > 0$, we can rewrite that

$$\log(j(\eta \approx 0)) \cong \begin{cases} \log(nFk_{ana}C_{tot}) - \log(K) - \dfrac{1}{2.303}\eta f + \dfrac{1}{2.303}(-\alpha f\eta) & \text{for } \Delta G_{\mathrm{H}} < 0 \\ \log(nFk_{ana}C_{tot}) + \log(K) - \dfrac{1}{2.303}\eta f + \dfrac{1}{2.303}(-\alpha f\eta) & \text{for } \Delta G_{\mathrm{H}} > 0 \end{cases}$$

Taking the derivative with respect to η for both cases, we can obtain

$$\frac{d\log\big(j(\eta \approx 0)\big)}{d\eta} \cong -\frac{1}{2.303}f(\alpha+1)$$

The Tafel slope is defined as $d\eta/d\log(j)$, therefore, near $\eta \sim 0$,

$$\frac{d\eta}{d\log\big(j(\eta \approx 0)\big)} = -\frac{2.303RT}{F(\alpha+1)}$$

Table 7-4. The k_{ana} fitted from experimental values by choosing α in the range of 0.3 and 0.4.

EXP. 1 (Ref. 23, Fig. 4a)	$\boldsymbol{\alpha}$	$\boldsymbol{k_{ana}}$
Mo_2C/NC750	0.3	168
Mo_2C/NCS750	0.4	189
Mo_2C/G3-NCS750	0.4	295
EXP. 2 (Ref. 24, Fig. 4a)		
MoCx@C-1	0.3	214
EXP. 3 (Ref. 25, Fig. 5a)		
1.1g	0.3	162
2.2g	0.3	263
3.3g	0.4	383

8-0 MoS_2 Supported Platinum Nanoparticles for the Hydrogen Evolution Reaction

Note: The chapter is created from the published manuscript *High activity for hydrogen evolution reaction on the edges of MoS_2 supported platinum nanoparticles from cluster expansion and electrochemical modeling* (Timothy T. Yang, Teck Leong Tan, and Wissam A. Saidi, Chem. Mater. 2020, 32, 3, 1315–1321). Most of the writings are not rephrased.

Platinum nanoparticles (NPs) show advanced activity for the hydrogen evolution reaction (HER) than bulk platinum. I posit that in addition to exposed surface-area effect, there are additional edge sites that are created on the nanoparticles. I show that tuning the edge sites of catalysts can as well enhance HER activities from studying platinum NPs supported on a single-layer molybdenum disulfide. First, I determine the active catalytic sites using a cluster expansion method in conjunction with an *ab initio* thermodynamic approach, and show that the system is thermodynamically active at HER reversible potential under electrochemical conditions. I show that the Volmer-Tafel pathway is the preferred reaction mechanism with the Volmer reaction as rate-determining step in the HER potential window. Using a novel Butler-Volmer kinetic model to simulate linear sweep voltammogram, I obtain exchange current densities of $10^{-3} \sim 10^{-2}$ A/cm^2 that are in the same order as those measured on Pt (111) and supported platinum NPs. Importantly, I show that contrary to expectations, the enhanced HER mechanism is only attributable to the edges of the supported platinum NPs but not due to support interactions. My findings are general and are applicable for NPs with different sizes and shapes on various supports, as well as to different catalytic reactions.

8-1 Introduction

The diminishing supply of fossil fuels and the pollution problems associated with their combustion led to the search for sustainable and environmentally benign energy sources. Hydrogen is one of the potential alternatives that can be produced via HER, a critical reaction of water electrolysis by splitting water using electrical energy from solar or wind power.[301] While platinum is the most efficient catalyst for HER, its relatively high cost of $34 per gram limits commercial applications.[302] This explains the huge interest in reducing the content of platinum in HER electrodes or in finding cost-effective and equally efficient alternative catalysts.[303-305]

Platinum NPs offer a very attractive route to reduce the usage of platinum.[306,307] platinum NPs are tiny building blocks of matter containing a finite number of platinum atoms, which are often attached to substrates to prevent agglomeration. In contrast to the bulk counterparts, the efficiency of metallic NP catalysts can be tuned by modifying their morphology or supports. For example, Anderson et al. demonstrated that the size of platinum NPs affects oxygen reduction and carbon oxidation;[308] Nakajima et al. showed that HER activity can be maximized for a certain size of platinum NPs.[309] Recently, Huang et al. found that supported platinum NPs on MoS_2 have superior catalytic activities towards HER, that is comparable to bulk platinum despite a $\sim$70% reduction in platinum content.[8] However, the atomistic mechanism of the HER activity of the supported platinum NPs on MoS_2 is lacking thus hampering further improvements and optimizations of the catalyst.

There are several challenges associated with understanding the HER mechanism of supported or even unsupported metal particles. platinum NPs mainly expose (111) and (100) low-index surfaces[310,311] both of which exhibit similar HER rates, as evidenced by less than one order magnitude difference in the exchange currents.[312,313] However, the hydrogen adsorption and hence

the mechanism for the catalytic activity of the NPs can differ from that of the corresponding bulk counterparts.[6,314] This difference is because the NPs are rich in edges and vertices that could dominate the HER activity over the facets.[315,316] Additionally, the supporting substrate of the NPs can also influence the HER activity either through exposing edge sites, modifying charges in basal plane[317] or due to a concerted interplay between the support and the NP.[318]

Experimentally, it is also challenging to infer the HER mechanism using conventional electrochemical analysis. First, most experimental methods can only provide an ensemble assessment over different active sites.[319] For example, previous studies have shown that the HER activity from either platinum atoms or platinum clusters cannot be distinguished.[10,307,319] Second, the HER rates for high-catalytic surfaces system such as platinum are relatively fast, which results in a depletion of the reactants near electrode surface. The concentration gradients in both oxidants and reactants make the hydrogen mass transport the dominant rate for HER. Sheng et al. argued that such limitation cannot be avoided using conventional rotating electrodes.[320] Additionally, the impendence resistance from electrolyte can also affect the current measurements on fast HER electrodes even with a highly conductive electrolyte such as 0.1M $HClO_4$.[321]

First-principles calculations are attractive alternatives to experiments that can provide atomistic descriptions of active sites and mechanisms of supported platinum systems. However, in comparison to surfaces and periodic systems, supported metal clusters pose a significant challenge due to the combination of periodic (supports) and non-periodic (platinum NPs) elements in the hybrid system. Thus, it is computationally daunting to find the optimum hydrogen adsorption configurations on non-equivalent adsorption sites of supported metal clusters.[2] under electrochemical conditions.

8-2 Adsorption Configurations on Platinum Nanoparticles

We use CP2K[322] for the first-principles density functional theory (DFT) calculations employing the revised Perdew-Burke-Ernzerhof exchange-correlational functional to solve the Kohn-Sham equations.[149] More details are given in the Supporting Information. We investigate MoS_2/Pt_{20} as a representative of a supported platinum NPs on 2H-MoS_2. The 20-atom-platinum NPs (Pt_{20}) has ~ 1 nm in diameter with 12 atoms in the bottom layer that is in contact with MoS_2 and 8 platinum atoms in the top layer with an average Pt-Pt distance of 2.7 ± 0.2, in agreement with experimental HRTEM analysis.[8,323] To evaluate hydrogen adsorption strength, we define the hydrogen adsorption energy as,

$$\Delta E_{\mathrm{H}^*} = E_{(n+1)\mathrm{H}/slab} - E_{n\mathrm{H}/slab} - \frac{1}{2} E_{\mathrm{H}_2} \tag{8-1}$$

where $E_{(n+1)\mathrm{H}/slab}$ and $E_{n\mathrm{H}/slab}$ are the DFT energies of the system with $n+1$ and n adsorbed hydrogen H^*, and E_{H_2} is the energy of H_2 in the gas phase.

We use a cluster expansion (CE) method, as implemented in the TTK code package,[324,325] to model the effective interactions between H^* at different coverages. We identify the symmetry-unique adsorption sites including hollow, bridge, corner and atop sites. For each site, k, we assign an occupation variable ξ_k with the value of 1 (0) to represent a site with (without) H^*.[314] Using σ to represent a particular configuration of small hydrogen clusters α described by $\phi_\alpha = \prod_{k\in\alpha} \xi_k$, the cluster expansion energy is written as

$$E_{\mathrm{CE}}(\sigma) = \sum_{\alpha} V_\alpha \phi_\alpha \tag{8-2}$$

where V_α is the effective cluster interaction (ECI). In practice, a properly truncated Hamiltonian will predict the energies accurately as most V_α is close to zero with increasing distances between

H*. Only the symmetrical ECIs in the truncated Hamiltonian are evaluated from a finite set of DFT configuration energies as the training set. In the initial iteration, random distributions of H* with their energies $E_{CE}(\sigma)$ are obtained via Monte Carlo sampling across different coverages as well as the optimal ECIs. Another round of Monte Carlo sampling is required to obtain new low-energy structures to compare with the DFT structures. The DFT-verified structures are added to the training set for the subsequent round of cluster expansion, except for the highly distorted structures at high coverages. This process is repeated three times for finding low-energy hydrogen adsorption configurations, until no new low-energy σ are suggested by the Monte Carlo simulations. We note that structural relaxations for the Pt and H atoms are allowed during DFT calculations.

Hydrogen mainly interacts with the platinum NP but not with the MoS_2 support.[326,327] Figure 8-1(a) shows a schematic of the supported platinum cluster with three main potential hydrogen adsorption sites, namely atop site (*t*) of a Pt atom, bridge (*b*) site in between two Pt atoms, and edge (e) site associated a single Pt atom at the edges of the cluster. Further, the adsorption strength is also found to be sensitive to the platinum cluster's local topology as identified by micro facets f_i. The strongest adsorption is at bridge sites b_{12} ($-0.71 < \Delta E_{\mathrm{H}^*(n=0)} < -0.68$ eV) located at the edges of side facets f_1 and f_2, while as the weakest are atop sites t_{45} ($-0.15 < \Delta E_{\mathrm{H}^*(n=0)} < -0.10$ eV) of the corner Pt at the edges of f_4 and f_5. The other strong adsorption sites are bridge sites b_{i5}/b_{i6} ($-0.60 < \Delta E_{\mathrm{H}^*(n=0)} < -0.47$ eV) at top/bottom layer f_5/f_6, and the edges/corners of two/three facets such as e_{i5}, e_{i6}/e_{ij5}, e_{ij6} ($-0.45 < \Delta E_{\mathrm{H}^*(n=0)} < -0.28$ eV) for any i and j with $i \neq j$. There are few moderate adsorption sites such as the bridge sites on top of the platinum cluster, b_5, and the top site at Pt terrace, t_5 ($-0.38 < \Delta E_{\mathrm{H}^*(n=0)} < -0.26$ eV). We find that the adsorption strength near f_4 is relatively weaker while is stronger near f_1.

We have trained a CE effective Hamiltonian using 400 different configurations with up to 57 adsorbed hydrogen atoms distributed among 47 adsorption sites on the platinum NP. Figure 8-1(b) shows the total hydrogen adsorption energy $\sum_i^n \Delta E_{\mathrm{H}^*}$ for configurations with $n = 1, 2 \ldots 57$. For each n, we identify the lower-energy configurations with the lowest $\sum_i^n \Delta E_{\mathrm{H}^*}$ as indicated by red dots.[314] The inset in the figure depicts a few of these low-energy configurations. The hydrogen coverage $\theta = 1$ corresponds to $n = 47$ at which $\sum_i^n \Delta E_{\mathrm{H}^*}$ has the lowest value among all n. This indicates that the adsorption sites on the NP are fully occupied. The defintion of full occupation is chosen to be consisent with the periodic metal surfaces that undergo a sharp weakening of hydrogen adsorption strength at $\theta = 1$.[123] As θ increases, the top layer of the platinum NP distorts to a less symmetrical form while as the bottom layer remains relatively intact due to its strong affinity with MoS_2.[328]

Hydrogen adsorption strength is highly affected by adsorption configurations due to adsorbate-adsorbate and adsorbate-surface interactions. In agrees with our previous findings on

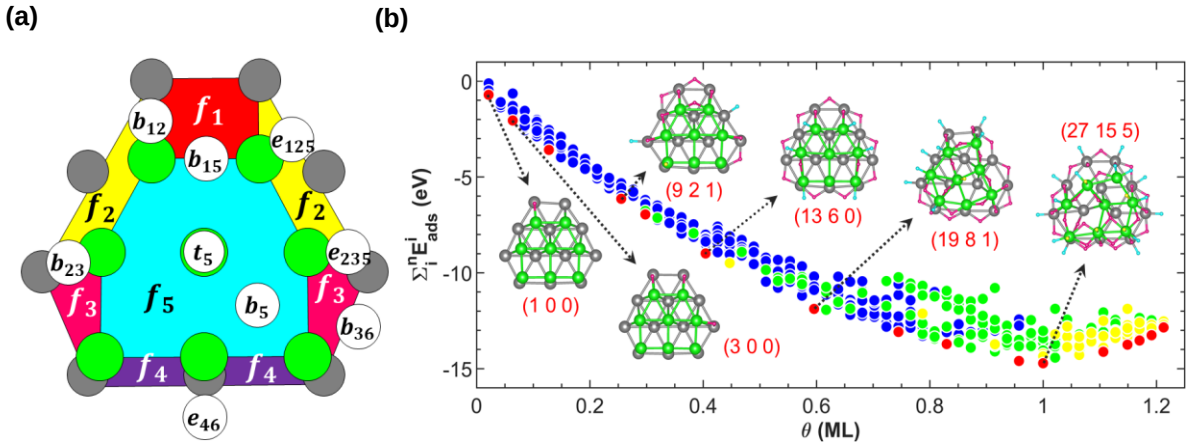

Figure 8-1. (a) Schematic of MoS_2/Pt_{20} and hydrogen adsorption sites. Facets of the supported Pt_{20} labeled as f_i $(i = 1 - 4)$ correspond to the sides of the cluster. f_5 and f_6 (not shown) are top and the bottom facets. Few adsorption sites are labeled as white spheres while as Pt atoms at the top/bottom layer are represented by green/grey spheres. **(b)** The total adsorption energies $\sum_i^n \Delta E_{\mathrm{H}^*}$ for different adsorption configurations on MoS_2/Pt_{20}. The configurations with the distortion of the supported Pt_{20} is measured by the displacement of top Pt atoms for less than 0.5, between 0.5 and 1, and above 1 Å/atom, are represented by blue, green and yellow dots, respectively. The number of adsorbed hydrogen atoms at bridge/corner/top sites, are represented respectively by magenta/blue/yellow spheres in the insets, are shown as triplets in prentices.

the surface with non-equivalent adsorption sites,[124] we show that the filling sequence follows the adsorption strength of single H^* as shown Figure 8-1(b); b_{12}, b_{23} and b_{15} are occupied starting at $\theta = 0.06$, followed by b_{i5}, b_{i6}, e_{i5}, e_{i6}, e_{ij5} and e_{ij6} up to $\theta = 0.4$. Moderate adsorption sites b_5 are filled at $\theta = 0.6$ followed by t_5 up to $\theta = 1$.

8-3 *Ab Initio* Thermodynamics under Electrochemical Environments

The overall hydrogen evolution reaction $2H^+ + 2e^- \rightarrow H_2$ describes the formation of hydrogen gas H_2 from hydrogen ions. Parsons argued that HER rate is related to atomic hydrogen adsorption ability on surface,[108] which was quantified by Nørskov using the hydrogen adsorption free energy ΔG_H from first principles calculations defined as[25]

$$\Delta G_H = \Delta E_{H^*} + \Delta E_{ZPE} - T\Delta S \tag{8-3}$$

where ΔE_{H^*} is from Eq. (8-1), ΔE_{ZPE} and ΔS are respectively the differences of zero-point energy and entropy between H^* and H_2. Using experimental thermodynamic results for H_2, we determine

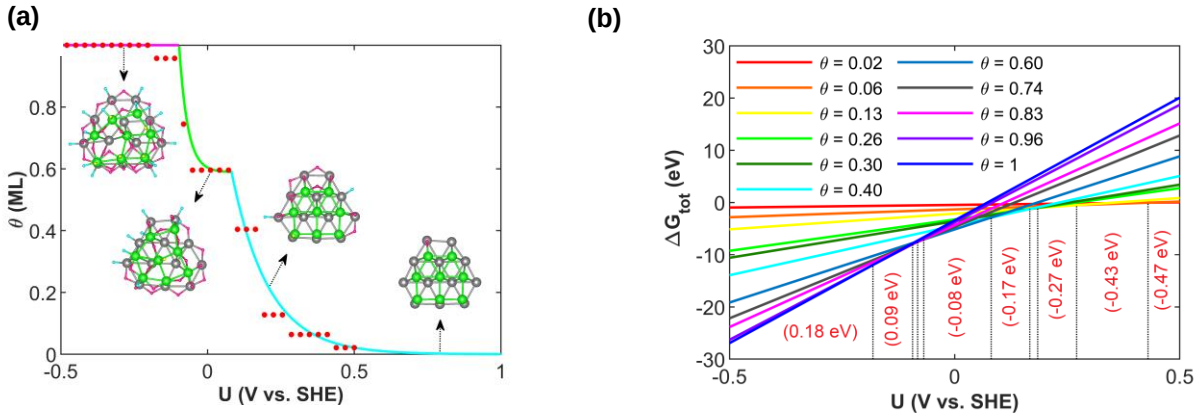

Figure 8-2. (a) Thermodynamic isotherm constructed using Eq. (8-4). At a given potential, the lowest line indicates the corresponding hydrogen coverage on the cluster. The corresponding ΔG_H for each θ are shown in parenthesis. **(b)** θ as a function of E extracted from (a). Inset shows the low-energy hydrogen configurations at different E.

$T\Delta S$ to be -0.2 eV at room temperature assuming that H* entropy is approximately zero.[329] We obtain ΔE_{ZPE} ~0.04 eV that is similar to that of Pt (111) and other metal surfaces.[2] For $\Delta G_{\mathrm{H}} = 0$, hydrogen interacts neither too strongly nor too weakly with catalytic surface resulting in an optimal HER activity. Away from $\Delta G_{\mathrm{H}} = 0$, HER activity decreases as hydrogen in adsorbed state is more favored than in gas state for $\Delta G_{\mathrm{H}} < 0$ while the opposite for $\Delta G_{\mathrm{H}} > 0$.

Figure 8-2(a) shows hydrogen adsorption isotherms obtained from evaluating the total adsorption free energy,

$$\Delta G_{tot} = \sum_{i}^{n} \Delta G_{\mathrm{H}} - n|e|\eta \tag{8-4}$$

where $\eta = U - U_{\mathrm{SHE}}$ is the overpotential.[311] For an applied external potential U with respect to the standard hydrogen potential U_{SHE}, the most stable coverage has the lowest value of ΔG_{tot}. The coverages at different potentials are summarized in Figure 8-2(b). As seen in the figure, the hydrogen coverage is nearly zero above 0.5 V vs. SHE. At 0 V vs. SHE where the HER is reversible, the high activity is indicated by $\Delta G_{\mathrm{H}} = -0.08$ eV in line with previous study[6] showing $\Delta G_{\mathrm{H}} = 0$ eV for Pt (111). Meanwhile, the corner and edge sites are mainly occupied whereas the site on top of the NP remains empty, as shown in Figure 8-1(b). Such draws an important conclusion that the high HER activity is due to the edges of the platinum NP.

In an acidic solution, there are two pathways for HER, namely the Volmer-Tafel and Volmer-Heyrovsky with the elementary reactions as,

$$\mathrm{H_3O^+} + e^- \rightarrow \mathrm{H^*} + \mathrm{H_2O} \qquad \text{(Volmer)}$$

$$\mathrm{H_3O^+} + \mathrm{e^-} + \mathrm{H^*} \rightarrow \mathrm{H_2O} + \mathrm{H_2} \qquad \text{(Heyrovsky)}$$

$$\mathrm{H^*} + \mathrm{H^*} \rightarrow \mathrm{H_2} \qquad \text{(Tafel)}$$

The corresponding reaction free energies of the three elementary steps can be written as (see detailed derivation in Supporting Information),

$$\Delta g = \begin{cases} \Delta G_{\mathrm{H}} + e\eta & \text{(Volmer)} \\ -\Delta G_{\mathrm{H}} + e\eta & \text{(Heyrovsky)} \\ -2\Delta G_{\mathrm{H}} & \text{(Tafel)} \end{cases} \quad (8\text{-}5)$$

To mechanistically understand the HER kinetics on MoS_2/Pt_{20} and quantify the HER rate in an electrochemical environment, we determine the minimum energy pathways for the three elementary reactions using a standard setup for solid-liquid interface (see Supporting Information).[11] We focus at $\theta = 0.6$ and 1, which are the equilibrium coverages under 0 V and below -0.2 V, as shown in Figure 8-2. For the Volmer and Heyrovsky reactions, we investigate several reaction sites focusing mainly on t_5 and b_5. For the Tafel reaction, we tested several combinations on adsorption sites including t and b sites. In real electrochemical solid-water interface, the potential across the Helmholtz layer does not change during redox reactions while it is not the case for finite-size solid-water interface models. To correct for this finite-size supercell effect, we use the extrapolation scheme which was recently employed for HER on Pt (111) surface (see Supporting Information).[330]

8-4 Kinetics of the Hydrogen Evolution Reaction on Platinum Nanoparticles

Figure 8-3 shows Δg of Eq. (8-5) for three different potentials -0, -0.6 and -0.8 V. Additionally, we show in the figure the reaction pathways where the peaks of the curves represent the kinetic barriers. At 0 V vs. SHE, the kinetic barrier 1.1 eV of the Heyrovsky reaction is the highest followed by the Volmer 0.7 eV while the Tafel 0.6 eV is the lowest. Thus, the HER follows the Volmer-Tafel pathway with the Volmer as the rate-determining step (rds). This pathway remains unchanged until the applied voltage decreases to -0.6 V. At -0.8 V, the barrier of the Volmer reaction decreases below that of the Tafel reaction, thus the rds for the preferred Volmer-Tafel

pathway becomes the Tafel reaction. As the kinetic barriers of the redox reactions (the Volmer and the Heyrovsky) decreases with increasing negatively applied potential, and the nearly unchanging barrier of the Tafel reaction, we expect that the Volmer-Heyrovsky route will eventually become the preferred reaction pathway at a sufficiently large overpotential below −0.8 V. Our result is consistent with bulk platinum where the contributions of the Volmer-Tafel or the Volmer-Heyrovsky pathways to the HER current is found to be potential dependent.[331] Further discussions on the comparison between the HER reactions on the MoS_2/Pt_{20} and periodic Pt (111) system are in the SI. While these investigations are not exhaustive, we do not expect the results to appreciably underestimate the kinetic barriers given that H^* diffusion on the cluster is fast with barriers less than 0.1 eV (see Supporting Information).

The Butler-Volmer relation is commonly used to study the HER on platinum catalysts,[10,130,320,332,333] which describes the total Faradaic current, j, as the sum of cathodic $j_0 e^{-\alpha f \eta}$ and anodic $j_0 e^{-(1-\alpha) f \eta}$ currents,

$$j = j_0\left(e^{-\alpha f \eta} - e^{(1-\alpha) f \eta}\right) \tag{8-6}$$

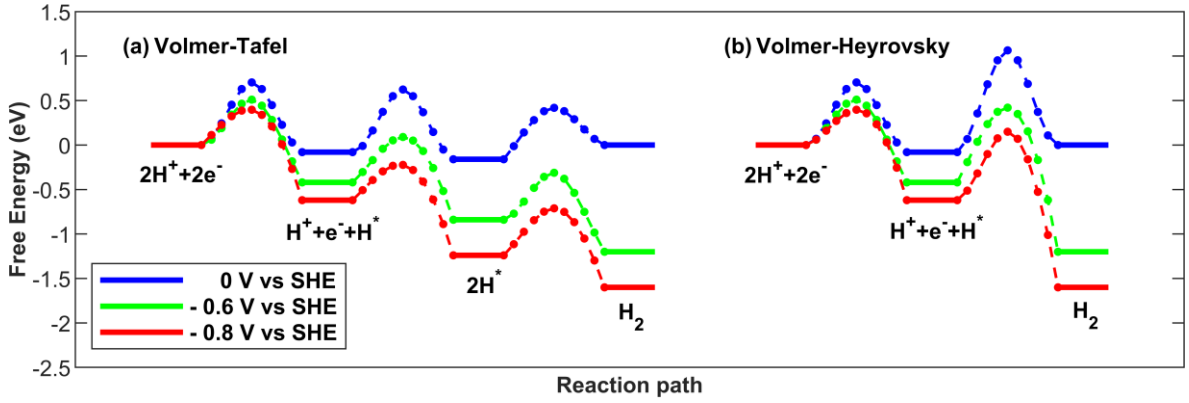

Figure 8-3. The reaction pathways at three selected overpotentials. The solid horizontal lines represent the free energies calculated from Eq. (8-5), and the dashed curves represent reaction paths with the kinetic barriers E_{avt} at the peaks.

Here $f = F/k_BT$ with F the Faraday's constant and k_B Boltzmann constant. α is the transfer coefficient that implicitly describes the charge transfer kinetics from water layer to electrode surface between initial and transition state. Experimentally, α is determined to be 0.5 for platinum NPs.[10] The exchange current density j_0 can be written as,

$$j_0 = nFC_{tot}(1-\theta)\frac{k_BT}{h}\exp\left(-\frac{E_{avt}}{k_BT}\right) \quad (8\text{-}7)$$

where C_{tot} is the total concentration of H^+ and H^* near electrode surface. Thus, we can define $nFC_{tot} = eN_{site}(1-\theta)/A$, where N_{site} is the number of active sites on the surface with area A. The energy barrier E_{avt} corresponds to the rds (Volmer reaction) determined at zero potential. Using the upper/lower limit of E_{avt}, 0.79/0.70 eV to account for variations in kinetic barriers at non-homogeneous activation sites, we find the minimum/maximum j_0 to be $6 \times 10^{-4} \sim 2 \times 10^{-2}$ A/cm^2. Figure 8-4 shows the MoS_2/Pt_{20} current using the Butler-Volmer kinetic model of Eqs. (8-6) and (8-7) with the minimum/maximum j_0. We further compute the current of Pt (111) for comparison. Note that Pt (111) surface is one of the most exposed termination on bulk platinum as well as stable in electrochemical conditions.[310-312] In Ref. [8], the current of MoS_2 supported platinum cluster is smaller than our prediction of MoS_2/Pt_{20}. We believe that the origin of this

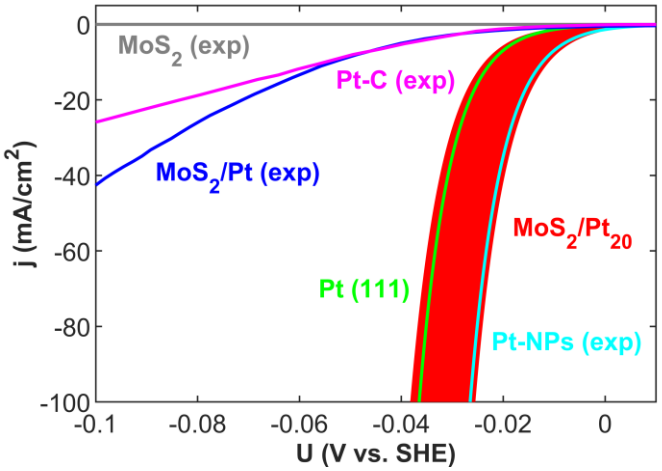

Figure 8-4. Exchange currents of MoS_2/Pt_{20} and Pt (111) computed from the Butler-Volmer kinetic model are compared with experimental results for MoS_2, Pt-C and MoS_2/Pt NP from Ref. [8], and for platinum NP from Ref. [10]. The red shaded region corresponds to the currents of MoS_2/Pt_{20} computed by the upper/lower limit of j_0.

discrepancy is due to the slow mass diffusion of H^+ onto surface as well as solution impedance, a well-known effect in catalysts with a fast HER redox rate.[321] To validate this conclusion, we compute the Tafel slopes of Pt-C (commercial 10% platinum supported on activated charcoal) obtained from the same experimental setup and find a values of 40 and 300 mv/dec^{-1} at 0V and above -0.15V, respectively.[8] These values are previously reported for platinum NPs without correcting for the solution impendence and diffusion limits.[321] To further collaborate our arguments, we show in Figure 8-4 that our computed currents are in excellent agreement with currents of carbon supported 2 nm platinum NPs, which have been corrected for H_2 diffusion and solution impedance.[10,334]

Finally, we discuss the potential role of MoS_2 on the catalytic activity of the supported platinum NPs. Besides the beneficence of MoS_2 in hindering the sintering of NPs, MoS_2 can also modulate HER catalytic activities due to charge transfer effects.[335] To investigate this, we examined an isolated Pt_{20} using the similar procedure as done for MoS_2/Pt_{20}. Further to aid in the comparison, we keep the morphology of the Pt_{20} as that of the supported one, although this configuration is clearly not optimum without the substrate. Also, we block hydrogen adsorption on the bottom surface of the Pt_{20} as it is in contact with MoS_2 for MoS_2/Pt_{20}. Figure 8-8 shows the isotherm of the Pt_{20}, which is very similar to that of the MoS_2/Pt_{20}. Further, at the HER reversible potential, we obtain $\theta = 0.69$ with $\Delta G_{\mathrm{H}} = -0.08$ eV that is very close to $\theta = 0.60$ with $\Delta G_{\mathrm{H}} = -0.08$ eV for MoS_2/Pt_{20}. Therefore, we conclude that the MoS_2 support does not have a significant effect on the catalytic activity of the Pt_{20} despite that the NPs adheres strongly to the support.[323] Indeed this is also corroborated by noting that our results are in agreement with supported NPs on carbon supported 2 nm platinum NPs[10,334] that have weaker interactions with the substrates compared to MoS_2. The minimal impact of the substrate on the HER activity concluded in our

study is in contrast to previous studies, which showed that the HER activity of a single or few atoms supported metal clusters have strong dependence on substrates.[303,336] The different behavior can be explained by the differences in the thickness of the cluster; our study shows that only a single Pt layer can shield the reactants from the support interactions. Hence, this makes our findings general for metal NPs of different shapes and sizes as well as to different substrates and different reactions.[262,337]

We have carried out first-principles calculations to understand the electrochemical hydrogen evolution reaction on MoS_2 supported platinum NPs. We use a cluster expansion method in conjunction with thermodynamic analysis to show that the HER adsorption free energy on MoS_2/Pt_{20} is comparable to that of Pt (111). We find that the preferred HER reaction pathway for MoS_2/Pt_{20} is the Volmer-Tafel with Volmer as rate-determining step at HER reversible potential, in agreement with experimental results on platinum electrode. To best explain the experimental findings, we develop a kinetic Butler-Volmer model to study the voltammograms of platinum systems. We find that the current-potential characteristics of MoS_2/Pt_{20} with exchange current density 6×10^{-4} to 2×10^{-2} A/cm^{-2} that is comparable to that of Pt (111) as well as the experimental results of platinum NPs. We also argue that the experimental HER currents on MoS_2 supported platinum NPs in Ref. [8] are underestimated due to solution impedance or diffusion limitations in electrochemical environments. Finally, we show that substrate interactions have no effect on the intrinsic HER activity of the NPs, which is different from the behaviors reported for single or few atom catalysts. The underpinning of this behavior is because metal NPs with at least two layers of thickness would be exempt from the impact of substrates. Thus, our findings are general and are applicable for NPs with different sizes and shapes on various supports, as well as to different catalytic reactions.

8-5 Supporting Information

Computational Details. We use CP2K[322] for the first-principles DFT calculations employing the revised Perdew-Burke-Ernzerhof exchange-correlational functional to solve the Kohn-Sham equations. The electronic self-consistent loops are terminated within energy-change tolerance of 1×10^{-6} eV. We use Gamma centered sampling for Brillion zone and a planewave cutoff of 400 eV. To model the electrochemical environment, we placed a single water monolayer at 3Å above Pt surface to replicate bulk water (see Supporting Information).[11] The water layer has an ice-like configuration[297] at a ratio of 1/8 for to , with each bonded with three H_2O in Eigen structure.[296] There are three different configurations for molecules such that H points toward (H-down), away (H-up) from the surface, or its molecular plane is parallel to surface (H-flat). The most stable water layer corresponds to half of H_2O in H-down and the other half in H-flat configuration, and a less stable water layer is also found by turning 1/4 H_2O from H-down to H-up configuration. The water configurations are implicit to Helmholtz layer potential, which we account for to determine the activation energies. We also verified that the water layer will have negligible effects on hydrogen adsorption as indicated by a variation of adsorption energy to less than 0.1 eV.

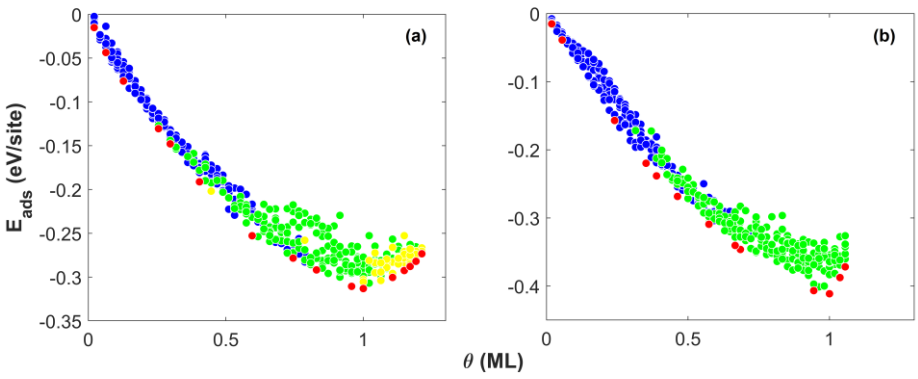

Figure 8-5. The total adsorption energy of hydrogen configurations for **(a)** unsupported Pt **(b)** Pt/MoS_2

We contrast between the activation energies of the HER reactions on the cluster and the periodic Pt (111) system. At 0 V vs. SHE, our values for the kinetic barriers of the Volmer, Tafel and the Heyrovsky reactions are respectively 0.7, 0.6 and 1.1 eV, as seen in Figure 8-3. On the other hand, Nørskov and co-workers showed that the reaction barriers for the corresponding three reactions on Pt (111) are 0.5, 0.6 and 0.6 eV.[6] As seen, the Heyrovsky reaction has a smaller barrier for Pt (111) compared to the supported cluster while as the Volmer and Tafel reactions have similar values. The differences in the Heyrovsky reaction are because the coverage employed in the periodic system θ = 1.1 is larger than that for the cluster θ = 0.9. To verify this, we re-examined the Heyrovsky reaction on Pt (111) at a lower coverage of θ = 0.9 and indeed found a higher barrier of ~1.0 eV that is equivalent to that of the platinum nanoclusters on MoS_2. Additionally, we observe that the mechanism of Heyrovsky reaction on Pt (111) and MoS_2/Pt_{20} are different. While charge exchange occurs when a proton is directly on top of H^* without being in contact with surface Pt on Pt (111), such a process results in a high activation barrier of 1.8 eV on MoS_2/Pt_{20}. Instead on the cluster, we find that the proton reduction requires the assistance of a surface Pt, at

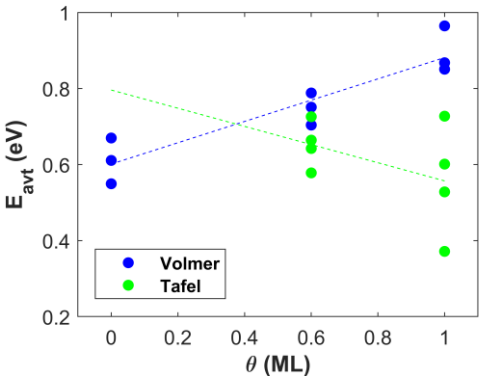

Figure 8-6. The energy barriers E_k of the Volmer and the Tafel reactions at selected hydrogen coverages θ. The lines show the increasing or decreasing trend of E_{avt} along θ for the Volmer or the Tafel reactions.

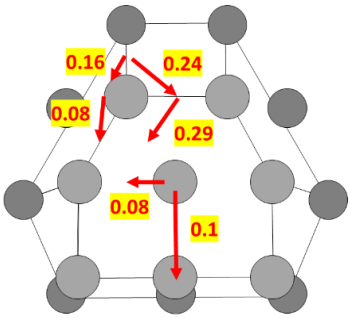

Figure 8-7. Hydrogen diffusion barriers (eV) on platinum cluster. The red arrows indicate diffusion pathways.

which a proton is first in contact with surface Pt to form a hydrogen pair with another H^* on the same surface Pt before the formation of H_2. This two-step process significantly reduces the barrier from 1.8 eV to 1.1 eV.

We have showed that surface sites of MoS_2 neither participate in HER due to weak hydrogen adsorption nor affect the hydrogen adsorption events on supported platinum cluster. This suggests that the HER kinetics on Pt/MoS_2 are similar to the unsupported platinum cluster. Measuring the Tafel slope $b = -2.303RT/F\alpha$ is the most simple and common strategy to verify the HER kinetics. For the Volmer, Heyrovsky or Tafel reaction as the rate-limiting step, the value of is found to be 120, 40 and 30 mv/dec^{-1} corresponding to the transfer coefficient of 0.5, 1 and 2.[338] Such argument is in line with the theoretical explanation by Erdley-Gruz of treating the HER into a sequence of elementary steps with a single rds.[339] The HER mechanisms on platinum electrodes are mostly determined to be the Tafel reactions as the rate-determining steps with 30 mV/dec^{-1} in acidic environment. However, Sheng et al. argued that this value of 30 mV/dec^{-1} reflect the mass-limiting current as the conventional rotating disk electrode cannot eliminate the

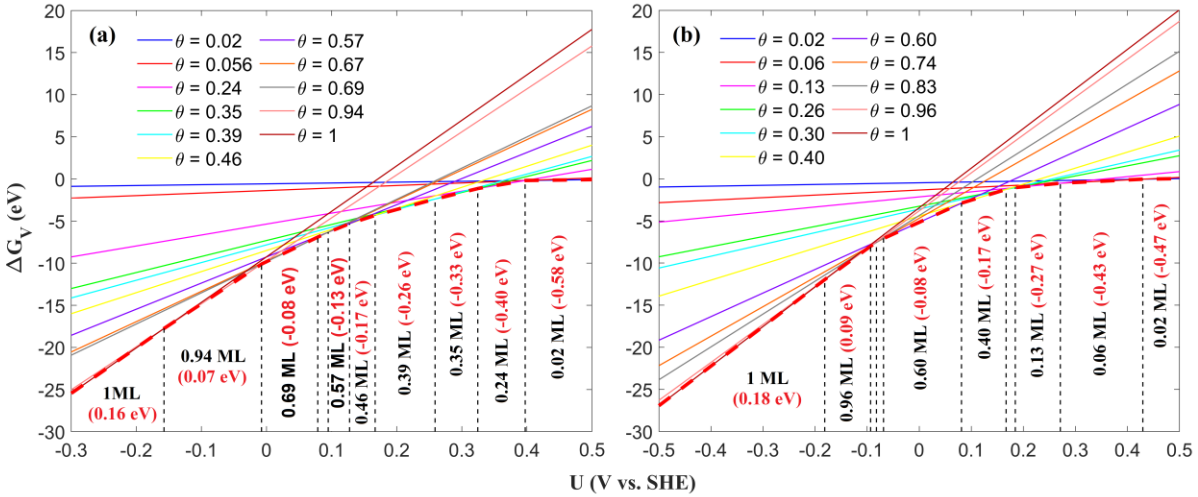

Figure 8-8. Thermodynamic isotherm of **(a)** unsupported Pt and **(b)** Pt/MoS_2.

effects of hydrogen diffusion from bulk solution to electrode surface. To overcome the diffusion complications, analytical strategies such H_2 pump and microelectrode are used for studying the fast kinetics of HER on platinum. Durst et.al used hydrogen pump to limit the diffusion effects, and found that the Volmer reaction is the rate-determining step with 120 mV/dec^{-1}. On the other hand, Shinagawa et. at argues that the Tafel slope of 120 mV/dec^{-1} also calls the Heyrovsky reaction at high hydrogen coverage.[338] Watzele et. al, using an electrochemical impedance spectroscopy, showed that both of the total HER contribution from the Volmer−Heyrovsky and Volmer−Tafel varies with overpotential as well as the Tafel slope, which raises the question whether the Tafel slope is valid to identify the HER kinetics on platinum systems with multiple reaction pathways. In conclusion, it is generally believed that relying on the Tafel slope to determine the HER kinetics is too simple to be conclusive. In addition, most studies report j_0 for platinum class catalysts as 1×10^{-3} A/cm^2 without correcting for issues with the diffusion limitation, thus their rates are under-estimated.[307,340] Using H_2 pump measurement or Koutecky-Levich type analysis to avoid the diffusion limit, previous studies reported $j_0 = 7 \times 10^{-2}$ A/cm^2 and 4.5×10^{-3} A/cm^2.[321,341] To compute MoS_2/Pt_{20} and Pt (111) currents, we Eq. (8-8) and (8-9) with the parameters shown below. The parameters for Pt (111) are obtained from Ref. [6]We also use the parameters in Ref. [10], as recorded below, to compute for platinum NP.

Table 8-1. The parameters for computing the current for platinum NP.

	E_{avt} (eV)	α	$Site/cm^2$	j_0 (A/cm^2)
MoS_2/Pt_{20}	0.70/0.79	0.63/0.70	1.45×10^{15}	$1.54\times10^{-2}/5.78\times10^{-4}$
Pt (111)	0.6	0.4	6.17×10^{15}	1.54×10^{-1}
Pt-NP		0.5		1.6×10^{-1}

9-0 Doped β-Mo_2C Catalysts Toward the Hydrogen Evolution Reaction

Note: The chapter is created from the published manuscript *Computationally Guided Design to Accelerate Discovery of Doped β-Mo_2C Catalysts toward Hydrogen Evolution Reaction* (Timothy T. Yang, Anqi Wang, Stephen D. House, Judith Yang, Jung-Kun Lee, and Wissam A. Saidi, ACS Catal. 2022, 12, 19, 11791–11800). Most of the writings are not rephrased.

Low-cost molybdenum carbides have shown a rapid increase in their efficiency of catalyzing the hydrogen evolution reaction owing to their structural flexibility for metal doping and nanostructure engineering. I posit that the hydrogen evolution reaction (HER) activity of β-Mo_2C can be further enhanced by metals doping. I employ first-principles quantum mechanical calculations in conjunction with thermodynamic analysis to shortlist ideal single metal dopants that improve hydrogen evolution reaction catalytic activity of β-Mo_2C. I show that Ir or Ti substitutional doping at the Mo sites of β-Mo_2C introduce thermoneutral hydrogen adsorption sites for HER, while the other elements in the first-row transition metals as well as Pt and Ag are not effective dopants for HER. To validate the computational results, I employ a microwave-assisted solvothermal method to synthesize metal-doped β-Mo_2C nanoparticles, and assess their HER performance and structure using a suite of electrochemical and *ex situ* structural characterization. From cyclic voltammetry, I find that the hydrogen evolution reaction onset voltage of pristine β-Mo_2C nanoparticles decreases by more than 20% through impurity doping with Ti or Ir, and is accompanied by a discernable increase in exchange current density. Transmission electron microscopy, high-angle annular dark-field scanning transmission electron microscopy, and energy-dispersive X-ray spectroscopy confirm that such increase in hydrogen evolution reaction activities originates from

the impurity doping, and not due to morphological or phase changes of the catalyst. The present study demonstrates that a combined and synergistic experimental and computational approach is indispensable to uncover the atomistic origins of catalytic activity, and to provide a rational design of the catalyst.

9-1 Introduction

Green hydrogen produced from electrolysis – the electrochemical process of splitting water using electricity generated from solar or wind power, is a key enabler of the global transition to sustainability and net-zero emission by 2050.[301] Hydrogen has high potential to be stored cost-effectively[342] and thus can support the integration of different renewables in the electric grid. Also, hydrogen can be utilized to decarbonize a range of energy sectors such as iron and steel, chemical, and cement production that are proven difficult to reduce emissions.[343] One of the central challenges in the production of hydrogen from water electrolysis is the use of expensive precious metals to catalyze the hydrogen evolution reaction (HER) – the critical process in water splitting to generate hydrogen via combining electrons and protons. This is emphasized in a 2020 workshop on Advances, Challenges, and Long-Term Opportunities in Electrochemistry[344]. Among the newly investigated HER catalysts, low-cost molybdenum carbides (Mo_yC) are reported to have high HER activities.[251,345,346]

Mo_yC can be stabilized into several phases including α-Mo_2C, β-Mo_2C, α-MoC, γ-MoC, δ-MoC, and η-MoC.[251,347-349] Among these phases, β-Mo_2C is found to be the most catalytically active phase.[251,350] In a previous study, we showed that the active sites of β-Mo_2C originate from the (011) surface that exposes Mo-C atoms, and is found to have low surface energy and to bind

hydrogen optimally.[124] In the past few years, considerable attention has been devoted to further improving the HER efficiency of Mo_yC catalysts via a complex nano-structuring approach that involves a hybrid of several mechanisms. For example, Wu and collaborators synthesized η-MoC_{1-x} via a confined *in situ* carburization process of Mo-based polyoxometalates and Cu-based metal-organic framework, and showed that the composite system exhibits excellent HER activity.[351] Notably, incorporation of carbon supports – such as carbon nanotubes[352-354], graphene (GA) [54,261,262,355-358], reduced GA oxide (RGO)[261,359], or nitrogen-doped carbon nanostructues[360-362] – are found to appreciably enhance HER for β-Mo_2C and δ-MoC[262,356,357]. Non-metallic (P[363,364], N[361,365,366], and S[367,368]) and metal dopants (Fe[38] and Co[39]) have also been reported to improve HER activity. In addition, coupling of Mo_yC phases[369-374] or MoS_2 [375-378] also has been shown to improve activity. Recently, Yang and Saidi showed that nano-structuring not only create HER active sites

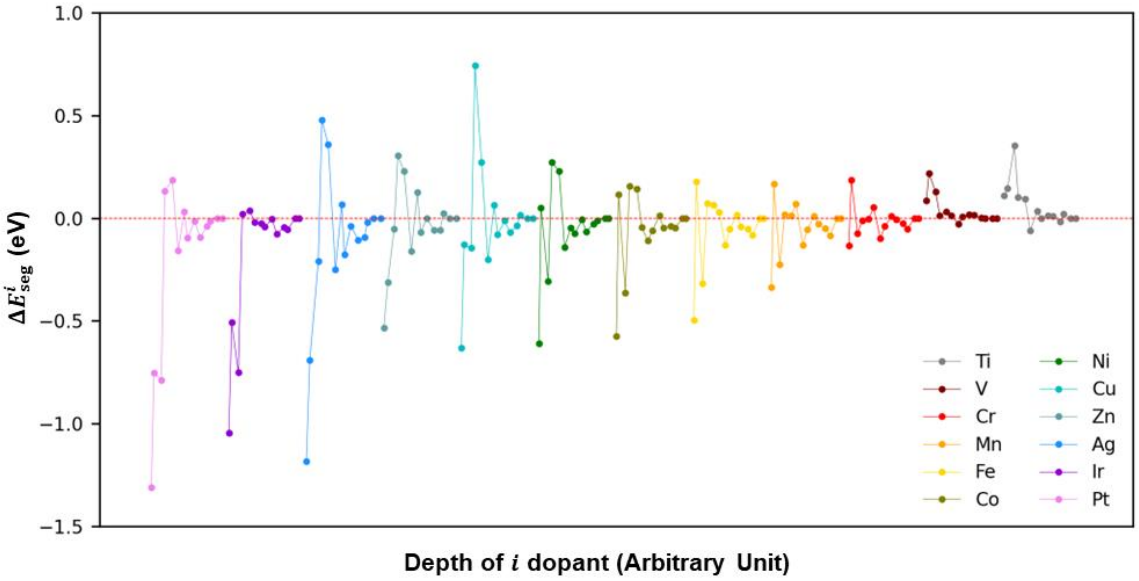

Figure 9-1. The segregation energy ΔE^i_{seg} in eV. For each metal-doped surface, the doping layer i increases from left to right with $i = 1$ corresponding to the top exposed surface layer and $i = 7$ for the bulk-like layer. Each two consecutive values correspond to the same i with slightly different depth. Odd (even) numbers correspond to layers that are composed of Mo-C (Mo), as shown in Figure 9-2(b).

on Mo_yC but also on the supports due to the modification of the support electronic structure through the interactions with Mo_yC.[86]

While it has been widely observed that heteroatom doping into Mo_yC enhances HER activity, there is inconsistency across studies.[87,379] Leonard and Wang groups observed an insignificant improvement for the HER overpotential of Mo_2C with Fe doping[87,380] (300 ~ 400 mV at 10 mA/cm^2); however, Li group reported a much lower overpotential of 150 mV at 10 mA/cm^2.[379] In addition, the reported exchange currents between the Fe, Co, Ni, and Cu doped Mo_2C are similar with differences less than 1.7×10^{-2} mA/cm^2,[380] while we show that the corresponding computed hydrogen adsorption free energies differ by 0.4 eV suggesting a significantly larger difference up to a fourth order of magnitude in exchange currents according to the volcano trend[2,189,224]. These controversies underscore the complexity of uncovering the HER mechanisms of the doped structures. For instance, HER enhancements could originate from different mechanisms, such as modulations in the morphology of nanoparticles (NPs), evolution of Mo_yC phases under electrochemical conditions, or the modifications of catalytic sites under doping. We posit that while it is challenging for a solely experimental or computational approach to discern between the different mechanisms, a combined approach could provide an effective route for untangling the problem, if any, and enable a rational design of the catalyst[381].

Using *ab initio* thermodynamics in conjunction with density functional theory (DFT) calculations, we investigate the modulations of the morphology and hydrogen adsorption sites of β-Mo_2C via doping with first-row transition metals and three precious metals. The main criterion for our investigations is focused on the long-term stability and enhanced HER activity of the new catalyst. We find that all studied dopants are thermodynamically stable on the exposed β-Mo_2C surface layer *albeit* with different tendencies. However, only Ir and Ti dopants are predicted to

introduce optimum HER active sites on β-Mo_2C surface. To validate the computational findings, we synthesize Ir- and Ti-doped β-Mo_2C NPs using a microwave-assisted solvothermal method. From cyclic voltammetry, we confirm the enhanced HER activities on Ti- and Ir-doped β-Mo_2C indicated by an overpotential that is 20% less than pristine β-Mo_2C NPs. In addition, the exchange current densities of the Ir- and Ti-doped β-Mo_2C NPs are, respectively, 1.78×10^{-4} and 2.24×10^{-4} A/cm^2, which are higher than the 5.37×10^{-5} A/cm^2 for the pristine β-Mo_2C NPs. Using high-angle annular dark-field scanning transmission electron microscopy (HAADF-STEM), high-resolution transmission electron microscopy (HRTEM), and energy-dispersive X-ray spectroscopy (EDS), we confirm that the enhanced HER activities on the Ir- and Ti-doped β-Mo_2C NPs are due to the electronic structure modulations and not due to morphological changes of the catalysts.

9-2 Computational Investigation of the Hydrogen Evolution Reaction

Using first-principles calculations, we examine the hexagonal β-Mo2C (011) surface with single-metal dopants that substitutes at all Mo sites resulting in one-to-four dopant-to-Mo ratio per layer. We have systematically investigated all different Mo sites up to the seventh subsurface layer. The dopants are selected from the first-row transition and precious metals, namely, Ti, V, Cr, Mn, Fe, Co, Ni, Cu, Zn, Pt, Ir, and Ag. Clearly, the list of the investigated elements is not complete but here our emphasis is on developing a strategy to explore the materials space rather than performing an exhaustive search over all elements. Note that the (011) termination, which may be referred to as (101) in some literature[382], has been identified as the most stable β-Mo_2C termination[124,383,384]. To assess the segregation tendencies of the dopants, we compute the segregation energy ΔE_{seg},

defined as the energy of a doped surface layer with respect to the energy of a doped "bulk-like" layer,

$$\Delta E^{i}_{\text{seg}} = E_{M(i)} - E_{M(\text{bulk})} \tag{9-1}$$

where $E_{M(i)}$ and $E_{M(\text{bulk})}$ are the energies of the slab with a metal dopant M in the i^{th} and in a "bulk-like" layer, respectively. Beyond the 7$^{\text{th}}$ surface layer of the slab model, $E_{M(i)}$ is found to converge to a constant value and hence $E_{M(i)} \approx E_{M(\text{bulk})}$. From Eq. (9-1), a negative $\Delta E^{i}_{\text{seg}}$ indicates that a dopant located at the i^{th} layer is more thermodynamically stable than at bulk sites. Figure 9-1 summarizes $\Delta E^{i}_{\text{seg}}$ as a function of the depth of the doping metal site. As seen from the figure, $\Delta E^{1}_{\text{seg}}$ for Pt, Ag, Ir, Cu, Ni, Co, Zn, Fe, and Mn are significantly lower than $\Delta E^{7}_{\text{seg}}$, suggesting that these dopants stabilize at exposed layers rather than at bulk layers. This is notably

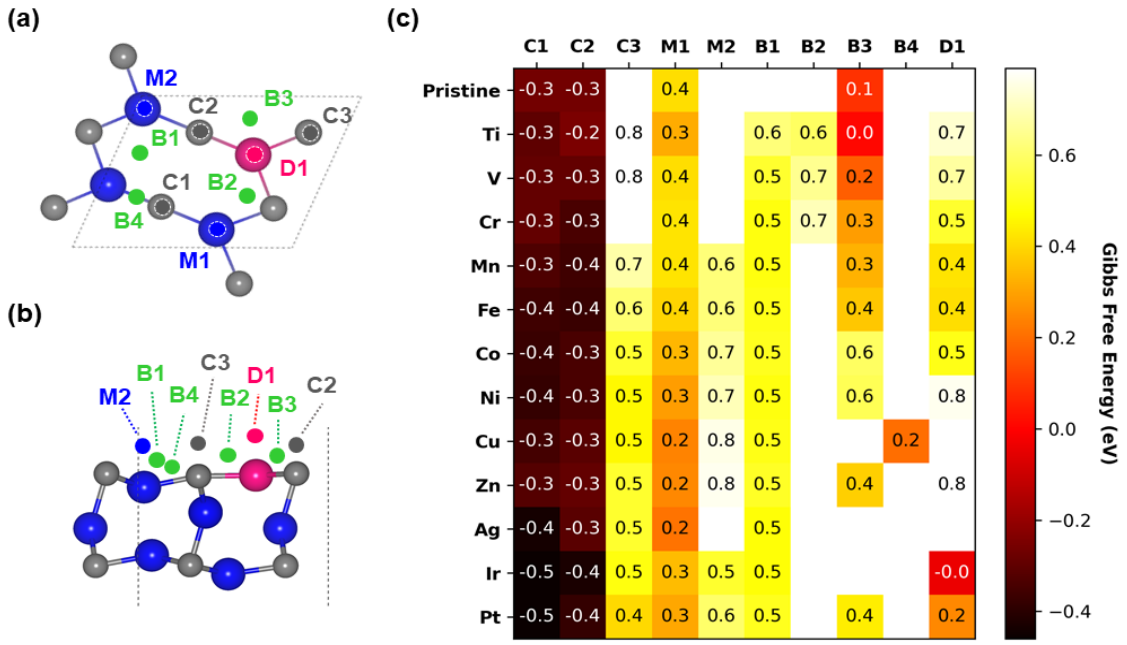

Figure 9-2. (a) Top and **(b)** side views for the most stable adsorption sites of the metal-doped β-Mo_2C (011) surface. Mo atoms are shown as blue, C as gray, H as green, and a metal dopant as pink. Potential hydrogen adsorption sites are shown: C1, C2, and C3 are C top sites; M1 and M2 are Mo top sites; B1, B2, B3, and B4 are bridge sites; and D1 is top site of a dopant. **(c)** Hydrogen Gibbs free energy (in eV) at the potential adsorption sites. The whiteouts correspond to unstable adsorption sites.

the case for the precious metals Pt, Ir, and Ag. On the other hand, $\Delta E_{\mathrm{seg}}^{i}$ approaches zero for all i for Cr, Ti, and V dopants, and hence these dopants are likely to spread equally among the different layers. Also, we observe an inverse correlation between the stability of the first-row transition metals and their radii where smaller-sized dopants are more stable than the larger ones. It is to be noted that the lack of a surface-segregation tendency is not cost-effective for precious metal dopants, as only dopants that are on the top surface layers are expected to influence the catalytic activity. In summary, although there are some variations in their segregation tendencies, all dopants can thermodynamically occupy exposed surface sites, and thus could potentially influence the HER activity of β-Mo_2C.

The hydrogen adsorption Gibbs adsorption energy ΔG_{H} has been widely accepted[2,189,224] to accurately predict the experimental measurement on HER rates. For $\Delta G_{\mathrm{H}} = 0$, the HER activity is maximum while the activity decreases with increasing $|\Delta G_{\mathrm{H}}|$, in accordance with Sabatier's principle where a reaction has the maximum rate when intermediates interact neither strongly nor weakly with a catalytic surface. ΔG_{H} is defined as

$$\Delta G_{\mathrm{H}} = \Delta E_{\mathrm{H}^*} + \Delta E_{ZPE} - T\Delta S \tag{9-2}$$

where ΔE_{ZPE} is the zero-point energy, which is found to be less than 0.05 eV for the doped β-Mo_2C (011), consistent with prior results for metal surfaces.[111,189,224] ΔS is the change of entropy between hydrogen atoms in the adsorbed state and in the gas state. From experimental measurements, $\Delta S \sim -\frac{1}{2} S_{\mathrm{H}_2}^0$ where $S_{\mathrm{H}_2}^0 = 1.35\times10^{-3}$ eV/K is the entropy of hydrogen gas at room temperature[125]. The hydrogen adsorption energy ΔE_{H^*} is defined as,

$$\Delta E_{\mathrm{H}^*} = \frac{1}{n}\left(E_{n\mathrm{H}/slab} - E_{slab} - \frac{1}{2} n E_{\mathrm{H}_2}\right) \tag{9-3}$$

where $E_{n\mathrm{H}/slab}$ and E_{slab} are the energies of the slab with n adsorbed hydrogen atoms (H^*) and of the clean slab, respectively, and E_{H_2} is the energy of H_2 in gas phase.

Figure 9-2 summarizes the hydrogen adsorption sites on the pristine and the metal-doped β-Mo_2C (011) with their corresponding ΔG_{H} probed by a single hydrogen atom. We have verified that ΔG_{H} is nearly independent of hydrogen coverage β-Mo_2C (011) due to negligible hydrogen-hydrogen interactions. For the pristine surface, the unique Mo/C composition creates moderate adsorption bridge sites (B3) between two Mo atoms. With the safe assumption that HER largely proceeds through the B3 sites with $\Delta \mathrm{G_H} =$ ~0.1 eV, the exchange currents are predicted to be 10^{-5} A/cm^2 using a simple kinetic model, which is consistent with experimental results[124]. The other sites on the pristine surface, namely the strong adsorption sites with $\Delta \mathrm{G_H} = -0.3$ eV, such as C atop (C1 and C2) sites, and weak adsorption sites with $\Delta \mathrm{G_H} = 0.4$ eV, such as Mo atop (M1) sites, are HER inactive.

Metal doping creates new adsorption sites on the β-Mo_2C (011) surface, such as C3, M2, B1, B2, B4, and D1 (see Figure 9-2(a) and 9-2(b)). As indicated by large positive ΔG_{H} values in Figure 9-2(c), hydrogen adsorption on C3, M2, B1, and B2 sites is endothermic and requires a substantial overpotential in the Volmer step. Doping, however, introduces thermoneutral sites – B3 on the Ti-doped surface and D1 on the Ir-doped surface – that are expected to be more HER active than on the pristine β-Mo_2C (011), as the sites are characterized by $\Delta \mathrm{G_H} = -0.01$ eV and -0.04 eV, respectively. The concentration of the active sites on the pristine, Ir- and Ti-doped β-Mo_2C (011) are identical assuming that only sites with $|\Delta G_{\mathrm{H}}| < 0.1$ eV are active for HER. Compared to the pristine surface, Ir and Ti dopants significantly improve the HER activities by introducing new HER active sites while the other dopants annihilate the original active sites of the β-Mo_2C (011) surface. Given that (011) is a stable termination representing the β-Mo_2C catalyst

under electrochemical and synthesis conditions, and only the sites corresponding to $\Delta G_H \approx 0$ contribute the most to HER among the other sites, we expect that Ir and Ti doping can significantly improve HER activity.

9-3 Experimental Investigation of the Hydrogen Evolution Reaction

To validate the computational predictions, we use a microwave-assisted solvothermal method to synthesize pristine β-Mo_2C, Ir-doped, Ti-doped, and Fe-doped β-Mo_2C NPs supported on graphene oxide nanosheets. Note that we will focus first on comparing experimental results for pristine β-Mo_2C, Ir-doped, and Ti-doped. Figure 9-3(a) shows the XRD patterns of pristine β-Mo_2C NPs, and the NPs doped with 4% Ir and Ti. The pristine β-Mo_2C NPs exhibit sharp diffraction peaks that are indexed as hexagonal β-Mo_2C (JCPDS pattern: 35-05-0787). No second phase is found in the XRD pattern for pristine β-Mo_2C NPs. When the pristine β-Mo_2C NPs are

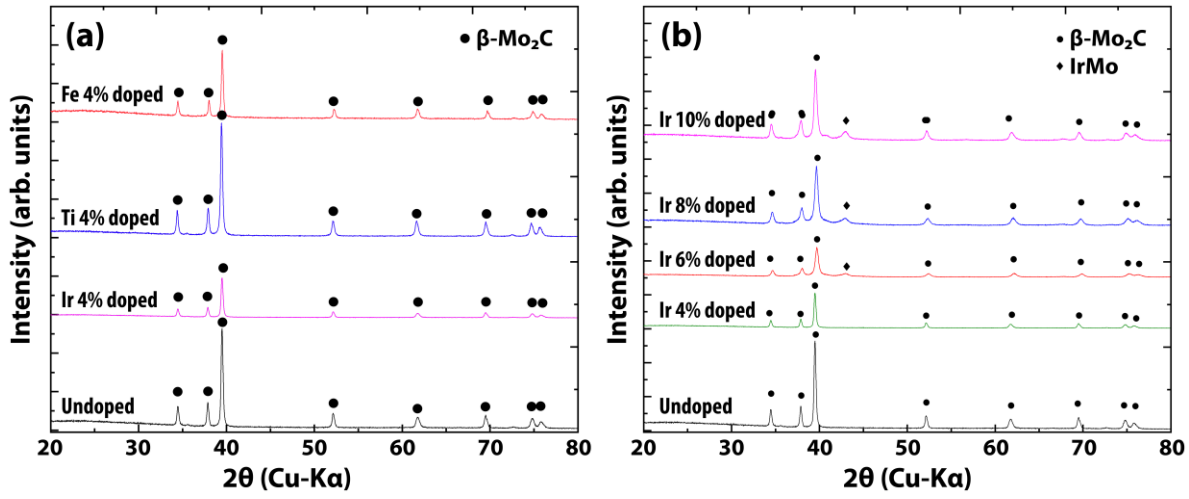

Figure 9-3. (a) XRD patterns of pristine and 4% Ir/Ti/Fe-doped Mo_2C NPs supported on 3wt% graphene oxide mixture films. **(b)** XRD patterns of pristine and (4, 6, 8, 10%) Ir-doped β-Mo_2C NPs supported on 3wt% graphene oxide mixture films.

doped with 4% Ir and Ti, we observe no crystal structure change other than a small decrease in lattice parameters. In Figure 9-3(b), we show the XRD patterns of the pristine β-Mo_2C NPs doped with different percentages of Ir dopants. When more than 4% of Ir is doped, the formation of an Ir-Mo phase is indicated by the broad diffraction peak at $2\theta = 43^{o}$. In none of the patterns is an amorphous or non-crystalline Mo_yC phase detected in any meaningful quantity. As the Ir-Mo phase exhibits different HER behaviors than the Ir-doped phase (see Figures 9-10(a) and 9-11(b)), we limited the doping concentration to 4% for all dopants for subsequent electrochemical analysis of HER activity.

Linear sweep voltammetry is performed at a 20 mVs^{-1} scan rate in 0.5 M H_2SO_4 electrolyte on pristine, 4% Ir-doped, and 4% Ti-doped β-Mo_2C NPs. The cyclic voltammograms of the samples are shown in Figure 9-4(a). To compare relative HER activities, the overpotential values η_{10} determined at a current density of 10 mA/cm^2 are 134, 106, and 103 mV for the pristine, 4% Ir-doped, and 4% Ti-doped β-Mo_2C NPs, respectively. With Ir or Ti doping, η_{10} is reduced by ~20% compared to the pristine β-Mo_2C NPs. Figure 9-4(b) shows the Tafel plots deduced from Figure 9-4(a). For pristine, 4% Ir-doped, and 4% Ti-doped β-Mo_2C NPs, the Tafel slopes are 64,

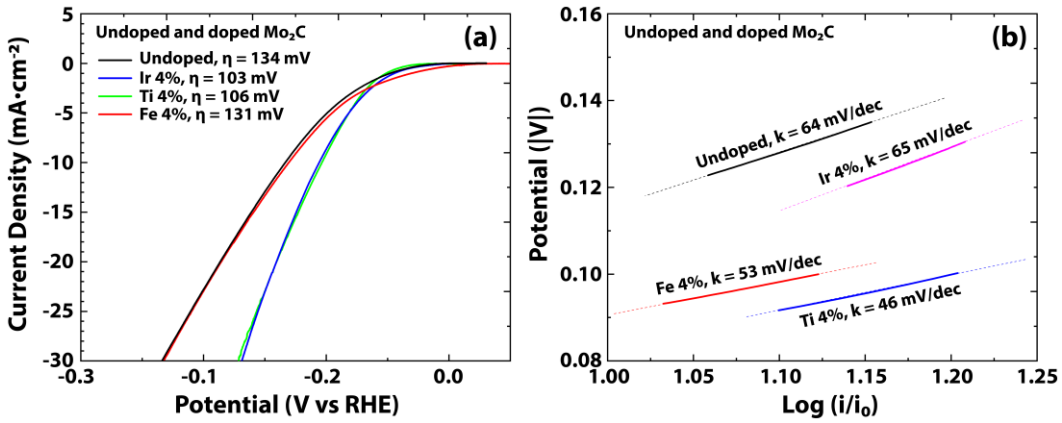

Figure 9-4. (a) HER polarization curves and **(b)** Tafel plots for pristine and Ir, Ti, and Fe-doped β-Mo_2C.

53, and 46 mV/dec, respectively. The corresponding exchange current densities are 5.37×10^{-5}, 1.78×10^{-4}, and 2.24×10^{-4} A/cm^2, as obtained based on Tafel slope.

Electrochemically active surface area (ECSA) analysis is performed using cyclic voltammetry. Figure 9-5 shows the changes of the current densities as a function of scan rate. The double-layer capacitance (C_{dl}) is measured at scan rates from 5 to 200 mV/s, with an increment of 16 mV/s, in non-Faradic potentials from 0.1 to 0.3 V vs. RHE. The C_{dl} of pristine β-Mo_2C is 12 mF/cm^2 as determined in our recent study.[385] In contrast, 4% Ir- and 4% Ti-doping increases C_{dl} to 18.3 and 22.8 mF/cm^2, respectively, almost doubling that of the pristine β-Mo_2C NPs. According to our computational predictions the concentration of active sites on the pristine and metal doped

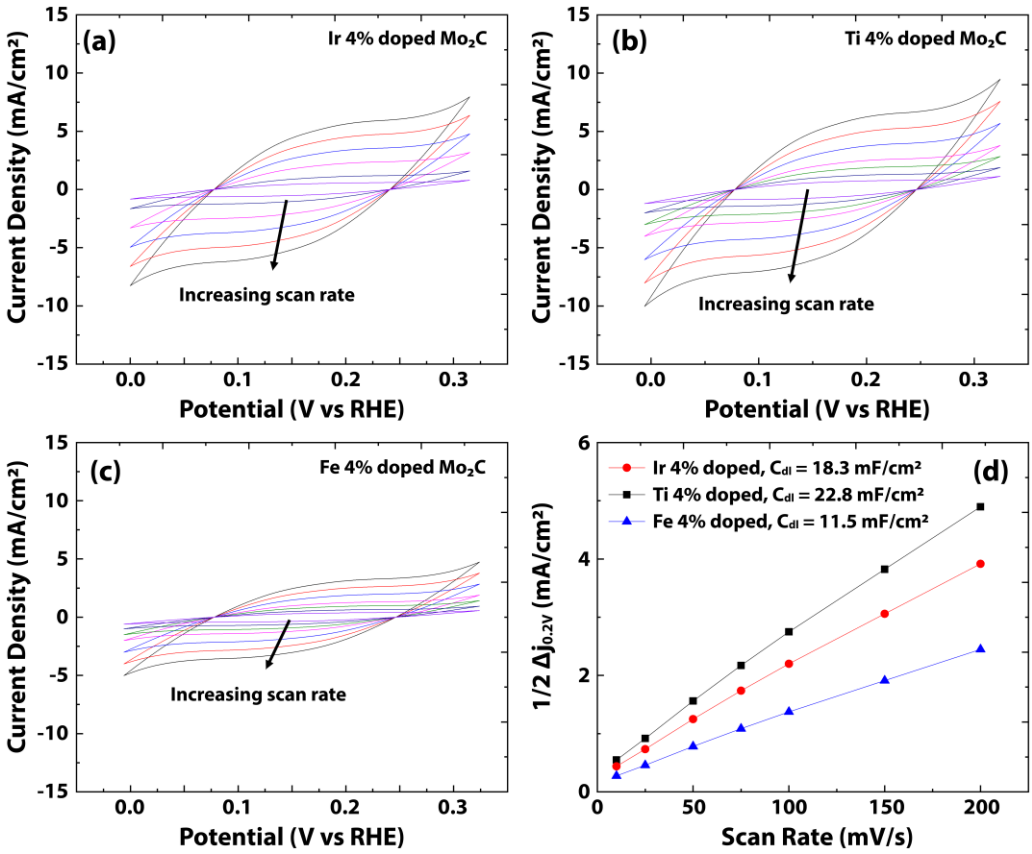

Figure 9-5. Current density – potential curves of **(a)** Ir 4%-doped, **(b)** Ti 4%-doped, **(c)** Fe 4%-doped Mo_2C-3wt% graphene oxide (GO) mixture films, cycled between 0.0 and 0.3 V (vs. RHE) at a scan rate from 5 to 200 mV s^{-1} in an acidic medium, **(d)** $0.5\triangle J_{0.2V}$ (half of current density difference at 0.2V) as a function of scan rate.

Mo_2C β-(011) are the same, which indicates that Ti and Ir dopants have a dramatic effect on the chemistry of electrochemical active sites of β-Mo_2C.

The experimentally measured electrochemical performances for Ir and Ti show HER enhancements based on lower overpotentials and higher exchange currents than the pristine β-Mo_2C, which agrees with theoretical predictions that Ir doping creates new active sites i.e., D1 sites and Ti doping alters the active sites on pristine β-Mo_2C to be thermoneutral. However, based only on electrochemical measurements, it is premature to argue for agreement, or lack thereof, between theory and experiment. Namely, it is important to ensure that the theoretical models in terms of the Mo_2C phase, metals dispersion and surface terminations are consistent with the synthesized samples.

Fully interpreting the electrochemical data requires knowledge of the nanoscale structure and chemistry from which it arises; in particular, particle size and morphology, and the presence of dopant dispersion or segregation. To obtain this information, we employed Transmission electron microscopy (TEM), high-angle annular dark-field scanning TEM (HAADF-STEM), and

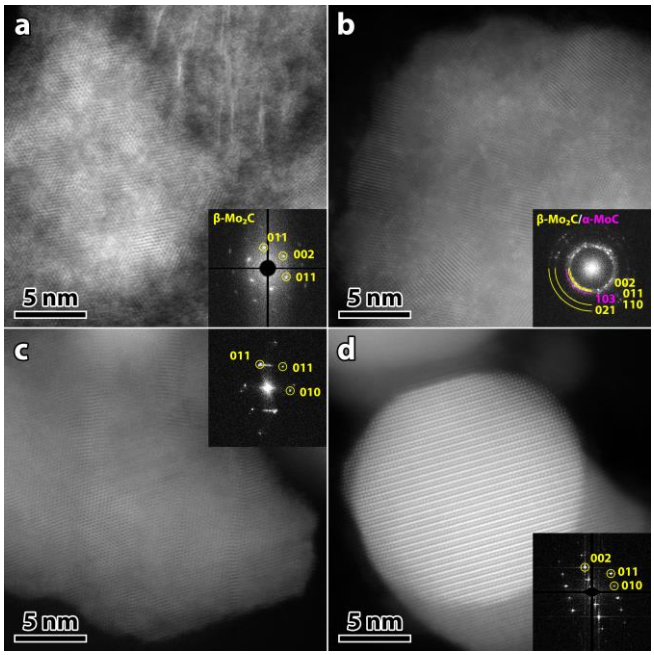

Figure 9-6. Representative atomic-resolution HAADF-STEM micrographs of the **(a)** pristine β-Mo_2C, **(b)** 4% Ir-doped, **(c)** 8% Ti-doped, and **(d)** 7.5% Fe-doped samples. Insets show the corresponding FFTs for each image, indexed to (yellow) β-Mo_2C and (magenta) α-MoC. (Note: some plane spacings have many potential corresponding planes. Here, one plane has been chosen to represent each given spacing.)

energy-dispersive X-ray spectroscopy (EDS). In general, the pristine and metal-doped β-Mo_2C NPs are fused together either directly or with a carbonaceous material between, possessing morphologies ranging from nearly spherical to faceted, and isotropic to high-aspect ratio, as shown in Figure 9-11. Atomic-resolution HAADF-STEM and HRTEM examples of the NPs are shown in Figures 9-6 and 9-11, respectively. Selected area electron diffraction (SAED) (Figure 9-11) and Fast Fourier Transform (FFT) analysis reveals that the NPs are predominantly in the β-Mo_2C phase, but with varying amounts of NPs in the α-MoC phase observed, especially for 4% Ir-doped NPs. For simplicity, and due to the significantly smaller presence of α-MoC, only β-Mo_2C is mentioned in subsequent references to the Mo_yC with the existence of additional phases in this work. Most of the NPs are not sharply faceted, but in those NPs with a high degree of faceting, such as Figure 9-12(a) and 9-12(d), the (011), (002), and (100) facets predominated, with the former being slightly more common. Additional morphological and structural details are included in the Supporting Information. No evidence of dopant segregation is observed from the contrast in HAADF-STEM images of the Fe- and Ti-doped specimens (e.g., Figure 9-6(d) and 9-6(c)). In the 4% Ir-doped

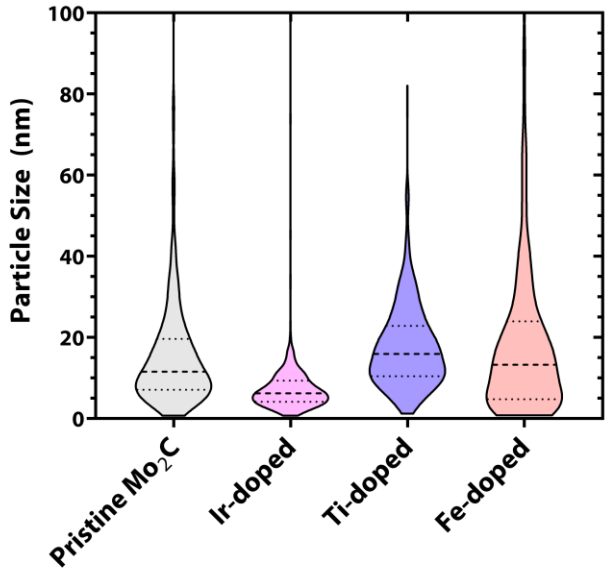

Figure 9-7. Violin plots (kernel density estimates) of β-Mo_2C NPs sizes. Dashed lines indicate the median and dotted lines indicate the quartiles. The vertical axis has been truncated for easier comparison of the distributions. Nominal metal doping for Ir, Ti, and Fe is 8, 8, and 7.5%, respectively. Swarm plot versions of these distributions are included in Figure 9-13. Color corresponds to those used in Figure 9-3(a) for identifying the dopants.

specimen (Figure 9-6(b)), copious amounts of few-atom nanoclusters are observed uniformly distributed all over the β-Mo_2C particles, either decorating the surface or incorporated into the surface layer(s). The increased image intensity of these nanoclusters compared to the Mo_2C support indicates they are Ir, as the image intensity is predominantly atomic-mass-dependent under the imaging conditions used. Occasional small Ir-rich NPs are also observed on the surface, but they are uncommon in comparison.

The size distributions of the pristine and metal doped β-Mo_2C NPs are plotted in Figure 9-7. Population summary statistics and the calculation details are described in Table 9-1. The average size of pristine β-Mo_2C NPs (15.8 ± 15.0 nm) is slightly smaller than the size of Ti-doped NPs (17.8 ± 10.6 nm). In contrast, the size of Ir-doped NPs is significantly narrower and of smaller mean (8.9 ± 22.6 nm, with a 75% percentile of 9.3 nm) than any other sample. The Ir-doped β-Mo_2C NPs possessed large quantities of small (<10 nm) particles, whereas relatively few are observed in the Ti-doped NPs.

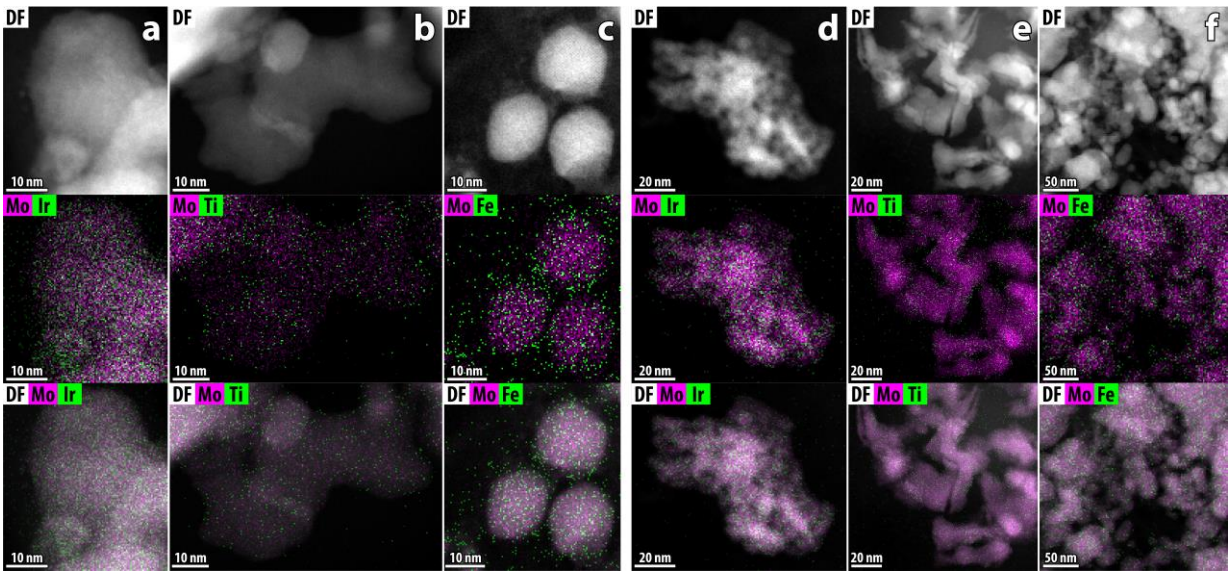

Figure 9-8. Background-subtracted EDS elemental maps from β-Mo_2C NPs doped with (a,d) 4% Ir, (b,e) 8% Ti, and (c,f) 7.5% Fe. Middle images are Mo (magenta) + primary metal (Ir, Ti, Fe; green) maps, while the bottom images have been overlain onto the HAADF image. Elemental quantification is provided in Table 9-2.

EDS elemental mapping is employed to verify and quantify NP composition and dopant dispersion. Example maps are provided in Figure 9-8(a) ~ 9-8(c) – at higher magnification to observe intra-particle distribution – and Figure 9-8(d) ~ 9-8(f) – at lower magnification to examine distribution at the aggregate level. The sum spectra for these maps are shown in Figures 9-15 and 9-16, respectively, and a quantification of the ratio of dopant metals to Mo are listed in Table 9-2. Ti-doped samples exhibit a uniform incorporation of dopants, with no segregation observed. The surface segregation of the Ir dopant, and appearance of occasional Ir-rich NPs, suggest that 4 at% is at the limit of Ir incorporation in β-Mo_2C prepared via these methods. Above 4 at%, Ir-rich NPs nucleated on the β-Mo_2C, which have additional HER active sites other than our focus on the Ir-doped β-Mo_2C. Although the Ti- and Fe-doped samples examined in TEM are of higher dopant concentration than those tested electrochemically, the lack of any observed segregation even at these higher dopant levels indicates that segregation is highly unlikely to occur at lower concentrations. This is in contrast to the Ir-doped sample, where segregation is observed at 8%, and thus the lower concentration warranted examination. More information on the Ir-doped β-Mo_2C morphology characterization with different at% is included in the Supporting Information.

9-4 Linkage between Experiments and Computations

The experimental results are in accordance with computational analysis. From cyclic voltammetry, we find that the exchange current densities for Ir- and Ti-doped β-Mo_2C NPs are 1.78×10^{-4} and 2.24×10^{-4} A/cm^2, respectively, which are nearly one-order of magnitude higher than that of pristine β-Mo_2C NPs with 5.37×10^{-5} A/cm^2. In addition, the overpotential for the pristine β-Mo_2C

NPs is ~20% less than the Ir- and Ti-doped β-Mo_2C NPs. This agrees with the computational findings that Ir- and Ti- doped β-Mo_2C (011) have nearly thermoneutral sites with $\Delta G_H \approx 0$ that are more HER active than the sites on the pristine β-Mo_2C (011) with $\Delta G_H \approx 0.1$ eV. We posit that the enhanced HER on Ir- and Ti-doped β-Mo_2C is due to the new active sites facilitated by the dopants based on the following reasons: (1) The Tafel slopes of the Ir-doped and Ti-doped β-Mo_2C NPs are different than the Tafel slope of the pristine β-Mo_2C NPs. This supports our modeling results that there are new active sites for HER that are generated by doping. (2) XRD, STEM, and EDS confirm that doping with Ir and Ti does not cause a phase change of β-Mo_2C; only a negligible amount of α-MoC phase appears in Ir-doped β-Mo_2C NPs. This agrees with our computational results showing that the Ir dopants homogeneously segregate into the upper layers of the β-Mo_2C NPs while the Ti dopants are equally distributed among all layers. As we do not detect any of the amorphous or non-crystalline phases of the metal-doped β-Mo_2C, and we have ruled out the effects of Ir segregation, these findings suggest that the HER activities mainly come from the metal-doped β-Mo_2C (011) terminations. (3) From ECSA, the values of C_{dl} for Ir- and Ti-doped β-Mo_2C NPs nearly double the value of pristine β-Mo_2C NPs. The larger ECSA on the doped β-Mo_2C NPs suggests higher HER activities than the pristine β-Mo_2C NPs, assuming that the surface areas of the samples are similar.

To further enhance our rationalization of the connections between the computational and experimental results, we also examined Fe-doped β-Mo_2C NPs, which are predicted to be non-optimal for HER based on our first-principles calculations (see Figure 9-2(c)). Fe doping is selected because previous studies were controversial, reporting both insignificant[87] and significant[87,379] improvements for the HER activity of Fe-doped β-Mo_2C. From the electrochemical analysis, we find for the Fe-doped NPs, that the overpotential 131 mV, exchange

current 4.79 × 10^{-5} A/cm^2, and C_{dl} 11.5 mF/cm^2 are of similar magnitude to the corresponding values of the pristine β-Mo_2C NPs. We posit that the HER activity on Fe-doped β-Mo_2C NPs arises from the active sites of pristine β-Mo_2C NPs based on the findings: **(**1) Our computations show that the sites on pristine β-Mo_2C (011) with $\Delta G_H = 0.1$ eV are significantly more active than the new sites on Fe-doped β-Mo_2C (011) that are either too strong, $\Delta G_H = -0.4$, or too weak, $\Delta G_H >$ 0.4 eV; (2) The experiments found that Fe doping generate NPs of smaller size. Although the mean size of β-Mo_2C NPs somewhat increase with Fe-doping compared to pristine, 15.8 ± 15.0 nm and 20.4 ± 24.7 nm, respectively, it substantially increased the relative number of small particles (<5 nm, see Figure 9-13). This suggests that the HER current for Fe-doped β-Mo_2C NPs is expected to be slightly higher than that of the pristine β-Mo_2C NPs as the active sites on pristine β-Mo_2C NPs are more exposed on smaller particles than on larger ones.

We computationally screen twelve metal dopants from first-row transition metals (Ti, V, Cr, Mn, Fe, Co, Ni, Cu, Zn) and precious metals (Pt, Ir, Ag) on β-Mo_2C with respect to HER activity enhancement. We find that only Ir and Ti doping introduce new HER active sites that bind hydrogen thermoneutrally, and thus are expected to enhance the catalytic activity. For validation, we synthesize metal-doped β-Mo_2C NPs using a microwave-assisted solvothermal method. Cyclic voltammetry measurements show that the overpotential decreases by ~20% when pristine β-Mo_2C NPs are doped with Ir or Ti. Also, the exchange currents for Ir- and Ti-doped β-Mo_2C are, respectively, 1.78 ×10^{-4} A/cm^2 and 2.24 ×10^{-4} A/cm^2, which are nearly one-order of magnitude larger than the corresponding value of 5.37×10^{-5} A/cm^2 for the pristine β-Mo_2C NPs. Fe-doping is found not to enhance the HER currents based on computational and electrochemical experimental results. Further, we employ TEM, HAADF-STEM, and EDS to examine the atomic structure of the metal-doped β-Mo_2C. We find that Ir and Fe are favorable to segregate on the exposed surface

and Ti tends to distribute equally among the layers, which agrees with our computational analysis of segregation tendencies. From showing that there is a larger proportion of small NPs in Fe-doped β-Mo_2C NPs than for the Ir- and Ti-doped β-Mo_2C NPs, we justify that the HER is activated by Ir and Ti dopants rather than by exposing original sites due to the increase of effective surface area. We have confirmed that Ir and Ti doping enhance HER activity by manipulating the catalytic chemistry, which demonstrates the synergetic role of computational and experimental approaches to rationalize the design of enhanced catalysts.

9-5 Supporting Information

Computational Details. The Vienna Ab Initio Simulation Package (VASP) with the Revised Perdew-Burke-Ernzerhof (rPBE) functional is carried out for the first-principles DFT calculations. The pristine and doped systems are metallic, and thus the employed semi-local functional is expected to be accurate for these systems. We use the PAW pseudopotentials to describe electron-nucleus interactions.[160-163] In addition, the dDsC dispersion correction is used for Van der Waals (vdW) interactions. The electronic self-consistent loops are terminated when the energy change is

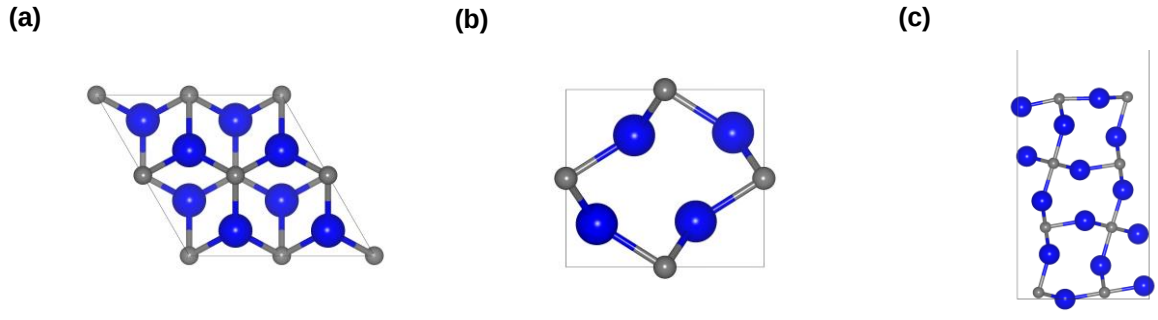

Figure 9-9. (a) The top view and **(b)** side view of β-Mo_2C primitive cell, and **(c)** the β-Mo_2C (011) surface model. The blue spheres are Mo atoms and the gray spheres are C atoms.

within 1×10^{-6} eV with 400 eV planewave cutoff. For all doped systems, we confirmed that spin polarization effects are negligible. Also, all calculations correspond to neutral charged systems. The surface models are cleaved from the bulk β-Mo_2C with hexagonal structure.[386] We focus on the mixed Mo/C (011) as it is the most stable termination among low-Miller index surfaces of β-Mo_2C at common synthesis conditions.[124,383,384] Further, such surface shows an enhanced activity towards HER. Note that the (011) surface is referred to as (101) surface in some studies.[124,383] We use a supercell approach to represent the slab models with 14 layers cleaved from (1×1) supercells with the same atomic structure in the top and the bottom layers. All the atoms in the slab models are relaxed to assess their stability. Atoms that are more than 3 layers below the exposed layer showed very little relaxations compared to the pristine bulk positions, suggesting that the slab models have negligible finite-size dependence. The minimum reaction pathways are determined using the NEB theory[387] with the spring constant of -5 between images. The images are converged when their ionic relaxation loops are within the tolerance of 0.05 eV/Å. The computational surface models are cleaved from the most stable hexagonal β-Mo_2C structure among all possible arrangements of carbon atoms that are partially occupied at defined carbon sites.[386] The primitive cell of the β-Mo_2C has the lattice constants of 6.09, 6.08, 4.73, 90.00, 90.00 and 120.00 optimized using the k-points of 4×4×4 to sample the Brillouin zone. We have verified that the k-grid is sufficient to converge all energy differences to less than 0.05 eV. The (011) surface models, with a 15 Å vacuum perpendicular to the surfaces, have ten atomic layers with the bottom four layers fixed at bulk positions during optimization. The exposed layer has the Mo:C of 1:1, and the second and the third layers are composed by Mo atoms only.

Pristine and Metal-Doped β-Mo_2C Synthesis. β-Mo_2C nanoparticles (NPs) are synthesized by the microwave-assisted solvothermal method using $MoCl_5$ (99.6%, Alfa Aesar), ethanol (200 proof, Decon), urea (Sigma Aldrich), $TiCl_4$ (0.09M in 20% HCl, Sigma Aldrich), $IrCl_3 \cdot 3H_2O$ (53-56% Ir, Acros Organics), $FeCl_3 \cdot 6H_2O$ (97%, Sigma Aldrich) and graphene oxide nanosheets (ACS Material). Doping is achieved by mixing 1g $MoCl_5$ and dopant in 5 ml ethanol for 10 min, followed by the addition of urea (7 molar ratio). After vigorous mixing, 3 wt% of graphene oxide (GO) nanosheets (1~5μm in diameter) in comparison to the weight of β-Mo_2C NP is added to the precursor solution. The fully mixed solution is reacted with microwave radiation (CEM microwave reactor) until the solution temperature reached 150 ℃ and is then held at this temperature for 10 minutes. Microwave power and pressure are maintained at 800 W and 800 kpsi, respectively, throughout the reaction. After the reaction, the amorphous solid is collected and subsequently

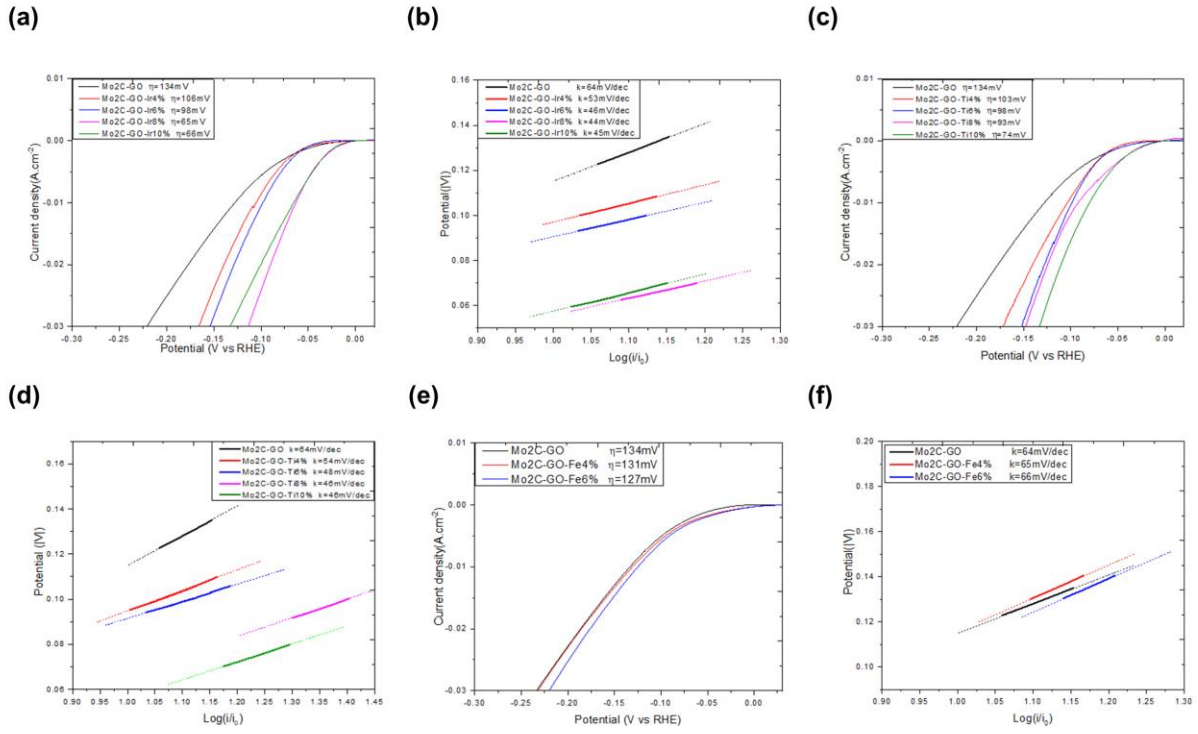

Figure 9-10. **(a), (c), (e)** HER polarization curves of Ir, Ti, and Fe doped Mo_2C, **(b), (d), (f)** Tafel plots of Ir, Ti, and Fe doped Mo_2C NPs.

crystallized at 800 ℃ for 180 min under N_2 atmosphere. Specimens for TEM examination is prepared via drop-casting, wherein small quantities of powdered sample are dispersed in ethanol and sonicated for 1 minute to uniformly disperse the particles in solution. A 4 μL droplet of each solution is then pipetted onto ultrathin carbon-coated Cu TEM grids (Ted Pella Inc.) and allowed

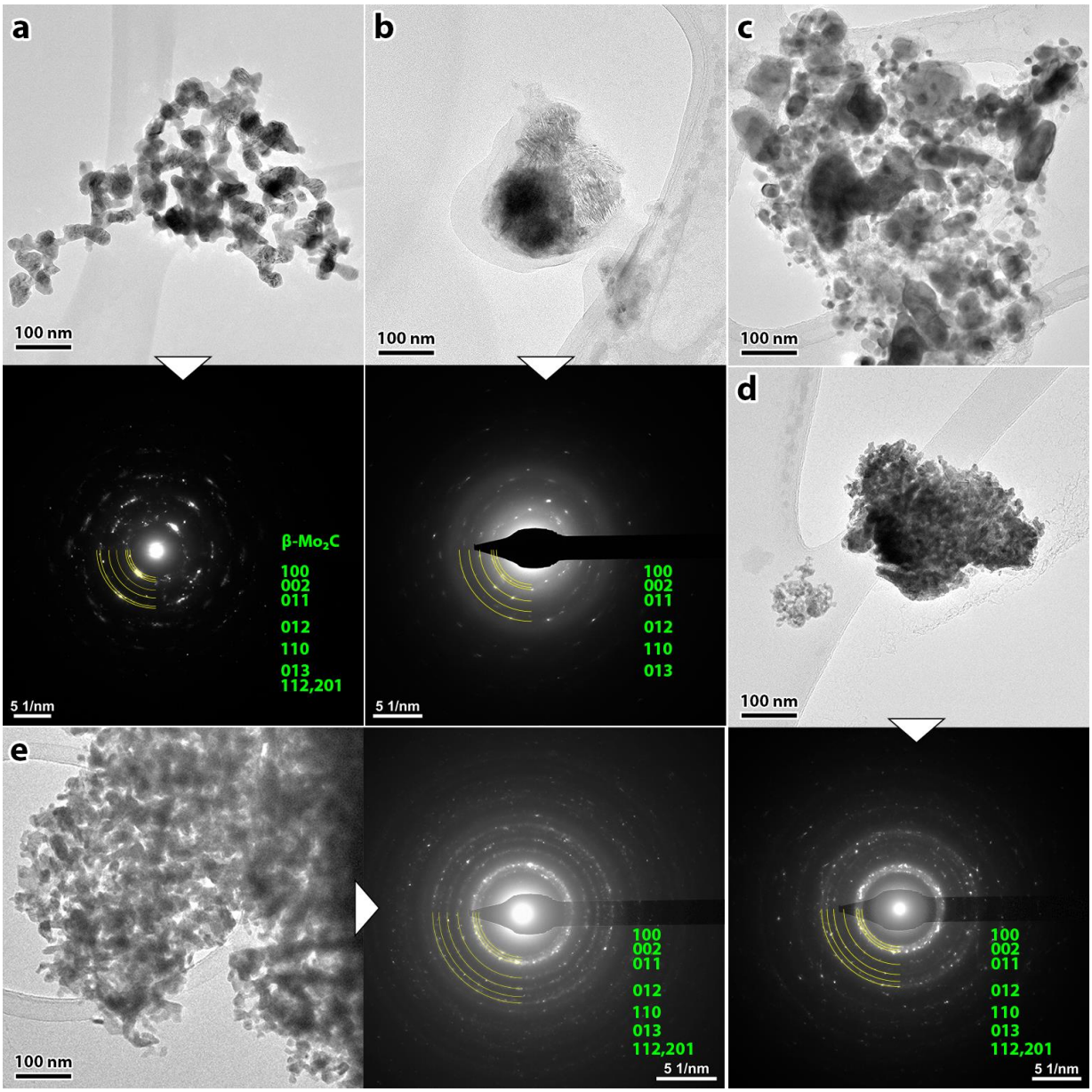

Figure 9-11. TEM micrographs of representative β-Mo_2C aggregates, showing typical particle sizes and morphologies of **(a)** pristine β-Mo_2C (with no GO support), **(b)** pristine β-Mo_2C (with GO support), **(c)** Fe-doped, **(d)** 8% Ir-doped, and **(e)** 8% Ti-doped material. The white arrowheads indicate the corresponding selected-area electron diffraction patterns of the aggregates. The major rings of diffraction spots have been labeled with colored arcs, indexed to β-Mo_2C.

to dry. These specimens are subsequently examined using a Thermo Fisher Themis G2 200 probe-aberration-corrected S/TEM operated at 200 kV and equipped with a Super-X energy-dispersive X-ray spectroscopy system for elemental mapping and quantification (using Velox software). A probe current of 45 pA is used for High-angle annular dark-field (HAADF) STEM imaging and a 300-425 pA probe current for EDS mapping. The Circular Hough Transform plugin[388] for Gatan Digital Micrograph is used to measure diffraction ring spacing in any ring patterns, and a custom-scripted worksheet is employed to match diffraction and FFT spacings against a library of plane spacings.

Electrochemistry and XRD. The crystal structure, size, morphology, and composition of the synthesized materials are determined using X-ray diffraction (XRD), scanning electron microscopy (SEM), and scanning transmission electron microscopy (STEM). XRD (X'Pert PaNalytical) patterns of the samples are measured. For HER testing, 1 g of undoped or doped Mo_2C NPs is mixed with 0.08 g of ethyl cellulose and 4.46 g of α-terpinol. Each mixture is then processed with a three-roll mill (Model: 50i, Exakt) to form a paste. The paste is coated onto fluorine-doped tin oxide (FTO) glass using a screen-printing process, and the organic part of the paste is slowly burned away at 250 ℃ for 3 hr in a tubular furnace under N_2 atmosphere. The geometrical surface area of the electrode is 1 cm^2 and the catalyst loading is 0.54 mg/cm^2 for all β-Mo_2C NPs or Mo_2C-GO electrodes. The electronic properties of the printed thick films are determined using 4-point probe electric conductivity measurements. All electrochemical measurements are performed using a three-electrode electrochemical workstation (CHI 660 potentiostat). A saturated calomel electrode (SCE) and Pt plate are chosen as the reference and counter electrodes, respectively, and are de-aerated with argon before use. The β-Mo_2C electrode

is tested in a 0.5 M H_2SO_4 aqueous electrolyte. Polarization curves are obtained through linear sweep voltammetry (LSV) in 0.5 M H_2SO_4 at a scan rate of 20 mVs^{-1}.

Aggregate Packing Density. The density of particle packing in the aggregates appeared to vary somewhat by sample, with the Ir- being most tightly packed, but this may merely a byproduct of

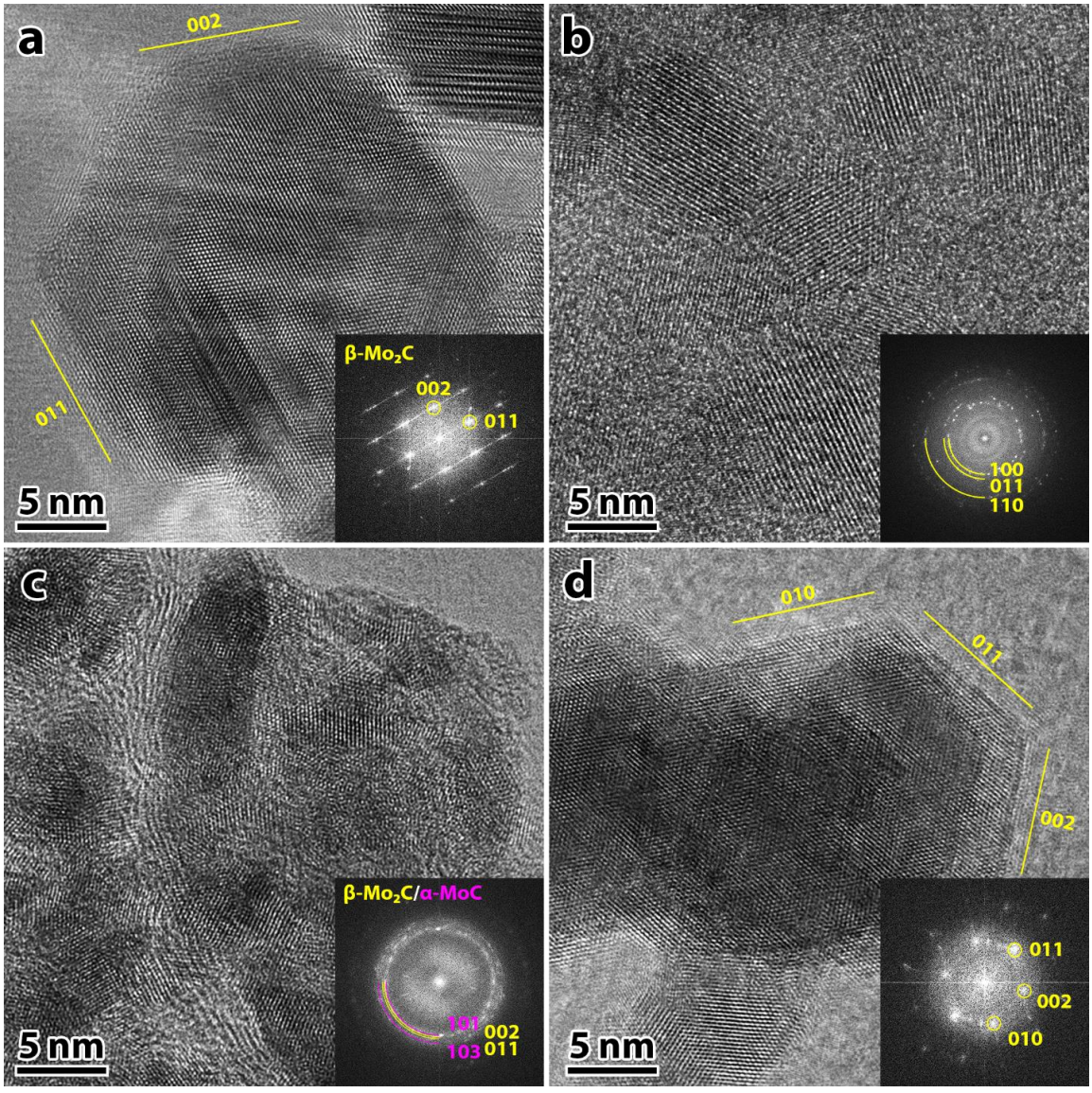

Figure 9-12. HRTEM micrographs of example Mo-C particles – showing the crystallinity and surfaces – of **(a)** pristine β-Mo_2C (with no GO support), **(b)** pristine β-Mo_2C (with GO support), **(c)** Ir-doped, and **(d)** Ti-doped samples. Insets show the corresponding indexed FFTs for each image – β-Mo_2C in yellow, α-MoC in magenta. Some of the facets of the highly faceted particles in (a) and (d) are labeled.

constituent particle size and/or processing. The Fe-doped sample exhibited the lowest degree of particle connectivity.

Mo_2C Particle Morphology and Structure. As noted in the main document, the Mo_2C particles possessed wide variety of morphologies, from nearly spherical, to highly faceted, to shard/flake-like. The example particles in the main text and Supporting Information have been selected to present some examples of this variety. Twinning, such as in Figure 9-6(d) and Figure 9-12(a), was observed in all, but particularly common in the pure β-Mo_2C and Ti-doped specimens. The quantity and close proximity of plane spacings in the assorted β-Mo_2C polymorphs can make completely indexing ED ring patterns a difficult task, so we typically only focused on the strongest/major diffraction rings. Fast Fourier Transform (FFT) analysis from many individual particles in each sample also

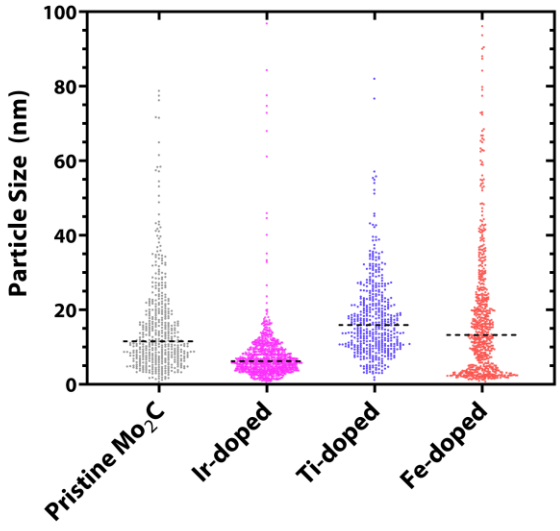

Figure 9-13. Swarm plots of particle size, to better show the significant increase in the relative number of smallest-size particles in the Fe-doped sample.

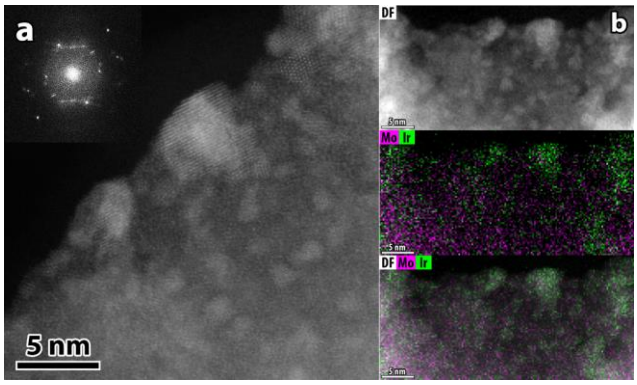

Figure 9-14. (a) HAADF-STEM micrograph and **(b)** corresponding EDS elemental maps from the 8 at% Ir-doped sample, showing the extensive presence of Ir-rich nanoparticles decorating the β-Mo_2C.

Table 9-1. Summary statistics for the particle size distributions in Figure 9-7 and Figure 9-13. All values other than the number of measured particles is in units of nanometers.

	Pristine β-Mo_2C (No GO)	**Pristine β-Mo_2C (with GO)**	**Fe-doped**	**Ir-doped**	**Ti-doped**
# of Particles Measured	247	479	647	805	487
Minimum	3.0	0.7	0.8	0.7	1.2
25% Percentile	19.5	7.1	4.7	4.1	10.4
Median	28.9	11.5	13.2	6.2	15.9
75% Percentile	39.6	19.6	24.0	9.3	22.8
Maximum	80.7	161.1	204.2	565.6	82.0
Mean	30.8	15.8	20.4	8.9	17.8
Std. Deviation	15.4	15.0	24.7	22.6	10.6
Std. Error of Mean	1.0	0.7	1.0	0.8	0.5

revealed predominantly hexagonal (P63/mmc) β-Mo_2C, but with occasional hexagonal α-MoC particles, more so in the Ir-doped material than the others. A deeper examination of the crystal structures and their potential reliance on synthesis details, are the subject of a later study. No appreciable amount of amorphous or non-crystalline Mo_yC phase is observed in any of the samples examined. Given the aggregated nature of most particles, the β-Mo_2C particle size was determined using the following criteria. Where particles were polycrystalline and/or connected, e.g., a "string of pearls" or denser aggregates, a particle was designated as such if (1) it possessed a different lattice orientation than its neighbors and it had (2.1) a distinct neck between its neighbors OR (2.2) was clearly protruding from an underlying particle. The resulting size distributions are shown in Figures 9-5 and 9-13, and assorted summary statistics are included in Table 9-1.

Table 9-2. Quantification of the EDS spectral images in Figure 9-8 and Figures 9-14 to 9-16. All values are atomic %. All elements except those listed were used in the deconvolution only. C was not attempted to be quantified as the samples were supported on C membranes.

Figures	**Material**	**Ti**	**Fe**	**Mo**	**Ir**
8a, S7a	4% Ir-doped	0.0	0.0	96.4	3.6
8b, S7b	8% Ti-doped	1.3	0.0	98.7	0.0
8c, S7c	Fe-doped	0.0	11.9	88.1	0.0
S5, S7d	8% Ir-doped	0.0	0.0	93.1	6.9
S8a	Mo_2C-GO	0.0	0.0	100.0	0.0
8d, S8b	4% Ir-doped	0.0	0.0	96.5	3.5
8e, S8c	8% Ti-doped	0.8	0.0	99.2	0.0
8f, S8d	7.5% Fe-doped	0.0	9.6	90.4	0.0

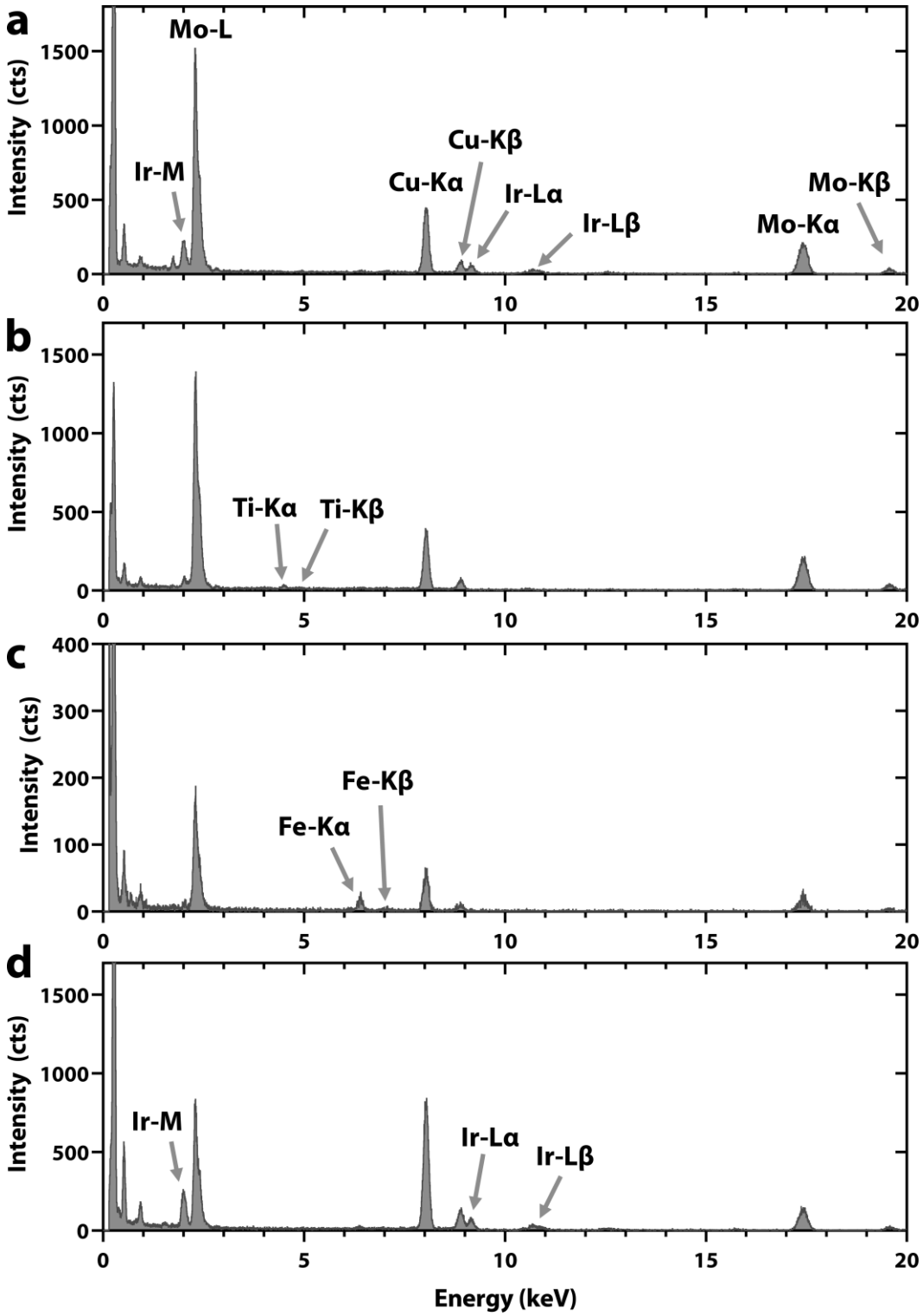

Figure 9-15. Whole-map sum spectra corresponding to the EDS spectral images in **(a-c)** Figure 9-8(a)-(c), respectively, and **(d)** Figure 9-14. The Cu peaks are from the copper washers, clamps, and TEM grids.

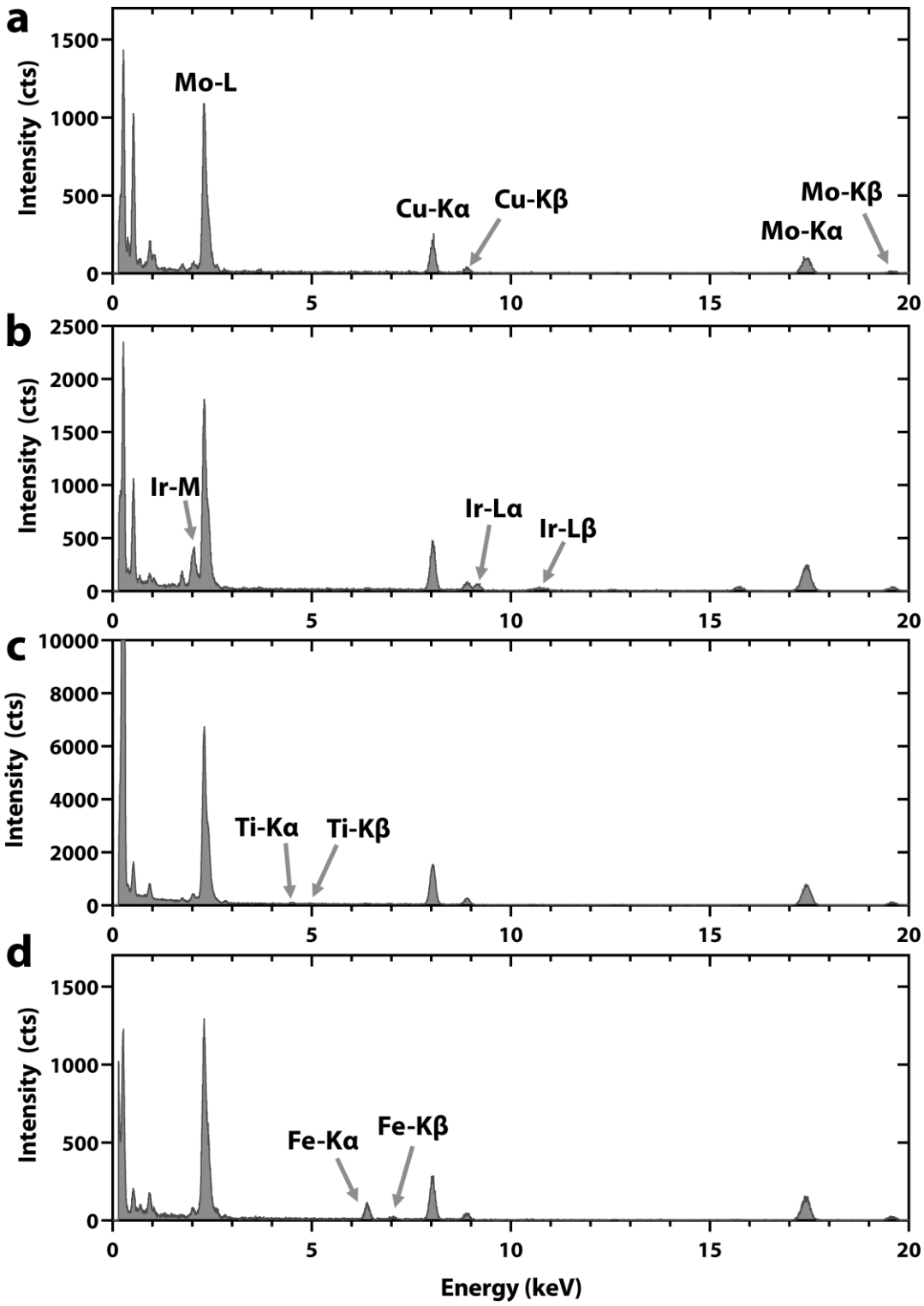

Figure 9-16. Whole-map sum spectra corresponding to the EDS spectral images of **(a)** a pristine β-Mo_2C aggregate, and **(b-d)** Figure 8d-f, respectively. The Cu peaks are from the copper washers, clamps, and TEM grids.

Discussion on Composition of the Catalysts. Fe concentration (9.6-11.9 at%) is found to be reasonably consistent with the nominal doping. Ti concentration, however, is significantly lower (0.6-1.2 at%) in all areas mapped than would be expected from the nominal doping of 8 at%. Other than the occasional small Ti oxide particle – not nearly enough to explain such low overall concentrations – no segregation of Ti was observed, leaving the remaining Ti's residence unclear. This suggests the Ti is not fully incorporated into the β-Mo_2C, remaining in solution, and thus removed, during synthesis. Ir concentration (3.5-3.6 at%) is effectively identical to the expected 4 at%, and is uniformly present across the particles.

The surface segregation of the Ir dopant, and appearance of occasional Ir-rich NPs, suggested that 4 at% may be near or at the limit of Ir incorporation in β-Mo_2C prepared via these methods. To investigate this, an 8 at% Ir-doped sample was examined using the same methods. As seen in the example HAADF-STEM image and corresponding EDS maps of Figure 9-8, in addition to the surface nanoclusters, copious amounts of Ir-rich nanoparticles decorated the β-Mo_2C

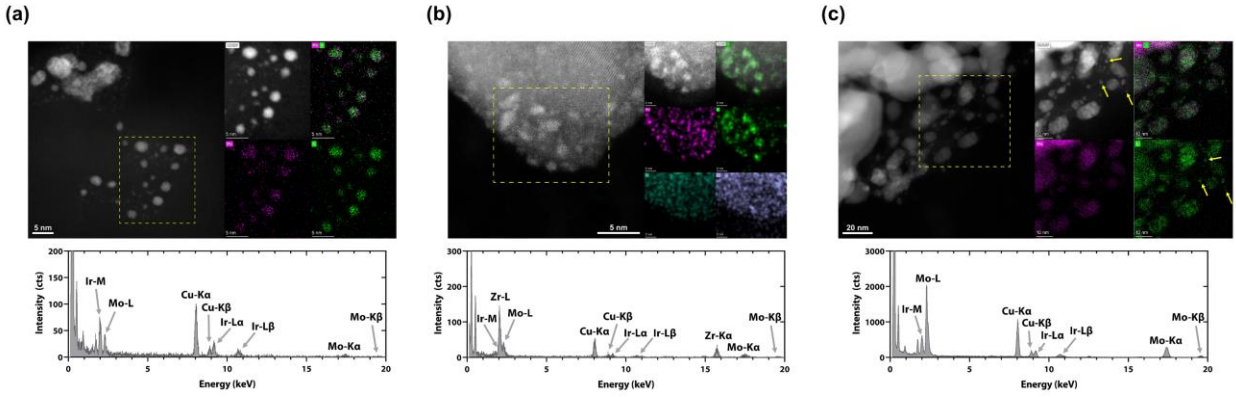

Figure 9-17. **(a)** HAADF-STEM image and corresponding EDS elemental maps and sum spectrum from a patch of Ir-rich nanoparticles in the 8% Ir-doped material. Quantification of various regions features are listed on Table 9-3. **(b)** HAADF-STEM and corresponding EDS elemental maps and sum spectrum from a patch Ir nanoparticles on the surface of a Zn oxide particles in the 8% Ir-doped material. Quantification of the map area is listed on Table 9-3. **(c)** HAADF-STEM image and corresponding EDS elemental maps and sum spectrum from a patch of Mo-C and Ir-rich nanoparticles in the 4% Ir-doped material. Some predominantly Ir particles are indicated by arrows (they appear in the Ir map but not the Mo). Quantification of the map area is listed on Table 9-3.

particles. The size of the Ir-rich decorations also appeared to be concentration-dependent: in the 4% Ir sample, they are mostly small nanoclusters, whereas in the 8% Ir sample they formed NPs of ~1-2 nm in size (with some up to ~5 nm).

In the Ir-doped samples, some areas were found where the Ir-rich NPs were detached from the β-Mo_2C (e.g., Figures 9-17), allowing for their composition to be determined via sub-region segmentation without confounding signal from underlying support particles. The resulting average composition as a function of particle size is included in Table 9-3 and Figure 9-18. These clearly indicated that NP composition was dependent both on doping level and on particle size. In the former case, the higher the nominal doping, the higher Ir concentration in the NPs. For example, particles of <2 nm in size averaged ~30:70 Ir:Mo in the 4% Ir-doped sample yet ~60:40 in the 8% Ir-doped sample. This is consistent with there being a maximum amount of Ir that remains in the β-Mo_2C particles, and that excess Ir beyond this level segregates into increasingly Ir-rich NPs on the surface. At both doping levels, a size-dependent composition was also measured, when comparing the compositions of <2 nm and 2-5 nm. For 4% doping, the Ir:Mo ratio decreased from 30:70 to 89:11, respectively, and for 8% doping from 60:40 to 46:54, respectively. Individual measurement of the few-atom nanoclusters, particularly prevalent in the 4% specimen, are beyond the practical ability of this approach and so were not included in this analysis. The nucleation of

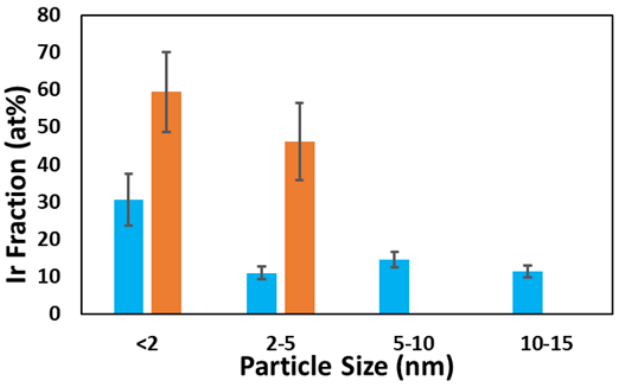

Figure 9-18. Plot of 4% (blue) and 8% (orange) Ir concentration as a function of particle size, measured from unsupported particles in the EDS maps of Figure 9-17 and one other 4% Ir-doped map. Elements other than Mo and Ir were deconvolved for the quantification. Error bars are the quantification error.

nanoparticles from “excess” dopant can explain the appearance of the Ir-Mo XRD peak in the 6% Ir sample (Figure 9-4(c)). The observed trends suggest that Ir doping concentration – and judicious tailoring of processing parameters – can be used to control the size and relative population of Ir-rich nanoclusters/particles and, if sufficient control over their size can be achieved, potentially even enable tuning of their composition.

Table 9-3. Quantification of segmented sub-regions of unsupported nanoparticles from the EDS spectral images in Figure 9-17, and one other 4% Ir-doped EDS map. All values are atomic %. Elements other than Mo and Ir were deconvolved for the quantification. These data are plotted in Figure 9-18.

Material	**Particle Size (nm)**	**At %**		**At% Error**	
		Mo	**Ir**	**Mo**	**Ir**
4% Ir-doped	<2	69.5	30.5	16.9	7.0
	2-5	89.0	11.0	11.3	1.7
8% Ir-doped	<2	40.6	59.4	7.3	10.8
	2-5	53.8	46.2	14.9	10.3

10-0 Interplay of Oxidation and Nitrogen Doping on β-Mo_2C for Hydrogen Evolution

β-Mo_2C does not show the expected activity for the hydrogen evolution reaction, as predicted using first-principles. I posit that surface oxidation under electrochemical and synthesis environments negatively impacts the catalytic properties for the hydrogen evolution reaction and explains the difference between predicted and measured hydrogen evolution reaction activities. Herein, using first-principles, I study the impact of water on the hydrogen evolution reaction activity for. I find that water adsorption and dissociation are thermodynamically spontaneous, which leads to surface oxidation and its decoration with O and OH. On the oxidized β-Mo_2C surface, I find that the hydrogen adsorption strength, with the adsorption free energy ($\Delta G_H \sim -0.15$ eV) is stronger than that of the pristine unoxidized surface ($\Delta G_H \sim -0.09$ eV). The stronger hydrogen adsorption in absolute value on the oxidized surface is indicative of its lesser catalytic activity towards hydrogen evolution compared to the pristine surface. This finding explains why modeling of the hydrogen evolution reaction on pristine surface results in favorable hydrogen adsorption similar to Pt while experimental studies show that hydrogen evolution reaction exchange currents on β-Mo_2C are three orders of magnitude smaller than that of platinum catalysts. Furthermore, I show that nitrogen doping can appreciably rectify the negative oxidation effects as it hinders the water adsorption and dissociation, and preserves the active sites of the pristine β-Mo_2C surface. The findings on nitrogen doping are consistent with experimental results.

10-1 Introduction

The beta-phase of molybdenum carbide β-Mo_2C exhibits high activity for the hydrogen evolution reaction (HER). [9] Further, the efficiency of the HER activity for β-Mo_2C can be improved through surface engineering such as modifying the Mo-valence states by creating Mo vacancies in Mo_yC,[389] substitutional doping with transition metals at the Mo sites of β-Mo_2C[219], and coupling β-Mo_2C with 2-D materials[385]. In our previous study, I found that the (011) termination is the most HER active among low-Miller index surfaces. In addition, this HER active termination is expected to be exposed with over 80% of the surface area on β-Mo_2C nanoparticles based on *ab initio* thermodynamics.[124] I found that the high activity of β-Mo_2C (011) originates from the bridge sites between surface Mo and C that have a moderate binding strength $\Delta G_{\mathrm{H}} \sim -0.09$ eV. Using the Yang-Saidi computational model of Eq. (5-6) for HER exchange currents, $\Delta G_{\mathrm{H}} \sim -0.09$ eV corresponds to a high HER activity similar to that of the Pt electrodes.[189,224] However, while the experimental exchange current for β-Mo_2C is relatively high (1.7×10^{-5} A/cm^2)[9], the current is nearly 3 orders magnitude less than the platinum electrodes[390], and thus is not consistent with the modeling results. Also, other noble metals that have larger $|\Delta G_{\mathrm{H}}|$ than the corresponding value on β-Mo_2C (011), have also their exchange currents that are more than 2 orders magnitude larger than that of the β-Mo_2C electrodes. For example, Ir, Pd and Rh have respectively ΔG_{H} values of -0.14, -0.18 and -0.16 eV, which correspond to the exchange currents of 1×10^{-1}, 4×10^{-2}, 3×10^{-3}, and 5×10^{-3} A/cm^2.[390] These findings strongly suggest that the β-Mo_2C (011) is not in its pristine form and is likely to have an interaction with hydrogen that is in absolute value appreciably larger than 0.09 eV.

Under standard or electrochemical conditions, β-Mo_2C is prone to oxidization since transition metals are exophilic. Using first-principles studies, Tian et. al. argued that the adsorption

of oxygen and hydronium are more stable on β-Mo_2C than water molecules suggesting that water molecules can thermodynamically dissociate into O and OH thus inducing surface oxidation.[391] It has also been reported that surface oxidation of β-Mo_2C degrades the HER activity.[392,393] In contrast, another study argued that tuning the β-Mo_2C surface to be superhydrophilic increases the HER activity[89], which is expected to increase water deposition and dissociation that leads to surface oxidation.

Various studies have shown that N-doping at the substitutional C sites increases the HER activity.[365,367,394,395] However, it is unknown whether the increased HER activity originates from the change of surface electronic properties for moderating the hydrogen adsorption, or by preventing surface oxidation effects, if any. From the study of Ang et. al.[367] showing that nitrogen doping induces hydrophilic effects on Mo_2C, I posit that nitrogen doping may also affect the water adsorption and dissociation. It is not obvious, however, how the interplay between nitrogen doping and surface oxidation may impact the HER activity.

Herein, I use *ab initio* thermodynamic analysis to study water adsorption and dissociation on the most stable β-Mo_2C (011), both for pristine and N-doped surfaces, and their impacts on the HER activity. At standard conditions, I show that water adsorption and dissociation are endothermic, thus resulting in a surface that is covered with O or OH. Further, I find that the O- and OH-decoration degrade the HER activity on β-Mo_2C (011) as indicated by a stronger hydrogen adsorption free energy in absolute value compared to the pristine surface. Nitrogen doping is shown to have beneficial effects on the HER activity that can mitigate negative oxidation effects. Specifically, I find that N-dopants prevent the surface oxidation by increasing the barriers for water dissociation into O and OH, as well as for OH dissociation into O and H_2. In addition, N-dopants are found to preserve the HER active site on the pristine β-Mo_2C (011).

10-2 *Ab Initio* Thermodynamics for Surface Oxidation

The *ab initio* thermodynamic analysis is conducted on the surface slab model of the (011) termination of β-Mo_2C in order to study the potential reaction pathways for the surface oxidation process from water adsorption and dissociation namely:

$$H_2O_{(l)} \rightarrow H_2O^* \rightarrow OH^* + H^* \rightarrow O^* + H_2 \qquad (\textit{Pathway A})$$

$$H_2O_{(l)} \rightarrow H_2O^* \rightarrow OH^* + \frac{1}{2}H_2 \rightarrow O^* + H_2 \qquad (\textit{Pathway B})$$

where the asterisk sign denotes the species in the adsorbed state, $H_2O_{(l)}$ is water in the liquid state, and H_2 is hydrogen in the gas state. Computational details are presented in the Supporting Information of Chapter 9. The reaction free energy Δg of the elementary steps of the two reaction *Pathways A* and *Pathway B* are computed using DFT,

$$\Delta g = \begin{cases} \frac{1}{n}\left(E_{n\mathrm{H_2O}} - E_{slab}\right) - E_{\mathrm{H_2O}} - T\Delta S_{\mathrm{H_2O}} + E_{ZPE}^{(1)} & (H_2O_{(l)} \rightarrow H_2O^*) \\ \frac{1}{n}\left(E_{n\mathrm{OH^*}+n\mathrm{H^*}} - E_{slab}\right) - \frac{1}{m}\left(E_{m\mathrm{H_2O^*}} - E_{slab}\right) + E_{ZPE}^{(2)} & (H_2O^* \rightarrow OH^* + H^*) \\ \frac{1}{n}\left(E_{n\mathrm{OH^*}} - E_{slab}\right) + E_{\mathrm{H_2}} - \frac{1}{m}\left(E_{m\mathrm{H_2O^*}} - E_{slab}\right) + \frac{1}{2}T\Delta S_{\mathrm{H_2}} + E_{ZPE}^{(3)} & (H_2O^* \rightarrow OH^* + \frac{1}{2}H_2) \\ \frac{1}{n}\left(E_{n\mathrm{O^*}} - E_{slab}\right) + E_{\mathrm{H_2}} - \frac{1}{m}\left(E_{n\mathrm{OH^*}+n\mathrm{H^*}} - E_{slab}\right) + T\Delta S_{\mathrm{H_2}} + E_{ZPE}^{(4)} & (OH^* + H^* \rightarrow O^* + H_2) \\ \frac{1}{n}\left(E_{n\mathrm{O^*}} - E_{slab}\right) + E_{\mathrm{H_2}} - \frac{1}{m}\left(E_{n\mathrm{OH^*}+n\mathrm{H^*}} - E_{slab}\right) + \frac{1}{2}T\Delta S_{\mathrm{H_2}} + E_{ZPE}^{(5)} & (OH^* + \frac{1}{2}H_2 \rightarrow O^* + H_2) \end{cases}$$

E_{ni} is the energy of the slab system with the number of n adsorbed i species, E_{slab} is the energy of the pure slab; $E_{\mathrm{H_2O}}$ and $E_{\mathrm{H_2}}$ are the energies of H_2O and H_2 molecules, respectively. At room temperature, $T\Delta S_{\mathrm{H_2O}} = 0.67$ eV is the entropy change of H_2O from the liquid state to the adsorbed state, and $T\Delta S_{\mathrm{H_2}} = 0.41$ eV is the entropy change of H_2 from the gas state to the adsorbed state. The entropic values are determined from thermodynamic data.[7] For each of the elementary steps, E_{ZPE}^{j}, for $j = 1$, 2, 3, 4 or 5, is the zero-point energy difference between the final and the initial

state. For example, $E_{ZPE}^{(3)} = E_{ZPE}^{OH^*} + \frac{1}{2}E_{ZPE}^{H_2} - E_{ZPE}^{H_2O^*}$ where $E_{ZPE}^{OH^*}$, $E_{ZPE}^{H_2}$ and $E_{ZPE}^{H_2O^*}$ are respectively the zero-point energies of OH^*, H_2 and H_2O^*. For the adsorbed configurations, I use *ab initio* thermodynamical, as explained in Chapter 3.4, to determine the most stable adsorption configurations and coverage under standard electrochemical conditions, i.e., 1 atm and 298 K.

Figure 10-1(a) and 10-1(b) show the computed thermodynamic reaction *Pathways A* and *Pathway B* for the oxidation processes on pristine β-Mo_2C (011), respectively. For the *Pathway A*, a water molecule adsorbs on the surface and further dissociates into OH^* and H^* endothermically. The co-adsorbed OH^*/H^* is the most stable state along the pathway with the lowest energy. To further proceed toward the surface oxidation, hydrogen from OH^* and H^* combine to form H_2 molecule and leave the surface. This hydrogen formation process is exothermic with a barrier larger than 0.2 eV. *Pathway B* is similar to *Pathway A* except that the most stable state is a single species OH^* adsorption with a hydrogen molecule in gas phase. The $(OH^* + H^*)$ state of *Pathway B* is ~ 0.3 eV less stable than the OH^*/H^* co-adsorbed state suggesting that the surface is more probable to be occupied by OH^* and H^* species at the same time rather than being occupied by only OH^*. In addition, compared to *Pathway B*, *Pathway A* experiences a ~ 0.3 eV larger barrier

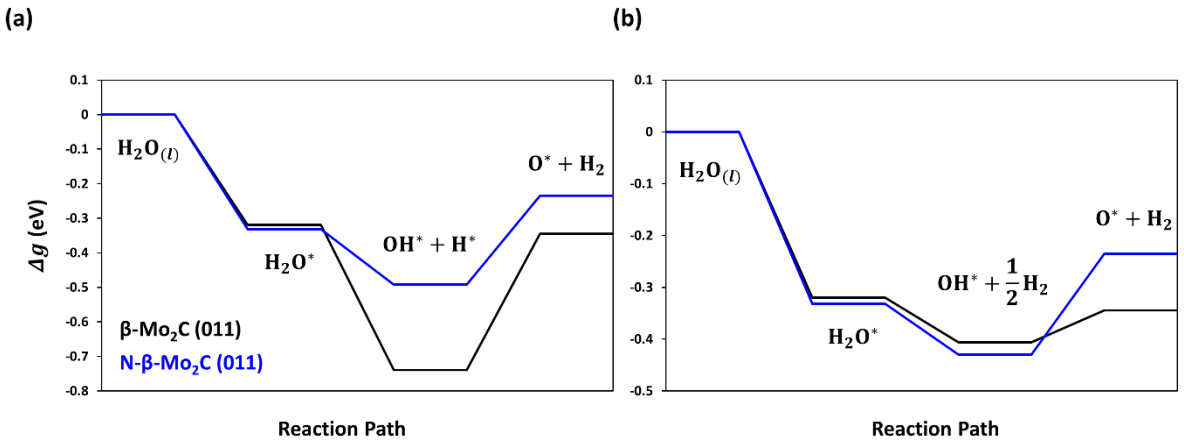

Figure 10-1. (a) Reaction *Pathway A* and **(b)** *Pathway B* for the oxidation processes on the pure β-Mo_2C (011) and the N-doped β-Mo_2C (011), as indicated by the black and the blue lines, respectively.

from the state with OH^* adsorption (the $OH^* + H^*$ state for *Pathway A* or the $OH^* + \frac{1}{2}H_2$ state for *Pathway B*) to the surface oxidation state ($O^* + H_2$). All of these suggest that the ($OH^* + H^*$) state is the most probable for the pristine surface followed by the ($OH^* + \frac{1}{2}H_2$) state, then ($O^* + H_2$), and the water adsorbed state, as shown in Figure 10-1. The clean pristine surface state denoted as ($H_2O_{(l)}$) in Figure 10-1 is the least stable state among the investigated oxidized surfaces. Since the oxygen decorated state ($O^* + H_2$) and the water adsorbed state have comparable energies, and the hydroxide decorated state ($OH^* + H^*$) must be achieved by overcoming a large energy barrier, I posit that the water adsorbed state is more probable than the surface oxidation state. In summary, based on *ab initio* thermodynamic analysis, the most probable state is ($OH^* + H^*$) followed by ($OH^* + \frac{1}{2}H_2$) > (H_2O^*) > ($O^* + H_2$) > ($H_2O_{(l)}$), as shown schematically in Figure 10-1.

To evaluate the most stable structure of the N-doped β-Mo_2C, I study the segregation energy defined in Eq. (9-1) by substituting C with N in each of the layers. I find that the most stable substitutional site is on the exposed layer with the C/N ratio of 4/1, as shown in Figure 10-2. Using this most stable N-doped β-Mo_2C (011), I employ ab initio thermodynamics to study water adsorption and dissociation, as I have done for the pristine β-Mo_2C (011). Figure 10-1 shows that the water dissociation via *Pathway A* becomes less spontaneous than that of the pristine β-Mo_2C (011). However, the barrier from the OH^*- saturated state ($OH^* + H^*$) to the oxidation state ($OH^* + \frac{1}{2}H_2$) is smaller than that of the pristine surface in *Pathway A*. This suggests that the N-doped surface has a less favored state for OH^* adsorption than that of the pristine surface. For *Pathway B*, the pristine and the N-doped surface have comparable tendency for the water dissociation while the N doping-doped β-Mo_2C (011) has a higher barrier for surface oxidation from the OH^* adsorbed state. When comparing the overall oxidation process from $H_2O_{(l)}$ to $O^* +$

H_2 state, the N-doping has a smaller barrier than the pristine surface. All of these results suggest that N-doping prevents, to a certain degree, surface oxidation compared to the pristine surface.

10-3 Surface Activity for Pristine and Nitrogen Doped β-Mo_2C

It is important to verify that N-doping does not annihilate the HER active site on the pristine surface. Thus, I study the hydrogen adsorption free energy ΔG_H on the pristine and N-doped surfaces using Eq. (3-1) and (3-3) in Chapter 3. Here, E_{slab} in Eq. (3-3) is the energy of the surface with the pre-adsorbed species (OH^* or O^*, or the surface with both of the OH^* and H^*) at the most stable configuration, as shown in Figure 10-2. These configurations are determined using the *ab initio* thermodynamic strategy explained in Section 3-6. Comparing the pristine and the N-doped surfaces, the pristine, O^* and OH^* decorated surfaces have similar ΔG_H suggesting that N-doping does not create or annihilate the HER sites on the pristine surface. When the pristine surface is covered by OH^* or O^*, the ΔG_H values decrease from 0.09 eV to -0.13 eV and -0.16 eV, respectively. Employing the Yang-Saidi model of Eq. (5-6), I predict that the OH^* saturated and the oxidized pristine β-Mo_2C (011) have the exchange current ~1×10^{-5} A/cm^2, which is in

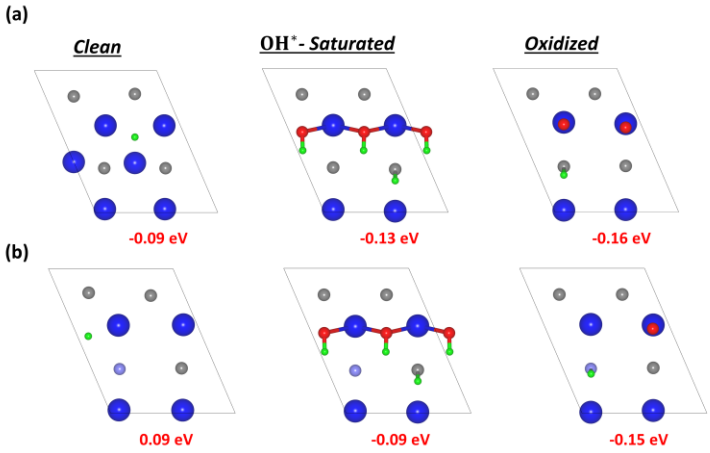

Figure 10-2. Hydrogen adsorption free energy ΔG_H (eV) on the most stable OH^*-adsorbed and oxidized **(a)** pristine and **(b)** N-doped β-Mo_2C (011). The Mo atoms are in blue, C atoms are in gray, N atoms are in purple, oxygen atoms are in red, and hydrogen atoms are in green.

agreement with the experimental values.[9] Because the pristine surface tends to be O^* or OH^* decorated, as shown in Figure 10-1, these adsorption energies suggest that the exchange currents of β-Mo_2C electrodes are ~3 orders of magnitudes less than that of the platinum electrodes, which resolve the controversy that platinum and β-Mo_2C electrodes have similar ΔG_H while the platinum electrodes are significantly more HER active than the β-Mo_2C electrodes.

In summary, I analyze the energetics of surface oxidation from water adsorption on the pristine and N-doped β-Mo_2C (011). For both systems, I find that surface oxidation is spontaneous following energetically favorable adsorption and dissociation of water molecules. Examining the energy profiles of the oxidation pathways, I find that the OH-decorated surfaces are the most probable followed by the O-decorated surfaces. For the N-doped β-Mo_2C (011), the energy barriers from the OH-saturated state to O -decorated surface are larger compared to that of the pristine surface, suggesting that N-doping mitigates the surface oxidation. Further, for the pristine β-Mo_2C (011), I find that the hydrogen adsorption free energies ΔG_H on the O - and OH-decorated surfaces are respectively -0.13 eV and -0.16 eV, which are less optimal than that of the clean surface. These results explain why although the pristine β-Mo_2C has a comparable ΔG_H with that of the platinum electrodes, the exchange current of β-Mo_2C is nearly 3 orders of magnitudes lower than that of platinum. Last, I show that N doping does not annihilate the HER active sites of the pristine surfaces under the clean, with O- or OH-decorations, as indicated from the comparable ΔG_H values to those of the pristine surfaces. These results explain the atomistic mechanisms for the enhanced HER activity with nitrogen doping reported experimentally, and show that N-doping can prevent the surface oxidation of β-Mo_2C.

11-0 Conclusion and Perspectives

Though still in its early days, the potential of the hydrogen economy is enormous. Hydrogen is an energy carrier that can replace fossil fuels for energy generation. However, only 10% of hydrogen is generated from electrolysis using sustainable, renewable energies with no greenhouse gas emissions. One of the central drawbacks in hydrogen production from electrolysis is the use of expensive precious metal catalysts to facilitate the hydrogen evolution reaction. To search for alternative catalysts, first-principles simulations provide an efficient way to screen across materials accessibility for HER.

In the first part of the dissertation (Chapters 4-6), I develop an electrochemical model for HER building on the Butler-Volmer relation for a one-step, one-charge transfer process. I reconcile the model with the Nørskov's volcano trend for the exchange current, and identify the absolute rate constant and the universal value of the charge transfer coefficient for a one-step, one-charge transfer process. These findings enable the electrochemical model to quantify the exchange current with high fidelity, requiring only using the easy-to-compute hydrogen adsorption free energy. Further, from fitting the model to experimental cyclic voltammograms, I confirm the universality of the absolute rate constant and the transfer coefficient at the potential-dependent limit. This opens the opportunity to quantify experimental cyclic voltammograms only using the easy-to-compute hydrogen adsorption free energy.

In the second part of the dissertations (Chapters 7-11), I apply first-principles calculations in conjunction with *ab initio* thermodynamics/kinetics as well as my electrochemical model to design novel HER catalysts via materials engineering. In Chapter 7, I show that the HER-inert

graphene surface can be HER active via coupling with Mo-terminated γ-MoC as well as via vacancy engineering in graphene including Stone-Wales vacancies, mono vacancies and divacancies. In Chapter 8, I show that tailoring the morphology of platinum nanoclusters is a cost-effective way for HER catalyst design. Different from Pt (111) surface where the optimal HER active sites are fcc hollow, I show that platinum nanoclusters have of a variety of edge sites that have equivalent HER activities to those of the hollow sites on Pt (111). In addition, these edge sites are more compact than the fcc hollow sites suggesting that platinum nanoclusters are more mass-effective than platinum bulk for HER. In Chapter 9, I design enhanced molybdenum carbides catalysts for HER through doping with metals. From screening a large number of transition metals via applying the electrochemical model discussed in the first part of the dissertation, I find that Ti- and Ir-doping enhance the HER activity of the pristine β-Mo_2C. These findings are further verified experimentally by *ex situ* structural characterization and cyclic voltammetry. In Chapter 10, I study the impact of surface oxidation and nitrogen doping on HER of β-Mo_2C. While hydroxide can easily block the HER active sites on pristine β-Mo_2C due to spontaneous water dissociation processes, I show that nitrogen doping can largely mitigate this effect. This finding is consistent with experimental results, which show that HER nitrogen doping on β-Mo_2C significantly improves the HER activity. I further illustrate that this is not because nitrogen doping creates new HER active sites on β-Mo_2C but rather because of its mitigation of negative oxidation effects. The study also underscores the importance of mitigation strategies to inhibit surface oxidation.

I list below few research directions that are of interest to explore in future investigations on developing the electrochemical model for effectively and accurately screening the cyclic voltammograms

- My electrochemical model is justified based on identifying an absolute reaction rate. From a theoretical perspective, the rate is equivalent to that of an optimal HER catalyst that has a thermoneutral hydrogen adsorption free energy, i.e., $\Delta G_{\mathrm{H}} = 0$ eV. There is a need to develop this connection further.
- In the electrochemical model, the transfer coefficient is assumed to be universal with the value of 0.5. However, there is a lack of theoretical insight that can either explain or quantify the transfer coefficient solely based on first-principles calculations. Importantly, this is the missing piece for an end-to-end approach to compute HER cyclic voltammograms using first-principles calculations.
- It will be interesting to explore applying a similar computational framework as developed to HER for studying other reactions including CO_2 reduction, metal oxidation, and lithium (de)intercalation reactions.

Hydrogen economy has been considered to be one of the most promising solutions to the Net-Zero Emission by 2050. Developing the electrochemical model and the computational framework is essential for designing catalysts not only for HER but any electrochemical reactions that are essential for the hydrogen economy.

12-0 Bibliography

1 Bard, A. J. & Faulkner, L. R. Electrochemical Method: Fundamentals and Applications. *John Wiley & Sons, Inc.* (2010).

2 Nørskov, J. K. *et al.* Trends in the Exchange Current for Hydrogen Evolution. *Journal of The Electrochemical Society* **152**, J23-J26 (2005).

3 Pan, L. F. *et al.* Molybdenum carbide stabilized on graphene with high electrocatalytic activity for hydrogen evolution reaction. *Chemical Communications* **50**, 13135-13137 (2014).

4 Markovića, N. M., Sarraf, S. T., Gasteiger, H. A. & Ross, P. N. Hydrogen electrochemistry on platinum low-index single-crystal surfaces in alkaline solution. *Journal of the Chemical Society, Faraday Transactions* **92**, 3719-3725 (1996).

5 Marković, N. M., Grgur, B. N. & Ross, P. N. Temperature-Dependent Hydrogen Electrochemistry on Platinum Low-Index Single-Crystal Surfaces in Acid Solutions. *The Journal of Physical Chemistry B* **101**, 5405-5413 (1997).

6 Skúlason, E. *et al.* Density functional theory calculations for the hydrogen evolution reaction in an electrochemical double layer on the Pt(111) electrode. *Physical Chemistry Chemical Physics* **9**, 3241-3250 (2007).

7 Nørskov, J. K. *et al.* Trends in the Exchange Current for Hydrogen Evolution. *Journal of The Electrochemical Society* **152**, J23 (2005).

8 Huang, X. *et al.* Solution-phase epitaxial growth of noble metal nanostructures on dispersible single-layer molybdenum disulfide nanosheets. *Nature Communications* **4**, 1444 (2013).

9 Wan, C., Regmi, Y. N. & Leonard, B. M. Multiple Phases of Molybdenum Carbide as Electrocatalysts for the Hydrogen Evolution Reaction. *Angewandte Chemie International Edition* **53**, 6407-6410 (2014).

10 Durst, J., Simon, C., Hasché, F. & Gasteiger, H. A. Hydrogen Oxidation and Evolution Reaction Kinetics on Carbon Supported Pt, Ir, Rh, and Pd Electrocatalysts in Acidic Media. *J. Electrochem. Soc.* **162**, F190-F203 (2015).

11 Rossmeisl, J., Skúlason, E., Björketun, M. E., Tripkovic, V. & Nørskov, J. K. Modeling the electrified solid–liquid interface. *Chemical Physics Letters* **466**, 68-71 (2008).

12 Tian, Y. *et al.* Plasma-etched, S-doped graphene for effective hydrogen evolution reaction. *International Journal of Hydrogen Energy* **42**, 4184-4192 (2017).

13 Lindsey, R. & Dahlman, L. Climate Change: Global Temperature. *NOAA Climate.gov* (2021).

14 Lumpkin, R., Johnson, G., Thompson, P. & Sweet, W. Climate Change: Global Sea Level. *NOAA Climate.gov* (2020).

15 Arrhenius, S. XXXI. On the influence of carbonic acid in the air upon the temperature of the ground. *The London, Edinburgh, and Dublin Philosophical Magazine and Journal of Science* **41**, 237-276 (1896).

16 Friedlingstein, P. e. a. Global Carbon Budget. *Earth Syst. Sci. Data* **11**, 1783–1838 (2019).

17 Jackson, R. B. *et al.* Persistent fossil fuel growth threatens the Paris Agreement and planetary health. *Environmental Research Letters* **14**, 121001 (2019).

18 Peters, G. P. *et al.* Carbon dioxide emissions continue to grow amidst slowly emerging climate policies. *Nature Climate Change* **10**, 3-6 (2020).

19 Balderas-Xicohténcatl, R., Schmieder, P., Denysenko, D., Volkmer, D. & Hirscher, M. High Volumetric Hydrogen Storage Capacity using Interpenetrated Metal–Organic Frameworks. **6**, 510-512 (2018).

20 Abánades, A., Rubbia, C. & Salmieri, D. Thermal cracking of methane into Hydrogen for a CO_2-free utilization of natural gas. *International Journal of Hydrogen Energy* **38**, 8491-8496 (2013).

21 Wang, S. *et al.* Modifying Ionic Membranes with Carbon Dots Enables Direct Production of High-Purity Hydrogen through Water Electrolysis. *ACS Applied Materials & Interfaces* **13**, 39304-39310 (2021).

22 Walter, M. G. *et al.* Solar Water Splitting Cells. *Chemical Reviews* **110**, 6446-6473 (2010).

23 Benck, J. D., Hellstern, T. R., Kibsgaard, J., Chakthranont, P. & Jaramillo, T. F. Catalyzing the Hydrogen Evolution Reaction (HER) with Molybdenum Sulfide Nanomaterials. *ACS Catalysis* **4**, 3957-3971 (2014).

24 Suen, N.-T. *et al.* Electrocatalysis for the oxygen evolution reaction: recent development and future perspectives. *Chemical Society Reviews* **46**, 337-365 (2017).

25 Trotochaud, L., Young, S. L., Ranney, J. K. & Boettcher, S. W. Nickel–Iron Oxyhydroxide Oxygen-Evolution Electrocatalysts: The Role of Intentional and Incidental Iron Incorporation. *Journal of the American Chemical Society* **136**, 6744-6753 (2014).

26 Roy, C. *et al.* Impact of nanoparticle size and lattice oxygen on water oxidation on NiFeOxHy. *Nature Catalysis* **1**, 820-829 (2018).

27 Zhang, B. *et al.* Homogeneously dispersed multimetal oxygen-evolving catalysts. **352**, 333-337 (2016).

28 Huang, Z.-F. *et al.* Chemical and structural origin of lattice oxygen oxidation in Co–Zn oxyhydroxide oxygen evolution electrocatalysts. *Nature Energy* **4**, 329-338 (2019).

29 Dionigi, F. & Strasser, P. NiFe-Based (Oxy)hydroxide Catalysts for Oxygen Evolution Reaction in Non-Acidic Electrolytes. **6**, 1600621 (2016).

30 Matsumoto, Y., Yamada, S., Nishida, T. & Sato, E. Oxygen Evolution on $La_{1-x}Sr_xFe_{1-y}Co_yO_3$ Series Oxides. *Journal of The Electrochemical Society* **127**, 2360-2364 (1980).

31 Suntivich, J., May, K. J., Gasteiger, H. A., Goodenough, J. B. & Shao-Horn, Y. A Perovskite Oxide Optimized for Oxygen Evolution Catalysis from Molecular Orbital Principles. **334**, 1383-1385 (2011).

32 May, K. J. *et al.* Influence of Oxygen Evolution during Water Oxidation on the Surface of Perovskite Oxide Catalysts. *The Journal of Physical Chemistry Letters* **3**, 3264-3270 (2012).

33 Lee, Y., Suntivich, J., May, K. J., Perry, E. E. & Shao-Horn, Y. Synthesis and Activities of Rutile IrO_2 and RuO_2 Nanoparticles for Oxygen Evolution in Acid and Alkaline Solutions. *The Journal of Physical Chemistry Letters* **3**, 399-404 (2012).

34 Abbott, D. F. *et al.* Iridium Oxide for the Oxygen Evolution Reaction: Correlation between Particle Size, Morphology, and the Surface Hydroxo Layer from Operando XAS. *Chemistry of Materials* **28**, 6591-6604 (2016).

35 Naito, T., Shinagawa, T., Nishimoto, T. & Takanabe, K. Recent advances in understanding oxygen evolution reaction mechanisms over iridium oxide. *Inorganic Chemistry Frontiers* **8**, 2900-2917 (2021).

36 Laha, S. *et al.* Ruthenium Oxide Nanosheets for Enhanced Oxygen Evolution Catalysis in Acidic Medium. **9**, 1803795 (2019).

37 Kibsgaard, J., Hellstern, T. R., Choi, S.-J., Reinecke, B. N. & Jaramillo, T. F. Mesoporous Ruthenium/Ruthenium Oxide Thin Films: Active Electrocatalysts for the Oxygen Evolution Reaction. **4**, 2480-2485 (2017).

38 Hammett, L. P. The mechanism of hydrogen overvoltage and of the electrolytic oxidation of hydrogen. *Transactions of the Faraday Society* **29**, 770-775 (1933).

39 Bockris, J. O. M. & Conway, B. E. Studies in hydrogen overpotential. The effect of catalytic poisons at platinized platinum and nickel. *Transactions of the Faraday Society* **45**, 989-999 (1949).

40 Bockris, J. O. M. & Parsons, R. The kinetics of the hydrogen evolution reaction at mercury cathodes. The effect of temperature, pH, and pressure on hydrogen overpotential in aqueous, mixed and methanolic solutions. *Transactions of the Faraday Society* **45**, 916-928 (1949).

41 Hans Wedepohl, K. The composition of the continental crust. *Geochimica et Cosmochimica Acta* **59**, 1217-1232 (1995).

42 Reith, F., Campbell, S. G., Ball, A. S., Pring, A. & Southam, G. Platinum in Earth surface environments. *Earth-Science Reviews* **131**, 1-21 (2014).

43 Jaksic, M. M., Johansen, B. & Tunold, R. Electrochemical behaviour of platinum in alkaline and acidic solutions of heavy and regular water. *International Journal of Hydrogen Energy* **18**, 817-837 (1993).

44 Kim, J. *et al.* Crystal Phase Transition Creates a Highly Active and Stable RuCX Nanosurface for Hydrogen Evolution Reaction in Alkaline Media.

45 Wu, Y.-L. *et al.* Ordered Macroporous Superstructure of Nitrogen-Doped Nanoporous Carbon Implanted with Ultrafine Ru Nanoclusters for Efficient pH-Universal Hydrogen Evolution Reaction. **33**, 2006965 (2021).

46 Ma, R. *et al.* Tuning the oxidation state of Ru to surpass Pt in hydrogen evolution reaction. *Nano Research* **14**, 4321-4327 (2021).

47 Li, H. *et al.* Paired Ru–O–Mo ensemble for efficient and stable alkaline hydrogen evolution reaction. *Nano Energy* **82**, 105767 (2021).

48 Deng, L. *et al.* Electronic Modulation Caused by Interfacial Ni-O-M (M=Ru, Ir, Pd) Bonding for Accelerating Hydrogen Evolution Kinetics. **60**, 22276-22282 (2021).

49 Fu, Q. *et al.* Phase-Junction Electrocatalysts towards Enhanced Hydrogen Evolution Reaction in Alkaline Media. **60**, 259-267 (2021).

50 Xiao, Z. *et al.* FeNiP/MoO_x integrated electrode grown on monocrystalline $NiMoO_4$ nanorods with multi-interface for accelerating alkaline hydrogen evolution reaction. *Applied Catalysis B: Environmental* **303**, 120913 (2022).

51 Wang, R. *et al.* Two-Dimensional High-Entropy Metal Phosphorus Trichalcogenides for Enhanced Hydrogen Evolution Reaction. *ACS Nano* (2022).

52 Cheng, Z. *et al.* All-pH-Tolerant In-Plane Heterostructures for Efficient Hydrogen Evolution Reaction. *ACS Nano* **15**, 11417-11427 (2021).

53 Qu, J. *et al.* Direct Thermal Enhancement of Hydrogen Evolution Reaction of On-Chip Monolayer MoS_2. *ACS Nano* **16**, 2921-2927 (2022).

54 Reynard, D., Nagar, B. & Girault, H. Photonic Flash Synthesis of Mo_2C/Graphene Electrocatalyst for the Hydrogen Evolution Reaction. *ACS Catalysis* **11**, 5865-5872 (2021).

55 Lori, O., Zion, N., Honig, H. C. & Elbaz, L. 3D Metal Carbide Aerogel Network as a Stable Catalyst for the Hydrogen Evolution Reaction. *ACS Catalysis* **11**, 13707-13713 (2021).

56 Liu, X. *et al.* Enhancing Hydrogen Evolution Activity of Monolayer Molybdenum Disulfide via a Molecular Proton Mediator. *ACS Catalysis* **11**, 12159-12169 (2021).

57 Zhou, K. L. *et al.* Platinum single-atom catalyst coupled with transition metal/metal oxide heterostructure for accelerating alkaline hydrogen evolution reaction. *Nature Communications* **12**, 3783 (2021).

58 Tang, P. *et al.* Elucidating the Formation and Structural Evolution of Platinum Single-Site Catalysts for the Hydrogen Evolution Reaction. *ACS Catalysis*, 3173-3180 (2022).

59 Kwon, I. S. *et al.* Concurrent Vacancy and Adatom Defects of Mo1–xNbxSe_2 Alloy Nanosheets Enhance Electrochemical Performance of Hydrogen Evolution Reaction. *ACS Nano* **15**, 5467-5477 (2021).

60 Rodrigues, M. P. d. S. *et al.* Gold–Rhodium Nanoflowers for the Plasmon-Enhanced Hydrogen Evolution Reaction under Visible Light. *ACS Catalysis* **11**, 13543-13555 (2021).

61 McCrory, C. C. L., Jung, S., Peters, J. C. & Jaramillo, T. F. Benchmarking Heterogeneous Electrocatalysts for the Oxygen Evolution Reaction. *Journal of the American Chemical Society* **135**, 16977-16987 (2013).

62 Shinagawa, T., Garcia-Esparza, A. T. & Takanabe, K. Insight on Tafel slopes from a microkinetic analysis of aqueous electrocatalysis for energy conversion. *Scientific Reports* **5**, 13801 (2015).

63 Sabatier, F. La catalyse en chimie organique; Berauge: Paris. (1920).

64 Gao, G. *et al.* Metal-free graphitic carbon nitride as mechano-catalyst for hydrogen evolution reaction. *Journal of Catalysis* **332**, 149-155 (2015).

65 Chou, S. S. *et al.* Understanding catalysis in a multiphasic two-dimensional transition metal dichalcogenide. *Nature Communications* **6**, 8311 (2015).

66 Zheng, Y., Jiao, Y., Jaroniec, M. & Qiao, S. Z. Advancing the Electrochemistry of the Hydrogen-Evolution Reaction through Combining Experiment and Theory. **54**, 52-65 (2015).

67 Kang, Z. *et al.* Recent progress of MXenes and MXene-based nanomaterials for the electrocatalytic hydrogen evolution reaction. *Journal of Materials Chemistry A* **9**, 6089-6108 (2021).

68 Durst, J., Simon, C., Hasché, F. & Gasteiger, H. A. Hydrogen Oxidation and Evolution Reaction Kinetics on Carbon Supported Pt, Ir, Rh, and Pd Electrocatalysts in Acidic Media. *Journal of The Electrochemical Society* **162**, F190-F203 (2014).

69 deKay Thompson, M. & Kaye, A. L. The Electrochemical Oxidation of Molybdenum in Potassium Hydroxide Solutions. *Transactions of The Electrochemical Society* **62**, 255 (1932).

70 Okonkwo, I. A. *et al.* Oxidation states of molybdenum in oxide films formed in sulphuric acid and sodium hydroxide. **520**, 6318-6327 (2012).

71 Lillard, R. S., Kanner, G. S. & Butt, D. P. The Nature of Oxide Films on Tungsten in Acidic and Alkaline Solutions. *Journal of The Electrochemical Society* **145**, 2718-2725 (1998).

72 Asselin, E., Ahmed, T. M. & Alfantazi, A. Corrosion of niobium in sulphuric and hydrochloric acid solutions at 75 and 95°C. *Corrosion Science* **49**, 694-710 (2007).

73 Sul, Y.-T., Johansson, C. B., Jeong, Y. & Albrektsson, T. The electrochemical oxide growth behaviour on titanium in acid and alkaline electrolytes. *Medical Engineering & Physics* **23**, 329-346 (2001).

74 Ushikubo, T. Recent topics of research and development of catalysis by niobium and tantalum oxides. *Catalysis Today* **57**, 331-338 (2000).

75 Sheng, W., Gasteiger, H. A. & Shao-Horn, Y. Hydrogen Oxidation and Evolution Reaction Kinetics on Platinum: Acid vs Alkaline Electrolytes. *Journal of The Electrochemical Society* **157**, B1529 (2010).

76 Zoski, C. G. Ultramicroelectrodes: Design, Fabrication, and Characterization. **14**, 1041-1051 (2002).

77 Zhou, M., Bao, S. & Bard, A. J. Probing Size and Substrate Effects on the Hydrogen Evolution Reaction by Single Isolated Pt Atoms, Atomic Clusters, and Nanoparticles. *Journal of the American Chemical Society* **141**, 7327-7332 (2019).

78 Mou, J., Gao, Y., Wang, J., Ma, J. & Ren, H. Hydrogen evolution reaction activity related to the facet-dependent electrocatalytic performance of NiCoP from first principles. *RSC Advances* **9**, 11755-11761 (2019).

79 Zhong, W. *et al.* RhSe2: A Superior 3D Electrocatalyst with Multiple Active Facets for Hydrogen Evolution Reaction in Both Acid and Alkaline Solutions. **33**, 2007894 (2021).

80 Wu, T. *et al.* Crystallographic Facet Dependence of the Hydrogen Evolution Reaction on CoPS: Theory and Experiments. *ACS Catalysis* **8**, 1143-1152 (2018).

81 Abghoui, Y. Superiority of the (100) Over the (111) Facets of the Nitrides for Hydrogen Evolution Reaction. *Topics in Catalysis* **65**, 262-269 (2022).

82 Yang, Z., He, R., Wu, H., Ding, Y. & Mei, H. Needle-like CoP/rGO growth on nickel foam as an efficient electrocatalyst for hydrogen evolution reaction. *International Journal of Hydrogen Energy* **46**, 9690-9698 (2021).

83 Huang, J., Hong, W. & Liu, W. Molybdenum carbide nanosheets decorated with $Ni(OH)_2$ nanoparticles toward efficient hydrogen evolution reaction in alkaline media. *Applied Surface Science* **579**, 152152 (2022).

84 Wang, R., Jing, Y., Sun, P. & Wang, X. The partially unzipped carbon nanotubes supported molybdenum carbide composite for enchanced hydrogen evolution reaction. *Materials Letters* **294**, 129779 (2021).

85 Lee, Y.-H., Brahma, S., Huang, P.-C., Wang, S.-C. & Huang, J.-L. Molybdenum carbide (Mo_2C) and reduced graphene oxide (rGO) nano-composites as an efficient electrocatalyst for water splitting. *Materials Letters* **316**, 131934 (2022).

86 Yang, T. T. & Saidi, W. A. Graphene Activation Explains the Enhanced Hydrogen Evolution on Graphene-Coated Molybdenum Carbide Electrocatalysts. *The Journal of Physical Chemistry Letters* **11**, 2759-2764 (2020).

87 Wan, C. & Leonard, B. M. Iron-Doped Molybdenum Carbide Catalyst with High Activity and Stability for the Hydrogen Evolution Reaction. *Chemistry of Materials* **27**, 4281-4288 (2015).

88 Hu, Z. *et al.* Porous N-doped Mo_2C@C nanoparticles for high-performance hydrogen evolution reaction. *International Journal of Hydrogen Energy* **47**, 4641-4652 (2022).

89 Liu, W. *et al.* Tuning Ni dopant concentration to enable co-deposited superhydrophilic self-standing Mo_2C electrode for high-efficient hydrogen evolution reaction. *Applied Catalysis B: Environmental* **307**, 121201 (2022).

90 El-Refaei, S. M., Russo, P. A. & Pinna, N. Recent Advances in Multimetal and Doped Transition-Metal Phosphides for the Hydrogen Evolution Reaction at Different pH values. *ACS Applied Materials & Interfaces* **13**, 22077-22097 (2021).

91 Lin, Y., Wu, Z., Wen, J., Poeppelmeier, K. R. & Marks, L. D. Imaging the Atomic Surface Structures of CeO_2 Nanoparticles. *Nano Letters* **14**, 191-196 (2014).

92 Hinnemann, B. *et al.* Biomimetic Hydrogen Evolution: MoS_2 Nanoparticles as Catalyst for Hydrogen Evolution. *Journal of the American Chemical Society* **127**, 5308-5309 (2005).

93 Jaramillo, T. F. *et al.* Identification of Active Edge Sites for Electrochemical H_2 Evolution from MoS_2 Nanocatalysts. **317**, 100-102 (2007).

94 Lindgren, P., Kastlunger, G. & Peterson, A. A. A Challenge to the G ~ 0 Interpretation of Hydrogen Evolution. *ACS Catalysis* **10**, 121-128 (2020).

95 Kronberg, R. & Laasonen, K. Reconciling the Experimental and Computational Hydrogen Evolution Activities of Pt(111) through DFT-Based Constrained MD Simulations. *ACS Catalysis*, 8062-8078 (2021).

96 Ooka, H., Wintzer, M. E. & Nakamura, R. Non-Zero Binding Enhances Kinetics of Catalysis: Machine Learning Analysis on the Experimental Hydrogen Binding Energy of Platinum. *ACS Catalysis* **11**, 6298-6303 (2021).

97 Shinagawa, T. & Takanabe, K. New Insight into the Hydrogen Evolution Reaction under Buffered Near-Neutral pH Conditions: Enthalpy and Entropy of Activation. *The Journal of Physical Chemistry C* **120**, 24187-24196 (2016).

98 Marozzi, C. A., Canto, M. R., Costanza, V. & Chialvo, A. C. Analysis of the use of voltammetric results as a steady state approximation to evaluate kinetic parameters of the hydrogen evolution reaction. *Electrochimica Acta* **51**, 731-738 (2005).

99 Kucernak, A. R. & Zalitis, C. General Models for the Electrochemical Hydrogen Oxidation and Hydrogen Evolution Reactions: Theoretical Derivation and Experimental Results

under Near Mass-Transport Free Conditions. *The Journal of Physical Chemistry C* **120**, 10721-10745 (2016).

100 Chase, M. W. *et al.* JANAF Thermochemical Tables, 1982 Supplement. *Journal of Physical and Chemical Reference Data* **11**, 695 (1982).

101 Tymoczko, J., Calle-Vallejo, F., Schuhmann, W. & Bandarenka, A. S. Making the hydrogen evolution reaction in polymer electrolyte membrane electrolysers even faster. *Nature Communications* **7**, 10990 (2016).

102 Trasatti, S. The Absolute electrode potential: ab explanatory note. *Pure & AppL Chem.* **58**, 955-966 (1986).

103 Bockris, J. O. M. Electrolytic polarisation—I. The overpotential of hydrogen on some less common metals at high current densities. Influence of current density and time. *Transactions of the Faraday Society* **43**, 417-429 (1947).

104 Conway, B. E. & Bockris, J. O. M. Electrolytic Hydrogen Evolution Kinetics and Its Relation to the Electronic and Adsorptive Properties of the Metal. *The Journal of Chemical Physics* **26**, 532-541 (1957).

105 Petrenko, A. T. & Fiz., Z. *Khim* **39** (1965).

106 Kita, H. Periodic Variation of Exchange Current Density of Hydrogen Electrode Reaction with Atomic Number and Reaction Mechanism. *Journal of The Electrochemical Society* **113**, 1095 (1966).

107 Trasatti, S. Work function, electronegativity, and electrochemical behaviour of metals: III. Electrolytic hydrogen evolution in acid solutions. *Journal of Electroanalytical Chemistry and Interfacial Electrochemistry* **39**, 163-184 (1972).

108 Parsons, R. The rate of electrolytic hydrogen evolution and the heat of adsorption of hydrogen. *Transactions of the Faraday Society* **54**, 1053-1063 (1958).

109 Gerischer, H. Mechanismus der Elektrolytischen Wasserstoffabscheidung und Adsorptionsenergie von Atomarem Wasserstoff. **67**, 506-527 (1958).

110 Eley, D. D. A calculation of heats of chemisorption. *Discussions of the Faraday Society* **8**, 34-38 (1950).

111 Nørskov, J. K. *et al.* Trends in the Exchange Current for Hydrogen Evolution. *Journal of The Electrochemical Society* **152** (2005).

112 Wang, L. *et al.* Optimizing the Volmer Step by Single-Layer Nickel Hydroxide Nanosheets in Hydrogen Evolution Reaction of Platinum. *ACS Catalysis* **5**, 3801-3806 (2015).

113 Sarma, P. V. *et al.* Nanostructured Tungsten Oxysulfide as an Efficient Electrocatalyst for Hydrogen Evolution Reaction. *ACS Catalysis* **10**, 6753-6762 (2020).

114 Seh, Z. W. *et al.* Combining theory and experiment in electrocatalysis: Insights into materials design. *Science* **355**, eaad4998 (2017).

115 Greeley, J. Theoretical Heterogeneous Catalysis: Scaling Relationships and Computational Catalyst Design. *Annual Review of Chemical and Biomolecular Engineering* **7**, 605-635 (2016).

116 Koper, M. T. M. Theory of multiple proton–electron transfer reactions and its implications for electrocatalysis. *Chemical Science* **4**, 2710-2723 (2013).

117 Nørskov, J. K., Bligaard, T., Rossmeisl, J. & Christensen, C. H. Towards the computational design of solid catalysts. *Nature Chemistry* **1**, 37-46 (2009).

118 Nørskov, J. K., Abild-Pedersen, F., Studt, F. & Bligaard, T. Density functional theory in surface chemistry and catalysis. *Proc. Natl. Acad. Sci. U. S. A.* **108**, 937 (2011).

119 Quaino, P., Juarez, F., Santos, E. & Schmickler, W. Volcano plots in hydrogen electrocatalysis – uses and abuses. *Beilstein Journal of Nanotechnology* **5**, 846-854 (2014).

120 Kronberg, R. & Laasonen, K. Coupling Surface Coverage and Electrostatic Effects on the Interfacial Adlayer–Water Structure of Hydrogenated Single-Crystal Platinum Electrodes. *The Journal of Physical Chemistry C* **124**, 13706-13714 (2020).

121 Holmberg, N. & Laasonen, K. Ab Initio Electrochemistry: Exploring the Hydrogen Evolution Reaction on Carbon Nanotubes. *The Journal of Physical Chemistry C* **119**, 16166-16178 (2015).

122 Ooka, H. & Nakamura, R. Shift of the Optimum Binding Energy at Higher Rates of Catalysis. *The Journal of Physical Chemistry Letters* **10**, 6706-6713 (2019).

123 Skúlason, E. *et al.* Modeling the Electrochemical Hydrogen Oxidation and Evolution Reactions on the Basis of Density Functional Theory Calculations. *The Journal of Physical Chemistry C* **114**, 18182-18197 (2010).

124 Yang, T. T. & Saidi, W. A. Tuning the hydrogen evolution activity of β-Mo_2C nanoparticles via control of their growth conditions. *Nanoscale* **9**, 3252-3260 (2017).

125 Chase, M. W., Jr. NIST-JANAF Themochemical Tables, Fourth Edition. *J. Phys. Chem. Ref. Data, Monograph 9* (1998).

126 Marcus, R. A. Electron transfer reactions in chemistry. Theory and experiment. *Reviews of Modern Physics* **65**, 599-610 (1993).

127 Kant, R., Kaur, J. & Mishra, G. K. Theory for Influence of the Metal Electrolyte Interface on Heterogeneous Electron Transfer Rate Constant: Fractional Electron Transferred Transition State Approach. *J. Phys. Chem. C* **124**, 2273-2288 (2020).

128 Shi, H. *et al.* Monitoring Local Electric Fields at Electrode Surfaces Using Surface Enhanced Raman Scattering-Based Stark-Shift Spectroscopy during Hydrogen Evolution Reactions. *ACS Applied Materials & Interfaces* **10**, 33678-33683 (2018).

129 Tang, M. T., Liu, X., Ji, Y., Norskov, J. K. & Chan, K. Modeling Hydrogen Evolution Reaction Kinetics through Explicit Water–Metal Interfaces. *The Journal of Physical Chemistry C* **124**, 28083-28092 (2020).

130 Zheng, J., Sheng, W., Zhuang, Z., Xu, B. & Yan, Y. Universal dependence of hydrogen oxidation and evolution reaction activity of platinum-group metals on pH and hydrogen binding energy. *Science Advances* **2**, e1501602 (2016).

131 Xu, W. *et al.* A highly efficient electrocatalyst based on amorphous Pd–Cu–S material for hydrogen evolution reaction. *Journal of Materials Chemistry A* **5**, 18793-18800 (2017).

132 Kuhn, A. T. & Wright, P. M. The cathodic evolution of hydrogen on ruthenium and osmium electrodes. *Journal of Electroanalytical Chemistry and Interfacial Electrochemistry* **27**, 319-323 (1970).

133 Pentland, N., Bockris, J. O. M. & Sheldon, E. Hydrogen Evolution Reaction on Copper, Gold, Molybdenum, Palladium, Rhodium, and Iron. *Journal of The Electrochemical Society* **104**, 182 (1957).

134 Kuhn, A. T., Mortimer, C. J., Bond, G. C. & Lindley, J. A critical analysis of correlations between the rate of the electrochemical hydrogen evolution reaction and physical properties of the elements. *Journal of Electroanalytical Chemistry and Interfacial Electrochemistry* **34**, 1-14 (1972).

135 Navarro-Flores, E., Chong, Z. & Omanovic, S. Characterization of Ni, NiMo, NiW and NiFe electroactive coatings as electrocatalysts for hydrogen evolution in an acidic medium. *Journal of Molecular Catalysis A: Chemical* **226**, 179-197 (2005).

136 Perez, J., Gonzalez, E. R. & Villullas, H. M. Hydrogen Evolution Reaction on Gold Single-Crystal Electrodes in Acid Solutions. *The Journal of Physical Chemistry B* **102**, 10931-10935 (1998).

137 Štrbac, S., Srejić, I. & Rakočević, Z. Electrocatalysis of Hydrogen Evolution Reaction on Au(111) by Spontaneously Deposited Iridium in Acid Solution. *Journal of The Electrochemical Society* **165**, J3335-J3341 (2018).

138 Rivera, J. G., Garcia-Garcia, R., Coutino-Gonzalez, E. & Orozco, G. Hydrogen evolution reaction on metallic rhenium in acid media with or without methanol. *International Journal of Hydrogen Energy* **44**, 27472-27482 (2019).

139 Garcia-Garcia, R., Ortega-Zarzosa, G., Rincón, M. E. & Orozco, G. The Hydrogen Evolution Reaction on Rhenium Metallic Electrodes: A Selected Review and New Experimental Evidence. *Electrocatalysis* **6**, 263-273 (2015).

140 Bockris, J. O. M. & Srinivasan, S. Elucidation of the mechanism of electrolytic hydrogen evolution by the use of H-T separation factors. *Electrochimica Acta* **9**, 31-44 (1964).

141 Wu, Y. M. *et al.* Effect of bismuth on hydrogen evolution reaction on lead in sulfuric acid solution. *Journal of Power Sources* **144**, 338-345 (2005).

142 Butler, J. N. & Dienst, M. Hydrogen Evolution at a Solid Indium Electrode. *Journal of The Electrochemical Society* **112**, 226 (1965).

143 Zheng, J., Sheng, W., Zhuang, Z., Xu, B. & Yan, Y. Universal dependence of hydrogen oxidation and evolution reaction activity of platinum-group metals on pH and hydrogen binding energy. *Sci Adv* **2**, e1501602-e1501602 (2016).

144 Gelin, S., Champagne-Ruel, A. & Mousseau, N. Enthalpy-entropy compensation of atomic diffusion originates from softening of low frequency phonons. *Nature Communications* **11**, 3977 (2020).

145 G. Kresse, J. F. Efficient iterative schemes for ab initio total-energy calculations using a plane-wave basis set. *Phys. Rew.* **54**, 11168 (1996).

146 Shishkin, M., Marsman, M. & Kresse, G. Accurate Quasiparticle Spectra from Self-Consistent GW Calculations with Vertex Corrections. *Phys. Rev. Lett.* **99**, 246403 (2007).

147 Kresse, G. & Joubert, D. From ultrasoft pseudopotentials to the projector augmented-wave method. *Phys. Rev. B* **59**, 1758 (1999).

148 John P. Perdew, K. B., Matthias Ernzerhof. Generalized Gradient Approximation Made Simple. *Phys. Rev. Lett.* **77**, 4 (1996).

149 Perdew, J. P., Burke, K. & Ernzerhof, M. Generalized Gradient Approximation Made Simple. *Physical Review Letters* **77**, 3865-3868 (1996).

150 Tkatchenko, A. & Scheffler, M. Accurate Molecular Van Der Waals Interactions from Ground-State Electron Density and Free-Atom Reference Data. *Phys. Rev. Lett.* **102**, 073005 (2009).

151 Al-Saidi, W., Voora, V. K. & Jordan, K. D. An assessment of the vdW-TS method for extended systems. *Journal of Chemical Theory and Computation* **8**, 1503-1513 (2012).

152 Pourbaix, M. *Atlas of Electrochemical Equilibria in Aqueous Solutions*. (National Association of Corrosion Engineers, 1974).

153 Krishnamurthy, D., Sumaria, V. & Viswanathan, V. Maximal Predictability Approach for Identifying the Right Descriptors for Electrocatalytic Reactions. *J. Phys. Chem. Lett.* **9**, 588-595 (2018).

154 Trasatti, S. Work function, electronegativity, and electrochemical behaviour of metals: II. Potentials of zero charge and "electrochemical" work functions. *Journal of Electroanalytical Chemistry and Interfacial Electrochemistry* **33**, 351-378 (1971).

155 Trasatti, S. Electronegativity, work function, and heat of adsorption of hydrogen on metals. *Journal of the Chemical Society, Faraday Transactions 1: Physical Chemistry in Condensed Phases* **68**, 229-236 (1972).

156 Andersen, M., Levchenko, S. V., Scheffler, M. & Reuter, K. Beyond Scaling Relations for the Description of Catalytic Materials. *ACS Catal.* **9**, 2752 (2019).

157 Mazheika, A. *et al.* Ab initio data-analytics study of carbon-dioxide activation on semiconductor oxide surfaces (2021).

158 Ghiringhelli, L. M., Vybiral, J., Levchenko, S. V., Draxl, C. & Scheffler, M. Big data of materials science: Critical role of the descriptor. *Phys. Rev. Lett.* **114**, 105503 (2015).

159 Ghiringhelli, L. M. *et al.* Learning physical descriptors for materials science by compressed sensing. *New Journal of Physics* **19**, 023017 (2017).

160 Kresse, G. & Hafner, J. Ab initio molecular dynamics for liquid metals. *Phys. Rev. B* **47**, 558-561 (1993).

161 Kresse, G. & Hafner, J. Ab initio molecular dynamics for open-shell transition metals. *Physical Review B* **48**, 13115-13118 (1993).

162 Kresse, G. & Hafner, J. Ab-initio molecular-dynamics simulation of the liquid-metal amorphous-semiconductor transition in germanium *Phys. Rev. B* **49**, 14251-14269 (1994).

163 Kresse, G. & Joubert, D. From ultrasoft pseudopotentials to the projector augmented-wave method. *Physical Review B* **59**, 1758-1775 (1999).

164 Wen, Y. & Zhang, J. J. S. S. C. Surface energy calculation of the fcc metals by using the MAEAM. **144**, 163-167 (2007).

165 Zhang, J.-M., Wang, D.-D. & Xu, K.-W. Calculation of the surface energy of hcp metals by using the modified embedded atom method. *Applied Surface Science* **253**, 2018-2024 (2006).

166 Hofmann, P. The surfaces of bismuth: Structural and electronic properties. *Progress in Surface Science* **81**, 191-245 (2006).

167 Che, J. G., Chan, C. T., Jian, W. E. & Leung, T. C. Surface atomic structures, surface energies, and equilibrium crystal shape of molybdenum. *Physical Review B* **57**, 1875-1880 (1998).

168 Safavi, A., Kazemi, S. H. & Kazemi, H. Electrocatalytic behaviors of silver–palladium nanoalloys modified carbon ionic liquid electrode towards hydrogen evolution reaction. *Fuel* **118**, 156-162 (2014).

169 Kawashima, K. *et al.* Cobalt Metal–Cobalt Carbide Composite Microspheres for Water Reduction Electrocatalysis. *ACS Applied Energy Materials* **3**, 3909-3918 (2020).

170 Li, J., Stenlid, J. H., Ludwig, T., Lamoureux, P. S. & Abild-Pedersen, F. Modeling Potential-Dependent Electrochemical Activation Barriers: Revisiting the Alkaline Hydrogen Evolution Reaction. *Journal of the American Chemical Society* **143**, 19341-19355 (2021).

171 Kronberg, R., Lappalainen, H. & Laasonen, K. Revisiting the Volmer–Heyrovský mechanism of hydrogen evolution on a nitrogen doped carbon nanotube: constrained

molecular dynamics versus the nudged elastic band method. *Physical Chemistry Chemical Physics* **22**, 10536-10549 (2020).

172 Yang, T. T., Tan, T. L. & Saidi, W. A. High Activity toward the Hydrogen Evolution Reaction on the Edges of MoS2-Supported Platinum Nanoclusters Using Cluster Expansion and Electrochemical Modeling. *Chemistry of Materials* **32**, 1315-1321 (2020).

173 Sun, T. *et al.* Engineering the Coordination Environment of Single Cobalt Atoms for Efficient Oxygen Reduction and Hydrogen Evolution Reactions. *ACS Catalysis* **11**, 4498-4509 (2021).

174 Ding, J., Ji, Y., Li, Y. & Hong, G. Monoatomic Platinum-Embedded Hexagonal Close-Packed Nickel Anisotropic Superstructures as Highly Efficient Hydrogen Evolution Catalyst. *Nano Letters* **21**, 9381-9387 (2021).

175 Zhang, J. *et al.* Single-Atom Pt Anchored on Oxygen Vacancy of Monolayer $Ti_3C_2T_x$ for Superior Hydrogen Evolution. *Nano Letters* **22**, 1398-1405 (2022).

176 Jia, Y. *et al.* Stable Pd–Cu Hydride Catalyst for Efficient Hydrogen Evolution. *Nano Letters* **22**, 1391-1397 (2022).

177 Zhao, G. *et al.* Atomic-Level Modulation of the Interface Chemistry of Platinum–Nickel Oxide toward Enhanced Hydrogen Electrocatalysis Kinetics. *Nano Letters* **21**, 4845-4852 (2021).

178 Greeley, J. & Nørskov, J. K. Large-scale, density functional theory-based screening of alloys for hydrogen evolution. *Surface Science* **601**, 1590-1598 (2007).

179 Santos, E., Lundin, A., Pötting, K., Quaino, P. & Schmickler, W. Model for the electrocatalysis of hydrogen evolution. *Physical Review B* **79**, 235436 (2009).

180 Xiao, Y., Shen, C. & Long, T. Theoretical Establishment and Screening of an Efficient Catalyst for N_2 Electroreduction on Two-Dimensional Transition-Metal Borides (MBenes). *Chemistry of Materials* **33**, 4023-4034 (2021).

181 Zhang, Y.-J., Sethuraman, V., Michalsky, R. & Peterson, A. A. Competition between CO_2 Reduction and H2 Evolution on Transition-Metal Electrocatalysts. *ACS Catalysis* **4**, 3742-3748 (2014).

182 Gauthier, J. A. *et al.* Transition Metal Arsenide Catalysts for the Hydrogen Evolution Reaction. *The Journal of Physical Chemistry C* **123**, 24007-24012 (2019).

183 Abghoui, Y. & Skúlason, E. Hydrogen Evolution Reaction Catalyzed by Transition-Metal Nitrides. *The Journal of Physical Chemistry C* **121**, 24036-24045 (2017).

184 Tang, Q. & Jiang, D.-e. Mechanism of Hydrogen Evolution Reaction on 1T-MoS_2 from First Principles. *ACS Catalysis* **6**, 4953-4961 (2016).

185 Di Liberto, G., Cipriano, L. A. & Pacchioni, G. Role of Dihydride and Dihydrogen Complexes in Hydrogen Evolution Reaction on Single-Atom Catalysts. *Journal of the American Chemical Society* **143**, 20431-20441 (2021).

186 Feng, G. *et al.* Sub-2 nm Ultrasmall High-Entropy Alloy Nanoparticles for Extremely Superior Electrocatalytic Hydrogen Evolution. *Journal of the American Chemical Society* **143**, 17117-17127 (2021).

187 Li, Y. *et al.* Hydrogen Evolution Electrocatalyst Design: Turning Inert Gold into Active Catalyst by Atomically Precise Nanochemistry. *Journal of the American Chemical Society* **143**, 11102-11108 (2021).

188 Gu, G. H. *et al.* Autobifunctional Mechanism of Jagged Pt Nanowires for Hydrogen Evolution Kinetics via End-to-End Simulation. *Journal of the American Chemical Society* **143**, 5355-5363 (2021).

189 Yang, T. T., Patil, R. B., McKone, J. R. & Saidi, W. A. Revisiting trends in the exchange current for hydrogen evolution. *Catalysis Science & Technology* **11**, 6832-6838 (2021).

190 Guidelli, R. *et al.* Defining the transfer coefficient in electrochemistry: An assessment (IUPAC Technical Report) %J Pure and Applied Chemistry. **86**, 245-258 (2014).

191 Dickinson, E. J. F. & Wain, A. J. The Butler-Volmer equation in electrochemical theory: Origins, value, and practical application. *Journal of Electroanalytical Chemistry* **872**, 114145 (2020).

192 Rheinländer, P. J., Herranz, J., Durst, J. & Gasteiger, H. A. Kinetics of the Hydrogen Oxidation/Evolution Reaction on Polycrystalline Platinum in Alkaline Electrolyte Reaction Order with Respect to Hydrogen Pressure. *Journal of The Electrochemical Society* **161**, F1448-F1457 (2014).

193 Durst, J. *et al.* New insights into the electrochemical hydrogen oxidation and evolution reaction mechanism. *Energy & Environmental Science* **7**, 2255-2260 (2014).

194 Huang, Y., Nielsen, R. J. & Goddard, W. A. Reaction Mechanism for the Hydrogen Evolution Reaction on the Basal Plane Sulfur Vacancy Site of MoS2 Using Grand Canonical Potential Kinetics. *Journal of the American Chemical Society* **140**, 16773-16782 (2018).

195 Dreyer, W., Guhlke, C. & Müller, R. A new perspective on the electron transfer: recovering the Butler–Volmer equation in non-equilibrium thermodynamics. *Physical Chemistry Chemical Physics* **18**, 24966-24983 (2016).

196 Liu, S. *et al.* Butler–Volmer-Equation-Based Electrical Model for High-Power Lithium Titanate Batteries Used in Electric Vehicles. *IEEE Transactions on Industrial Electronics* **62**, 7557-7568 (2015).

197 Fraggedakis, D. *et al.* Theory of coupled ion-electron transfer kinetics. *Electrochimica Acta* **367**, 137432 (2021).

198 Allagui, A., Benaoum, H. & Wang, C. Deformed Butler–Volmer Models for Convex Semilogarithmic Current-Overpotential Profiles of Li-ion Batteries. *The Journal of Physical Chemistry C* **126**, 3029-3036 (2022).

199 Azhagurajan, M., Kajita, T., Itoh, T., Kim, Y.-G. & Itaya, K. In Situ Visualization of Lithium Ion Intercalation into MoS2 Single Crystals using Differential Optical Microscopy with Atomic Layer Resolution. *Journal of the American Chemical Society* **138**, 3355-3361 (2016).

200 Noren, D. A. & Hoffman, M. A. Clarifying the Butler–Volmer equation and related approximations for calculating activation losses in solid oxide fuel cell models. *Journal of Power Sources* **152**, 175-181 (2005).

201 Vijay, P. & Tadé, M. O. Improved approximation for the Butler-Volmer equation in fuel cell modelling. *Computers & Chemical Engineering* **102**, 2-10 (2017).

202 Li, Q. & Li, G. Modeling of the solid oxide fuel cell anode based on a new analytical model using nonlinear Butler-Volmer expression. *Ionics* **27**, 3063-3076 (2021).

203 Jiang, H., Yang, Y., Sun, S. & Yu, J. Adsorption of lithium ions on lithium-aluminum hydroxides: Equilibrium and kinetics. *The Canadian Journal of Chemical Engineering* **98**, 544-555 (2020).

204 Recepoğlu, Y. K. *et al.* Equilibrium and Kinetic Studies on Lithium Adsorption from Geothermal Water by λ-MnO2. *Solvent Extraction and Ion Exchange* **35**, 221-231 (2017).

205 Zhong, J., Lin, S. & Yu, J. Li+ adsorption performance and mechanism using lithium/aluminum layered double hydroxides in low grade brines. *Desalination* **505**, 114983 (2021).

206 Levi, M. D. & Aurbach, D. Frumkin intercalation isotherm — a tool for the description of lithium insertion into host materials: a review. *Electrochimica Acta* **45**, 167-185 (1999).

207 Lane, J. M. D., Leung, K., Thompson, A. P. & Cuneo, M. E. Water desorption from rapidly-heated metal oxide surfaces—first principles, molecular dynamics, and the Temkin isotherm. *Journal of Physics: Condensed Matter* **30**, 465002 (2018).

208 Foo, K. Y. & Hameed, B. H. Insights into the modeling of adsorption isotherm systems. *Chemical Engineering Journal* **156**, 2-10 (2010).

209 Hossain, M. D., Huang, Y., Yu, T. H., Goddard Iii, W. A. & Luo, Z. Reaction mechanism and kinetics for CO_2 reduction on nickel single atom catalysts from quantum mechanics. *Nature Communications* **11**, 2256 (2020).

210 van Ede, M. C., Earls, C. J., Fichtner, A. & Angst, U. Electrochemical tomography as a nondestructive technique to study localized corrosion of metals. *npj Materials Degradation* **5**, 58 (2021).

211 Bai, P. & Bazant, M. Z. Charge transfer kinetics at the solid–solid interface in porous electrodes. *Nature Communications* **5**, 3585 (2014).

212 Ahn, H. S. & Bard, A. J. Electrochemical Surface Interrogation of a MoS_2 Hydrogen-Evolving Catalyst: In Situ Determination of the Surface Hydride Coverage and the

Hydrogen Evolution Kinetics. *The Journal of Physical Chemistry Letters* **7**, 2748-2752 (2016).

213 Tanaka, S., Tajiri, H., Sakata, O., Hoshi, N. & Nakamura, M. Interfacial Structure of Pt(110) Electrode during Hydrogen Evolution Reaction in Alkaline Solutions. *The Journal of Physical Chemistry Letters* **13**, 8403-8408 (2022).

214 Tan, S., Ji, Y. & Li, Y. Single-Atom Electrocatalysis for Hydrogen Evolution Based on the Constant Charge and Constant Potential Models. *The Journal of Physical Chemistry Letters* **13**, 7036-7042 (2022).

215 Yang, Y. *et al.* Electronic Modulation of Pt Nanoparticles on Ni_3N–Mo_2C by Support-Induced Strategy for Accelerating Hydrogen Oxidation and Evolution. *The Journal of Physical Chemistry Letters* **13**, 2107-2116 (2022).

216 Pandit, N. K., Roy, D., Mandal, S. C. & Pathak, B. Rational Designing of Bimetallic/Trimetallic Hydrogen Evolution Reaction Catalysts Using Supervised Machine Learning. *The Journal of Physical Chemistry Letters* **13**, 7583-7593 (2022).

217 Sen, P., Alam, K., Das, T., Banerjee, R. & Chakraborty, S. Combinatorial Design and Computational Screening of Two-Dimensional Transition Metal Trichalcogenide Monolayers: Toward Efficient Catalysts for Hydrogen Evolution Reaction. *The Journal of Physical Chemistry Letters* **11**, 3192-3197 (2020).

218 Saidi, W. A., Nandi, T. & Yang, T. Designing multinary noble metal-free catalyst for hydrogen evolution reaction. *Electrochemical Science Advances*, e2100224

219 Yang, T. T. *et al.* Computationally Guided Design to Accelerate Discovery of Doped β-Mo_2C Catalysts toward Hydrogen Evolution Reaction. *ACS Catalysis* **12**, 11791-11800 (2022).

220 Leonard, K. C. & Bard, A. J. The Study of Multireactional Electrochemical Interfaces via a Tip Generation/Substrate Collection Mode of Scanning Electrochemical Microscopy: The Hydrogen Evolution Reaction for Mn in Acidic Solution. *Journal of the American Chemical Society* **135**, 15890-15896 (2013).

221 Liang, Z., Ahn, H. S. & Bard, A. J. A Study of the Mechanism of the Hydrogen Evolution Reaction on Nickel by Surface Interrogation Scanning Electrochemical Microscopy. *Journal of the American Chemical Society* **139**, 4854-4858 (2017).

222 Costentin, C. & Savéant, J.-M. Catalysis of Electrochemical Reactions by Surface-Active Sites: Analyzing the Occurrence and Significance of Volcano Plots by Cyclic Voltammetry. *ACS Catalysis* **7**, 4876-4880 (2017).

223 Karlberg, G. S. *et al.* Cyclic Voltammograms for H on Pt(111) and Pt(100) from First Principles. *Physical Review Letters* **99**, 126101 (2007).

224 Yang, T. T. & Saidi, W. A. Reconciling the Volcano Trend with the Butler–Volmer Model for the Hydrogen Evolution Reaction. *The Journal of Physical Chemistry Letters* **13**, 5310-5315 (2022).

225 Bard, A. J. & Faulkner, L. R. Electrochemical Method. *John Wiley & Sons, Inc. 2* (2001).

226 Conway, B. E. & Bockris, J. O. M. Electrolytic Hydrogen Evolution Kinetics and Its Relation to the Electronic and Adsorptive Properties of the Metal. **26**, 532-541 (1957).

227 Bockris, J. O. M., McBreen, J. & Nanis, L. The Hydrogen Evolution Kinetics and Hydrogen Entry into a-Iron. *Journal of The Electrochemical Society* **112**, 1025 (1965).

228 Bockris, J. O. M. & Potter, E. C. The Mechanism of Hydrogen Evolution at Nickel Cathodes in Aqueous Solutions. **20**, 614-628 (1952).

229 Montero, M. A., Fernández, J. L., Gennero de Chialvo, M. R. & Chialvo, A. C. Kinetic Study of the Hydrogen Oxidation Reaction on Nanostructured Iridium Electrodes in Acid Solutions. *The Journal of Physical Chemistry C* **117**, 25269-25275 (2013).

230 Ono, Y. *et al.* The Analysis of Performance Loss with Low Platinum Loaded Cathode Catalyst Layers. *ECS Transactions* **28**, 69-78 (2010).

231 Greszler, T. A., Caulk, D. & Sinha, P. The Impact of Platinum Loading on Oxygen Transport Resistance. *Journal of The Electrochemical Society* **159**, F831-F840 (2012).

232 Garcia-Garcia, R., Rivera, J. G., Antaño-Lopez, R., Castañeda-Olivares, F. & Orozco, G. Impedance spectra of the cathodic hydrogen evolution reaction on polycrystalline rhenium. *International Journal of Hydrogen Energy* **41**, 4660-4669 (2016).

233 Bard, A. J. & Faulkner, L. R. Electrochemical Methods - Fundamentals and Applications. *John Wiley & Sons, Inc.* (2001).

234 Marcus, R. A. On the Theory of Oxidation-Reduction Reactions Involving Electron Transfer. I. *The Journal of Chemical Physics* **24**, 966-978 (1956).

235 Marcus, R. A. On the Theory of Electron-Transfer Reactions. VI. Unified Treatment for Homogeneous and Electrode Reactions. *The Journal of Chemical Physics* **43**, 679-701 (1965).

236 Bajdich, M., García-Mota, M., Vojvodic, A., Nørskov, J. K. & Bell, A. T. Theoretical Investigation of the Activity of Cobalt Oxides for the Electrochemical Oxidation of Water. *Journal of the American Chemical Society* **135**, 13521-13530 (2013).

237 Conway, B. E. & Bai, L. Determination of adsorption of OPD H species in the cathodic hydrogen evolution reaction at Pt in relation to electrocatalysis. *Journal of Electroanalytical Chemistry and Interfacial Electrochemistry* **198**, 149-175 (1986).

238 Conway, B. E. & Tilak, B. V. Interfacial processes involving electrocatalytic evolution and oxidation of H2, and the role of chemisorbed H. *Electrochimica Acta* **47**, 3571-3594 (2002).

239 Li, C. *et al.* Ultrafast self-heating synthesis of robust heterogeneous nanocarbides for high current density hydrogen evolution reaction. *Nature Communications* **13**, 3338 (2022).

240 Li, Y. *et al.* MoS2 nanoparticles grown on graphene: an advanced catalyst for the hydrogen evolution reaction. *J Am Chem Soc* **133**, 7296-7299 (2011).

241 Cao, D. *et al.* Volcano-type relationship between oxidation states and catalytic activity of single-atom catalysts towards hydrogen evolution. *Nature Communications* **13**, 5843 (2022).

242 Li, Q. *et al.* Local Structure Insight into Hydrogen Evolution Reaction with Bimetal Nanocatalysts. *Journal of the American Chemical Society* **144**, 20298-20305 (2022).

243 Zhao, Y. *et al.* Non-metal Single-Iodine-Atom Electrocatalysts for the Hydrogen Evolution Reaction. *Angewandte Chemie International Edition* **58**, 12252-12257 (2019).

244 Zhou, S. *et al.* Boosting Hydrogen Evolution Reaction by Phase Engineering and Phosphorus Doping on Ru/P-TiO2. *Angewandte Chemie International Edition* **61**, e202212196 (2022).

245 Shen, L.-f. *et al.* Interfacial Structure of Water as a New Descriptor of the Hydrogen Evolution Reaction. *Angewandte Chemie International Edition* **59**, 22397-22402 (2020).

246 Zheng, J., Yan, Y. & Xu, B. Correcting the Hydrogen Diffusion Limitation in Rotating Disk Electrode Measurements of Hydrogen Evolution Reaction Kinetics. *Journal of The Electrochemical Society* **162**, F1470 (2015).

247 Steinmann, S. N. & Corminboeuf, C. Comprehensive Benchmarking of a Density-Dependent Dispersion Correction. *Journal of Chemical Theory and Computation* **7**, 3567-3577 (2011).

248 Steinmann, S. N. & Corminboeuf, C. A generalized-gradient approximation exchange hole model for dispersion coefficients. **134**, 044117 (2011).

249 Bockris, J. O. M., Ammar, I. A. & Huq, A. K. M. S. The Mechanism of the Hydrogen Evolution Reaction on Platinum, Silver and Tungsten surfaces in Acid Solutions. *J. Phys. Chem* **61**, 879-886 (1957).

250 Lua, J., Hugossonb, H., Erikssonb, O., NordstroÈmb, L. & Janssona, U. Chemical vapour deposition of molybdenum carbides: aspects of phase stability. *Thin Solid Films* **370** 203-212 (2000).

251 Wan, C., Regmi, Y. N. & Leonard, B. M. Multiple phases of molybdenum carbide as electrocatalysts for the hydrogen evolution reaction. *Angew Chem Int Ed Engl* **53**, 6407-6410 (2014).

252 Liao, L. *et al.* A nanoporous molybdenum carbide nanowire as an electrocatalyst for hydrogen evolution reaction. *Energy Environ. Sci.* **7**, 387-392 (2014).

253 Chen, J. *et al.* Porous molybdenum carbide microspheres as efficient binder-free electrocatalysts for suspended hydrogen evolution reaction. *International Journal of Hydrogen Energy* **42**, 6448-6454 (2017).

254 Meng, T., Zheng, L., Qin, J., Zhao, D. & Cao, M. A three-dimensional hierarchically porous Mo_2C architecture: salt-template synthesis of a robust electrocatalyst and anode material towards the hydrogen evolution reaction and lithium storage. *J. Mater. Chem. A* **5**, 20228-20238 (2017).

255 Wu, H. B., Xia, B. Y., Yu, L., Yu, X. Y. & Lou, X. W. Porous molybdenum carbide nano-octahedrons synthesized via confined carburization in metal-organic frameworks for efficient hydrogen production. *Nat Commun* **6**, 6512 (2015).

256 Deng, Y. *et al.* Enhanced Electrochemical Performance in Ni-Doped $LiMn_2O_4$-Based Composite Cathodes for Lithium-Ion Batteries. *ChemElectroChem* **4**, 1362-1371 (2017).

257 Politi, J. R., Vines, F., Rodriguez, J. A. & Illas, F. Atomic and electronic structure of molybdenum carbide phases: bulk and low Miller-index surfaces. *Phys Chem Chem Phys* **15**, 12617-12625 (2013).

258 Kitchin, J. R., Nørskov, J. K., Barteau, M. A. & Chen, J. G. Trends in the chemical properties of early transition metal carbide surfaces: A density functional study. *Catalysis Today* **105**, 66-73 (2005).

259 Liu, Y. *et al.* Coupling Mo2C with Nitrogen-Rich Nanocarbon Leads to Efficient Hydrogen-Evolution Electrocatalytic Sites. *Angew Chem Int Ed Engl* **54**, 10752-10757 (2015).

260 Ma, R. *et al.* Ultrafine Molybdenum Carbide Nanoparticles Composited with Carbon as a Highly Active Hydrogen-Evolution Electrocatalyst. *Angew Chem Int Ed Engl* **54**, 14723-14727 (2015).

261 Pan, L. F. *et al.* Molybdenum carbide stabilized on graphene with high electrocatalytic activity for hydrogen evolution reaction. *Chem Commun (Camb)* **50**, 13135-13137 (2014).

262 Li, J. S. *et al.* Coupled molybdenum carbide and reduced graphene oxide electrocatalysts for efficient hydrogen evolution. *Nat Commun* **7**, 11204 (2016).

263 Huang, Y. *et al.* Mo_2C Nanoparticles Dispersed on Hierarchical Carbon Microflowers for Efficient Electrocatalytic Hydrogen Evolution. *ACS Nano* **10**, 11337-11343 (2016).

264 Youn, D. H. *et al.* Highly Active and Stable Hydrogen Evolution Electrocatalysts Based on Molybdenum Compounds on Carbon Nanotube Graphene Hybrid Support. *Acs Nano* **8**, 5164-5173 (2014).

265 Zhang, K., Zhao, Y., Fu, D. & Chen, Y. Molybdenum carbide nanocrystal embedded N-doped carbon nanotubes as electrocatalysts for hydrogen generation. *Journal of Materials Chemistry A* **3**, 5783-5788 (2015).

266 Tsai, C., Abild-Pedersen, F. & Nørskov, J. K. Tuning the MoS_2 Edge-Site Activity for Hydrogen Evolution via Support Interactions. *Nano Lett.* **14**, 7 (2014).

267 Wang, J. *et al.* Graphene Porous Foam Loaded with Molybdenum Carbide Nanoparticulate Electrocatalyst for Effective Hydrogen Generation. *ChemSusChem* **9**, 855-862 (2016).

268 Geim, A. K. & Grigorieva, I. V. Van der Waals heterostructures. *Nature* **499**, 419-425 (2013).

269 Ge, L. *et al.* Predicted Optimal Bifunctional Electrocatalysts for the Hydrogen Evolution Reaction and the Oxygen Evolution Reaction Using Chalcogenide Heterostructures Based on Machine Learning Analysis of in Silico Quantum Mechanics Based High Throughput Screening. *The Journal of Physical Chemistry Letters* **11**, 869-876 (2020).

270 Wu, C. *et al.* Monoatomic Platinum-Anchored Metallic MoS_2: Correlation between Surface Dopant and Hydrogen Evolution. *The Journal of Physical Chemistry Letters* **10**, 6081-6087 (2019).

271 Zheng, Y. *et al.* Hydrogen evolution by a metal-free electrocatalyst. **5**, 3783 (2014).

272 Biroju, R. K. *et al.* Hydrogen Evolution Reaction Activity of Graphene–MoS_2 van der Waals Heterostructures. *ACS Energy Letters* **2**, 1355-1361 (2017).

273 Zur, A. & McGill, T. C. Lattice match: An application to heteroepitaxy. *Journal of applied physics* **55**, 378-386 (1984).

274 Vines, F., Sousa, C., Liu, P., Rodriguez, J. A. & Illas, F. A systematic density functional theory study of the electronic structure of bulk and (001) surface of transition-metals carbides. *J Chem Phys* **122**, 174709 (2005).

275 Tian, W., Li, W., Yu, W. & Liu, X. A Review on Lattice Defects in Graphene: Types, Generation, Effects and Regulation. *Micromachines* **8**, 163 (2017).

276 Yang, T. T. & Saidi, W. A. Tuning the hydrogen evolution activity of beta-Mo_2C nanoparticles via control of their growth conditions. *Nanoscale* **9**, 3252-3260 (2017).

277 Goler, S. *et al.* Influence of Graphene Curvature on Hydrogen Adsorption: Toward Hydrogen Storage Devices. *The Journal of Physical Chemistry C* **117**, 11506-11513 (2013).

278 Pan, H. Waved graphene: Unique structure for the adsorption of small molecules. *Materials Chemistry and Physics* **189**, 111-117 (2017).

279 Tada, K., Furuya, S. & Watanabe, K. Ab initio study of hydrogen adsorption to single-walled carbon nanotubes. *PHYSICAL REVIEW B* **63** (2001).

280 Hornekaer, L. *et al.* Clustering of chemisorbed H(D) atoms on the graphite (0001) surface due to preferential sticking. *Phys Rev Lett* **97**, 186102 (2006).

281 Saidi, W. A. Oxygen Reduction Electrocatalysis Using N-Doped Graphene Quantum-Dots. *The Journal of Physical Chemistry Letters* **4**, 4160-4165 (2013).

282 Skulason, E. *et al.* Density functional theory calculations for the hydrogen evolution reaction in an electrochemical double layer on the Pt(111) electrode. *Phys Chem Chem Phys* **9**, 3241-3250 (2007).

283 Chan, K. & Norskov, J. K. Potential Dependence of Electrochemical Barriers from ab Initio Calculations. *J Phys Chem Lett* **7**, 1686-1690 (2016).

284 Chan, K. & Norskov, J. K. Electrochemical Barriers Made Simple. *J Phys Chem Lett* **6**, 2663-2668 (2015).

285 Shinagawa, T., Garcia-Esparza, A. T. & Takanabe, K. Insight on Tafel slopes from a microkinetic analysis of aqueous electrocatalysis for energy conversion. *Sci Rep* **5**, 13801 (2015).

286 Butler, J. A. V. Studies in heterogeneous equilibria. Part II.—The kinetic interpretation of the nernst theory of electromotive force. *Transactions of the Faraday Society* **19**, 729-733 (1924).

287 Guidelli, R. *et al.* Defining the transfer coefficient in electrochemistry: An assessment (IUPAC Technical Report). *Pure and Applied Chemistry* **86**, 245-258 (2014).

288 Yang, X. *et al.* N-Doped graphene-coated molybdenum carbide nanoparticles as highly efficient electrocatalysts for the hydrogen evolution reaction. *Journal of Materials Chemistry A* **4**, 3947-3954 (2016).

289 Wei, H. *et al.* Molybdenum Carbide Nanoparticles Coated into the Graphene Wrapping N-Doped Porous Carbon Microspheres for Highly Efficient Electrocatalytic Hydrogen Evolution Both in Acidic and Alkaline Media. *Adv Sci (Weinh)* **5**, 1700733 (2018).

290 Pizzochero, M., Leenaerts, O., Partoens, B., Martinazzo, R. & Peeters, F. M. Hydrogen adsorption on nitrogen and boron doped graphene. *J Phys Condens Matter* **27**, 425502 (2015).

291 Huang, L. F. *et al.* Modulation of the thermodynamic, kinetic, and magnetic properties of the hydrogen monomer on graphene by charge doping. *J Chem Phys* **135**, 064705 (2011).

292 Tuomi, S., Guil-Lopez, R. & Kallio, T. Molybdenum carbide nanoparticles as a catalyst for the hydrogen evolution reaction and the effect of pH. *Journal of Catalysis* **334**, 102-109 (2016).

293 Gong, P. L., Huang, L. F., Zheng, X. H., Zhang, Y. S. & Zeng, Z. Nonlocal and Local Electrochemical Effects of Doping Impurities on the Reactivity of Graphene. *The Journal of Physical Chemistry C* **119**, 10513-10519 (2015).

294 Wang, L., Sofer, Z. & Pumera, M. Will Any Crap We Put into Graphene Increase Its Electrocatalytic Effect? *ACS Nano* **14**, 21-25 (2020).

295 Henkelman, G., Uberuaga, B. P. & Jónsson, H. A climbing image nudged elastic band method for finding saddle points and minimum energy paths. *The Journal of Chemical Physics* **113**, 9901-9904 (2000).

296 Eigen, M. Proton transfer, acid-base aatalysis, and enzymatic hydrolysis. *Angew Chem Int Ed Engl* **3**, 72 (1964).

297 Ogasawara, H. *et al.* Structure and bonding of water on Pt(111). *Phys Rev Lett* **89**, 276102 (2002).

298 Hugosson, H. W., Eriksson, O. & Nordström, L. Theory of phase stabilities and bonding mechanisms in stoichiometric and substoichiometric molybdenum carbide. *J. Appl. Phys.* **86** (1999).

299 KuO, K. & HÄGG, G. A New Molybdenum Carbide. *Nature* **170** (1952).

300 Gao, W., Xiao, P., Henkelman, G., Liechti, K. M. & Huang, R. Interfacial adhesion between graphene and silicon dioxide by density functional theory with van der Waals corrections. *Journal of Physics D: Applied Physics* **47** (2014).

301 Dresselhaus, M. S. & Thomas, I. L. Alternative energy technologies. *Nature* **414**, 332+ (2001).

302 Parsons, R. The Rate of Electrolytic Hydrogen Evolution and the Heat of Adsorption of Hydrogen *Trans. Faraday Soc.* **54**, 1053-1063 (1957).

303 Jiang, K. *et al.* Single platinum atoms embedded in nanoporous cobalt selenide as electrocatalyst for accelerating hydrogen evolution reaction. *Nat Commun* **10**, 1743 (2019).

304 Zhang, H. *et al.* Dynamic traction of lattice-confined platinum atoms into mesoporous carbon matrix for hydrogen evolution reaction. *Science Advances* **4**, eaao6657 (2018).

305 Zhang, J. *et al.* Single platinum atoms immobilized on an MXene as an efficient catalyst for the hydrogen evolution reaction. *Nature Catalysis* **1**, 985-992 (2018).

306 Grigoriev, S. A., Millet, P. & Fateev, V. N. Evaluation of carbon-supported Pt and Pd nanoparticles for the hydrogen evolution reaction in PEM water electrolysers. *Journal of Power Sources* **177**, 281-285 (2008).

307 Cheng, N. *et al.* Platinum single-atom and cluster catalysis of the hydrogen evolution reaction. *Nat Commun* **7**, 13638 (2016).

308 Proch, S., Wirth, M., White, H. S. & Anderson, S. L. Strong effects of cluster size and air exposure on oxygen reduction and carbon oxidation electrocatalysis by size-selected Pt(n) (n </= 11) on glassy carbon electrodes. *J Am Chem Soc* **135**, 3073-3086 (2013).

309 Tsunoyama, H. *et al.* Size-Effect on Electrochemical Hydrogen Evolution Reaction by SingleSize Platinum Nanocluster Catalysts Immobilized on Strontium Titanate. *Topics in Catalysis* **61**, 126–135 (2018).

310 Liao, H.-G. *et al.* Facet development during platinum nanocube growth. *Science* **345** (2014).

311 McCrum, I. T., Hickner, M. A. & Janik, M. J. First-Principles Calculation of Pt Surface Energies in an Electrochemical Environment: Thermodynamic Driving Forces for Surface Faceting and Nanoparticle Reconstruction. *Langmuir* **33**, 7043-7052 (2017).

312 B.E.Conway & B.V.Tilak. Interfacial processes involving electrocatalytic evolution and oxidation of H2, and the role of chemisorbed H. *Electrochimica Acta* **47**, 3571-3594 (2002).

313 Gomez, R., Fernandez-Vega, A., Feliu, J. M. & Aldaz, A. Hydrogen evolution on platinum single crystal surfaces: effects of irreversibly adsorbed bismuth and antimony on hydrogen adsorption and evolution on platinum (100). *The Journal of Physical Chemistry* **97**, 4769-4776 (1993).

314 Tan, T. L., Wang, L.-L., Zhang, J., Johnson, D. D. & Bai, K. Platinum Nanoparticle During Electrochemical Hydrogen Evolution: Adsorbate Distribution, Active Reaction Species, and Size Effect. *ACS Catalysis* **5**, 2376-2383 (2015).

315 Zalitis, C. M., Kucernak, A. R., Sharman, J. & Wright, E. Design principles for platinum nanoparticles catalysing electrochemical hydrogen evolution and oxidation reactions: edges are much more active than facets. *Journal of Materials Chemistry A* **5**, 23328-23338 (2017).

316 Wei, G. F. & Liu, Z. P. Restructuring and Hydrogen Evolution on Pt Nanoparticle. *Chem Sci* **6**, 1485-1490 (2015).

317 Voiry, D. *et al*. Conducting MoS(2) nanosheets as catalysts for hydrogen evolution reaction. *Nano Lett* **13**, 6222-6227 (2013).

318 Tsai, C., Abild-Pedersen, F. & Norskov, J. K. Tuning the MoS_2 edge-site activity for hydrogen evolution via support interactions. *Nano Lett* **14**, 1381-1387 (2014).

319 Zhou, M., Bao, S. & Bard, A. J. Probing Size and Substrate Effects on the Hydrogen Evolution Reaction by Single Isolated Pt Atoms, Atomic Clusters, and Nanoparticles. *J Am Chem Soc* **141**, 7327-7332 (2019).

320 Sheng, W., Gasteiger, H. A. & Shao-Horn, Y. Hydrogen Oxidation and Evolution Reaction Kinetics on Platinum: Acid vs Alkaline Electrolytes. *J. Electrochem. Soc.* **157**, B1529-B1536 (2010).

321 Zheng, J., Yan, Y. & Xu, B. Correcting the Hydrogen Diffusion Limitation in Rotating Disk Electrode Measurements of Hydrogen Evolution Reaction Kinetics. *Journal of The Electrochemical Society* **162**, F1470-F1481 (2015).

322 VandeVondele, J. *et al.* Quickstep: Fast and accurate density functional calculations using a mixed Gaussian and plane waves approach. *Computer Physics Communications* **167**, 103-128 (2005).

323 Shi, Y., Song, B., Shahbazian-Yassar, R., Zhao, J. & Saidi, W. A. Experimentally Validated Structures of Supported Metal Nanoclusters on MoS2. *The Journal of Physical Chemistry Letters* **9**, 2972-2978 (2018).

324 Zarkevich, N. A., Tan, T. L. & Johnson, D. D. First-principles prediction of phase-segregating alloy phase diagrams and a rapid design estimate of their transition temperatures. *Physical Review B* **75** (2007).

325 Zarkevich, N. A., Tan, T. L., Wang, L. L. & Johnson, D. D. Low-energy antiphase boundaries, degenerate superstructures, and phase stability in frustrated fcc Ising model and Ag-Au alloys. *Physical Review B* **77** (2008).

326 Tsai, C. *et al.* Electrochemical generation of sulfur vacancies in the basal plane of MoS2 for hydrogen evolution. *Nat Commun* **8**, 15113 (2017).

327 Li, H. *et al.* Activating and optimizing MoS2 basal planes for hydrogen evolution through the formation of strained sulphur vacancies. *Nat Mater* **15**, 48-53 (2016).

328 Gnanasekar, P., Periyanagounder, D. & Kulandaivel, J. Vertically aligned MoS2 nanosheets on graphene for highly stable electrocatalytic hydrogen evolution reactions. *Nanoscale* **11**, 2439-2446 (2019).

329 Chase, M. W., Jr. NIST-JANAF Themochemical Tables, Fourth Edition *J. Phys. Chem. Ref. Data, Monograph 9*, 1-1951 (1998).

330 Chan, K. & Nørskov, J. K. Potential Dependence of Electrochemical Barriers from ab Initio Calculations. *The Journal of Physical Chemistry Letters* **7**, 1686-1690 (2016).

331 Watzele, S., Fichtner, J., Garlyyev, B., Schwämmlein, J. N. & Bandarenka, A. S. On the Dominating Mechanism of the Hydrogen Evolution Reaction at Polycrystalline Pt Electrodes in Acidic Media. *ACS Catalysis* **8**, 9456-9462 (2018).

332 Sheng, W. *et al.* Correlating hydrogen oxidation and evolution activity on platinum at different pH with measured hydrogen binding energy. *Nat Commun* **6**, 5848 (2015).

333 Elbert, K. *et al.* Elucidating Hydrogen Oxidation/Evolution Kinetics in Base and Acid by Enhanced Activities at the Optimized Pt Shell Thickness on the Ru Core. *ACS Catalysis* **5**, 6764-6772 (2015).

334 Kibsgaard, J. & Jaramillo, T. F. Molybdenum phosphosulfide: an active, acid-stable, earth-abundant catalyst for the hydrogen evolution reaction. *Angew Chem Int Ed Engl* **53**, 14433-14437 (2014).

335 Tsai, C., Abild-Pedersen, F. & Nørskov, J. K. Tuning the MoS_2 Edge-Site Activity for Hydrogen Evolution via Support Interactions. *Nano Letters* **14**, 1381-1387 (2014).

336 Wang, D., Li, Q., Han, C., Xing, Z. & Yang, X. Single-atom ruthenium based catalyst for enhanced hydrogen evolution. *Applied Catalysis B: Environmental* **249**, 91-97 (2019).

337 Ojani, R., Valiollahi, R. & Raoof, J.-B. Comparison between graphene supported Pt hollow nanospheres and graphene supported Pt solid nanoparticles for hydrogen evolution reaction. *Energy* **74**, 871-876 (2014).

338 Shinagawa, T., Garcia-Esparza, A. T. & Takanabe, K. Insight on Tafel slopes from a microkinetic analysis of aqueous electrocatalysis for energy conversion. *Scientific Reports* **5**, 13801 (2015).

339 Erdey-Gruz, T. Kinetics of Electrode Processes. *Adam Hilger, London*, 56–59 (1972).

340 Bockris, J. O. M., Ammar, I. A. & Huq, A. K. M. S. The Mechanism of the Hydrogen Evolution Reaction on Platinum, Silver and Tungsten surfaces in Acid Solutions. *The Journal of Physical Chemistry* **61**, 879-886 (1957).

341 Durst, J. *et al.* New insights into the electrochemical hydrogen oxidation and evolution reaction mechanism. *Energy Environ. Sci.* **7**, 2255-2260 (2014).

342 Rivard, E., Trudeau, M. & Zaghib, K. Hydrogen Storage for Mobility: A Review. **12**, 1973 (2019).

343 Griffiths, S., Sovacool, B. K., Kim, J., Bazilian, M. & Uratani, J. M. Industrial decarbonization via hydrogen: A critical and systematic review of developments, socio-technical systems and policy options. *Energy Research & Social Science* **80**, 102208 (2021).

344 National Academies of Sciences, E. & Medicine. *Advances, Challenges, and Long-Term Opportunities in Electrochemistry: Addressing Societal Needs: Proceedings of a Workshop—in Brief*. (The National Academies Press, 2020).

345 Humagain, G. *et al.* Highly Efficient, Biochar-Derived Molybdenum Carbide Hydrogen Evolution Electrocatalyst. *Advanced Energy Materials* (2018).

346 Huang, Y. *et al.* Nitrogen-Doped Porous Molybdenum Carbide and Phosphide Hybrids on a Carbon Matrix as Highly Effective Electrocatalysts for the Hydrogen Evolution Reaction. *Advanced Energy Materials* **8** (2018).

347 Politi, J. R. d. S., Viñes, F., Rodriguez, J. A. & Illas, F. Atomic and electronic structure of molybdenum carbide phases: bulk and low Miller-index surfaces. *Physical Chemistry Chemical Physics* **15**, 12617-12625 (2013).

348 Hugosson, H. W. *et al.* Theory of phase stabilities and bonding mechanisms in stoichiometric and substoichiometric molybdenum carbide. **86**, 3758-3767 (1999).

349 Baek, D. S., Lee, J., Kim, J. & Joo, S. H. Metastable Phase-Controlled Synthesis of Mesoporous Molybdenum Carbides for Efficient Alkaline Hydrogen Evolution. *ACS Catalysis* **12**, 7415-7426 (2022).

350 Tang, C. *et al.* Unconventional molybdenum carbide phases with high electrocatalytic activity for hydrogen evolution reaction. *Journal of Materials Chemistry A* **7**, 18030-18038 (2019).

351 Wu, H. B., Xia, B. Y., Yu, L., Yu, X.-Y. & Lou, X. W. Porous molybdenum carbide nano-octahedrons synthesized via confined carburization in metal-organic frameworks for efficient hydrogen production. *Nature Communications* **6**, 6512 (2015).

352 Chen, W. F. *et al.* Highly active and durable nanostructured molybdenum carbide electrocatalysts for hydrogen production. *Energy & Environmental Science* **6**, 943 (2013).

353 Sljukic, B. *et al.* Molybdenum Carbide Nanoparticles on Carbon Nanotubes and Carbon Xerogel: Low-Cost Cathodes for Hydrogen Production by Alkaline Water Electrolysis. *ChemSusChem* **9**, 1200-1208 (2016).

354 Youn, D. H. *et al.* Highly Active and Stable Hydrogen Evolution Electrocatalysts Based on Molybdenum Compounds on Carbon Nanotube–Graphene Hybrid Support. *ACS Nano* **8**, 5164-5173 (2014).

355 Wang, B., Wang, G. & Wang, H. Hybrids of Mo_2C nanoparticles anchored on graphene sheets as anode materials for high performance lithium-ion batteries. *J. Mater. Chem. A* **3**, 17403-17411 (2015).

356 He, C. & Tao, J. Exploration of the electrochemical mechanism of ultrasmall multiple phases molybdenum carbides nanocrystals for hydrogen evolution reaction. *RSC Adv.* **6**, 9240-9246 (2016).

357 He, C. & Tao, J. Synthesis of nanostructured clean surface molybdenum carbides on graphene sheets as efficient and stable hydrogen evolution reaction catalysts. *Chem Commun (Camb)* **51**, 8323-8325 (2015).

358 Liu, X. *et al.* Engineering Low-Coordination Single-Atom Cobalt on Graphitic Carbon Nitride Catalyst for Hydrogen Evolution. *ACS Catalysis* **12**, 5517-5526 (2022).

359 Ojha, K., Saha, S., Kolev, H., Kumar, B. & Ganguli, A. K. Composites of graphene-Mo 2 C rods: highly active and stable electrocatalyst for hydrogen evolution reaction. *Electrochimica Acta* **193**, 268-274 (2016).

360 Zhang, K., Zhao, Y., Fu, D. & Chen, Y. Molybdenum carbide nanocrystal embedded N-doped carbon nanotubes as electrocatalysts for hydrogen generation. *J. Mater. Chem. A* **3**, 5783-5788 (2015).

361 Lu, C. *et al.* Molybdenum Carbide-Embedded Nitrogen-Doped Porous Carbon Nanosheets as Electrocatalysts for Water Splitting in Alkaline Media. *ACS Nano* **11**, 3933-3942 (2017).

362 Cheng, Y. *et al.* An Ingenious Strategy to Integrate Multiple Electrocatalytically Active Components within a Well-Aligned Nitrogen-Doped Carbon Nanotube Array Electrode for Electrocatalysis. *ACS Catalysis* **11**, 3958-3974 (2021).

363 Tang, Y., Yang, C., Sheng, M., Yin, X. & Que, W. Synergistically Coupling Phosphorus-Doped Molybdenum Carbide with MXene as a Highly Efficient and Stable Electrocatalyst for Hydrogen Evolution Reaction. *ACS Sustainable Chemistry & Engineering* **8**, 12990-12998 (2020).

364 Chen, Y.-Y. *et al.* Pomegranate-like N,P-Doped Mo_2C@C Nanospheres as Highly Active Electrocatalysts for Alkaline Hydrogen Evolution. *ACS Nano* **10**, 8851-8860 (2016).

365 Jia, J. *et al.* Ultrathin N-Doped Mo_2C Nanosheets with Exposed Active Sites as Efficient Electrocatalyst for Hydrogen Evolution Reactions. *ACS Nano* **11**, 12509-12518 (2017).

366 Anjum, M. A. R., Lee, M. H. & Lee, J. S. Boron- and Nitrogen-Codoped Molybdenum Carbide Nanoparticles Imbedded in a BCN Network as a Bifunctional Electrocatalyst for Hydrogen and Oxygen Evolution Reactions. *ACS Catalysis* **8**, 8296-8305 (2018).

367 Ang, H. *et al.* Hydrophilic Nitrogen and Sulfur Co-doped Molybdenum Carbide Nanosheets for Electrochemical Hydrogen Evolution. *Small* **11**, 6278-6284 (2015).

368 Tang, C. *et al.* Sulfur-Decorated Molybdenum Carbide Catalysts for Enhanced Hydrogen Evolution. *ACS Catalysis* **5**, 6956-6963 (2015).

369 Wei, Z., Hu, X., Ning, S., Kang, X. & Chen, S. Supported Heterostructured MoC/Mo_2C Nanoribbons and Nanoflowers as Highly Active Electrocatalysts for Hydrogen Evolution Reaction. *ACS Sustainable Chemistry & Engineering* **7**, 8458-8465 (2019).

370 Liu, C. *et al.* Integration of Ni Doping and a Mo_2C/MoC Heterojunction for Hydrogen Evolution in Acidic and Alkaline Conditions. *ACS Applied Materials & Interfaces* **13**, 22646-22654 (2021).

371 Lin, H. *et al.* Heteronanowires of MoC–Mo_2C as efficient electrocatalysts for hydrogen evolution reaction. *Chemical Science* **7**, 3399-3405 (2016).

372 Liu, W. *et al.* A durable and pH-universal self-standing MoC–Mo_2C heterojunction electrode for efficient hydrogen evolution reaction. *Nature Communications* **12**, 6776 (2021).

373 Chen, Y. *et al.* Dual-phase MoC-Mo_2C nanosheets prepared by molten salt electrochemical conversion of CO_2 as excellent electrocatalysts for the hydrogen evolution reaction. *Nano Energy* **90**, 106533 (2021).

374 Upadhyay, S. & Pandey, O. P. Synthesis of Mo_2C/MoC/C nanocomposite for hydrogen evolution reaction. *Journal of Solid State Electrochemistry* **26**, 559-564 (2022).

375 Jeon, J. *et al.* Epitaxial Synthesis of Molybdenum Carbide and Formation of a Mo_2C/MoS_2 Hybrid Structure via Chemical Conversion of Molybdenum Disulfide. *ACS Nano* **12**, 338-346 (2018).

376 Jia, L. *et al.* Structure design of MoS_2@Mo_2C on nitrogen-doped carbon for enhanced alkaline hydrogen evolution reaction. *Journal of Materials Science* **55**, 16197-16210 (2020).

377 Zhao, Z. *et al.* Vertically Aligned MoS_2/Mo_2C hybrid Nanosheets Grown on Carbon Paper for Efficient Electrocatalytic Hydrogen Evolution. *ACS Catalysis* **7**, 7312-7318 (2017).

378 Zhang, K. *et al.* MoS_2 nanosheet/Mo_2C-embedded N-doped carbon nanotubes: synthesis and electrocatalytic hydrogen evolution performance. *Journal of Materials Chemistry A* **2**, 18715-18719 (2014).

379 Yu, F. *et al.* Electrocatalytic performance of ultrasmall Mo_2C affected by different transition metal dopants in hydrogen evolution reaction. *Nanoscale* **10**, 6080-6087 (2018).

380 Chen, M. *et al.* Influence of Transition Metal on the Hydrogen Evolution Reaction over Nano-Molybdenum-Carbide Catalyst. *Catalysts* **8**, 294 (2018).

381 Sun, F., Tang, Q. & Jiang, D.-e. Theoretical Advances in Understanding and Designing the Active Sites for Hydrogen Evolution Reaction. *ACS Catalysis*, 8404-8433 (2022).

382 Wang, F., Tian, X. & Jiao, H. Adsorption of CO, H_2, H_2O, and CO_2 on Fe-, Co-, Ni-, Cu-, Pd-, and Pt-Doped Mo_2C(101) Surfaces. *The Journal of Physical Chemistry C* **125**, 11419-11431 (2021).

383 Wang, T. *et al.* Stability of β-Mo_2C Facets from ab Initio Atomistic Thermodynamics. *The Journal of Physical Chemistry C* **115**, 22360-22368 (2011).

384 Luo, Y. *et al.* Morphology and surface chemistry engineering toward pH-universal catalysts for hydrogen evolution at high current density. *Nature Communications* **10**, 269 (2019).

385 Caliskan, S., Wang, A., Qin, F., House, S. D. & Lee, J.-K. Molybdenum Carbide-Reduced Graphene Oxide Composites as Electrocatalysts for Hydrogen Evolution. *ACS Applied Nano Materials* **5**, 3790-3798 (2022).

386 Shi, X.-R. *et al.* Structure and stability of β-Mo_2C bulk and surfaces: A density functional theory study. *Surface Science* **603**, 852-859 (2009).

387 Henkelman, G., Uberuaga, B. P. & Jo´nsson, H. A climbing image nudged elastic band method for finding saddle points and minimum energy paths. *J. Chem. Phys.* **113**, 9901 (2000).

388 Mitchell, D. R. G. Circular Hough transform diffraction analysis: A software tool for automated measurement of selected area electron diffraction patterns within Digital Micrograph™. *Ultramicroscopy* **108**, 367-374 (2008).

389 Kim, S. *et al.* Interaction Mediator Assisted Synthesis of Mesoporous Molybdenum Carbide: Mo-Valence State Adjustment for Optimizing Hydrogen Evolution. *ACS Nano* **14**, 4988-4999 (2020).

390 Durst, J., Simon, C., Hasché, F. & Gasteiger, H. A. Hydrogen Oxidation and Evolution Reaction Kinetics on Carbon Supported Pt, Ir, Rh, and Pd Electrocatalysts in Acidic Media. *Journal of The Electrochemical Society* **162**, F190 (2015).

391 Tian, X., Wang, T. & Jiao, H. Oxidation of the hexagonal $Mo_2C(101)$ surface by H2O dissociative adsorption. *Catalysis Science & Technology* **7**, 2789-2797 (2017).

392 Huang, X. *et al.* Unraveling the oxide layer on Mo_2C as the active center for hydrogen evolution reaction. *Journal of Catalysis* **389**, 461-467 (2020).

393 Lv, C. *et al.* The in situ removal of surface molybdenum oxide for making binder-free porous $Mo_{1.98}C_{1.02}$ film a more efficient electrocatalyst for alkaline rather than acidic hydrogen production. *Sustainable Energy & Fuels* **5**, 3373-3381 (2021).

394 Wu, C., Liu, D., Li, H. & Li, J. Molybdenum Carbide-Decorated Metallic Cobalt@Nitrogen-Doped Carbon Polyhedrons for Enhanced Electrocatalytic Hydrogen Evolution. *Small* **14**, 1704227 (2018).

395 Du, C.-F. *et al.* Ni-Directed biphase N-doped Mo_2C as an efficient hydrogen evolution catalyst in both acidic and alkaline conditions. *Dalton Transactions* **51**, 6464-6472 (2022).